

SCIENCES

MECHANICS

Biomechanics

Biological Flow in Large Vessels

*Dialog Between Numerical Modeling
and In Vitro/In Vivo Experiments*

**Coordinated by
Valérie Deplano
José-Maria Fullana
Claude Verdier**

ISTE

WILEY

Biological Flow in Large Vessels

SCIENCES

Mechanics, Field Director – Gilles Pijaudier-Cabot

Biomechanics, Subject Head – Claude Verdier

Biological Flow in Large Vessels

*Dialog Between Numerical Modeling
and In Vitro/In Vivo Experiments*

Coordinated by
Valérie Deplano
José-Maria Fullana
Claude Verdier

ISTE

WILEY

First published 2022 in Great Britain and the United States by ISTE Ltd and John Wiley & Sons, Inc.

Apart from any fair dealing for the purposes of research or private study, or criticism or review, as permitted under the Copyright, Designs and Patents Act 1988, this publication may only be reproduced, stored or transmitted, in any form or by any means, with the prior permission in writing of the publishers, or in the case of reprographic reproduction in accordance with the terms and licenses issued by the CLA. Enquiries concerning reproduction outside these terms should be sent to the publishers at the undermentioned address:

ISTE Ltd
27-37 St George's Road
London SW19 4EU
UK

www.iste.co.uk

John Wiley & Sons, Inc.
111 River Street
Hoboken, NJ 07030
USA

www.wiley.com

© ISTE Ltd 2022

The rights of Valérie Deplano, José-Maria Fullana and Claude Verdier to be identified as the authors of this work have been asserted by them in accordance with the Copyright, Designs and Patents Act 1988.

Any opinions, findings, and conclusions or recommendations expressed in this material are those of the author(s), contributor(s) or editor(s) and do not necessarily reflect the views of ISTE Group.

Library of Congress Control Number: 2021952699

British Library Cataloguing-in-Publication Data
A CIP record for this book is available from the British Library
ISBN 978-1-78945-065-1

ERC code:

PE8 Products and Processes Engineering

PE8_5 Fluid mechanics, hydraulic-, turbo-, and piston- engines

LS4 Physiology, Pathophysiology and Endocrinology

LS4_1 Organ physiology and pathophysiology

Contents

Preface	xi
Valérie DEPLANO, José-Maria FULLANA and Claude VERDIER	
Chapter 1. Hemodynamics and Hemorheology.	1
Thomas PODGORSKI	
1.1. Structure and function of the circulatory system	1
1.2. Blood composition	5
1.3. The red blood cell: structure and dynamics	8
1.3.1. Red blood cell properties	8
1.3.2. Erythrocyte pathologies	11
1.3.3. Red blood cell dynamics.	15
1.4. Rheology and dynamics	17
1.4.1. Phenomenology of blood rheology.	17
1.4.2. Red blood cell aggregation	21
1.4.3. Dynamics of microcirculation	27
1.5. Conclusion	31
1.6. References	32
Chapter 2. CFD Analyses of Different Parameters Influencing the Hemodynamic Outcomes of Complex Aortic Endovascular Repair.	43
Sabrina BEN-AHMED, Jean-Noël ALBERTINI, Jean-Pierre FAVRE, C. Alberto FIGUEROA, Eugenio ROSSET, Francesca CONDEMI and Stéphane AVRIL	
2.1. Introduction.	43

2.2. Methods	45
2.3. Results.	48
2.3.1. Model without stenosis.	50
2.3.2. Model with 40% diameter stenosis.	53
2.3.3. Model with 70% diameter stenosis.	56
2.4. Discussion	58
2.4.1. Velocity and flow	59
2.4.2. Pressure.	60
2.4.3. TAWSS.	60
2.4.4. PAS	61
2.4.5. Limitations	62
2.5. Conclusion	63
2.6. Acknowledgments.	63
2.7. References	64

Chapter 3. Vascular Geometric Singularities, Hemodynamic Markers and Pathologies 69

Valérie DEPLANO and Carine GUIVIER-CURIEN

3.1. Introduction.	69
3.2. General characteristics of blood flows at the macroscopic scale.	70
3.3. Several geometric singularities of the cardiovascular system	73
3.3.1. Curvatures and bifurcations	73
3.3.2. Cross-section constriction	78
3.3.3. Cross-section enlargement.	80
3.3.4. Valves.	82
3.4. Hemodynamic markers	85
3.4.1. Indexes derived from wall shear stress	86
3.4.2. Indexes describing VSs	88
3.5. Correlation between hemodynamic markers and pathologies: some examples	90
3.5.1. WSS and pathologies.	92
3.5.2. Hemodynamic markers and thrombus.	95
3.6. Conclusion and perspectives.	98
3.7. References	99

Chapter 4. Role of Arterial Blood Flow in Atherosclerosis 109

Guillermo VILAPLANA and Abdul I. BARAKAT

4.1. Introduction.	109
4.2. Role of arterial fluid mechanics in atherosclerosis.	110

4.2.1. Atherosclerosis initiation and progression	110
4.2.2. Role of arterial flow in atherosclerosis	113
4.3. An illustrative example of the complexity of arterial flow fields: fluid dynamic interactions between two arterial branches	115
4.3.1. The specific problem addressed	115
4.3.2. Materials and methods	116
4.3.3. Results	118
4.3.4. Discussion	134
4.4. Concluding remarks	135
4.5. References	136

**Chapter 5. Patient-specific Hemodynamic Simulations:
Model Parameterization from Clinical Data to Enable
Intervention Planning 139**

Irene E. VIGNON-CLEMENTEL and Sanjay PANT

5.1. Introduction.	139
5.2. Multiscale models: do we need patient-specific data?	142
5.2.1. Assessing function of a new procedure/device.	142
5.2.2. Optimizing the procedure/device for an individual patient.	143
5.2.3. Population studies.	143
5.3. How do we include patient-specific data?	144
5.3.1. Type of clinical data available and associated challenges	145
5.3.2. Establishing if the resistance of the 3D part is negligible or not, and parameterization in case it is	147
5.3.3. Resistance of the 3D part is not negligible	149
5.4. When models fall short of expectations: toward adaptation	154
5.4.1. Liver hepatectomy and blood loss	154
5.4.2. Pulmonary stenosis alleviation and vascular adaptation	155
5.5. Conclusion	156
5.6. Acknowledgments.	157
5.7. References	158

**Chapter 6. Reduced-order Models of Blood Flow:
Application to Arterial Stenoses 163**

Jeanne VENTRE, José-Maria FULLANA, Pierre-Yves LAGRÉE,
Francesca RAIMONDI and Nathalie BODDAERT

6.1. Introduction.	163
6.2. Blood flow modeling	165

6.2.1. Two-dimensional axisymmetric model	166
6.2.2. Multi-ring model	167
6.2.3. One-dimensional model	169
6.2.4. Zero-dimensional model	169
6.3. Validation of the models	170
6.3.1. The entry effect	170
6.3.2. The Womersley solution in an elastic artery	171
6.4. Application to arterial stenoses	173
6.5. Conclusion	179
6.6. References	179

Chapter 7. YALES2BIO: A General Purpose Solver

Dedicated to Blood Flows 183

Simon MENDEZ, Alain BÉROD, Christophe CHNAFA, Morgane GARREAU, Etienne GIBAUD, Anthony LARROQUE, Stephanie LINDSEY, Marco MARTINS AFONSO, Pascal MATTÉOLI, Rodrigo MENDEZ ROJANO, Dorian MIDOU, Thomas PUISEUX, Julien SIGÜENZA, Pierre TARACONAT, Vladeta ZMIJANOVIC and Franck NICOU

7.1. Methods and validation	184
7.1.1. Food and Drug Administration case	186
7.1.2. Optical tweezers	187
7.1.3. Red blood cell self-organization	189
7.2. Simulation as support of modeling efforts	189
7.2.1. Single cell dynamics	190
7.2.2. Flow diverters	191
7.2.3. Echocardiography	192
7.3. Simulations for industrial applications	194
7.3.1. Flow in the Carmat artificial heart	194
7.3.2. Red blood cell dynamics in Horiba Medical's blood analyzers	195
7.4. Current developments	195
7.4.1. Thrombosis	196
7.4.2. In Silico MRI	197
7.4.3. Multi-cells	199
7.5. Acknowledgments	200
7.6. References	200

Chapter 8. Capsule Relaxation Under Flow in a Tube 207

Bruno SARKIS, Anne-Virginie SALSAC and José-Maria FULLANA

8.1. Introduction	207
8.2. Overview of the physical problem	209

8.2.1. Fluid solver	210
8.2.2. Solid solver	212
8.2.3. Fluid–structure coupling by the IBM method	213
8.3. Transient flow of a microcapsule into a microfluidic channel with a step	215
8.3.1. Capsule flow in the Stokes regime	215
8.3.2. Relaxation dynamics in the Stokes regime	217
8.3.3. Relaxation dynamics in the Navier–Stokes regime	221
8.4. Discussion and conclusion	223
8.5. Acknowledgements	225
8.6. References	225
Conclusion: Words and Things	229
Valérie DEPLANO, José-Maria FULLANA and Claude VERDIER	
List of Authors	233
Index	237

Preface

Valérie DEPLANO¹, José-Maria FULLANA² and Claude VERDIER³

¹CNRS, IRPHE, Ecole Centrale Marseille,

Aix-Marseille University, France

²Institut Jean Le Rond d'Alembert, CNRS UMR 7190,

Sorbonne University, Paris, France

³Laboratoire Interdisciplinaire de Physique (LIPhy, UMR 5588),

Grenoble Alpes University & CNRS, France

At the 44th Annual Congress of the French Society of Biomechanics held in Poitiers in 2019, a thematic session was proposed on the state of the art of biomechanical modeling applied to blood flow in large vessels, as well as on the associated in vivo experiments based on experimental data from medical imaging. During this session, organized jointly with the “MEChAnics of BIOlogical materials and fluids” (MecaBio, CNRS) research group, particular focus was placed on the benefit of interactions between the clinical and biomechanical teams, and the indispensable dialog between numerical modeling and in vitro and in vivo experimental studies.

This book, which has grown from the presentations made at this thematic session, deals more specifically with numerical modeling in fluid and solid mechanics applied to biological systems. It provides some answers to the question of the benefit of combining medical and biomechanical knowledge to treat clinical issues. Theoretical and numerical modelings applied to biological systems aim to link together dynamic, biological or mechanical variables, which may or may not be accessible to experimental measurements (velocities, stresses or pressures, for example). These variables, which are used to build a theory, a model and then its numerical

Biological Flow in Large Vessels,

coordinated by Valérie DEPLANO, José-Maria FULLANA, Claude VERDIER. © ISTE Ltd 2022.

counterpart, are based on hypotheses and therefore require experimental verification in the form of comparison and validation with existing *in vitro* or *in vivo* data. The numerical model can then be used for predictive calculations.

Recent advances in medical imaging, particularly in the field of technical applications, and their integration into clinical routines, have been significant. Clinical trials today provide a large amount of *in vivo* data from imaging techniques, such as ultrasound, magnetic resonance imaging (MRI), elastography, confocal endomicroscopy, or optical coherence tomography, which give precise information on the internal structure of biological systems and their physiological function. Faced with these data, several questions arise: How is clinically relevant information extracted? How is this information processed? How can we predict the evolution of the variables observed?

The link between the medical field and research in living mechanics, numerical modeling and mathematics, more precisely between doctors and medical researchers and engineers, mechanics, and applied mathematicians, became possible because a dialog was established between seemingly remote disciplines; common interests emerged; and complementary approaches crossed paths.

One of the objectives of this book is to provide insight into the key points linking medical teams dealing with pathologies where a mechanical component is present, and mechanics and mathematics researchers developing numerical models and tools. We started from the observation that any theoretical/numerical research relies on experimental data, which evolve with technological advances, and that vice versa, experimental protocols will often tap into theoretical/numerical predictions.

When establishing such interdisciplinarity, the knowledge of the complexity inherent to each discipline is a key point. In addition to questions of growth, remodeling and the different spatiotemporal scales that biological systems obey, one of the complexities of the living also stems from the fact that the same cause can offer very varied effects. They depend, *inter alia*, on the pathology, its level of evolution, the patient-specific profile and environmental factors, among others. Let us consider the case of aortic dissection, a typical vascular-pathology example of medical and mechanical interactions. In aortic dissection, a mechanical cause, the wall shear stress that is a consequence of pulsatile blood flow, and a geometric cause, the

topology of the aortic arch, can lead to the genesis of the pathology or to deleterious events in its evolution. However, if we consider biological activation processes due to mechanical stimuli and/or specific conditions of the clinical protocol, wall shear stress and topology may cause different or indeed conflicting effects or “experimental data”; one textbook example being the effect of wall shear stress due to flow on atheroma growth. This complexity greatly complicates the determination of the variables relevant to the assessment of a pathology and, retrospectively, the establishment of a theory or model based on the available data.

The complexity of numerical models is diverse and appears at different levels: in the non-linearity of the fluid and solid mechanics models, in the complex geometries inherent to the living systems where the models are applied, in numerical implementation through the use of sophisticated numerical schemes and integration techniques, and even in parallelization techniques specific to numerical codes to accelerate calculations. This book will also show that the models deployed can either be complete, such as the Navier–Stokes equations for fluid mechanics, or reduced, such as simple models to model the mechanics of the arterial wall.

In either case, the two disciplines pursue a common translational dream of computational medicine, where faster numerical simulations, whose models have been validated, are conducted at the patient’s bedside, become tools for decision support and prediction of pathology evolution, become an integral part of the operating room and enable the planning of personalized interventional procedures.

This work, sponsored by the *Société de Biomécanique Francophone* and the “MécaBio”, CNRS research group, takes a stride in this direction. The first chapter proposes a state of the art on the structure and rheological properties of the blood, essential for understanding circulatory dynamics under different conditions. The topics proposed in the other chapters are varied, ranging from the study of parameters and hydrodynamic markers influencing endovascular repairs, the study of flows in some geometrical singularities of the cardiovascular system (native or pathological) and their correlation with the evolution of cardiovascular pathologies, and the role of hemodynamics in the development of atherosclerosis, to the simulation of flexible objects in flows, with the introduction of numerical tools such as YALES, Basilisk or Caps3D, which allow specific studies on biological

systems, as well as modeling via model reduction, used in order to obtain fast and reliable numerical tools.

We hope that this book will shed new light on biomechanical modeling applied to blood flow in vessels, and that it will provide avenues for further development and applications of digital models in clinical research and experimental protocols.

Marseille and Paris, March 2021

1

Hemodynamics and Hemorheology

Thomas PODGORSKI

CNRS, Université Grenoble Alpes, France

1.1. Structure and function of the circulatory system

Since the founding discovery by William Harvey, who demonstrated blood circulation in *De motu cordis* (Harvey and Leake 1928), blood and its circulation have received constant and renewed attention from doctors, physicists and fluid mechanics engineers. Further to Stephen Hales performing the first blood pressure measurements on horses (Hales 1733), Poiseuille (1835), motivated by a desire to understand blood flows at different scales, laid a solid foundation for rheology and fluid mechanics by establishing, through experimentation, the relationship linking flow rate, pressure drop and viscosity in a tube (Poiseuille 1844). More recently, these questions have formed the subject of numerous experimental, theoretical and numerical studies, in vivo and in vitro, with interest constantly renewed in light of technical and conceptual developments (imaging, velocimetry, rheometry, numerical methods, microfluidics, etc.) and ever greater coupling of different fundamental studies on model systems, clinical studies and questions of biomedical interest. The complexity of the cardiovascular system, which presents a multi-scale structure with time-dependent dynamics, regulated by numerous biological, physical and mechanical processes, cannot necessarily be reduced to the sum of its constituents or elementary behaviors, which interact in a nonlinear manner. Nevertheless, a quantitative understanding of this complexity always requires the study of

Biological Flow in Large Vessels,

coordinated by Valérie DEPLANO, José-Maria FULLANA, Claude VERDIER. © ISTE Ltd 2022.

Biological Flow in Large Vessels: Dialog Between Numerical Modeling and In Vitro/In Vivo Experiments,
First Edition. Valérie Deplano; José-Maria Fullana and Claude Verdier.

© ISTE Ltd 2022. Published by ISTE Ltd and John Wiley & Sons, Inc.

simpler subsystems or configurations, in order to validate the physical concepts incorporated into larger scale models.

Blood circulation performs a number of essential physiological functions, including:

- transport of oxygen and nutrients from the lungs and digestive tract to tissues, and to or from storage organs and tissues (liver and adipose tissues);
- elimination of carbon dioxide and metabolic wastes to the lungs and disposal organs, thus participating in the regulation of the internal medium;
- immune response by transporting leukocytes and antibodies, and injury repair processes, notably via coagulation processes;
- transport of internal messengers (hormones) and medicines, ensuring their rapid distribution throughout the body.

The circulatory system is composed of a pump (the heart) and a complex network of vessels in which blood circulates, which can be divided into two parts: pulmonary circulation and systemic circulation. As pulmonary circulation takes place in a shorter circuit close to the heart, the pressure is lower there (from about 3.3 kPa or 25 mm Hg in the right ventricle and the pulmonary artery to 0.6 kPa, or 5 mm Hg in the left atrium) than in systemic circulation, where the distances to be covered and the amount of tissue to be irrigated are greater (from about 13 kPa [100 mm Hg] in the left ventricle and the aorta, to 0.6 kPa [5 mm Hg] in the right atrium). Vessel diameters extend across almost five orders of magnitude, from the largest arteries (several cm) to the finest capillaries (several μm), with average velocities ranging from about 1 mm/s in capillaries to almost 1 m/s in the aorta, with a highly pulsed flow linked to the heart's operation in the arteries and veins close to the heart: during systole (contraction of the heart), the pressure reaches approximately 120 mm Hg (16 kPa) in the aorta and 25 mm Hg (3.3 kPa) in the pulmonary artery, and drops sharply within the heart during diastole. This results in very different natures of flow depending on the position in the network. These flows can be characterized by two dimensionless numbers: the Reynolds number, $Re = \rho UD/\eta$, where ρ is the blood density (about 1,060 kg/m³), U is the typical flow velocity, D is the vessel diameter and η is the dynamic viscosity (about 3–4 mPa·s); and the Womersley number, $\alpha = R(\omega\rho/\eta)^{1/2}$, where R is the vessel radius and ω is the pulsation (of the order of 20 rad/s for a heart rate of 60 beats/min). The typical values of these numbers in the different stages of circulation are given in Table 1.1. These values show that, first, flows are highly inertial in

the large vessels (arteries and veins) for which $Re \gg 1$, whereas in the finer vessels they are dominated by viscous effects and, second, the effects of the pulsed nature of the flow are mainly felt in the large vessels where $\alpha > 10$. The consequence of these large values of the Womersley number is that the velocity profile in these vessels does not have time to develop completely and is relatively flat, and that Poiseuille's law, for example, does not apply. In finer vessels, the viscous effects, combined with the elasticity of the upstream vascular walls, enable dampening of the pressure fluctuations and flow there is quasi-stationary. Wall shear rate, a significant parameter for the function of the endothelium lining the vessels, also varies significantly, with a maximum in the arterioles.

	Diameter (mm)	Average velocity (mm/s)	Reynolds, Re	Womersley α	Wall shear rate (1/s)
Aorta	25	400	3,000	17	130
Arteries	4	450	550	3	900
Arteriole	0.05	50	0.75	0.03	8,000
Capillary	0.008	1	0.002	0.006	1,000
Venule	0.02	2	0.01	0.01	800
Veins	5	100	150	3	160
Vena cava	30	380	3,500	20	100

Table 1.1. Typical values of flow parameters in different levels of the vascular network

Besides their geometric properties, the structure and mechanical properties of vessels contribute to circulatory dynamics through passive dilatation/relaxation mechanisms and active contraction/expansion mechanisms. Vascular walls are multi-layer structures presenting variations depending on their position in the vascular network, and therefore different mechanical properties. The internal surface of the vessels, common to the entire vascular system, consists of a layer of endothelial cells whose elongated shape varies with local shear stresses. The endothelium fulfills several exchange functions between blood, the vascular wall and surrounding tissues. It intervenes in the immune response through the processes of adhesion and extravasation of circulating cells, and also regulates coagulation and vasomotor processes and intervenes in angiogenesis. Endothelial cells are sensitive to hydrodynamic and mechanical stresses, thus allowing short-term adaptation

(vasoconstriction/vasodilatation) or longer term remodeling and adaptation via growth, migration or apoptosis of vascular cells. The presence of this nucleated cell layer on the inner surface of the vessels results in surface roughness, with height variations of up to 750 nm in endothelial cell nuclei. The shape of the cells, 10–15 μm wide and 60–100 μm long in the flow direction, adapts to local stresses. In addition, the surface of these cells is covered with a layer of glycoproteins and glycolipids forming a brush (glycocalyx), which plays a crucial role in hemostasis and coagulation, or the regulation of vasomotor processes (Reitsma *et al.* 2007; Weinbaum *et al.* 2007).

The walls of the large vessels have a layered, *tunic*-shaped structure successively composed, from the inside to the outside, of (i) the *intima*, composed of the endothelium and the underlying connective tissue, the internal elastic lamina whose thickness, structure and properties depend on the vessel type, (ii) the *tunica media*, composed of circumferential, smooth muscle cells, collagen and elastic tissue, and (iii) the *tunica externa* (*adventitia*), composed mainly of connective tissue (collagen and elastin), but also, for the large nerve arteries, of small vessels irrigating the arterial wall (*vasa vasorum*) and lymphatic vessels.

A common pathology of the arterial wall is atherosclerosis, which leads to coronary heart disease due to the progressive formation of atheromatous plaque in the artery, resulting in a narrowing of the lumen. It results from chronic inflammation of the arterial wall, which is most likely to occur in zones of disturbed flow, such as branches. It generally begins with endothelial dysfunction and disruptions in the elastin layer, causing the subendothelial accumulation of cholesterol (LDL), which forms atheroma by mixing with cell debris and becoming surrounded by a fibrous shell (Weber and Noels 2011).

Veins, which have thinner walls (thin *intima*, quasi-absent internal elastic lamina and weak *media* except in the lower limbs) and a more elliptical than circular cross-section, generally behave more passively than arteries. Medium-caliber veins generally feature valves with folding *intima*, which prevent backflow.

The small vessels have a simpler structure, composed of an endothelium surrounded by one or more layers of smooth muscle cells for the arterioles, allowing flow to be regulated in the organ concerned. The capillaries consist

of an endothelium supported by a basal membrane, whose structure and permeability depend on the organ (continuous and slightly permeable membrane in the muscles, lungs and skin, discontinuous and highly permeable in the glands, mucous membranes, liver, spleen, bone marrow, etc.). The postcapillary venules have a structure close to the latter, while the largest venules have smooth muscle cells.

The conditions and nature of flows are strongly influenced by the size, geometry and mechanical properties of the vascular walls. In the largest vessels, flows are inertial (generally without turbulence), often unsteady and may present secondary flows such as recirculations. In small vessels with a diameter less than a few dozen times the size of blood cells, the multiphase nature of the blood can no longer be reduced to a continuous medium-type approach, and a specific rheology is manifested. The following sections summarize the structure and rheological properties of blood in these different situations.

1.2. Blood composition

Blood is a complex fluid in terms of its composition and rheology. It is a dense suspension of generally deformable objects (blood cells) in a fluid with a composition that can be complex to a lesser or greater degree, plasma. A simple centrifugation of a whole tube of blood essentially reveals three fractions which, in order of increasing density, are a fluid phase containing various solutes (plasma), a layer called the buffy coat, consisting of leukocytes (white blood cells) and platelets representing less than 1% of the total volume, and a dense layer of red blood cells (erythrocytes or red corpuscles) representing a volume fraction (hematocrit) of 38–46% in women and 42–53% in men, or about 45% on average. The different blood cell types are summarized in Table 1.2.

Plasma is composed mainly of water (92%), proteins (7%), electrolytes (0.9%), lipoproteins and lipids (0.6%) and carbohydrates (0.1%). Electrolytes (predominantly Na^+ , followed by Ca^{++} , K^+ , and Mg^{++} for cations and predominantly Cl^- , followed by HCO_3^- , HPO_4^{2-} and So_4^{2-} for anions) control osmotic pressure, are regulated by the kidneys and are involved in cellular processes. Carbohydrates are energy sources for cells, and are divided into oligosaccharides (glucose, fructose and galactose), disaccharides (sucrose, lactose and maltose) and polysaccharides (glycogen). Lipoproteins are structures that encapsulate insoluble lipids (cholesterol and

triglycerides) in a shell of polar lipids and proteins. They are divided into chylomicrons, very low-density lipoproteins (VLDL), low-density lipoproteins (LDLs) and high-density lipoproteins (HDLs), which differ in size and content (80–500 nm for chylomicrons to 10 nm for HDLs) and participate in different functions.

Proteins, a number of which play a crucial role in blood rheology, are divided into different families representing different plasma fractions. Fibrinogen (0.03% or 195–365 mg/dL) acts on red blood cell aggregation (see section 1.5.2) and is involved in coagulation. Albumin is the main plasma protein (0.6% or 3.3–4.5 g/dL), used for the transport of small molecules and at this concentration level has a significant contribution to plasma osmolarity. Globulins (α , β , γ -globulins) and antibodies represent about 0.4% of plasma in total. Finally, other nitrogenous compounds are present, such as urea, ammonium salts, uric acid, creatine, creatinine and amino acids, many of which are waste eliminated by the kidneys.

Cell type	Count / μ L	Geometry
Red blood cells (erythrocytes), ~99.7%	~5,000,000	Biconcave disc diameter 8 μ m, thickness 2.5 μ m
White blood cells (leukocytes), ~0.2%	~7,500	Quasi-spherical diameter 20–100 μ m
Platelets (thrombocytes), ~0.1%	~250,000	Ellipsoid major axis 4 μ m, minor axis 1.5 μ m

Table 1.2. Blood cell types, relative fraction and geometrical data

In rheological and modeling terms, plasma is generally considered as a Newtonian fluid with a viscosity between 1.1 and 1.3 mPa·s (normal values independent of age and gender). However, recent studies involving a complete rheological characterization and molecular simulations of protein dynamics at high shear and extension rates have shown that it is viscoelastic in nature at high frequencies (Varchanis *et al.* 2018). Although the deformation rates considered (10^3 to 10^5 s⁻¹) are higher than those encountered in most of the vascular network (Table 1.1), these non-Newtonian effects could be significant in regions such as the arterioles or capillaries.

Among the factors that have a crucial influence on blood rheology, hematocrit plays a leading role, with an indirect influence on the mechanical

properties of red blood cells (see section 1.3). As in any suspension, the effective viscosity and possible viscoelastic properties increase with the volume fraction in particles. The hematocrit varies significantly around the mean value of 45%, with, first, a significant difference between men and women under normal conditions and, second, pathological deviations toward lower values (anemia) or higher values (polycythemia), resulting in significantly different blood viscosities, and thus an altered oxygen transport capacity. There are different types of anemia, which may be due to a hemorrhage, the destruction of red blood cells by different pathologies (see section 1.3) or a deficit in hemoglobin production. Polycythemia may result from adaptation to conditions of reduced oxygenation (living at high altitude, sleep apnea syndrome, etc.) or from diseases such as polycythemia vera (Vaquez disease), a myeloproliferative syndrome that can double, or more than double, the number of red blood cells (these are then often smaller than normal) and bring the hematocrit to above 55%. Finally, certain doping techniques in sport essentially aim to increase hematocrit to improve blood oxygenation capacity – with the circulatory risks that doing so entails – thus enabling blood viscosity to be doubled, with a 40–60% increase in hematocrit. It should be noted that even in the absence of doping or pathological conditions, hematocrit and blood viscosity may vary significantly during physical exercise due to dehydration or fluid exchange with the rest of the body, which may modify the ratio of red blood cell and plasma volumes (Connes *et al.* 2013). Strictly from the point of view of oxygen transport efficiency, there is an optimal concentration for blood systems (Jensen *et al.* 2013), ensuring maximum transport, otherwise equal in all aspects (with imposed pressure or pumping power): the transported flow is proportional to the concentration (hematocrit), but an increase in this concentration is accompanied by an increase in viscosity, such that between two extremes (zero hematocrit, for which the red blood cell flow is zero by definition, and maximum hematocrit, for which the viscosity is such that the flow stops), an optimum exists, located more or less in the physiological hematocrit range. This optimum may be influenced by a number of factors, such as the properties of red blood cells, but also other blood or extra-blood factors (Reinhart 2016). It should be noted, for example, that the mean hematocrit value varies significantly between different animal species (mammals, birds, reptiles and amphibians), with normal values ranging from 20% to 55% for highly variable red blood cell volumes, shapes and deformabilities (Hawkey 1975; Lewis 1996). The following section summarizes the properties of the human red blood cell, its pathologies and its dynamics.

1.3. The red blood cell: structure and dynamics

1.3.1. *Red blood cell properties*

The primary function of red blood cells is to transport oxygen and eliminate carbon dioxide from the body. The main oxygen carrier is hemoglobin, an organometallic protein contained in the cytoplasm of red blood cells, which has the ability to fix an amount of oxygen that is much higher than the solubility limit of plasma. The extraction of CO_2 is assisted by carbonic anhydrase, an enzyme located in the red blood cell membrane catalyzing the hydration of carbon dioxide into H_2CO_3 , which dissociates into HCO_3^- bicarbonate ions and H^+ protons, thus having an effect on blood pH, combined with the role of hemoglobin as a buffer.

Red blood cells, which lack nuclei, have a characteristic biconcave disc shape with an average diameter of $7.7 \pm 0.7 \mu\text{m}$ and a thickness at the thickest point of about $2.8 \pm 0.5 \mu\text{m}$ and about $1.4 \pm 0.5 \mu\text{m}$ in the center (Evans and Fung 1972). The mean corpuscular volume (MCV), which is an essential hematological parameter, is on average between 82 and $98 \mu\text{m}^3$, while the membrane surface area is about $140 \mu\text{m}^2$. These characteristics make it a highly deflated object (the red blood cell's membrane surface could contain a volume of about $150 \mu\text{m}^3$ if it were spherical in shape) that allows for substantial deformations, notably in order to circulate within the finer capillaries, whose diameter is less than $8 \mu\text{m}$. In theoretical models that require the characteristics of the model object representing the red blood cell to be fixed, a dimensionless parameter is generally defined. This may be a reduced volume (corpuscular volume/volume of a sphere with the same surface area), having a value of about 0.59 for an average blood cell, or a relative excess surface area (membrane surface/surface of a sphere of the same volume) of about 1.44 on average.

Since the cell is devoid of a nucleus and organelles, its internal medium essentially consists of a solution of hemoglobin (cytosol), which is considered as a Newtonian fluid (the range of shear rates accessible in this compartmentalized medium being restricted). The mean concentration of hemoglobin in cytosol (mean corpuscular hemoglobin concentration in hematology) is normally comprised between 32 and 36 g/dL . This concentration is responsible for the relatively high value of the internal viscosity of red blood cells. Since this concentration range is just below the solubility limit of hemoglobin, the viscosity can vary significantly, from $6 \text{ mPa}\cdot\text{s}$ at 32 g/dL to $10 \text{ mPa}\cdot\text{s}$ at 36 g/dL at 37°C (Ross and Minton 1977).

However, this mean value masks a significant dispersion within the same blood sample. Indeed, red blood cells that are produced in bone marrow from hematopoietic stem cells before being released into the circulation have an average lifespan of 120 days. Over this duration, their density increases due to dehydration (approximately 1,060 to 1,120 g/L), resulting in a 25–30% increase in the corpuscular hemoglobin concentration. The concentration within the individual red blood cells of the same sample can thus range from 19 to 25 mmol/L or 30–40 g/dL (Bosch *et al.* 1992), and corresponding viscosity variations from 5 to 20 mPa·s. This significant increase in red blood cell viscosity, combined with membrane alterations, significantly reduces their deformability (Linderkamp *et al.* 1993) and leads to their elimination by the spleen through a process of filtration and phagocytosis. The viscosity of hemoglobin is also sensitive to other parameters such as temperature and calcium concentration, and presents a transition within the vicinity of body temperature, notably for high hemoglobin concentrations (Kelemen *et al.* 2001). The internal viscosity of red blood cells is thus significantly higher at room temperature (20–25°C) than at 37°C, which may be a factor to be taken into consideration in the interpretation of *in vitro* experiments whose temperature is not necessarily regulated. Furthermore, the dispersion of hemoglobin concentration and viscosity values within the same sample and the influence that this dispersion may have on the red blood cell dynamics in flow represents a challenge for modeling and numerical simulations focusing on collective behavior.

The membrane consists of a phospholipid bilayer containing inclusions of transmembrane proteins (Band-3 ion channels, glycoporphins carrying antigens of the blood group, notably). Below the inner surface of the membrane is a cytoskeleton consisting of a dense network of spectrin filaments bound to the membrane by complexes involving anchoring proteins (association of spectrin-ankyrin-protein 4.2-band 3, or spectrin-actin-protein p55-protein 4.1-glycophorin C). These interactions allow the structural integrity of the red blood cell to be maintained. The phospholipid bilayer, which is a two-dimensional fluid, confers several significant mechanical properties to the red blood cells. The most obvious is a quasi-inextensibility with a surface expansion module (ratio between isotropic surface tension and relative surface expansion) of about 400 mN/m, an important value at the scale of a micrometer object. In practice, the surface area of the membrane can therefore be considered constant, with dilatations not exceeding 5% for hydrodynamic stresses, such as those experienced in circulation. The membrane also has a bending resistance that

is generally modeled by a Canham–Helfrich energy per unit surface taking the following form (Helfrich 1973; Seguin and Fried 2014):

$$E_b = \frac{1}{2} \kappa (H - H_0)^2 + \kappa_G G \quad [1.1]$$

where κ is the curvature modulus with a value of $1.15 \pm 0.9 \times 10^{-19}$ J, H is the local mean curvature, H_0 is the spontaneous curvature (linked to the asymmetry of the two lipid layers), κ_G is the Gaussian curvature modulus and G is the Gaussian curvature. With G being a topological invariant, the second term is therefore constant and only the first term is likely to vary with deformations of the membrane. It is essentially this bending elasticity that is responsible for the biconcave equilibrium shape of the red blood cell, which minimizes the integral of the bending energy at a given surface area and volume. Finally, friction between phospholipids and with transmembrane proteins produces a surface viscosity that plays a non-negligible role in the dynamics of the red blood cell.

In parallel with the fluid membrane, the spectrin network is an elastic shell characterized by a shear modulus of approximately 5 $\mu\text{N/m}$ (Table 1.3). The question of the reference shape of this elastic component (a shape for which the stresses are zero) remains a matter of debate (Švelc and Svetina 2012). Several hypotheses have been put forward, with some taking into account the formation of the red blood cell, and different shapes have been proposed, from a spherical reference shape (which assumes that the cytoskeleton retains a memory of its composition in an initially quasi-spherical cell with a nucleus) to a biconcave reference shape (which assumes that slow remodeling of the cytoskeleton leads it to relax toward the shape imposed by the minimization of the membrane bending energy). This question is far from anecdotal in the modeling of quantitative red blood cells, and numerical simulations have shown the influence of this choice in different situations (Hoore *et al.* 2018).

Since previous results showed a link between red blood cell metabolic activity and deformability (Weed *et al.* 1969), several works have suggested possibilities for remodeling the spectrin network and its links with the membrane involving ATP (adenosine triphosphate), which could provide the energy needed for this remodeling, and thus modulate the shape and deformability of the red blood cell to optimize its function in the microcirculation (Park *et al.* 2010). Other works also suggest that the high

stresses experienced by the red blood cell in the microcirculation lead to the release of ATP in the plasma, which could in turn serve as a signal to endothelial cells to trigger vasomotion mechanisms and adapt the resistance of the microcirculation network (see WAN *et al.* (2011) for a review). However, these possible interactions between ATP, red blood cell mechanical properties and signaling still remain to be fully clarified and are even a contentious issue (Betz *et al.* 2009).

The mean values of the main mechanical properties of the healthy red blood cell are summarized in Table 1.3. A review of the techniques for measuring these different properties is given in Tomaiuolo (2014).

	Mean values
Volume (μm^3)	89.4 ± 17.6
Surface area (μm^2)	138.1 ± 27.6
Internal viscosity ($\text{mPa}\cdot\text{s}$)	6.07 ± 3.8
Membrane viscosity ($\mu\text{N}\cdot\text{s}/\text{m}$)	0.7 ± 0.2
Membrane shear modulus ($\mu\text{N}/\text{m}$)	5.5 ± 3.3
Bending energy ($\times 10^{-19}$ J)	1.15 ± 0.9
Surface compressibility modulus (mN/m)	399 ± 110

Table 1.3. Main red blood cell mechanical parameters and typical values (according to Tomaiuolo (2014))

1.3.2. Erythrocyte pathologies

A number of conditions of congenital, infectious or metabolic origin are likely to significantly alter the properties of the red blood cell, and consequently the rheology of the blood. With regard to the mechanical and modeling consequences, they can affect the properties of the cytosol or the membrane, together with morphological modifications.

There are several hereditary hemoglobinopathies, the most emblematic of which is drepanocytosis (sickle cell disease), which affects around 300,000 births a year worldwide (Rees *et al.* 2010). It is caused by a mutation in a hemoglobin gene that results in the production of an abnormal hemoglobin, hemoglobin S (HbS). In homozygous patients, the high HbS concentration in red blood cells leads to its polymerization under low oxygen pressure conditions (notably when red blood cells deoxygenate substantially in the

microcirculation in situations of effort, stress and dehydration). This results in a rigidification of the red blood cells and, depending on the rate at which deoxygenation has occurred, a change in shape related to the polymerization of HbS in the form of fibers. The red blood cells then take on the characteristic shape of a rigid sickle, which can cause capillary occlusions (Figure 1.1). Altered red blood cells are also more fragile, resulting in hemolytic anemia (Figure 1.2). The severe complications, high prevalence of the disease, and the difficulty of its treatment make it an important topic of study for therapeutic purposes and diagnostic aid. Blood rheology is altered by several factors interacting in a complex manner (hematocrit, and composition of the plasma, which is generally more viscous due to increased protein concentration) and more widely speaking, an increase in viscosity is observed, even in oxygenated blood, due to a reduced deformability of the red blood cells (Barabino *et al.* 2010).

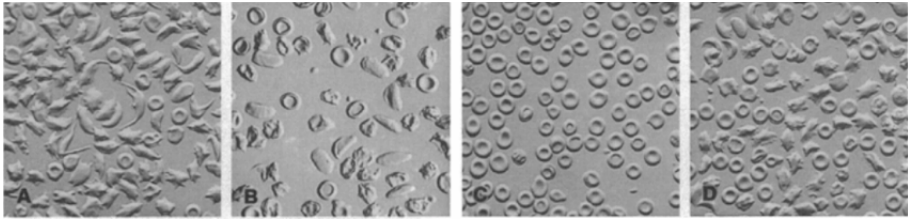


Figure 1.1. Sickle-cell morphologies under different oxygen partial pressures: (a–c) venous (deoxygenated) blood from three different patients; (d) after oxygenation of sample B with 25% O_2 ($PO_2 = 180$ mm Hg) (Asakura *et al.* 1994). Copyright National Academy of Sciences, U.S.A (1994)

A hemoglobinopathy commonly associated with sickle cell disease is hemoglobinosis C, caused by the production of another type of abnormal hemoglobin, HbC. This abnormal hemoglobin is less likely to polymerize than HbS, but still leads to a decrease in red blood cell deformability. In addition, the prevalence of HbC and HbS genes in the same populations means that HbSC heterozygotes are more common than HbCCs (Nagel *et al.* 2003).

Thalassemias (α or β depending on the type of hemoglobin subunit affected) are another family of highly prevalent hereditary hemoglobinopathies (Higgs *et al.* 2012). They are characterized by hypochromia (hemoglobin deficiency and therefore a lower internal viscosity) and microcytosis (smaller than normal red blood cells).

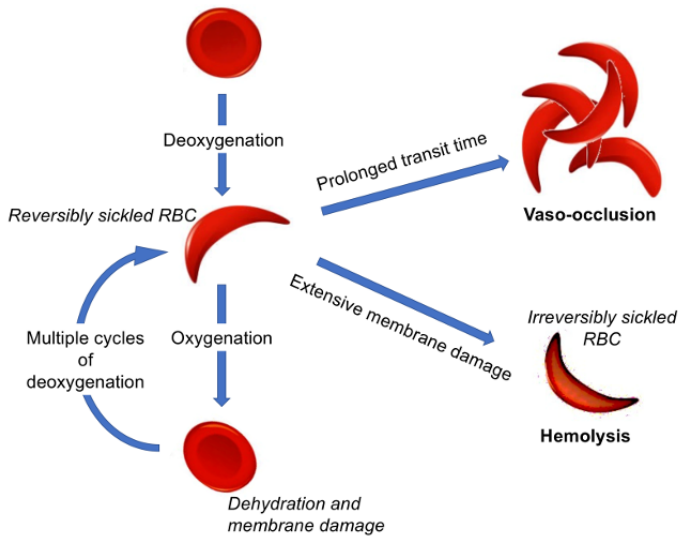


Figure 1.2. Sickling, hemolysis and capillary occlusion in sickle cell disease (according to Kumar et al. (2012)). For a color version of this figure, see www.iste.co.uk/deplano/biological.zip

Red blood cells maintain their biconcave shape (favoring their deformability) by regulating osmotic exchanges through their membrane. In particular, the internal sodium and calcium concentrations are maintained at a low level because of the ion channel activity (requiring energy in the form of ATP to function). A genetic modification of the AE1 anion exchanger (band 3) making it permeable to cations is linked to several forms of stomatocytosis, the most common form of which leads to dehydration of the red blood cells, and thus both an increase in internal viscosity and a change in shape (Da Costa *et al.* 2013). A number of hereditary membrane pathologies affect the cytoskeleton and lead to changes in the geometry of the red blood cell: spherocytosis, elliptocytosis, ovalocytosis, etc. The defects, which affect either the links between the cytoskeleton and the membrane, or the interactions within the spectrin network, lead to fragility of the membrane and a loss of its surface area to a lesser or greater degree, leading to an alteration in the shape and deformability of the red blood cells. Figure 1.3 shows several examples of morphological alterations associated with these pathologies, as well as the mechanical consequences characterized by the measurement of an elongation index in ektacytometry.

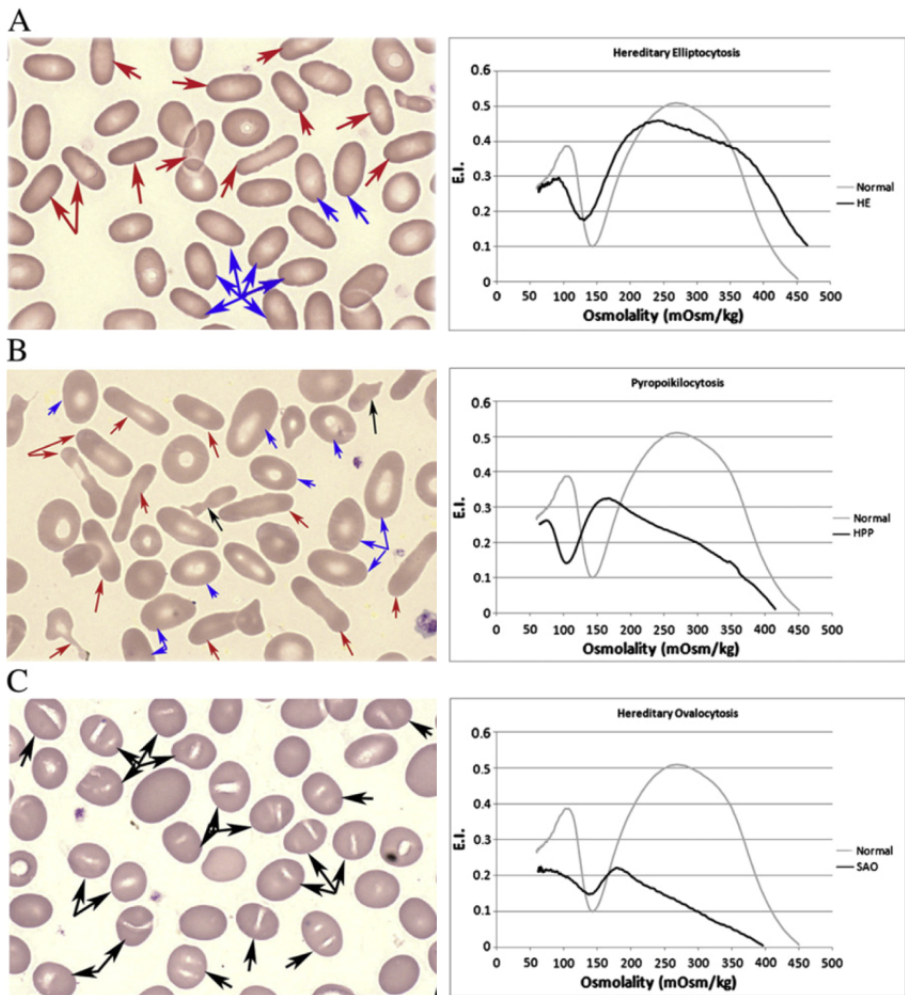


Figure 1.3. Examples of red blood cell membrane pathologies. a) Elliptocytosis, b) pyropoikilocytosis and c) ovalocytosis. The graphs represent measurements of deformability by ektacytometry (elongation index, EI) as a function of the osmolality of the medium. The light-colored curve represents normal red blood cells (according to Da Costa et al. (2013)). For a color version of this figure, see www.iste.co.uk/deplano/biological.zip

1.3.3. Red blood cell dynamics

As we saw above, a number of questions remain open regarding the structure and mechanical properties of the red blood cell, notably regarding the values and variability of membrane properties: bending rigidity, elastic modulus and membrane viscosity. The question of the reference shape of the cytoskeleton is also significant and unresolved: is this shape fixed, if so which shape is it, or is it subject to remodeling? Should these properties be considered fixed, or dynamic and capable of adapting to the flow through ATP-consuming active mechanisms? The alteration of the mechanical properties of red blood cells can be a consequence (and an indicator) of different hemoglobin and membrane pathologies, with repercussions on blood rheology: the dynamics of red blood cells (deformations, orientation with respect to flow) depend directly on them and condition the viscous dissipation, the elasticity of the suspension and the hydrodynamic interactions responsible for structuring under flow.

A simple shear flow is a reference rheometric configuration, in which the dynamics of a suspended red blood cell can be considered as a marker of its rheological properties. It is also a useful reference configuration to contrast theoretical and numerical models and compare them with the experiment, in order to validate their usage in more complex flows.

Many theoretical approaches have been proposed for modeling red blood cells, including models of elastic capsules (see, for example, Lac and Barthès-Biesel (2005)) or vesicles (Vlahovska *et al.* 2009; Biben *et al.* 2011). While these models, in their simple version (two-dimensional, incompressible fluid with bending elasticity for vesicles, quasi-two-dimensional solid with dilatation and shear elasticity for capsules), enable a number of red blood cell behaviors to be described in qualitative terms, more recent models tend to incorporate, to as great a degree as possible, the set of mechanical parameters that can influence the dynamics (inextensibility, bending and shear elasticity, and membrane viscosity). Many recent works focus on simple-shear red blood cell dynamics (see, in particular, Cordasco and Bagchi (2014), Peng *et al.* (2014), Sinha and Graham (2015), Lanotte *et al.* (2016) and Mauer *et al.* (2018)). On the experimentation side, a number of recent studies have confirmed or identified different dynamic regimes (Dupire *et al.* 2012; Fischer and Korzeniewski 2013; Lanotte *et al.* 2016; Levant and Steinberg 2016; Mauer *et al.* 2018) for the purpose of drawing up a diagram of the transitions between different motions of tank

treading, tumbling, rolling and other more complex motions combining rotations, oscillations or deformations.

The parameters influencing dynamics (viscosities of internal (η_i) and external (η_o) fluids, membrane viscosity, bending (κ) and shear (μ) moduli, flow shear rate $\dot{\gamma}$, volume (V) and surface area (S) of the blood cell) are generally combined into a set of dimensionless numbers that are the reduced volume (ν), viscosity ratio (λ) and capillary numbers (Ca_κ and Ca_μ) comparing the viscous stresses with the forces linked to the bending or shear elasticity of the membrane. These parameters are defined by:

$$\begin{aligned}\lambda &= \eta_i / \eta_o \\ \nu &= \frac{V}{\frac{4}{3}\pi\left(\frac{S}{4\pi}\right)^{\frac{3}{2}}} \\ Ca_\kappa &= \frac{\eta\dot{\gamma}\left(\frac{3V}{4\pi}\right)}{\kappa} \\ Ca_\mu &= \frac{\eta\dot{\gamma}\left(\frac{3V}{4\pi}\right)^{\frac{1}{3}}}{\mu}\end{aligned}\tag{1.2}$$

where $(3V/4\pi)^{1/3}$ is the mean radius of the red blood cell, defined as the radius of a sphere of the same volume.

Despite many dynamic modes having been identified in different studies, and the fact that the transitions between different regimes can be hysteretic in nature (Dupire *et al.* 2012), there is still no consensus regarding the general diagram of the shear red blood cell dynamics to serve as a common reference for validating theoretical and numerical models. It should be noted that variability in the properties of red blood cells between different subjects and within a sample from a given subject may be a cause of the differences observed between different experimental studies. To account for this property dispersity, a recent study statistically quantified cell populations in the different dynamic modes by measuring the orientations and shapes of a large number of cells within the same shear sample (Minetti *et al.* 2019). By

confirming the variety of dynamic modes, the ranges of parameters on which transitions occur and quantifying the fractions of the red blood cell population in the different modes, these statistical data complete the landscape of a reference flow situation for modeling (Figure 1.4).

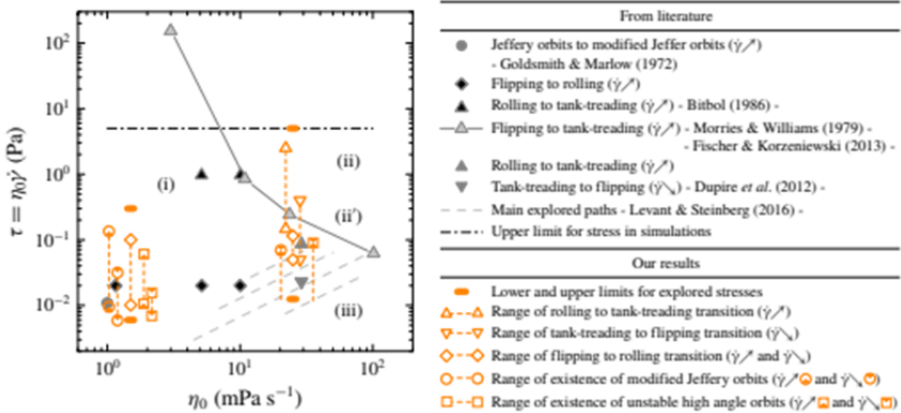


Figure 1.4. Transitions between dynamic regimes of the shear red blood cell identified in the literature and transition ranges observed on a large sample of red blood cells (Minetti *et al.* 2019). For a color version of this figure, see www.iste.co.uk/deplano/biological.zip

1.4. Rheology and dynamics

1.4.1. Phenomenology of blood rheology

From a macroscopic point of view, that is to say, at measurement scales significantly higher than that of the cellular constituents, the behavior presented by blood for shear rates typical of those encountered in large vessels (10^2 – 10^3 s^{-1}) is quasi-Newtonian, with a viscosity of the order of 3–4 $mPa \cdot s$. This simple rheology can be useful for modeling flows in large vessels in their broad outline (Ku 1997), in particular through the use of solvers of the Navier–Stokes equations in numerical simulation. Notably, it has been shown that at the scale of the large arteries, the imaging resolution does not make it possible to systematically distinguish significant non-Newtonian effects, and that a Newtonian rheology is sufficient in order to reasonably describe the flows as a whole – that is, in terms of pressure distributions and flow rates – in arteries that can measure as little as 5 mm in diameter, with renormalization of the viscosity (Lee and Steinman 2007).

This simplified perspective, nevertheless, masks a complexity that may be significant in specific regions of physiological flows or in artificial systems, and when considering details that can be crucial in pathological situations, and situations of biomedical interest, or in intermediate regions of the vascular tree. In these situations, it may be necessary to take into account the non-Newtonian aspects of blood rheology.

An essential phenomenon of constant-shear rheology of blood is its shear-thinning nature (Chien 1970): in a range of shear rates from 10^{-2} to 10 s^{-1} , blood viscosity falls by nearly two orders of magnitude, in direct relation to (i) the decrease in red blood cell aggregation and (ii) the influence of red blood cell deformability (Figure 1.5), the latter leading to a morphology and dynamics that depend on the shear rate. Several authors have focused on determining a blood yield stress resulting from the formation of aggregate networks at very low shear rates. These measurements at vanishing shear rates are technically difficult, notably due to artifacts related to red blood cell sedimentation, but it has been possible to produce estimates using a Casson law for rheology, in which the relationship between stress (τ) and shear rate $\dot{\gamma}$ is given by:

$$\sqrt{\tau} = \sqrt{\tau_y} + \sqrt{\eta\dot{\gamma}} \quad [1.3]$$

where τ_y is the yield stress. An adjustment of this type of law to rheometric measurements at low shear rates allows this yield stress to be estimated at about 5 mPa, under average physiological conditions (Picart *et al.* 1998).

On the circulatory side, shear-thinning, in particular associated with aggregation phenomena, can play a role at different levels. First, it can modify the velocity profiles by making them non-parabolic. In addition, for geometric reasons, secondary flow zones may appear transiently in the branches or curved portions of large vessels, constrictions (or irregularities related to the presence of stents, atherosclerosis etc.) due to the inertial, unsteady nature of the flow. A number of phenomenological rheological models are conventionally used in numerical simulation, from simple models such as power law or Carreau (Cho and Kensey 1991), to more elaborate models such as Carreau-Yasuda (Bird *et al.* 1987), modified Casson (Fung 1993), generalized power law (Ballyk *et al.* 1994) or Quemada (Quemada 1978). The latter model allows a good representation of blood rheology in steady shear to be obtained, avoiding the singular nature of the simple Casson model at near-zero shear rates, and the instabilities linked to the evolution of

aggregate structures to be taken into account. Furthermore, the Quemada model is equivalent to a modified Casson model (Buchanan *et al.* 2000). The generic forms of these different models are summarized in Table 1.4.

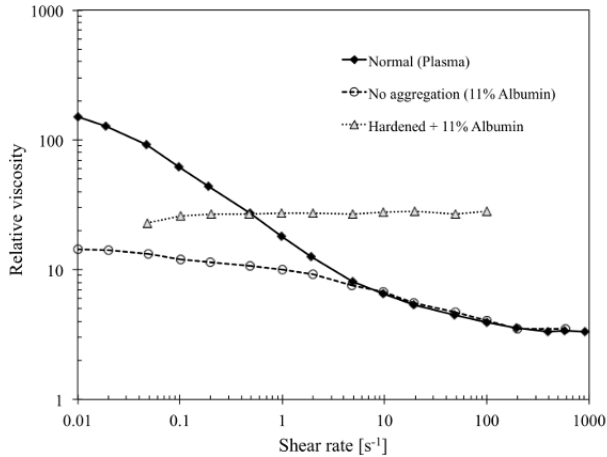


Figure 1.5. Relative viscosity (normalized by plasma viscosity) for a suspension of normal human red blood cells with a hematocrit of 45% in plasma (normal blood) in a buffer containing albumin (with no aggregation) and glutaraldehyde-stiffened red blood cells (data from Chien (1970))

The unsteady nature of blood flows in part of the vascular system, as well as the complex and variable cross-section flow geometries, lead us to consider the dynamic aspects of blood rheology. The characteristic times for the establishment of a microstructure related to red blood cell aggregation (as well as possible hysteresis in the force/distance relationship between the aggregation and disintegration processes; see section 1.5.2) are responsible for the thixotropic nature of blood. This has been revealed by a number of experimental measurements (Dintenfass 1962), but remains a weak and visible effect, mainly at low shear rates with relatively long relaxation times, and this effect is likely negligible under physiological flow conditions. Viscoelastic properties have been shown to emerge in frequency (or characteristic time) ranges relevant to blood circulation (Thurston 1973). Since these properties are closely related to the composition of blood and the mechanical properties of its constituents (red blood cell deformability), a quantitative understanding of the link between microscopic properties and viscoelastic characteristics may be of significant interest, in order to use rheology for diagnostic purposes, for example. However, this viscoelasticity

decreases significantly as the shear rate increases and for physiological hematocrits (McMillan *et al.* 1986), suggesting that in a vessel flow modeling approach, the main non-Newtonian characteristic to be taken into account remains the shear-thinning behavior.

Designation	Viscosity law	References
Power law	$\eta = k \dot{\gamma} ^{n-1}$	(Cho and Kensey 1991)
Carreau	$\eta = \eta_{\infty} + (\eta_0 - \eta_{\infty})(1 + A \dot{\gamma} ^2)^n$	(Cho and Kensey 1991)
Carreau-Yasuda	$\eta = \eta_{\infty} + \frac{\eta_0 - \eta_{\infty}}{(1 + \lambda \dot{\gamma} ^b)^a}$	(Bird <i>et al.</i> 1987)
Modified Casson	$\eta = \left[\sqrt{\tau_y \left(\frac{1 - e^{-m \dot{\gamma} }}{ \dot{\gamma} } \right)} + \sqrt{\eta_c} \right]^2$	(Fung 1993)
Generalized power law	$n = k(\dot{\gamma}) \dot{\gamma} ^{n(\dot{\gamma})-1}$ $k(\dot{\gamma}) = \eta_{\infty} + \Delta\eta \exp \left[- \left(1 + \frac{ \dot{\gamma} }{a} \right) \exp \left(\frac{-b}{\dot{\gamma}} \right) \right]$ $n(\dot{\gamma}) = n_{\infty} + \Delta n \exp \left[- \left(1 + \frac{ \dot{\gamma} }{c} \right) \exp \left(\frac{-d}{\dot{\gamma}} \right) \right]$	(Ballyk <i>et al.</i> 1994)
Quemada	$\eta = \frac{\eta_0}{\left[1 - \frac{1}{2} \left(\frac{k_0 + k_{\infty} \dot{\gamma}^{1/2}}{1 + \dot{\gamma}^{1/2}} \right) H \right]^2}$ Equivalent shape (modified Casson): $\eta = \left(\sqrt{\eta_{\infty}} + \frac{\sqrt{\tau_0}}{\sqrt{\lambda} + \sqrt{\dot{\gamma}}} \right)^2$	(Quemada 1978, Buchanan <i>et al.</i> 2000)

Table 1.4. Main models of macroscopic blood rheology

Taking this shear-thinning behavior into consideration, although it significantly complicates numerical simulations, leads to significantly different results from the Newtonian model in situations of medical interest in the presence of pulsatile flow, bifurcations or stenosis-like constrictions (Buchanan *et al.* 2000). As an example, Karimi *et al.* (2014) compare nine rheological models in blood flow simulations in the aortic arch that produce significantly different velocity fields and stress distributions at the walls. This demonstrates how taking the non-Newtonian nature of blood into

consideration can be important, even in regions where the flow velocities are fastest. Other simulations of flow in the coronary arteries show differences in peak pressure values of up to 50% between a Casson-type model and a Newtonian fluid (Apostolidis *et al.* 2016). The chosen rheological model can, moreover, have an effect on the transport of particles (cells and platelets) and can also influence secondary structures that establish themselves (vortex) in the vicinity of arterial stenoses, for example, and that may play a role in the appearance of microembolisms (Buchanan and Kleinstreuer 1998).

1.4.2. Red blood cell aggregation

In the presence of plasma proteins, red blood cells form aggregates at low shear rates, which are responsible for the shear-thinning nature of the blood mentioned above. The degree of aggregation is directly correlated with the rate of sedimentation of red blood cells, a test commonly used in hematology as a non-specific marker of inflammatory conditions or other blood abnormalities. While immunoglobulin abnormalities, or an abnormal C-reactive protein level associated with an inflammatory response may be associated with a high sedimentation rate, it has been shown that these factors alone are not sufficient to promote aggregation, but are generally associated with an increase in the fibrinogen level, which is considered the main factor of aggregation (Schechner *et al.* 2003; Flormann *et al.* 2015). The flattened shape of red blood cells favors the formation of aggregates in the form of “rouleaux”, similar to stacks of coins (Figure 1.6), which may also agglomerate into aggregates with a less regular shape, or connect to form a network responsible for the existence of a (low) yield stress for blood flow. It should be noted that (reversible) red blood cell aggregation is a fundamentally different phenomenon from (irreversible) coagulation, which leads to the formation of blood clots by polymerizing fibrinogen into a fibrin network, and which represents an important subject of research in itself in view of its biomedical implications (Yeromonahos *et al.* 2010).

Different techniques can be used to characterize aggregation and its structural consequences at the suspension scale: image analysis (Jan and Chien 1973; Chen *et al.* 1994), aggregometry or ektacytometry (Baskurt and Funda 2000; Baskurt *et al.* 2009), light scattering (Shin *et al.* 2005) or acoustic backscatter (Boynard and Lelievre 1990; Franceschini *et al.* 2020) to enable the characterization of the size distribution of aggregates in a flow. While these techniques enable the correlation of aggregate size statistics and

rheology, more local techniques have been used to study microscopic-scale aggregation and disaggregation mechanisms to derive information on underlying mechanisms and characterize cell-scale interaction forces. These include techniques of micropipette aspiration (Buxbaum *et al.* 1982) or atomic force microscopy measurement to determine the interaction energy between two red blood cells in a doublet disaggregation experiment (Steffen *et al.* 2013). Recently, measurements of interaction forces in an aggregation or disaggregation situation have been conducted using multiple optical tweezers, allowing better control of the interaction surface (Yaya 2021).

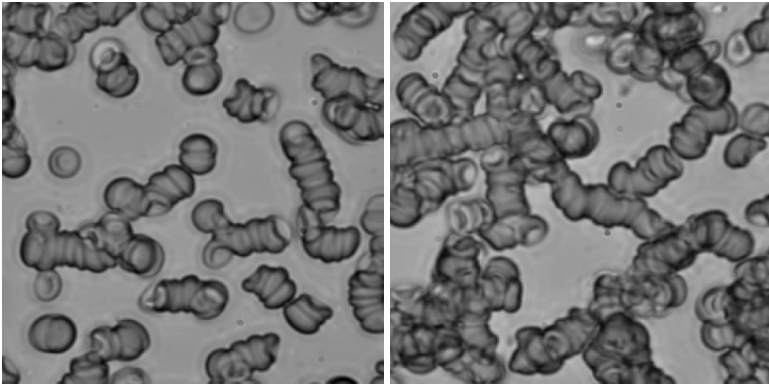


Figure 1.6. Aggregates (*rouleaux*) of red blood cells forming an interconnected network. For a color version of this figure, see www.iste.co.uk/deplano/biological.zip

Two mechanisms have been identified to explain aggregation: membrane bridging by aggregation molecules and depletion effects leading to forces of entropic origin. It should be noted that the experimental studies on these mechanisms were not only carried out in solutions containing fibrinogen, the main protein responsible for aggregation under physiological conditions, but also with the help of model molecules such as Dextran, which offers the advantage of existing in a wide range of molecular weights, allowing hypotheses of different theoretical aggregation models to be tested. Historically, the bridging interaction mechanism is the first to have been proposed and is supported by the evidence of macromolecule adsorption on the surface of red blood cells and the role of electrostatic forces (Chien and Jan 1973) to explain the non-monotonous nature of the interaction force as a function of the macromolecular concentration, for which a characteristic bell-shaped curve is generally observed. Models of non-specific interaction have been integrated into numerical simulations of red blood cells in

aggregation (Bagchi *et al.* 2005), based on association and dissociation rates and local ligand concentrations. In the case of fibrinogen, it has also been suggested that specific sites may be involved in adhesive interaction (Lominadze and Dean 2002). Within this context, Pereverzev *et al.* (2005) propose a model in which the receptor-ligand binding can be achieved by two types of bonds, called “slip” and “catch,” the latter being reinforced by the application of a low force. The second mechanism invoked, which is based on depletion effects, was originally proposed by Asakura and Oosawa (1958) and adapted by Neu and Meiselman (2002), to introduce the effects of macromolecular penetration into cell glycocalyx, in order to account for saturation effects responsible for the decrease in interaction at high macromolecular concentrations. In qualitative terms, the depletion effects are related to the finite size of the macromolecules (proteins) in solution, which results in the existence of a steric depletion layer on the surface of the red blood cells. When two red blood cells get close, this exclusion is responsible for a local decrease in the macromolecular concentration within the space separating the two membranes, relative to the concentration in the outer volume. The result is a gradient of concentration and therefore osmolarity, which leads to low pressure in this semi-confined space.

While these two models make it possible to account, at least in qualitative terms and after adjusting the parameters, for the phenomenology of the measurements of interaction energy or forces between red blood cells, questions still remain as to the relative importance of the two phenomena in real systems (fibrinogen, possibly with the synergistic effect linked to other plasma proteins, or dextran in model experiments). In complex situations of red blood cell suspensions in flow, with relative shear motions between membranes, it may be surmised that qualitative differences might have repercussions on the dynamics and mechanisms of aggregation/disintegration under flow. To the extent that only depletion forces are present, these depend only on the instantaneous distance between the red blood cell membranes, regardless of the history of the process. Conversely, a bridging mechanism first involves asymmetry between the aggregation and disaggregation processes from the perspective of the forces involved, all the more so if binding consolidation is established with the contact time. Furthermore, a specific ligand/receptor interaction has implications for the conditions of relative motion of the two membranes in a shear situation, for example. Recent investigations (Yaya 2021) tend to confirm this asymmetry in the force/displacement relationship between aggregation and disaggregation processes when bridging phenomena are involved, which may have repercussions on the stability of aggregates in circulation.

On a microscopic scale and in the absence of hydrodynamic stresses, the morphology of aggregates and their stability are governed by an equilibrium between the attractive or adhesion forces, on the one hand, and the membrane forces on the other. The result, even for the simplest aggregates made up of two cells, is a large variety in morphology, conditioned by the membrane bending energy (Ziherl and Svetina 2007; Flormann *et al.* 2017), as well as the shear modulus of the red blood cell spectrin network, or the differences in size and reduced volume that may result from the dispersity of red blood cell properties within the same sample (Hoore *et al.* 2018).

In flow, a complex interaction occurs between adhesive interaction forces between red blood cells and hydrodynamic effects that tend to both promote aggregation kinetics (by provoking interactions between red blood cells proportional to the local shear rate) and break up existing aggregates (Quemada 1978). Significant efforts have been made in recent years, first, to characterize the aggregate size distributions and their flow dynamics through experimentation, and second, to model aggregation/disaggregation phenomena on a microscopic scale and propose models linking aggregate dynamics, in statistical terms, with blood rheology. The fundamental process in the dynamics of aggregation under flow is that of the interaction between two cells. In modeling terms, this model situation has therefore logically received a certain amount of attention in numerical simulation using several methods. One of the first studies of this type, based on 2D simulations with a front tracking method and a model of a droplet surrounded by a viscoelastic membrane for red blood cells (Bagchi *et al.* 2005) suggests that the rheological properties of cells have a significant effect on stability and aggregate dynamics, with cytoplasmic viscosity and membrane rigidity tending to stabilize aggregates. In this model, the adhesion between cells is modeled by a set of equations reflecting the kinetics of formation and breaking of bonds between the membranes when the distance between them is below a critical distance. Although the authors state that this model does not specifically call on a specific molecular mechanism, it seems more suited to accounting for the effect of a bridging mechanism, rather than a depletion mechanism. Other models use a simple distance-dependent membrane interaction potential of the Morse potential type (Zhang *et al.* 2008; Ju *et al.* 2013) and Lattice–Boltzmann methods (LBM) for fluid dynamics. While qualitative information can be derived regarding the relative effects of adhesion, shear rate or even heterogeneity of red blood cell properties (Ju *et al.* 2013), these models are still limited in quantitative terms and when it comes to comparison with experimental results. Mechanical models of red blood cells remain approximations: neo-Hookean membranes, which do not

offer membrane inextensibility if corrections are not made to the model, and two-dimensional calculations, which cannot account for all of the dynamics and spatial interaction configurations of two red blood cells in a real flow. A similar model has also made it possible to examine the effect of aggregation on the structure and rheology of a red blood cell suspension in a channel (Zhang *et al.* 2009), with the authors notably concluding that aggregation, by making the suspension more compact, tends to increase the depletion layer in the vicinity of the walls (see Figure 1.7 and the following section for a description of this phenomenon) and, counter-intuitively, reduce the apparent viscosity. This influence of aggregation on the depletion layer is confirmed by several experimental studies (Ong *et al.* 2010; Sherwood *et al.* 2012). Other numerical works are based on models such as *coarsened graining* of red blood cells, enabling a large number of objects to be simulated more approximatively, and modeling their aggregation with a Lennard–Jones-type potential (Fedosov *et al.* 2011). While this type of large-scale simulation represents significant progress, allowing a link to be established between microscopic dynamics and rheology, and, notably, experimental viscosity curves to be reproduced (Figure 1.7) as a function of the shear rate or blood yield stress, it should be noted that the nature of the models can at times lead to the mechanical parameter values chosen not necessarily being consistent with the values measured independently or used to simulate other experiments. As a result, microscopic-scale modeling of the phenomena of aggregation under flow is a research pathway that still largely remains to be explored.

Other works suggest a more comprehensive theoretical and statistical approach based on phenomenological kinetic equations modeling the phenomena of aggregation and disaggregation (Chen and Huang 1996), and inclusion of the dynamics of the aggregate network through modeling of energy flows in the system (Kalevotiis and Yanneskis 2011). These models, which require parameter adjustment on experimental data, can represent an interesting intermediate step between microscopic and macroscopic rheological models. Advances in theoretical and numerical modeling of aggregation under flow require and generate experimental developments to characterize the dynamics of aggregation at different scales, from the elementary mechanisms of association and dissociation of red blood cells in aggregates, to the determination of the characteristics and distributions of aggregate sizes in concentrated and complex flows. A number of studies are participating in this effort, based on techniques using imaging (Mehri *et al.* 2014; Kalivotiis *et al.* 2016) or acoustics (Franceschini *et al.* 2020).

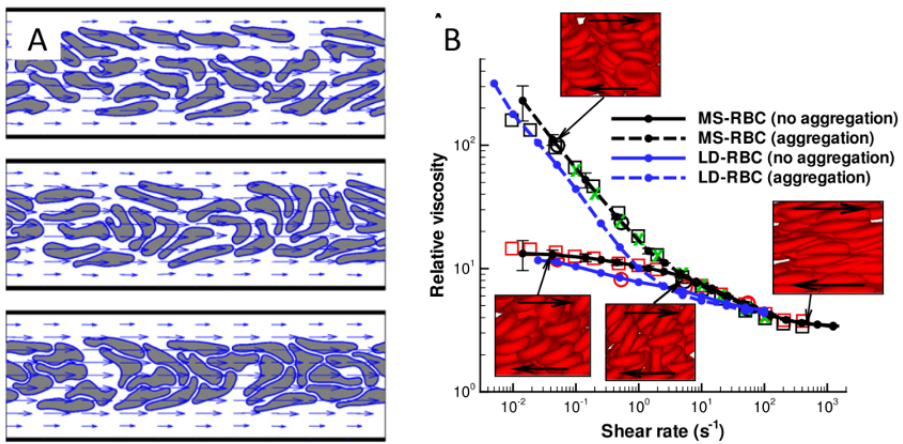


Figure 1.7. a) Effect of increasing aggregation (from top to bottom) on the structure of a 2D suspension of red blood cells (from Zhang *et al.* (2009)). b) Experimental and simulated rheology of a suspension of shear red blood cells. Open symbols: experimental data; solid lines: mesoscopic model (MS-RBC); dashed lines: low-dimensionality model (LD-RBC) (according to Fedosov *et al.* (2011)). For a color version of this figure, see www.iste.co.uk/deplano/biological.zip

Rheological data (see Figure 1.5) and mean shear rate values in capillaries (of the order of $1,000 \text{ s}^{-1}$) have long meant that aggregation can only play a role in the center of larger vessels (arteries, veins, venules and possibly arterioles), where shear rates are relatively lower. Trains of cells (clusters) are observed in capillaries *in vivo*, however, with their formation and stabilization mechanisms forming the subject of several recent studies (see Figure 1.8(a)). While it is recognized that these clusters of cells can form and even be stabilized by hydrodynamic interaction processes (Claveria *et al.* 2016), experimental and numerical studies have shown that there is a strong correlation between the probability of these clusters occurring and the concentration of the aggregating agent (dextran or fibrinogen), in ranges of concentration (and thus interaction energy) that may cover physiological ranges in healthy or pathological situations (Brust *et al.* 2014). With aggregation tending to stabilize red blood cell clusters in capillaries, aggregation is likely to play a role in microcirculation through local changes in flow resistance, and more generally in red blood cell behavior in microcirculation networks.

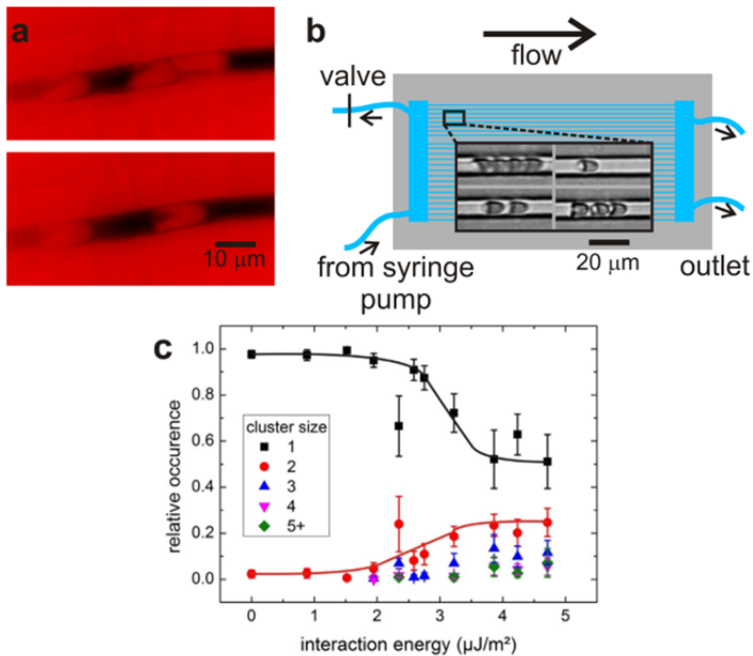


Figure 1.8. *a)* Red blood cell flow in a mouse capillary, showing both isolated blood cells and groups of cells potentially in adhesion. *b)* Study in microfluidic channels of the role of aggregation on the size of groups of red blood cells. *c)* Statistics of aggregate sizes as a function of interaction energy (controlled by Dextran or fibrinogen concentration (Brust et al. 2014)). For a color version of this figure, see www.iste.co.uk/deplano/biological.zip

1.4.3. Dynamics of microcirculation

In the systemic circulation, between the arterial system that conveys a highly pulsed flow of oxygenated blood from the heart and the venous system that brings it back to the heart, lies the domain of microcirculation, consisting of vessels whose diameter is less than a few hundred micrometers. These regions of the vascular system consist of complex networks of vessels, the finest of which, the capillaries, have a diameter of 4–8 μm, are preceded by arterioles and are followed by venules. The largest part of the pressure drop between leaving the heart through the aorta and returning through the vena cava occurs in these dense, branched networks, which irrigate all of the organs. The boundary conditions of the transport in large vessels are therefore determined by the resistance imposed by microcirculation, which,

moreover, is a system regulated by mechanisms of vasodilatation or vasoconstriction responding to local supply needs for oxygen, heat or immune response, for example. Indeed, it is in the microcirculation that the blood functions are manifested, and the walls of the arterioles are sensitive to shear stresses on the wall and can activate contractile cells, enabling the flow in the capillaries to be regulated. Significant, repeated variations of these wall stresses can also trigger an adaptation of the vessels (vascular remodeling) and the capillary network (angiogenesis).

The fundamental difference in the nature of flow between microcirculation and macrocirculation (large vessels) is not limited to differences in the order of magnitude of the characteristic numbers (Reynolds number and Womersley number). These aspects are certainly crucial: flows are dominated here by viscous effects, and fluid dynamics can generally be modeled by the Stokes equation at these scales. Cardiac pulsations are markedly dampened here, ensuring quasi-stationary conditions, but the scale of the flows also means that blood does not behave as a uniform continuous medium here, with its nature as a dense suspension of deformable particles giving rise to specific phenomena. In arterioles or venules, the vessel diameter is less than 30 times the diameter of a red blood cell, and in the finest capillaries, the red blood cells even have to deform to pass through a conduit smaller than their own diameter. The structure and rheology of the suspension are therefore dominated by cell–cell and cell–wall interactions, and depart significantly from the rheological laws applicable in large vessels or viscometric flows.

The structural characteristics of microcirculatory flows, revealed by Poiseuille (1835), can be seen in Figure 1.9, which shows his representation of the microvascular network of the frog mesentery and circulating red blood cells. Two observations stand out: (i) in the precapillary arterioles and postcapillary venules there is a depletion layer with no red blood cells in the vicinity of the walls, generally called the cell-free layer (CFL); (ii) the red blood cell distribution is very heterogeneous in the capillaries and the hematocrit is not homogeneous. More recent imaging techniques are able to confirm these observations and record network geometries useful for simulating blood flow models based, for example, on effective rheological laws and phase separation laws at the bifurcations responsible for the heterogeneities observed.

The non-uniform distribution of red blood cells in the cross-section of a vessel and the existence of a depletion layer (CFL) at the walls are responsible for two significant rheological effects in blood flows in a tube. The first, identified by Fåhræus, indicates that for a given systemic hematocrit, the apparent hematocrit in the microcirculation is less than the hematocrit of the reservoir that supplies it (artery), and decreases with the diameter of the vessels. This is a consequence of the conservation of red blood cell and plasma flows, and because the blood cells are on average more centered in the channel than the plasma, as their velocity is greater. A correlation between tube hematocrit, discharge (or reservoir) hematocrit and vessel diameter is proposed by Pries *et al.* (1990). The second effect correlated with the existence of the cell-free marginal layer is the Fåhræus–Lindqvist effect, which consists of a decrease in the apparent viscosity of the blood when the tube diameter decreases. This counterintuitive effect is the result of the lubricating effect of the marginal layer, whose viscosity (that of plasma) is lower than that of the dense suspension flowing through the middle of the channel (Fåhræus and Lindqvist 1931).

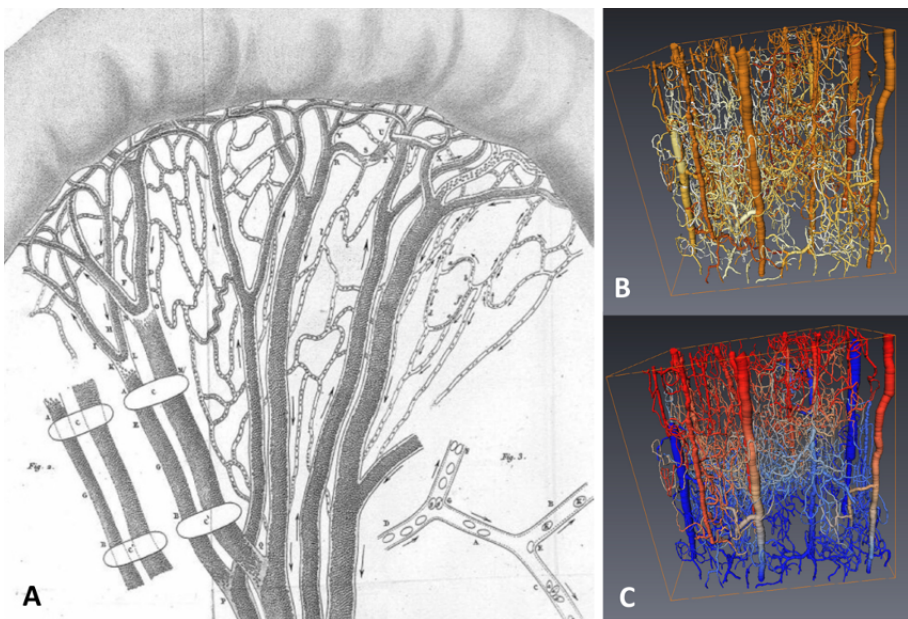


Figure 1.9. Microcirculation networks: (a) frog mesentery (Poiseuille 1835); (b and c) color-coded representations of simulated fields (b: hematocrit, c: flow) in a network geometry acquired by X-ray tomography in monkey brain (Guibert *et al.* 2010). Scale bar: 500 μm

On a microscopic scale, the structuring of the suspension responsible for these phenomena is governed by two antagonistic processes, which are, first, a migration of cells away from the walls and toward the center of the channel, and second, a shear-induced diffusion and interactions between red blood cells. These processes, which are common to all suspensions of deformable objects, have become the subject of works permitting scaling laws to be proposed (Podgorski *et al.* 2011; Grandchamp *et al.* 2013; Losserand *et al.* 2019), and are strongly influenced by the mechanical properties of circulating cells, which can make them tools of interest for diagnosis, indirect characterization of these properties or cell sorting (Geislinger and Franke 2013; Connolly *et al.* 2021). In a polydisperse system, such as blood, this sensitivity to cell properties also leads to margination and segregation phenomena, where the most rigid and smallest cells tend to be closer to the walls (white blood cells, platelets and, potentially, more rigid pathological red blood cells), on average. While there are continuous models to describe margination, as well as numerical works (Kumar and Graham 2012), the details of the mechanisms remain the subject of active research. There has been a renewed international interest in this subject among teams of theorists/numerical analysts, further to the evolution of numerical models and computing means (Fedosov and Gompper 2014; Qi and Shaqfeh 2017), underscoring a need for quantitative experimental data.

The heterogeneity of the distribution of hematocrit visible in Figure 1.9 is a consequence of the asymmetric separation of red blood cells in the network bifurcations. Model experiments in microfluidics have shown that in general, for perfectly symmetrical bifurcations where the two outlet branches are geometrically identical, if the flow rates are different in these two branches (e.g. because the outlet pressures or branch lengths are different), the red blood cell volume fraction (hematocrit) is higher in the branch of higher flow rate. This phenomenon, widely observed in microcirculation, is generally referred to as the Zweifach–Fung effect (Svanes and Zweifach 1968; Fung 1973). Under physiological conditions, it can be estimated that if the asymmetry of the bifurcation outlet flow rates is such that one branch receives only a quarter of the inlet flow rate, the hematocrit in that branch may fall to zero. There have been a large number of *in vivo* studies devoted to this phenomenon (Pries *et al.* 1996), as well as studies on model systems (Chien *et al.* 1985) or numerical simulations (Barber *et al.* 2008). The phenomenon is relatively subtle, and strongly depends on the configuration of the particles or blood cells that arrive at the bifurcation (Doyeux *et al.* 2011), which may even lead to the inversion of the partition in some cases (Shen *et al.* 2015). These effects, coupled with the dynamics of the

reorganization of red blood cells in the network branches between two bifurcations, under the effect of the migration/diffusion mechanisms mentioned above, are crucial for the distribution of red blood cells at the scale of a capillary network (Balogh and Bagchi 2018).

The strong coupling between (i) the structure of the suspension in the network branches, (ii) the apparent viscosity in these branches and (iii) the phase separation at the bifurcations cannot only lead to heterogeneities in the hematocrit distribution, but also to spatiotemporal fluctuations in the flow (Kiani *et al.* 1994). The oscillations and instabilities of microvascular flows have been observed in vivo (Mezentseva *et al.* 2016) and are suspected to have an impact on the regulation of blood flow and tissue oxygenation. To date, the question of the stability of these flows has formed the subject of some recent theoretical studies, but there is very little experimental validation (Davis and Pozrikidis 2014; Karst *et al.* 2017), making it a relatively active subject of study aimed at clarifying the purely passive mechanisms of microcirculation regulation. The inclusion of effects related to aggregation, its influence on red blood cell distribution and blood perfusion in the capillary networks is also an active research topic (Reinhart 2017; Kaliviotis *et al.* 2018).

1.5. Conclusion

According to the WHO, cardiovascular disease, affecting the circulatory system, is the leading cause of mortality worldwide, accounting for more than 30% of deaths, predominantly from coronary heart disease and strokes. In addition, hemopathies, which affect the components of the blood, constitute a group of diseases, many of which hereditary, that are highly prevalent. While the causes, mechanisms and consequences of these pathologies are extremely varied and affect different circulation levels, a common characteristic discussed in this chapter is their fundamentally multi-scale nature, coupling biology and physicochemistry, circulating cell mechanics and vascular walls, blood rheology and hydrodynamics at vessel and circulatory-network scale.

The quantitative understanding and modeling of the physical and mechanical aspects of blood circulation dynamics continue to represent a challenge related to its nonlinear character and extreme sensitivity to biomechanical and physicochemical parameters, which are likely to vary greatly in pathological cases. The past few decades have seen significant

developments in both in vivo and in vitro experimental techniques (optical and acoustic imaging and Magnetic Resonance Imaging). There have also been advances in numerical simulation, in terms of both methods and computing power, which now allow the study of large systems with a multiphysics approach. As a result, considerable progress has been made in understanding the rheological properties of blood and circulatory dynamics. In addition to a better fundamental understanding of hemodynamics and hemorrheology, these advances offer new scope for fruitful interactions at the interface between medicine, physics and mechanics in areas such as diagnosis, patient monitoring assistance and preoperative decision support within the framework of vascular surgery, because of the ever-increasing predictive ability of the models.

1.6. References

- Apostolidis, A.J., Moyer, A.P., Beris, A.N. (2016). Non-Newtonian effects in simulations of coronary arterial blood flow. *J. of Non-Newtonian Fluid Mech.*, 233, 155–165.
- Asakura, S. and Oosawa, F. (1958). Interaction between particles suspended in solutions of macromolecules. *J. Polym. Sci.*, 33, 183–192.
- Asakura, T., Mattiello, J.A., Obata, K., Asakura, K., Reilly, M.P., Tomassini, N., Schwartz, E., Ohene-Frempong, K. (1994). Partially oxygenated sickled cells: Sickle-shaped red cells found in circulating blood of patients with sickle cell disease. *Proc. Nat. Acad. Sci.*, 91, 1–5.
- Bagchi, P., Johnson, P.C., Popel, A.S. (2005). Computational fluid dynamic simulation of aggregation of deformable cells in a shear flow. *Biochem. Eng. J.*, 127, 1070–1080.
- Ballyk, P.D., Steinman, D.A., Ethier, C.R. (1994). Simulation of non-Newtonian blood flow in an end-to-end anastomosis. *Biorheology*, 31(5), 565–586.
- Balogh, P. and Bagchi, P. (2018). Analysis of red blood cell partitioning at bifurcations in simulated microvascular networks. *Phys. Fluids*, 30, 051902.
- Barabino, G.A., Platt, M.O., Kaul, D.K. (2010). Sickle cell biomechanics. *Annu. Rev. Biomed. Eng.*, 12, 345–367.
- Barber, J.O., Alberding, J.P., Restrepo, J.M., Secomb, T.W. (2008). Simulated two-dimensional red blood cell motion, deformation, and partitioning in microvessel bifurcations. *Ann. Biomech. Engng.*, 36, 1690–1698.

- Baskurt, O.K. and Funda, M. (2000). Importance of measurement temperature in detecting the alterations of red blood cell aggregation and deformability studied by ektacytometry: A study on experimental sepsis in rats. *Clin. Hemorheol. Microcirc.*, 23, 43–49.
- Baskurt, O.K., Uyuklu, M., Ulker, P., Cengiz, M., Nemeth, N., Alexy, T., Shin, S., Hardeman, M.R., Meiselman, H.J. (2009). Comparison of three instruments for measuring red blood cell aggregation. *Clin. Hemorheol. Microcirc.*, 43, 283–298.
- Betz, T., Lenz, M., Joanny, J.-F., Sykes, C. (2009). ATP-dependent mechanics of red blood cells. *Proc. Nat. Acad. Sci.*, 106, 15320–15325.
- Biben, T., Farutin, A., Misbah, C. (2011). Three-dimensional vesicles under shear flow: Numerical study of dynamics and phase diagram. *Phys. Rev. E.*, 83, 031921.
- Bird, R.B., Armstrong, R.C., Hassager, O. (1987). *Dynamics of Polymeric Liquids*, 2nd edition. Wiley, New York.
- Bosch, F.H., Werre, J.M., Roerdinkholder-Stoelwinder, B., Huls, T.H., Willekens, F.L., Halie, M.R. (1992). Characteristics of red blood cell populations fractionated with a combination of counterflow centrifugation and percoll separation. *Blood*, 79, 254–260.
- Boynard, M. and Lelievre, J.C. (1990). Size determination of red blood cell aggregates induced by dextran using ultrasound backscattering phenomenon. *Biorheology*, 27, 39–46.
- Brust, M., Aouane, O., Thiébaud, M., Flormann, D., Verdier, C., Kaestner, L., Laschke, M. W., Selmi, H., Benyoussef, A., Podgorski, T., Coupier, G., Misbah, C., Wagner, C. (2014). The plasma protein fibrinogen stabilizes clusters of red blood cells in micro capillary flows. *Sci. Rep.*, 4, 4348.
- Buchanan, J.R. and Kleinstreuer, C. (1998). Simulation of particle-hemodynamics in a partially occluded artery segment with implications to the initiation of microemboli and secondary stenoses. *J Biomech Eng.*, 120(4), 446–454.
- Buchanan, J.R., Kleinstreuer, C., Comer, J.K. (2000). Rheological effects on pulsatile hemodynamics in a stenosed tube. *Computers & Fluids*, 20, 695–724.
- Buxbaum, K., Evans, E., Brooks, D.E. (1982). Quantitation of surface affinities of red blood cells in dextran solutions and plasma. *Biochemistry*, 21, 3235–3239.
- Chen, J. and Huang, Z. (1996). Analytical model for effects of shear rate on rouleau size and blood viscosity. *Biophys. Chem.*, 58, 273–279.

- Chen, S., Barshtein, G., Gavish, B., Mahler, Y., Yedgar, S. (1994). Monitoring of red blood cell aggregability in a flow-chamber by computerized image analysis. *Clin. Hemorheol.*, 14, 497–508.
- Chien, S. (1970). Shear dependence of effective cell volume as a determinant of blood viscosity. *Science*, 168, 977–979.
- Chien, S. and Jan, K.M. (1973). Red cell aggregation by macromolecules: Roles of surface adsorption and electrostatic repulsion. *J. Supramol. Struct.*, 1, 385–409.
- Chien, S., Tvetenstrand, C.D., Epstein, M.A., Schmid-Schonbein, G.W. (1985). Model studies on distributions of blood cells at microvascular bifurcations. *Am. J. Physiol. Heart Circ. Physiol.*, 248, H568–H576.
- Cho, Y.I. and Kensey, K.R. (1991). Effects of the non-Newtonian viscosity of blood on flows in a diseased arterial vessel. Part 1: Steady flows. *Biorheology*, 28, 241–262.
- Claveria, V., Aouane, O., Thiébaud, M., Abkarian, M., Coupier, G., Misbah, C., John, T., Wagner, C. (2016). Clusters of red blood cells in microcapillary flow: Hydrodynamic versus macromolecule induced interaction. *Soft Matter*, 12, 8235–8245.
- Connes, P., Simmonds, M.J., Brun, J.-F., Baskurt, O. (2013). Exercise hemorheology: Classical data, recent findings and unresolved issues. *Clin. Hemorheol. Microcirc.*, 53, 187–199.
- Connolly, S., McGourty, K., Newport, D. (2021). The influence of cell elastic modulus on inertial positions in poiseuille microflows. *Biophys. J.*, 120, 855–865.
- Cordasco, D. and Bagchi, P. (2014). Intermittency and synchronized motion of red blood cell dynamics in shear flow. *J. Fluid Mech.*, 759, 472–488.
- Da Costa, L., Galimand, J., Fenneteau, O., Mohandas, N. (2013). Hereditary spherocytosis, elliptocytosis, and other red cell membrane disorders. *Blood Rev.*, 27(4), 167–178.
- Davis, J.M. and Pozrikidis, C. (2014). Self-sustained oscillations in blood flow through a honeycomb capillary network. *Bull. Math. Biol.*, 76, 2217–2237.
- Dintenfass, L. (1962). Thixotropy of blood and proneness to thrombus formation. *Circ. Res.*, 11, 233–239.
- Doyeux, V., Podgorski, T., Peponas, S., Ismail, M., Coupier, G. (2011). Spheres in the vicinity of a bifurcation: Elucidating the Zweifach–Fung effect. *J. Fluid Mech.*, 674, 359–388.
- Dupire, J., Socol, M., Viallat, A. (2012). Full dynamics of a red blood cell in shear flow. *Proc. Nat. Acad. Sci. USA*, 109, 20808–20813.

- Evans, E. and Fung, Y.-C. (1972). Improved measurements of the erythrocyte geometry. *Microvasc. Res.*, 4, 335–347.
- Fåhræus, R. and Lindqvist, T. (1931). The viscosity of the blood in narrow capillary tubes. *Am. J. Physiol.*, 96, 562–568.
- Fedosov, D.A. and Gompper, G. (2014). White blood cell margination in microcirculation. *Soft Matter*, 10, 2961–2970.
- Fedosov, D.A., Pan, W., Caswell, B., Gompper, G., Karniadakis, G.E. (2011). Predicting human blood viscosity in silico. *Proc. Nat. Acad. Sci.*, 108, 11772–11777.
- Fischer, T.M. and Korzeniewski, R. (2013). Threshold shear stress for the transition between tumbling and tank-treading of red blood cells in shear flow: Dependence on the viscosity of the suspending medium. *J. Fluid Mech.*, 736, 351–365.
- Flormann, D., Kuder, E., Lipp, P., Wagner, C., Kaestner, L. (2015). Is there a role of C-reactive protein in red blood cell aggregation? *Int. J. Laboratory Hematology*, 37(4), 474–482.
- Flormann, D., Aouane, O., Kaestner, L., Ruloff, C., Misbah, C., Podgorski, T., Wagner, C. (2017). The buckling instability of aggregating red blood cells. *Sci. Rep.*, 7, 7928.
- Franceschini, E., Yu, F.T.H., Destrempes, F. (2020). Ultrasound characterization of red blood cell aggregation with intervening attenuating tissue-mimicking phantoms. *J. Acoust. Soc. Amer.*, 127, 1104–1115.
- Fung, Y.C. (1973). Stochastic flow in capillary blood vessels. *Microvasc. Res.*, 5, 34–48.
- Fung, Y.C. (1993). *Biomechanics: Mechanical Properties of Living Tissues*, 2nd edition. Springer, Berlin.
- Geddes, J.B., Carr, R.T., Karst, N.J., Wu, F. (2007). The onset of oscillations in microvascular blood flow. *SIAM J. Appl. Dyn. Syst.*, 6, 694.
- Geislinger, T. and Franke, T. (2014). Hydrodynamic lift of vesicles and red blood cells in flow – From Fåhræus and Lindqvist to microfluidic cell sorting. *Adv. Coll. Interface Sci.*, 208, 161–176.
- Grandchamp, X., Coupier, G., Srivastav, A., Minetti, C., Podgorski, T. (2013). Lift and down-gradient shear-induced diffusion in red blood cell suspensions. *Phys. Rev. Lett.*, 110, 108101.
- Guibert, R., Fonta, C., Plouraboué, F. (2010). Cerebral blood flow modeling in primate cortex. *J. Cerebral Blood Flow and Metabolism*, 30, 1860–1873.

- Hales, S. (1733). *Statistical Essays: Containing Haemastaticks*. Innys, Manby & Woodward, London.
- Harvey, W. and Leake, C.D. (1928). *Exercitatio Anatomica de Motu Cordis and Sanguinis in Animalibus*. Facsimile of the original Latin ed. (1628) and English translation. Charles C. Thomas, Springfield.
- Hawkey, C.M. (1975). *Comparative Mammalian Haematology*. Butterworth-Heinemann, Elsevier, Oxford.
- Helfrich W. (1973). Elastic properties of lipid bilayers: Theory and possible experiments. *Z. Naturforsch.*, 28, 693–703.
- Higgs, D.R., Engel, J.D., Stamatoyannopoulos, G. (2012). Thalassaemia. *Lancet*, 379, 373–383.
- Hoore, M., Yaya, F., Podgorski, T., Wagner, C., Gompper, G., Fedosov, D.A. (2018). Effect of spectrin network elasticity on the shapes of erythrocyte doublets. *Soft Matter*, 14, 6278–6289.
- Jan, K.M. and Chien, S. (1973). Role of surface electric charge in red blood cell interactions. *J. Gen. Phys.*, 61, 638–654.
- Jensen, K.H., Kim, W., Holbrook, N.M., Bush, J.M.W. (2013). Optimal concentration in transport systems. *J. R. Soc. Interface*, 10, 20130138.
- Ju, M., Ye, S.S., Low, H.T., Zhang, J., Cabrales, P., Leo, H.L., Kim, S. (2013). Effect of deformability difference between two erythrocytes on their aggregation. *Phys. Biol.*, 10, 036001.
- Kaliviotis, E. and Yianneskis, M. (2011). Blood viscosity modelling: Influence of aggregate network dynamics under transient conditions. *Biorheology*, 48, 127–147.
- Kaliviotis, E., Dusing, J., Sherwood, J.M., Balabani, S. (2016). Quantifying local characteristics of velocity, aggregation and hematocrit of human erythrocytes in a microchannel flow. *Clin. Hemorheol. Microcirc.*, 63, 123–148.
- Kaliviotis, E., Sherwood, J.M., Balabani, S. (2018). Local viscosity distribution in bifurcating microfluidic blood flows. *Phys. Fluids*, 30, 030706.
- Karimi, S., Dabagh, M., Vasava, P., Dadvar, M., Dabir, B., Jalali, P. (2014). Effect of rheological models on the hemodynamics within human aorta: CFD study on CT image-based geometry. *J. Non-Newtonian Fluid Mech.*, 207, 42–52.
- Karst, N.J., Geddes, J.B., Carr, R.T. (2017). Model microvascular networks can have many equilibria. *Bull. Math. Biol.*, 79, 1–20.
- Kelemen, C., Chien, S., Artmann, G.M. (2001). Temperature transition of human hemoglobin at body temperature: Effects of calcium. *Biophys. J.*, 80, 2622–2630.

- Kiani, M.F., Pries, A.R., Hsu, L.L., Sarelius, I.H., Cokelet, G.R. (1994). Fluctuations in microvascular blood flow parameters caused by hemodynamic mechanisms. *Am. J. Physics*, 266, H1822.
- Ku, D.N. (1997). Blood flow in arteries. *Annu. Rev. Fluid Mech.*, 29, 399–434.
- Kumar, A. and Graham, M.D. (2012). Margination and segregation in confined flows of blood and other multicomponent suspensions. *Soft Matter*, 8, 10536–10548.
- Kumar, V., Abbas, A.K., Aster, J.C. (2012). *Robbins Basic Pathology*, 9th edition. Saunders, Philadelphia.
- Lac, E. and Barthès-Biesel. D. (2005). Deformation of a capsule in simple shear flow: Effect of membrane prestress. *Phys. Fluids*, 17, 072105.
- Lanotte, L., Mauer, J., Mendez, S., Fedosov, D.A., Fromental, J.-M., Claveria, V., Nicoud, F., Gompper, G., Abkarian, M. (2016). Red cells dynamic morphologies govern blood shear thinning under microcirculatory flow conditions. *Proc. Natl. Acad. Sci. USA*, 113, 13289–13294.
- Lee, S.W. and Steinman, D.A. (2007). On the relative importance of rheology for image-based CFD models of the carotid bifurcation. *J. Biomed. Engrg. – Trans. ASME*, 129, 273–278.
- Levant, M. and Steinberg, V. (2016). Intermediate regime and a phase diagram of red blood cell dynamics in a linear flow. *Phys. Rev. E*, 94, 062412.
- Lewis, J.H. (1996). *Comparative Hemostasis in Vertebrates*. Plenum Publishing Co., New York.
- Linderkamp, O., Friederichs, E., Boehler, R., Ludwig, A. (1993). Age dependency of red blood cell deformability and density: Studies in transient erythroblastopenia of childhood. *British J. Haematol.*, 83, 125.
- Lominadze, D. and Dean, W.L. (2002). Involvement of fibrinogen specific binding in erythrocyte aggregation. *FEBS Lett.*, 517, 1–3.
- Losserland, S., Coupier, G., Podgorski, T. (2019). Migration velocity of red blood cells in microchannels. *Microvasc. Res.*, 124, 30–36.
- Mauer, J., Mendez, S., Lanotte, L., Nicoud, F., Abkarian, M., Gompper, G., Fedosov, D.A. (2018). Flow-induced transitions of red blood cell shapes under shear. *Phys. Rev. Lett.*, 121, 118103.
- McMillan, D.E., Utterback, N.G., Nasrinasrabadi, M., Lee, M.M. (1986). An instrument to evaluate the time dependent flow properties of blood at moderate shear rates. *Biorheology*, 23, 63–74.

- Mehri R., Laplante, J., Mavriplis, C., Fenech, M. (2014). Investigation of blood flow analysis and red blood cell aggregation. *J. Med. Biol. Eng.*, 34, 469–474.
- Mezentseva, L.V., Pertsov, S.S., Hugaeva, V.K. (2016). A comparative analysis of the persistence of capillary blood flow oscillations in the left and right rat kidneys. *Biophysics*, 61, 656.
- Minetti, C., Audemar, V., Podgorski, T., Coupier, T. (2019). Dynamics of a large population of red blood cells under shear flow. *J. Fluid Mech.*, 864, 408–448.
- Nagel, R.L., Fabry, M.E., Steinberg, M.H. (2003). The paradox of hemoglobin SC disease. *Blood Reviews*, 17, 167–178.
- Neu, B. and Meiselman, H.J (2002). Red blood cell aggregation in polymer solutions. *Biophys. J.*, 83, 2482–2490.
- Ong, P.K., Namgung, B., Johnson, P.C., Kim, S. (2010). Effect of erythrocyte aggregation and flow rate on cell-free layer formation in arterioles. *Am. J. Physiol. Heart Circ. Physiol.*, 298, H1870–H1878.
- Park, Y., Best, C.A., Auth T., Gov, N.S., Safran, S.A., Popescu, G., Suresh, S., Feld, M.S. (2010). Metabolic remodeling of the human red blood cell membrane. *Proc. Natl. Acad. Sci. USA*, 107, 1289–1294.
- Peng, Z., Mashayekh, A., Zhu, Q. (2014). Erythrocyte responses in low-shear-rate flows: Effects of non-biconcave stress-free state in the cytoskeleton. *J. Fluid Mech.*, 742, 96–118.
- Pereverzev, Y.V., Prezhdo, O.V., Forero, M., Sokurenko, E.V., Thomas, W.E. (2005). The two-pathway model for the catch-slip transition in biological adhesion. *Biophys. J.*, 89, 1446–1454.
- Picart, C., Piau, J.-M., Gaillard, H., Carpentier, P. (1998). Human blood shear yield stress and its hematocrit dependence. *J. Rheol.*, 42, 1–12.
- Podgorski, T., Callens, N., Minetti, C., Coupier, G., Dubois, F., Misbah, C. (2011). Dynamics of vesicle suspensions in shear flow between walls. *Microgravity Sci. Technol.*, 23, 263–270.
- Poiseuille, J.-L.-M. (1835). *Recherches sur les causes du mouvement du sang dans les vaisseaux capillaires*. Imprimerie Royale, Paris.
- Poiseuille, J.-L.-M. (1844). *Recherches experimentales sur le mouvement des liquides dans les tubes de tres-petits diametres*. Imprimerie Royale, Paris.
- Pries, A.R., Secomb, T.W., Gaehtgens, P., Gross, J.F. (1990). Blood flow in microvascular networks: Experiments and simulation. *Circ. Res.*, 67, 826–834.

- Pries, A.R., Secomb, T.W., Gaethgens, P. (1996). Biophysical aspects of blood flow in the microvasculature. *Cardiovasc. Res.*, 32, 654–667.
- Qi, Q.M. and Shaqfeh, S.G. (2017). Theory to predict particle migration and margination in the pressure-driven channel flow of blood. *Phys. Rev. Fluids*, 2, 093102.
- Quemada, D. (1978). Rheology of concentrated disperse systems II. A model for non-Newtonian shear viscosity in steady flows. *Rheol. Acta*, 17, 632–642.
- Rees, D.C., Williams, T.N., Gladwin, M.T. (2010). Sickle-cell disease. *Lancet*, 376, 2018–2031.
- Reinhart, W.H. (2016). The optimum hematocrit. *Clin. Hemorheol. Microcirc.*, 64, 575–585.
- Reinhart, W.H., Piety, N.Z., Shevkopyas, S.S. (2017). Influence of red blood cell aggregation on perfusion of an artificial microvascular network. *Microcirculation*, 24, e12371.
- Reitsma, S., Slaaf, D.W., Vink, H., van Zandvoort, M.A.M.J., oude Egbrink, M.G.A. (2017). The endothelial glycocalyx: Composition, functions, and visualization. *Pflügers Arch – Eur. J. Physiol*, 454, 345–359.
- Ross, P.D. and Minton, A.P. (1977). Hard quasispherical model for the viscosity of hemoglobin solutions. *Biochem. Biophys. Res. Comm.*, 76, 971–976.
- Schechner, V., Shapira, I., Berliner, S., Comaneshter, D., Hershcovici, T., Orlin, J., Zeltser, D., Rozenblat, M., Lachmi, K., Hirsch, M., Beigel, Y. (2003). Significant dominance of fibrinogen over immunoglobulins, C-reactive protein, cholesterol and triglycerides in maintaining increased red blood cell adhesiveness/aggregation in the peripheral venous blood: A model in hypercholesterolaemic patients. *Eur. J. Clin. Invest.*, 33, 955–961.
- Seguin, B. and Fried, E. (2014). Microphysical derivation of the Canham–Helfrich free-energy density. *J Math. Biol.*, 68, 647–665.
- Shen, Z., Coupier, G., Kaoui, B., Polack, B., Harting, J., Misbah, C., Podgorski, T. (2015). Inversion of hematocrit partition at microfluidic bifurcations. *Microvasc. Res.*, 105, 40–46.
- Sherwood, J.M., Dusting, J., Kaliviotis, E., Balabani, S. (2012). The effect of red blood cell aggregation on velocity and cell-depleted layer characteristics of blood in a bifurcating microchannel. *Biomicrofluidics*, 6, 024119.
- Shin, S., Ku, Y., Park, M.-S., Suh, J.-S. (2005). Slit-flow ektacytometry: Laser diffraction in a slit rheometer. *Cytom. Part B: Clin. Cy.*, 65B, 6–13.

- Sinha, K. and Graham, M.D. (2015). Dynamics of a single red blood cell in simple shear flow. *Phys. Rev. E*, 92, 042710.
- Steffen, P., Verdier, C., Wagner, C. (2013). Quantification of depletion-induced adhesion of red blood cells. *Phys. Rev. Lett.*, 110, 018102.
- Stoltz, J.F. and Lucius, M. (1981). Viscoelasticity and thixotropy of human blood. *Biorheology*, 18, 453–473.
- Svanes, K. and Zweifach, B.W. (1968). Variations in small blood vessel hematocrits produced in hypothermic rats by micro-occlusion. *Microvasc. Res.*, 1, 210–220.
- Švelc, T. and Svetina, S. (2012). Stress-free state of the red blood cell membrane and the deformation of its cytoskeleton. *Cell. Mol. Biol. Lett.*, 17, 217–227.
- Thurston, G.B. (1973). Frequency and shear rate dependence of viscoelastic of human blood. *Biorheology*, 10(3), 375–381.
- Tomaiuolo, G. (2014). Biomedical properties of red blood cells in health and disease toward microfluidics. *Biomicrofluidics*, 8, 051501.
- Varchanis, S., Dimakopoulos, Y., Wagner, C., Tsamopoulos, J. (2018). How viscoelastic is human blood plasma? *Soft Matter*, 14, 4238–4251.
- Vlahovska, P.M., Podgorski, T., Misbah, C. (2009). Vesicles and red blood cells in flow: From individual dynamics to rheology. *C. R. Physique*, 10, 775–789.
- Wan, J., Forsyth, A.M., Stone, H.A. (2011). Red blood cell dynamics: From cell deformation to ATP release. *Integr. Biol.*, 3, 972–981.
- Weber, C. and Noels, H. (2011). Atherosclerosis: Current pathogenesis and therapeutic options. *Nat. Med.*, 17, 1410–1422.
- Weed, R.I., LaCelle, P.L., Merrill, E.W. (1969). Metabolic dependence of red cell deformability. *J. Clin. Invest.*, 48, 795–809.
- Weinbaum, S., Tarbell, J.M., Damiano, E.R. (2007). The structure and function of the endothelial glycocalyx layer. *Annu. Rev. Biomed. Eng.*, 9, 121–167.
- Yaya, F. (2021). Physical properties of red blood cells in aggregation. PhD Thesis, Universität des Saarlandes, Saarbücken and Université Grenoble Alpes, Grenoble.
- Yeromonahos, C., Polack, B., Caton, F. (2010). Nanostructure of the fibrin clot. *Biophys. J.*, 99, 2018–2027.
- Zhang, J., Johnson, P.C., Popel, A. (2008). Red blood cell aggregation and dissociation in shear flows simulated by lattice Boltzmann method. *J. Biomech.*, 41, 47–55.

- Zhang, J., Johnson, P.C., Popel, A. (2009). Effects of erythrocyte deformability and aggregation on the cell free layer and apparent viscosity of microscopic blood flows. *Microvasc. Res.*, 77, 265–272.
- Ziherl, P. and Svetina, S. (2007). Flat and sigmoidally curved contact zones in vesicle–vesicle adhesion. *Proc. Natl. Acad. Sci. USA*, 104, 761–765.

2

CFD Analyses of Different Parameters Influencing the Hemodynamic Outcomes of Complex Aortic Endovascular Repair

Sabrina BEN-AHMED¹, Jean-Noël ALBERTINI², Jean-Pierre FAVRE², C. Alberto FIGUEROA³, Eugenio ROSSET⁴, Francesca CONDEMI⁵ and Stéphane AVRIL⁵

¹*Service de Chirurgie Vasculaire et Médecine Vasculaire, CHU Limoges, France*

²*Service de Chirurgie Cardiovasculaire, CHU Saint-Etienne, France*

³*Department of Biomedical Engineering, University of Michigan, Ann Arbor, USA*

⁴*Service de Chirurgie Vasculaire, CHU Clermont-Ferrand, INSERM, Université Clermont Auvergne, France*

⁵*Mines Saint-Etienne, University of Lyon, Sainbiose INSERM U1059, Jean Monnet University, Centre CIS, Saint-Etienne, France*

2.1. Introduction

Over the past few decades, technologies in endovascular aortic aneurysm repair (EVAR) have evolved rapidly. Complex abdominal aneurysms with unfavorable neck (i.e. very short length of normal aorta between the lowest

For a color version of all the figures in this chapter, see www.iste.co.uk/deplano/biological.zip.

Biological Flow in Large Vessels,

coordinated by Valérie DEPLANO, José-Maria FULLANA, Claude VERDIER. © ISTE Ltd 2022.

Biological Flow in Large Vessels: Dialog Between Numerical Modeling and In Vitro/In Vivo Experiments,
First Edition. Valérie Deplano; José-Maria Fullana and Claude Verdier.

© ISTE Ltd 2022. Published by ISTE Ltd and John Wiley & Sons, Inc.

renal artery and the beginning of aneurysmal dilatation) or involving renal or digestive arteries are unsuitable for conventional EVAR. They carry a high risk for open surgery, with a high rate of renal complications (West *et al.* 2006). Innovative, minimally invasive approaches such as fenestrated (fEVAR), chimney (chEVAR) or periscope EVAR (pEVAR) were developed to treat complex aortic aneurysms and preserve target vessel perfusion. The advantages of these endovascular techniques over conventional open repair are the reduction of mortality and morbidity (such as blood loss and complications related to aortic and visceral arterial clamping that could lead to organ ischemia) (O'Neill *et al.* 2006, Nordon *et al.* 2009, Verhoeven *et al.* 2010, Oderich *et al.* 2014, Verhoeven *et al.* 2015, O'Donnell *et al.* 2019). The fEVAR devices include custom-made fenestrated stent grafts which usually take several weeks to be manufactured and, consequently, they are not available in emergency situations. Parallel stent graft techniques such as chEVAR and pEVAR are built using off-the-shelf devices with antegrade parallel renal stent grafts (chEVAR) or retrograde parallel renal stent grafts (pEVAR) associated with a main aortic endograft. Their main advantage is immediate availability. The different repair methodologies (fEVAR, chEVAR and pEVAR) may impact hemodynamics in target vessels such as the renal arteries, a major concern in EVAR. Renal events often complicate complex EVAR such as target vessel loss (3–4%), renal stenosis (7%) or postoperative renal dysfunction (20–29%) (Mohabbat *et al.* 2009, Martin-Gonzalez *et al.* 2015, Ou *et al.* 2015, Tran *et al.* 2016). Renal dysfunction may arise from perioperative arterial lesions caused by the device (Mohabbat *et al.* 2009) or from strong hemodynamic alterations following the procedure. Intrastent stenosis and thrombosis after stent implantation remain major clinical issues. Wall motion and flow disturbances distal to the stent graft are associated with increased intimal hyperplasia, particularly at the junction between the stent and the artery. The mechanisms are not fully understood but direct endothelial damage, reduced compliance and alteration of the distribution of the wall shear stress (WSS) within the stent graft (LaDisa Jr. *et al.* 2005) may be involved. Restenosis from intimal hyperplasia is often observed at the distal ends of the stent (Sutton *et al.* 1988). The stent rigidity relative to the native arterial compliance results in stiffness mismatch (LaDisa Jr. *et al.* 2005), which may also stimulate intimal hyperplasia. Moreover, since the aorta is fixed at the retroperitoneum, the proximal segment of the renal arteries undergoes limited motion compared to its distal counterpart. Moreover, respiration may cause kidney rigid-body motion leading to upward and downward deflections of the renal arteries, with a larger displacement distally than close to renal ostia (Draney *et al.* 2005). This mobility again

may contribute to intimal hyperplasia. Nevertheless, it should be noted that the stented length is usually greater in parallel stent graft techniques than in fEVAR (Ullery *et al.* 2016). Analyzing renal artery hemodynamics following fEVAR, chEVAR and pEVAR may help to understand the occurrence of renal complications such as intrastent or arterial stenosis from intimal hyperplasia or thrombosis in the renal arteries. Computational fluid dynamics (CFD) is a tool that enables detailed investigation and systematic comparison of hemodynamic descriptors in complex EVAR. Our aim was to analyze the hemodynamic impacts of fenestrated, chimney and periscope endovascular repair of complex abdominal aortic aneurysms on renal arteries. The study presented focused on the patterns of flow, pressure and WSS caused by complex EVAR and by the possible stenosis related to intimal hyperplasia. The influence on platelet transport and activation was also considered. Understanding the hemodynamic impact of different EVAR procedures can potentially help clinicians to prevent renal complications and to make optimal choices between the types of EVAR procedures (fEVAR vs. chEVAR or fEVAR vs. pEVAR).

2.2. Methods

A series of nine idealized computed aided design (CAD) models of complex EVAR was created in Autodesk Inventor 2016. These models were divided into three groups: fEVAR, chEVAR and pEVAR. In each group, three models were created with different degrees of renal arterial stenosis: no stenosis (baseline model), a non-clinically significant stenosis; 40% diameter reduction and a clinically significant one; 70% diameter reduction. The 40% stenosis is a non-hemodynamically stenosis, whereas the 70% stenosis represents a hemodynamically stenosis that leads to hemodynamically significant reductions in renal blood flow and pressure. The stenoses were created 2 cm after the renal ostium at both right and left renal arteries. They represent the intimal hyperplasia usually developed at the junction between the renal artery and the distal part of the renal stent graft (Sutton *et al.* 1988, Draney *et al.* 2005). All models were built with equal aortic inlet diameter (24 mm), iliac artery diameter (12 mm), renal artery diameter (6 mm) and length (62 mm). The total length of the fEVAR and pEVAR models was equal (286 mm). The chEVAR model was larger (339 mm) to minimize the disturbances triggered by the chimney inlet on the aortic velocity profiles. The same length was kept between the aortic inlet and the proximal end of the renal stent graft in order to have an established flow. In the fEVAR model, renal stents were aligned to the renal ostium and protruded 5 mm into the aortic lumen. In pEVAR and chEVAR, the renal stent protruded 40 mm

vertically into the aortic lumen. The angle between the renal artery segment of the stent graft and its aortic segment was 90° . An image of each model is shown in Figure 2.1. CFD analyses were performed using the validated finite element code CRIMSON (Cardiovascular integrated modelling and simulation crimson) on the high-performance computer of Mines Saint-Etienne (cluster of 11 Tflops with 26 nodes totaling 384 cores and 1 Tb of RAM). Tetrahedral mesh was created by discretizing the geometric model of the aorta and refined using a combination of global mesh, maximum curvature and boundary layer refinement. Pulsatile flow was run, followed by an iterative field-based anisotropic refinement operation until mesh independent results were obtained (Sahni *et al.* 2006, Youssefi *et al.* 2018). Mesh independency was assessed for each model in all patients. The results of the inlet and outlet pressure were compared between each mesh adaptation of the same model. Mesh adaptivity was stopped when the differences in inlet and outlet pressure between two consecutive mesh adaptations was below 1%. Two mesh adaptations were performed in order to reach mesh independency. Mesh sizes ranged between 0.6×10^6 and 2.4×10^6 elements. The vessel and stent graft walls were modeled as rigid. The blood was treated as a Newtonian and incompressible fluid with a dynamic viscosity of 4 mPa.s and a density of 1060 kg/m^3 . A liquid is said to be Newtonian if the coefficient of viscosity is constant at all rates of shear. This condition exists in most homogeneous liquids, including blood plasma (which, since it consists of mostly water, is Newtonian). But the mechanical behavior of a liquid containing a suspension of particles (like blood) can vary such that the liquid becomes non-Newtonian. These deviations become particularly significant when the particle size becomes appreciably large in comparison to the dimension of the channel in which the fluid is flowing. In the large vessels, such as aorta, iliac and renal arteries, it is reasonable to assume blood has a constant viscosity, because the vessel diameters are large compared with the individual cell diameters, and because shear rates are high enough for viscosity to be independent of them. Hence, in these vessels the non-Newtonian behavior becomes insignificant and blood can be considered to be a Newtonian fluid (Ottesen *et al.* 2004). A pulsatile adapted patient-specific flow waveform (Ahmed *et al.* 2016) was prescribed at the aortic inlet using a Womersley velocity profile (Williams and Leggett 1989, Odenstedt *et al.* 2001, Osinnski *et al.* 1995). The flow fraction that feeds the supra-aortic trunks and the digestive arteries was removed from the cardiac output (4 L/min) and the adapted aortic inflow represented 55% of the cardiac output (2.2 L/min). Outflow boundary conditions were prescribed using a coupled multi-domain method (Vignon-Clementel *et al.* 2006, Figueroa *et al.* 2006) in which three-element Windkessel models were coupled to each

outflow branch (renal and iliac arteries) (Vignon-Clementel *et al.* 2010). The Windkessel model represents the arterial tree beyond the outlet in an intuitive and physiological manner. It comprises a proximal resistance, compliance, and a distal resistance for each outlet. Specification of the Windkessel parameters requires knowledge of flow splits and pressure (Sahni *et al.* 2006). The prescribed mean, systolic and diastolic aortic pressure was 93.3, 120, and 80 mm Hg, respectively (Figure 2.1). The Windkessel parameters for outlets were estimated following the procedure described in Xiao *et al.* (2014) and are summarized in Table 2.1. The inflow waveform and the outlet boundary condition parameters were kept constant in all cases for the sake of comparison. Simulations were run until a periodic solution was achieved, imposing a total residual tolerance criterion (sum of all nodal residuals) of 10^{-3} . Only the results of the last cardiac cycle are reported. For each model, systolic pressure (SP), diastolic pressure (DP), mean pressure (MP), pulse pressure (PP) and mean flow (Qm) were measured at aortic inlet, all model outlets, and the proximal and distal segments of the renal arterial stenosis. Time averaged WSS (TAWSS) and platelet activation state (PAS) were determined in the renal arteries and in the renal stents. Peak velocities were also measured 3 cm downstream the renal artery ostium, that is, at the end of the stenosis for the stenosed models. Platelet activation state was calculated for each case according to the validated Lagrangian-based model of shear-induced platelet activation, proposed by Grigioni *et al.* (2005), adapted by Nobili *et al.* (2008) and applied to the carotid artery by Massai *et al.* (2012). PAS is a dimensionless parameter. It aimed to evaluate the hemodynamic risk related to platelet activation and aggregation that increase the risk for thromboembolic complications (Massai *et al.* 2012). Pressure, flow, velocity, TAWSS and PAS were compared between non-stenosed and stenosed models.

	Proximal resistance $\text{g}/(\text{mm}^4 \cdot \text{s})$	Compliance $\text{mm}^4 \cdot \text{s}^2/\text{g}$	Distal resistance $\text{g}/(\text{mm}^4 \cdot \text{s})$
Right renal artery	0.51	1.96	2.08
Left renal artery	0.51	1.96	2.08
Right iliac artery	0.11	4.96	0.81
Left iliac artery	0.11	4.96	0.81

Table 2.1. Boundary conditions of the renal and iliac outlets

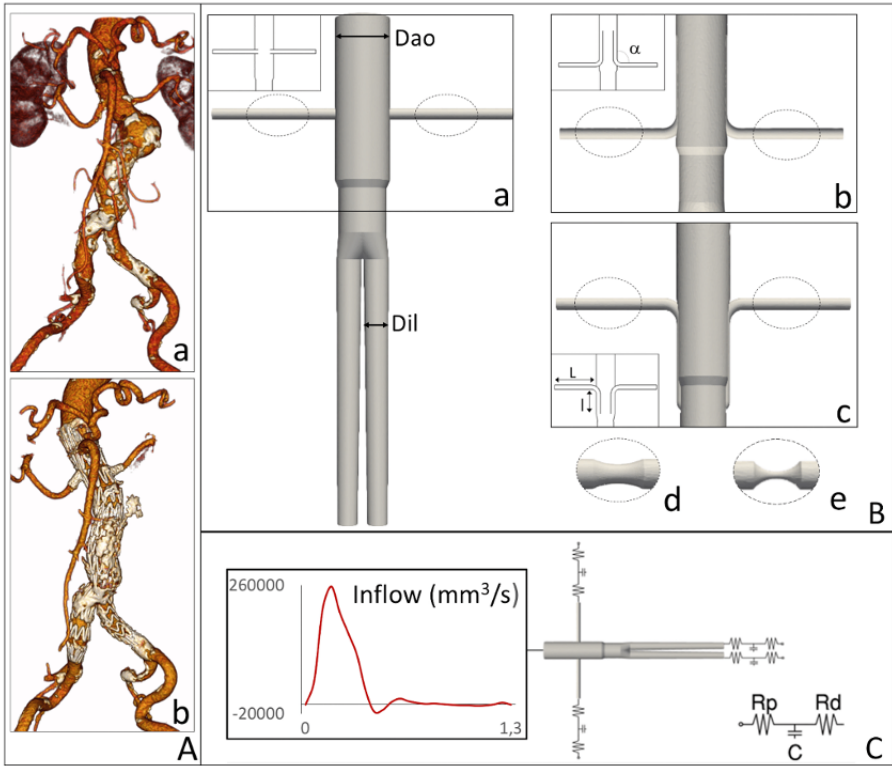


Figure 2.1. A) 3D CT-scan view of abdominal aortic aneurysm not eligible for conventional EVAR (a) and treated by fEVAR (b). B) Idealized model of fEVAR (a), chEVAR (b) and pEVAR (c) with sagittal slice view of each model in the black box. Surrounded by dashed lines, position of the 40% diameter renal stenosis (d) and 70% diameter renal stenosis (e) in the fEVAR, chEVAR and pEVAR models. C) Boundary conditions with patient-specific flow waveform applied at the aortic inlet, and the three-element-windkessel model (proximal resistance (R_p), compliance (C) and distal resistance (R_d) at each outlet. Dao, aortic diameter (24 mm); Dil, iliac diameter (12 mm); α , angle of the renal chimney and renal periscope and between the aorta and the renal stent graft in fEVAR (90°); L , length of the renal artery (62 mm); l , length of the vertical segment of the renal chimney and periscope (40 mm)

2.3. Results

Since all geometric models are symmetrical, pressure, flow and velocity values were identical in the left and right renal arteries. Thus, only the results

	fEVAR	chEVAR	pEVAR	fEVAR	chEVAR	pEVAR	fEVAR	chEVAR	pEVAR
				-40	-40	-40	-70	-70	-70
Mean renal outflow (mm ³ /s)	0.29	0.29	0.29	0.29	0.29	0.29	0.22	0.22	0.22
Mean iliac outflow (mm ³ /s)	0.81	0.81	0.81	0.81	0.81	0.81	0.88	0.88	0.88
Prestenosis renal systolic pressure (mm Hg)	156.4	127.9	134.1	155.9	142.9	137.7	179.5	170.1	167.1
Prestenosis renal diastolic pressure (mm Hg)	71.0	73.9	73.3	70.8	73.8	73.6	74.2	76.4	76.1
Prestenosis renal mean pressure (mm Hg)	92.4	90.6	90.9	92.3	92.5	91.5	100.4	100.9	100.0
Prestenosis renal pulse pressure (mm Hg)	85.3	54.1	60.8	85.1	69.2	64.1	105.2	93.7	91.0
Poststenosis renal systolic pressure (mm Hg)	156.1	127.9	133.6	146.6	127.9	124.1	82.6	77.1	76.0
Poststenosis renal diastolic pressure (mm Hg)	71.1	73.9	73.3	70.8	73.9	73.7	63.2	65.6	64.8
Poststenosis renal mean pressure (mm Hg)	92.3	90.6	90.8	90.9	90.6	89.7	69.9	70.3	69.4
Poststenosis renal pulse pressure (mm Hg)	85.1	54.1	60.2	75.7	54.1	50.5	19.4	11.5	11.2

Table 2.2. Pressure and flow values at inlet and outlets in all idealized models. *fEVAR*, fenestrated EVAR; *chEVAR*, chimney EVAR; *pEVAR*, periscope EVAR; -40, 40% stenosed renal arteries; -70, 70% stenosed renal arteries

2.3.1. Model without stenosis

2.3.1.1. Flow and velocity

Qm at aortic inlet, renal outlets (0.6 L/min) and at iliac outlets (1.6 L/min) were the same in all idealized models. The largest renal artery velocity (3 cm after the renal ostium) was found in chEVAR (1.6 m/s). In the same region, the peak velocity for pEVAR and fEVAR was 18% lower (Figure 2.2). Flow recirculation, indicating vortex formation, was found at the proximal intra

renal cranial part of the fenestrated stent graft and in the aortic segment located just below the fenestrated stent graft as well as at the entrance of the periscope stent graft, as represented in Figures 2.3 and 2.4.

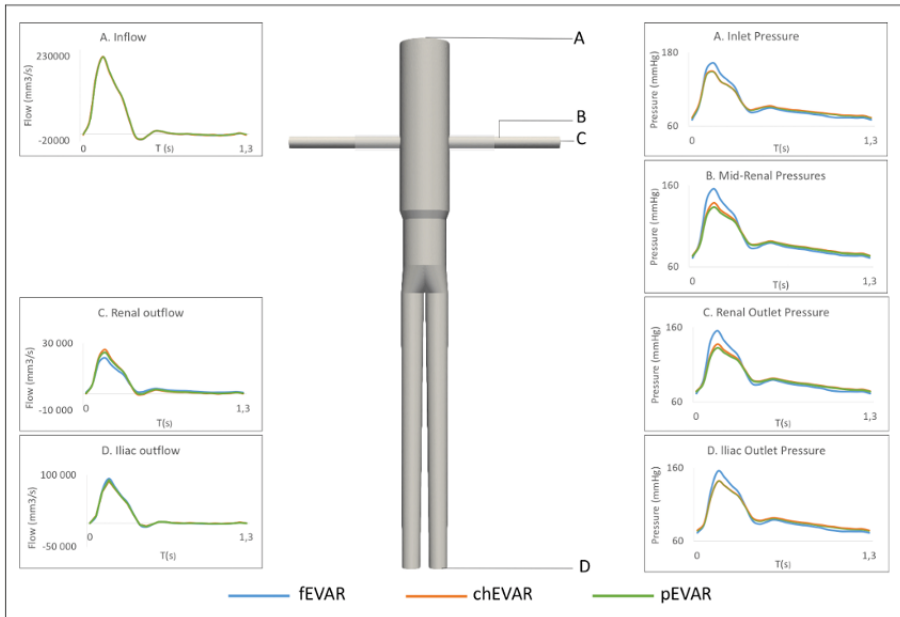


Figure 2.2. Flow and pressure at aortic inlet (A), mid-renal artery (B), renal artery outlet (C) and iliac artery outlet (D) in the baseline models (without stenosis). We chose to report only the results of the left renal artery and the left iliac artery as the models were symmetric and the results of the contralateral side were the same

2.3.1.2. Pressure

Aortic inlet SP and PP were 11% and 21% higher in fEVAR compared to chEVAR and pEVAR, respectively. MP was almost identical in all cases, around 93.5 mm Hg. SP at renal arteries was 12% and 15% higher in fEVAR compared to chEVAR and pEVAR, respectively. PP in renal arteries was 26% and 31% higher in fEVAR compared to chEVAR and pEVAR, respectively. DP ranged between 71 mm Hg and 74 mm Hg. MP was nearly identical in all cases, around 92 mm Hg.

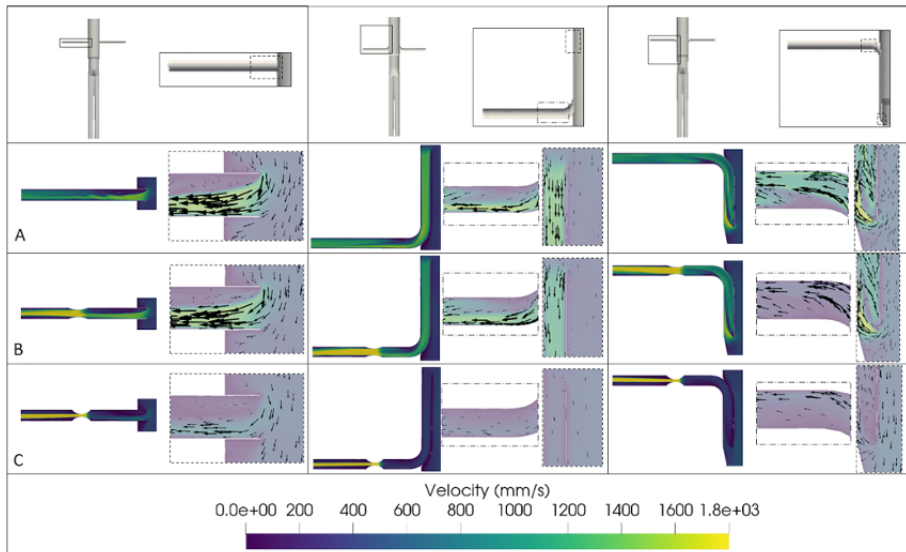


Figure 2.3. Velocity field in the renal arteries of the idealized models (surrounded by solid lines) without renal stenosis (A), with 40% diameter renal stenosis (B) and with 70% diameter renal stenosis at peak systole. Surrounded by dashed lines, close-up of the proximal part of the stent graft (fenestrated, chimney and periscope) and the horizontal portion of chimney and periscope stent graft

2.3.1.3. Renal artery WSS and PAS

As shown in Figure 2.5, TAWSS was the lowest (< 0.4 Pa) at the proximal intra renal segment of the fenestrated stent graft in fEVAR, and at the proximal horizontal segment of the chimney and periscope stent grafts. The TAWSS peak values (> 7 Pa) were reached at the proximal aortic end of the fenestrated stent graft, at the proximal vertical segment and at the curvature of the chimney stent graft, and at the proximal vertical part of periscope stent graft. PAS is presented in Figure 2.6. At systolic peak, PAS was the highest in the horizontal part of the periscope stent graft and in the renal artery in pEVAR. PAS was the lowest at the proximal part of the renal chimneys in chEVAR. The highest value for PAS in fEVAR was 0.01 and was found in the fenestrated stent graft and in the renal artery. The highest value of PAS in chEVAR was 0.0036, located at the renal stent angulation, the distal part of the chimney and the renal artery. The highest value for PAS in pEVAR was 0.02 and was found in the distal part of the periscope stent graft and in the renal artery.

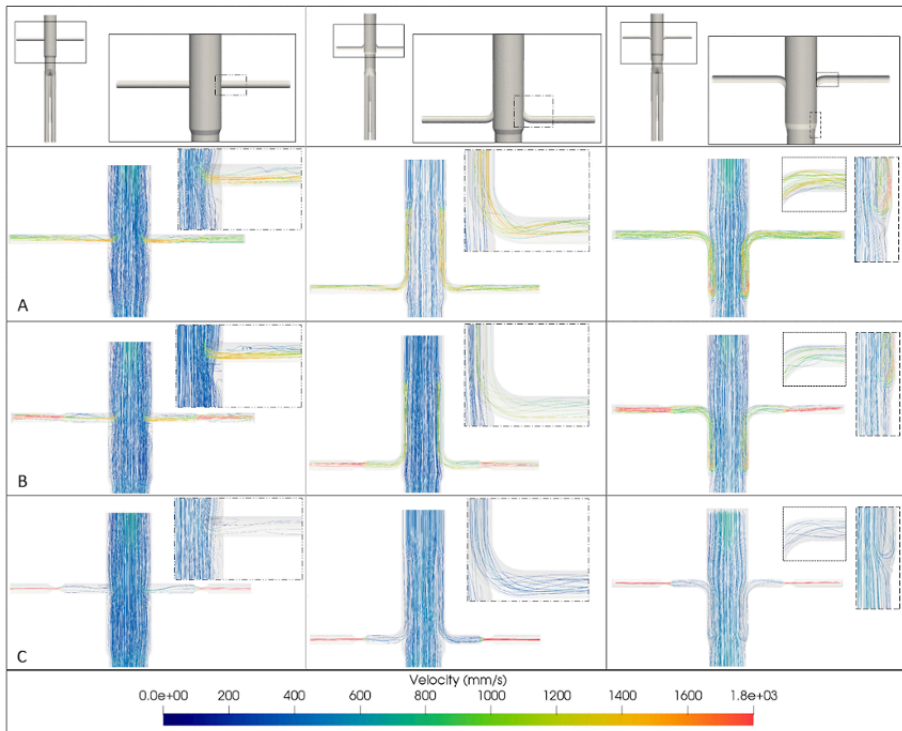


Figure 2.4. Velocity streamlines in each idealized model (solid lines) without renal stenosis (A), with 40% diameter renal stenosis (B) and with 70% diameter renal stenosis at peak systole. Surrounded by dashed lines, detailed view in portion of the model with complex flow streamlines

2.3.2. Model with 40% diameter stenosis

2.3.2.1. Flow and velocity

Q_m in renal and iliac arteries were identical for all three cases. This suggests renal artery stenosis has a greater impact on flow dynamics than the different effective resistances to flow set by the different renal stent graft configurations. Larger velocities resulting from the stenoses were recorded in the renal arteries. Peak velocity at the renal artery (3 cm after the renal ostium) was almost identical in chEVAR-40 and pEVAR-40 (2.38 m/s and 2.35 m/s) and 12% lower in fEVAR-40, as shown in Figure 2.7. Flow recirculation was found in the aortic segment distal to the fenestrated stent graft and at the proximal intrarenal part of the fenestrated stent graft, as well

as at the entrance of the periscope stent graft, as can be seen in Figures 2.3 and 2.4.

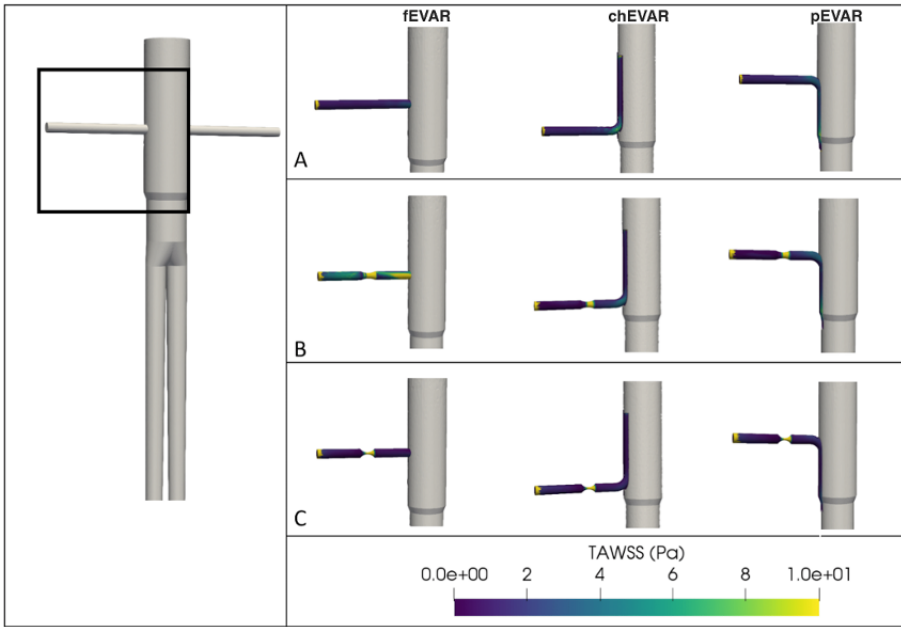


Figure 2.5. TAWSS in the renal arteries of the idealized models (solid lines) without renal stenosis (A), with 40% diameter renal stenosis (B) and with 70% diameter renal stenosis at peak systole

2.3.2.2. Pressure

As Figure 2.8 shows, the pressure variations (SP, PP, DP, MP) at the renal and iliac outlets were identical to the baseline models (without stenosis). Aortic inlet SP and PP were higher in fEVAR compared to chEVAR and pEVAR, respectively. MP was almost identical in all cases, around 93.3 mm Hg. SP at renal arteries were higher in fEVAR compared to chEVAR and pEVAR. PP in renal arteries were around 30% higher in fEVAR compared to chEVAR and pEVAR, respectively. DP ranged between 71 and 74 mm Hg. MP ranged between 89 and 92 mm Hg. Pre- and poststenosis SP and PP were higher in fEVAR-40 compared to chEVAR and pEVAR. The MP drop in renal stenosis was identical in all 40% stenosed models, that is, 2%. The SP drop in renal stenosis was 6% in fEVAR-40 and 10% in chEVAR and pEVAR. The PP drop in renal stenosis was 11% in fEVAR-40 and 21% in chEVAR and pEVAR. Pre- and post-renal stenosis DPs were similar in all models.

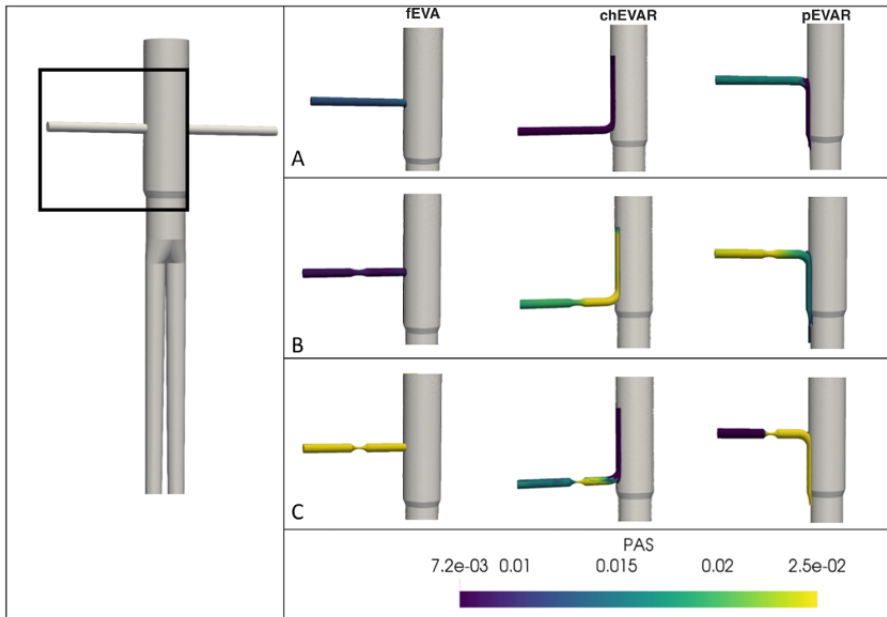


Figure 2.6. PAS in the renal arteries of the idealized models (solid lines) without renal stenosis (A), with 40% diameter renal stenosis (B) and with 70% diameter renal stenosis at peak systole

2.3.2.3. WSS and PAS in renal arteries

As presented in Figure 2.5, TAWSS was the lowest (< 0.4 Pa) in the post-stenotic renal artery in all models. Low TAWSS values also occurred in the cranial segment of the proximal intrarenal part of the fenestrated stent graft, in the cranial segment of the proximal horizontal part of the chimney and at the caudal segment of the proximal horizontal part of the periscope. TAWSS was the highest (around 15 Pa) at the proximal part of the renal stenosis in all models, followed by the proximal vertical part of pEVAR-40 (around 7 Pa). TAWSS was moderate (around 4 Pa) in the angulation of pEVAR-40 and chEVAR-40. PAS is represented in Figure 2.6. At systolic peak, the highest value for PAS, was found in chEVAR-40 and the lowest in fEVAR-40. The highest PAS value in fEVAR-40 was 0.009 at the renal stenosis. The highest value of PAS in chEVAR-40 was 0.032 and located above the renal artery stenosis to the proximal part of the chimney stent graft. The highest value of PAS in pEVAR-40 was 0.025 and was found from the stenosis to the end of the renal artery. Compared to the baseline models, the

values of PAS in fEVAR-40 and pEVAR-40 remained relatively constant. However, PAS in the chEVAR-40 increased nearly tenfold.

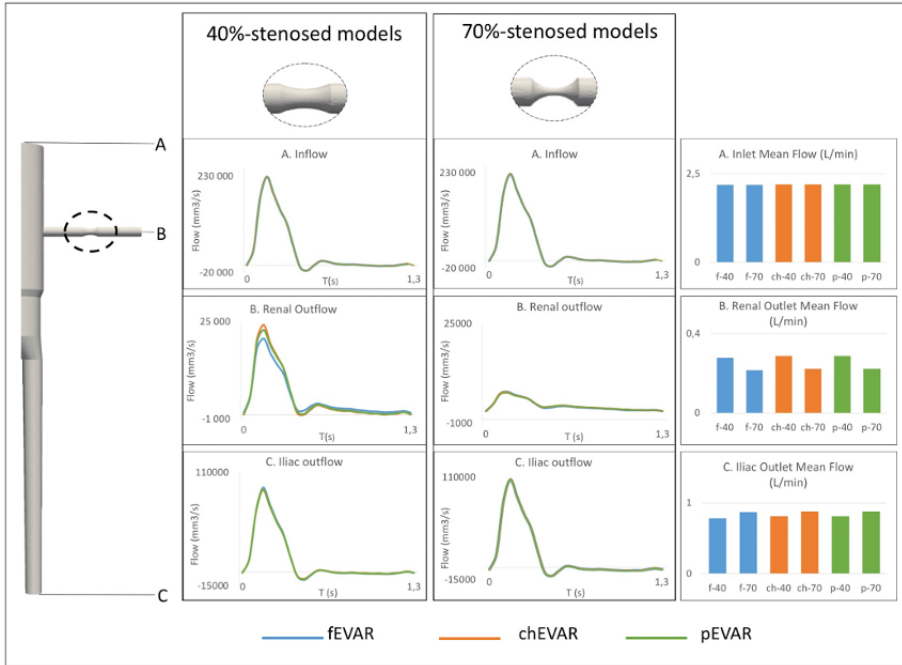


Figure 2.7. Flow waveforms and mean flow bar charts at aortic inlet (A), renal artery outlet (B) and iliac artery outlet (C) of the 40% and 70% renal artery stenosed models for the last cardiac cycle. The renal stenosis is surrounded by dashed lines in the model on the left. The results of the 40% stenosed models and 70% stenosed models are presented in two columns. The flow waveforms of the 40% stenosed fEVAR, chEVAR and PEVAR are shown in the first column. The flow waveforms of the 70% stenosed fEVAR, chEVAR and PEVAR are shown in the second column. Mean flow of the 40% stenosed fEVAR (f-40), 40% stenosed chEVAR (ch-40), 40% stenosed pEVAR (p-40), 70% stenosed fEVAR (f-70), 70% stenosed chEVAR (ch-70) and 70% stenosed pEVAR (p-70) are shown in bar charts in the last column. We chose to present only the results of the left renal artery and the left iliac artery as the model was symmetric and the results of the contralateral side were the same

2.3.3. Model with 70% diameter stenosis

2.3.3.1. Flow and velocity

Qm in renal and iliac arteries was identical in all three cases. Renal artery flow was 24% lower than in the non-stenosed models. As shown in

Figure 2.7, peak velocity was similar (around 5 m/s) in all three models. Flow recirculation was present at the proximal part of the fenestrated stent graft and at the aortic segment located just below the fenestrated stent graft, as well as at the entrance of the periscope stent graft, presented in Figures 2.3 and 2.4.

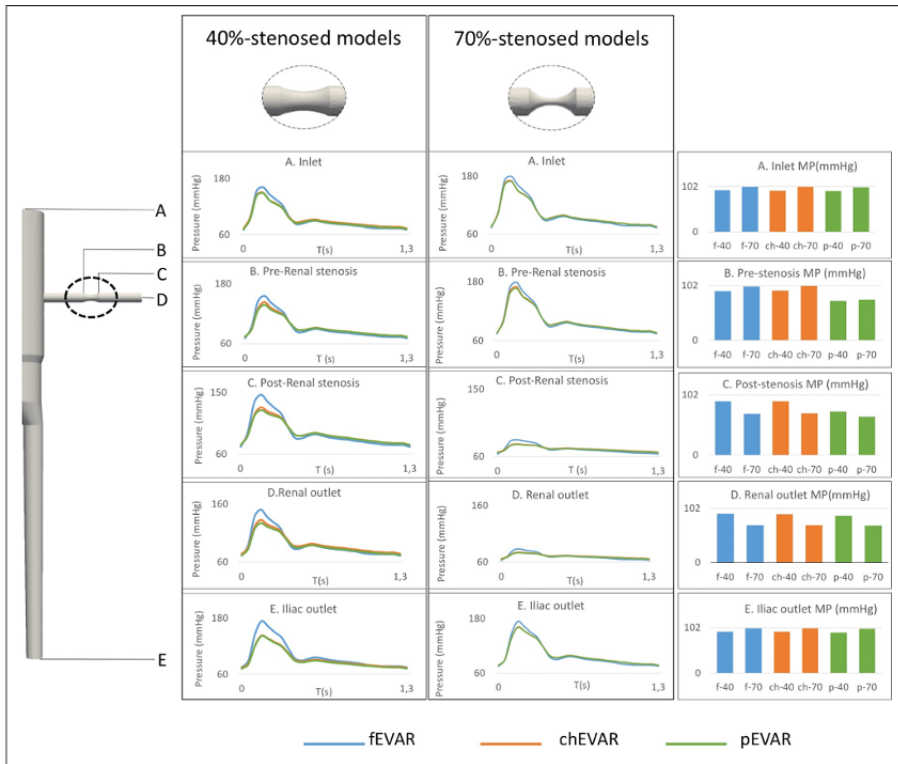


Figure 2.8. Pressure waveforms and mean pressure bar charts at aortic inlet (A), pre-renal stenosis (B), post-renal stenosis (C), renal artery outlet (D) and iliac artery outlet (E) of the 40% and 70% renal artery stenosed models. The renal stenosis is surrounded by dashed lines in the model on the left. The results of the 40% stenosed models and 70% stenosed models are presented in two columns. The pressure waveforms of the 40% stenosed fEVAR, chEVAR and pEVAR are shown in the first column. The pressure waveforms of the 70% stenosed fEVAR, chEVAR and pEVAR are shown in the second column. Mean pressure of the 40% stenosed fEVAR (f-40), 40% stenosed chEVAR (ch-40), 40% stenosed pEVAR (p-40), 70% stenosed fEVAR (f-70), 70% stenosed chEVAR (ch-70) and 70% stenosed pEVAR (p-70) are presented in bar charts in the last column. We chose to report only the results of the left renal artery and the left iliac artery as the model was symmetric and the results of the contralateral side were the same

2.3.3.2. Pressure

Aortic inflow pressure noticeably increased in all models (PP increases relative to the non-stenosis models of 13%, 15% and 14% for fEVAR, chEVAR and pEVAR, respectively) (Figure 2.8). This clearly indicates that greater pressure is needed to drive the same amount of flow in the presence of the hemodynamically significant renal stenoses. fEVAR SP at the renal arteries was approximately 9% larger than chEVAR-70 and pEVAR-70. Renal PP was around 44% higher in fEVAR-70 compared to chEVAR-70 and pEVAR-70. Renal DP ranged between 63 and 66 mm Hg. Renal MP was similar in all models, around 70 mm Hg. Pre- and post-renal stenosis SP and PP were higher in fEVAR-70 compared to chEVAR and pEVAR. The pressure drop in the renal stenosis was identical in all models: around 54% for the SP, 15% for the DP, 31% for the MP and 86% for the PP.

2.3.3.3. TAWSS and PAS in renal arteries

As shown in Figure 2.5, TAWSS was highest (around 100 Pa) at the renal stenosis in all models. TAWSS was the lowest (< 0.4 Pa) at the post-stenotic renal artery in all models and at the cranial intrarenal segment of the fenestrated stent graft as well as at the caudal intrarenal segment of the horizontal part of the periscope. PAS is presented in Figure 2.6. Compared to the baseline models, the values of PAS in the 70% stenosed models increased. At systolic peak, the highest value for PAS was found in pEVAR-70. The highest value for PAS in pEVAR-70 was 0.078 located above the stenosis (angulation and proximal vertical part of the periscope stent graft). The highest PAS value in chEVAR-70 was 0.034 located from the proximal part of the stenosis to the angulation of the chimney stent graft. The highest PAS in fEVAR-70 was 0.052 located between the stenosis and the end of the renal artery.

2.4. Discussion

The use of complex EVAR has increased in recent years. As fenestrated, chimney and periscope stent grafts protrude into the aortic lumen, these complex endovascular repairs could potentially interfere with the renal blood flow. One of the most serious complications is intimal hyperplasia, responsible for narrowing and occlusion of the target vessel, that can lead to organ ischemia. Platelet activation is one of the mechanisms involved in this phenomenon. High shear stress can stimulate platelet activation, aggregation and lytic process, whereas low shear stress leads to endothelium damage, atherosclerosis and intimal hyperplasia (Massai *et al.* 2012). Understanding the hemodynamic impact of fEVAR, ChEVAR and pEVAR configurations on

renal arteries, as well as the impact of renal stenosis could help physicians to choose the best endovascular option for each patient. Only a few studies in the literature have analyzed renal artery flow and pressure patterns following complex endovascular interventions. A close computational study published by Kandail *et al.* (2015) compared blood flow in chEVAR, pEVAR and fEVAR. The originality of our approach compared to this previous study is the introduction of a renal artery stenosis in these endovascular repairs of complex aortic aneurysms, and the comparison of the pressure, flow, TAWSS and PAS between the models. No studies have analyzed the hemodynamic impact of renal artery stenosis in idealized models of complex aortic aneurysm endovascular repairs. Abnormal flow and shear stress are involved in the occurrence of intimal hyperplasia. Following stent implantation, the stented segment of the artery can be stenosed by four key processes: thrombus formation, arterial inflammation, neointimal hyperplasia and remodeling. Neointimal hyperplasia appears within weeks of stent implantation followed by remodeling. Smooth muscle cells that normally sit in the middle layer of the artery migrate inwards toward the stent where they proliferate and form the bulk of the new tissue that narrows the artery. The migration and proliferation of smooth muscle cells is triggered by various chemical signals such as injured endothelial cells and dysfunctional endothelial cells, which activate platelets at the site of arterial injury. Abnormal hemodynamics near the stent result in altered stresses on the endothelial cells and potential mechanical activation of platelets. Then collagen deposits in the outer layer of the artery lead to arterial stiffening. This process increases the pressure on the stent and can squeeze the arterial wall between inter-strut spaces (Murphy and Boyle 2010). Stent implantation under low flow is associated with increased neointima formation (Richter *et al.* 1999). Tissue growth in a stented artery is prominent at the site of low WSS (< 0.5 Pa) (LaDisa Jr. *et al.* 2005).

2.4.1. Velocity and flow

Total renal blood flow usually accounts for 15–20% of the cardiac output under normal resting conditions (Williams and Leggett 1989, Moore Jr. and Ku 1994). Our total renal blood flow was physiologic as it represented 15% of the cardiac output (Weinstein and Anderson 2010). The stenosed geometries (both 40% and 70%) showed no noticeable differences in renal flow between the different renal stent designs. Šutalo *et al.* (2008) observed negligible differences in the outflow rates to a branch vessel in antegrade and retrograde directions for 40 mm-long conduits in their experimental study. For the baseline (without stenosis) geometry, the chEVAR design resulted in

the largest peak velocity in renal arteries. This result is in agreement with Kandail *et al.* (2015) in their computational study. The larger the renal artery stenosis, the lesser the flow recirculation in the aortic segment located just below the fenestrated stent graft and at the entrance of the periscope stent graft. No vortical structures were observed in the set of chEVAR models. However, they were observed in all fEVAR and pEVAR models.

2.4.2. Pressure

The fEVAR design resulted in the largest pulse and systolic pressure for all idealized anatomical models. This finding suggests that this design induces the largest viscous losses in the abdominal region. Under the assumption that the aortic flow is maintained, higher viscous losses result in the greatest pressure seen in the fEVAR design. The renal artery stenosis impacted the hemodynamics in all models. In clinical practice, renal artery stenosis has a hemodynamic impact when it reaches 50% of the diameter and it has a clinical impact when it reaches 70% of the diameter (Lao *et al.* 2011, Li *et al.* 2008). In the 40% stenosis models, negligible pressure variations were found before and after stenosis. However, in the 70% renal stenosis models, significant pressure drops were observed, confirming the significant hemodynamic impact of a 70% stenosis in the renal artery. At the aortic inlet, systolic, mean and pulse pressure was higher in fEVAR, regardless of the degree of stenosis. Pre- and post-stenosis renal artery pressure was also higher in fEVAR irrespective of the extent of the stenosis. This could be related to the increase in resistance in the fenestrated renal artery as the flow makes a 90° angulation before entering into the fenestrated renal stent that protrudes into the aortic lumen. Pulse pressure was reported as this parameter has an important role in remodeling, wall thickening and stiffening (Eberth *et al.* 2009). FEVAR had the highest PP whatever the degree of stenosis, meaning that it presents the highest risk of remodeling and wall thickening for the renal artery.

2.4.3. TAWSS

Low WSS values correlate with intimal hyperplasia and in-stent stenosis, whereas high WSS values correlate with endothelial damage. Low shear stress was found below and above the 40% and the 70% stenosis. Moderate TAWSS values were found in the following regions: proximal end of the fenestrated renal stent graft, angulation of the renal chimney stent graft, vertical ascending part and angulation of the renal periscope stent graft. These results corroborate the study of Suess *et al.* (2016). Low TAWSS was

found at the intra-renal proximal cranial segment of the fenestrated stent graft. Its configuration at the aortic inlet requires a 90° change in direction of the flow momentum, which results in separation of the flow and vortices. Recirculation and downstream flow were observed in the cranial extent of the proximal part of the renal stent, and this can lead to the development of intimal hyperplasia. However, the artery is not exposed to this phenomenon as the stent graft is usually covered, hence protecting the artery (Suess *et al.* 2016). In terms of flow recirculation, it seems to be more important during peak respiratory motion, which can reach 3 mm displacement at the proximal and distal ends of the renal artery. However, in fEVAR, the motion of the proximal and distal ends of the renal artery are reduced by 25% and 80%, respectively (Muhs *et al.* 2008). The fixation of the proximal part of the stent graft in the main body allows motion of the distal part of the stent graft, which can lead to intimal hyperplasia (Suess *et al.* 2016). Chimneys are usually further extended in the renal artery than they are in fEVAR, where the renal artery can move to a larger extent (Ullery *et al.* 2016), and this can again lead to an increased risk of intimal hyperplasia. In chEVAR, the antegrade part of the stent decreases flow disturbance. In the angulation, the changes in direction lead to oscillations and high WSS. The same trend as in fEVAR was observed in the cranial extent of the proximal entrance of the chimney in the renal artery. The periscope has a retrograde configuration with a takeoff angle that makes 180° to reach the lateral part of the periscope. The flow is dramatically disturbed at the proximal end of the periscope with oscillating flow and high WSS, which can lead to endothelial damage and thrombosis. At the angulation of the periscope, the trend was the same as in chEVAR but with less flow disturbance and moderate TAWSS. The TAWSS was low in the caudal extent of the proximal entrance of the periscope in the renal artery. The largest vortical structures were found at the cranial segment of the proximal part of the fenestrated stent graft and in the part of the main stent graft that was located below the renal fenestrated stent graft, where TAWSS was < 0.4 .

2.4.4. PAS

Thrombus formation was not simulated directly in this study, but PAS was used to identify regions with a high risk of thrombosis. These metrics were used to quantify the history of shear experienced by massless particles moving through the vasculature. This tool can be used to compare the performance of different endograft designs on a patient-specific basis (Massai *et al.* 2012). The impact of the renal stenosis was more significant in fEVAR

with a higher increase in PAS between the non-stented and the 70% diameter renal stenosis at systolic peak. In the 70% stenosed models, platelets were exposed to high shear stress for a short time due to the flow acceleration in the stenosis. Platelets were activated most quickly in fEVAR, followed by pEVAR and chEVAR. In the 40% renal stenosis models, platelets were activated more quickly in the proximal part of chEVAR and in the distal part of the renal artery in pEVAR. In the models without stenosis, platelets were activated more in the renal artery and in the part below the angulation of the periscope stentgraft. Platelets were less activated in chEVAR. Platelets were activated above both stenoses in chEVAR, and 70% stenosis in pEVAR. The physiological range of wall shear stress varies from 0.1 to 6 Pa, higher values activating platelets. Potential change from low to high shear induces platelet activation and thrombus formation (Holme *et al.* 1997), which explains the increased platelet activation in the stenosis. The chEVAR configurations revealed a smoother shear stress distribution along the renal branches, which predispose it to less material fatigue or a lower trend for renal events in the long term. In practice, chimneys have less acute angulations compared to fEVAR bridging stents (Georgakarakos *et al.* 2015). The effect of the stenosis on pressure and velocity was more significant in fEVAR, followed by pEVAR with highest PAS at systolic peak value in the non-stenosed and 70% stenosed models. fEVAR seems to be more sensitive to the occurrence and narrowing of a renal stenosis. In the non-stenosed models, chEVAR had the lowest value of PAS, followed by pEVAR and fEVAR. In the 40% stenosed models, fEVAR-40 had the lowest value of PAS, followed by chEVAR-40 and pEVAR-40. In the 70% stenosed models, chEVAR-70 had the lowest value of PAS followed by fEVAR-70 and pEVAR-70.

2.4.5. Limitations

Several assumptions were made in this study. The walls were assumed rigid. However, the material of the stent grafts has low compliance. The results of CFD-simulations can be highly coupled to boundary conditions used in the computed analysis. Only one geometry of fEVAR, chEVAR and pEVAR was analyzed in our study. Many geometries need to be analyzed in further studies. Georgakarakos *et al.* (2015) showed that the lowest value of WSS was found at 90°, whereas the highest was at 45°. Geometry was idealized in our analysis. Further study will be achieved on patient-specific models (specific anatomy and specific physiology). The study was focused on WSS and PAS but other criteria, including material fatigue, could be relevant in order to predict risks such as intimal hyperplasia or thrombosis. All models

represented an idealized geometry and made it possible to run sensitivity analyses without effects of interindividual variations of anatomy. All geometric models, in addition to being idealized, also neglected aortic curvature. Stented abdominal aneurysms typically have tortuosity in the coronal and sagittal directions, which can significantly affect the hemodynamics (Figuroa *et al.* 2009). Finally, the effect of renal autoregulation in response to alterations in flow was not included. With the modeling approach presented here, the Windkessel parameters were kept constant for all geometric models. Fundamentally, this means that the distal resistance of the renal vascular bed was assumed to not respond to a reduced flow situation such as that observed in the 70% renal stenosis geometry. In reality, alterations in renal flow and pressure would trigger the renin–angiotensin–aldosterone response (Textor and Lerman 2015). However, a given renal artery stenosis can generate widely variable hemodynamic effects in different patients. Mounier-Vehier *et al.* (2004) observed a significant increase in renal blood flow after angioplasty of renal artery stenosis in hypertensive patients, meaning renal artery stenosis decreased renal blood flow in these symptomatic patients.

2.5. Conclusion

Computational fluid dynamics is a powerful tool that enabled us to systematically compare the hemodynamic patterns obtained after different types of complex EVAR procedures and for different degrees of possible renal stenosis. Hemodynamic alterations appear to be more significant in fEVAR in the presence of renal stenosis. The fEVAR model appears to carry a higher risk of thrombosis. The chEVAR and pEVAR appear to induce fewer hemodynamic alterations but carry a higher risk of thrombosis in the presence of a renal stenosis. However, our findings in idealized models must be validated in anatomical models. Further studies with patient-specific analyses need to be performed as it is now evident that complex EVAR has a major hemodynamical impact which needs to be considered in the treatment of complex abdominal aortic aneurysms.

2.6. Acknowledgments

SA is grateful to the European Research Council (ERC grant Biolochanics, grant number 647067) for financial support.

2.7. References

- Ahmed, S.B., Dillon-Murphy, D., Figueroa, C.A. (2016). Computational study of anatomical risk factors in idealized models of type b aortic dissection. *European Journal of Vascular and Endovascular Surgery*, 52(6), 736–745.
- Draney, M.T., Zarins, C.K., Taylor, C.A. (2005). Three-dimensional analysis of renal artery bending motion during respiration. *Journal of Endovascular Therapy*, 12(3), 380–386.
- Eberth, J.F., Gresham, V.C., Reddy, A.K., Popovic, N., Wilson, E., Humphrey, J.D. (2009). Importance of pulsatility in hypertensive carotid artery growth and remodeling. *Journal of Hypertension*, 27(10), 2010.
- Figueroa, C.A., Vignon-Clementel, I.E., Jansen, K.E., Hughes, T.J., Taylor, C.A. (2006). A coupled momentum method for modeling blood flow in three-dimensional deformable arteries. *Computer Methods in Applied Mechanics and Engineering*, 195(41–43), 5685–5706.
- Figueroa, C.A., Taylor, C.A., Yeh, V., Chiou, A.J., Zarins, C.K. (2009). Effect of curvature on displacement forces acting on aortic endografts: A 3-dimensional computational analysis. *Journal of Endovascular Therapy*, 16(3), 284–294.
- Georgakarakos, E., Manopoulos, C., Lazarides, M.K., Tsangaris, S. (2015). Commentary: Occlusion of parallel/bridging stent-grafts in the treatment of complex aneurysms: A purely technical issue... or not? *Journal of Endovascular Therapy*, 22(3), 401–405.
- Grigioni, M., Morbiducci, U., D’Avenio, G., Di Benedetto, G., Del Gaudio, C. (2005). A novel formulation for blood trauma prediction by a modified power-law mathematical model. *Biomechanics and Modeling in Mechanobiology*, 4(4), 249–260.
- Holme, P.A., Ørvim, U., Hamers, M.J., Solum, N.O., Brosstad, F.R., Barstad, R.M., Sakariassen, K.S. (1997). Shear-induced platelet activation and platelet microparticle formation at blood flow conditions as in arteries with a severe stenosis. *Arteriosclerosis, Thrombosis, and Vascular Biology*, 17(4), 646–653.
- Kandail, H., Hamady, M., Xu, X.Y. (2015). Comparison of blood flow in branched and fenestrated stent-grafts for endovascular repair of abdominal aortic aneurysms. *Journal of Endovascular Therapy*, 22(4), 578–590.
- LaDisa Jr., J.F., Olson, L.E., Molthen, R.C., Hettrick, D.A., Pratt, P.F., Hardel, M.D., Kersten, J.R., Warltier, D.C., Pagel, P.S. (2005). Alterations in wall shear stress predict sites of neointimal hyperplasia after stent implantation in rabbit iliac arteries. *American Journal of Physiology–Heart and Circulatory Physiology*, 288(5), H2465–H2475.

- Lao, D., Parasher, P.S., Cho, K.C., Yeghiazarians, Y. (2011). Atherosclerotic renal artery stenosis—diagnosis and treatment. *Mayo Clinic Proceedings*, 86(7), 649–657.
- Li, J.-C., Jiang, Y.-X., Zhang, S.-Y., Wang, L., Ouyang, Y.-S., Qi, Z.-H. (2008). Evaluation of renal artery stenosis with hemodynamic parameters of doppler sonography. *Journal of Vascular Surgery*, 48(2), 323–328.
- Martin-Gonzalez, T., Pinçon, C., Hertault, A., Maurel, B., Labbé, D., Spear, R., Sobocinski, J., Haulon, S. (2015). Renal outcomes analysis after endovascular and open aortic aneurysm repair. *Journal of Vascular Surgery*, 62(3), 569–577.
- Massai, D., Soloperto, G., Gallo, D., Xu, X.Y., Morbiducci, U. (2012). Shear-induced platelet activation and its relationship with blood flow topology in a numerical model of stenosed carotid bifurcation. *European Journal of Mechanics B/Fluids*, 35, 92–101.
- Mohabbat, W., Greenberg, R.K., Mastracci, T.M., Cury, M., Morales, J.P., Hernandez, A.V. (2009). Revised duplex criteria and outcomes for renal stents and stent grafts following endovascular repair of juxtarenal and thoracoabdominal aneurysms. *Journal of Vascular Surgery*, 49(4), 827–837.
- Moore Jr., J.E. and Ku, D.N. (1994). Pulsatile velocity measurements in a model of the human abdominal aorta under resting conditions. *Journal of Biomechanical Engineering*, 116, 337–346 .
- Mounier-Vehier, C., Cochetoux, B., Haulon, S., Devos, P., Lions, C., Gautier, C., Carre, A., Beregi, J.-P. (2004). Changes in renal blood flow reserve after angioplasty of renal artery stenosis in hypertensive patients. *Kidney International*, 65(1), 245–250.
- Muhs, B.E., Vincken, K.L., Teutelink, A., Verhoeven, E.L., Prokop, M., Moll, F.L., Verhagen, H.J. (2008). Dynamic cine-computed tomography angiography imaging of standard and fenestrated endografts: Differing effects on renal artery motion. *Vascular and Endovascular Surgery*, 42(1), 25–31.
- Murphy, J. and Boyle, F. (2010). Predicting neointimal hyperplasia in stented arteries using time-dependant computational fluid dynamics: A review. *Computers in Biology and Medicine*, 40(4), 408–418.
- Nobili, M., Sheriff, J., Morbiducci, U., Redaelli, A., Bluestein, D. (2008). Platelet activation due to hemodynamic shear stresses: Damage accumulation model and comparison to in vitro measurements. *ASAIO Journal*, 54(1), 64.
- Nordon, I., Hinchliffe, R., Holt, P., Loftus, I., Thompson, M. (2009). Modern treatment of juxtarenal abdominal aortic aneurysms with fenestrated endografting and open repair – A systematic review. *European Journal of Vascular and Endovascular Surgery*, 38(1), 35–41.

- Odenstedt, H., Aneman, A., Oi, Y., Svensson, M., Stenqvist, O., Lundin, S. (2001). Descending aortic blood flow and cardiac output: A clinical and experimental study of continuous oesophageal echo-doppler flowmetry. *Acta Anaesthesiologica Scandinavica*, 45(2), 180–187.
- Oderich, G.S., Greenberg, R.K., Farber, M., Lyden, S., Sanchez, L., Fairman, R., Jia, F., Bharadwaj, P., *Zenith Fenestrated Study Investigators*. (2014). Results of the United States multicenter prospective study evaluating the zenith fenestrated endovascular graft for treatment of juxtarenal abdominal aortic aneurysms. *Journal of Vascular Surgery*, 60(6), 1420–1428.
- O'Donnell, T.F., Boitano, L.T., Deery, S.E., Schermerhorn, M.L., Schanzer, A., Beck, A.W., Green, R.M., Takayama, H., Patel, V.I. (2019). Open versus fenestrated endovascular repair of complex abdominal aortic aneurysms. *Annals of Surgery*, 271(5), 969–977.
- O'Neill, S., Greenberg, R., Haddad, F., Resch, T., Sereika, J., Katz, E. (2006). A prospective analysis of fenestrated endovascular grafting: Intermediate-term outcomes. *European Journal of Vascular and Endovascular Surgery*, 32(2), 115–123.
- Osinnski, J.N., Ku, D.N., Mukundan Jr., S., Loth, F., Pettigrew, R.I. (1995). Determination of wall shear stress in the aorta with the use of MR phase velocity mapping. *Journal of Magnetic Resonance Imaging*, 5(6), 640–647.
- Ottesen, J.T., Olufsen, M.S., Larsen, J.K. (2004). *Applied Mathematical Models in Human Physiology*, 9. SIAM, Philadelphia.
- Ou, J., Chan, Y.C., Cheng, S.W. (2015). A systematic review of fenestrated endovascular repair for juxtarenal and short-neck aortic aneurysm: Evidence so far. *Annals of Vascular Surgery*. 29(8), 1680–1688.
- Richter, G.M., Palmaz, J.C., Noeldge, G., Tio, F. (1999). Relationship between blood flow, thrombus, and neointima in stents. *Journal of Vascular and Interventional Radiology*, 10(5), 598–604.
- Sahni, O., Müller, J., Jansen, K.E., Shephard, M.S., Taylor, C.A. (2006). Efficient anisotropic adaptive discretization of the cardiovascular system. *Computer Methods in Applied Mechanics and Engineering*, 195(41–43), 5634–5655.
- Suess, T., Anderson, J., Danielson, L., Pohlson, K., Remund, T., Blears, E., Gent, S., Kelly, P. (2016). Examination of near-wall hemodynamic parameters in the renal bridging stent of various stent graft configurations for repairing visceral branched aortic aneurysms. *Journal of Vascular Surgery*, 64(3), 788–796.
- Šutalo, I.D., Lawrence-Brown, M.M., Ahmed, S., Liffman, K., Semmens, J.B. (2008). Modeling of antegrade and retrograde flow into a branch artery of the aorta: Implications for endovascular stent-grafting and extra-anatomical visceral bypass. *Journal of Endovascular Therapy*, 15(3), 300–309.

- Sutton, C.S., Oku, T., Harasaki, H., Kambic, H., Sugita, Y., Murabayashi, S., Shirey, E., Nose, Y. (1988). Titanium-nickel intravascular endoprosthesis: A 2-year study in dogs. *American Journal of Roentgenology*, 151(3), 597–601.
- Textor, S.C. and Lerman, L.O. (2015). Paradigm shifts in atherosclerotic renovascular disease: Where are we now? *Journal of the American Society of Nephrology*, 26(9), 2074–2080.
- Tran, K., Fajardo, A., Ullery, B.W., Goltz, C., Lee, J.T. (2016). Renal function changes after fenestrated endovascular aneurysm repair. *Journal of Vascular Surgery*, 64(2), 273–280.
- Ullery, B.W., Suh, G.-Y., Lee, J.T., Liu, B., Stineman, R., Dalman, R.L., Cheng, C.P. (2016). Comparative geometric analysis of renal artery anatomy before and after fenestrated or snorkel/chimney endovascular aneurysm repair. *Journal of Vascular Surgery*, 63(4), 922–929.
- Verhoeven, E., Vourliotakis, G., Bos, W., Tielliu, I., Zeebregts, C., Prins, T., Bracale, U., van den Dungen, J. (2010). Fenestrated stent grafting for short-necked and juxtarenal abdominal aortic aneurysm: An 8-year single-centre experience. *European Journal of Vascular and Endovascular Surgery*, 39(5), 529–536.
- Verhoeven, E., Katsargyris, A., Bekkema, F., Oikonomou, K., Zeebregts, C., Ritter, W., Tielliu, I. (2015). Ten-year experience with endovascular repair of thoracoabdominal aortic aneurysms: Results from 166 consecutive patients. *Journal of Vascular Surgery*, 61(5), 1378.
- Vignon-Clementel, I.E., Figueroa, C.A., Jansen, K.E., Taylor, C.A. (2006). Outflow boundary conditions for three-dimensional finite element modeling of blood flow and pressure in arteries. *Computer Methods in Applied Mechanics and Engineering*, 195(29–32), 3776–3796.
- Vignon-Clementel, I.E., Figueroa, C.A., Jansen, K.E., Taylor, C. (2010). Outflow boundary conditions for 3d simulations of non-periodic blood flow and pressure fields in deformable arteries. *Computer Methods in Biomechanics and Biomedical Engineering*, 13(5), 625–640.
- Weinstein, J.R. and Anderson, S. (2010). The aging kidney: Physiological changes. *Advances in Chronic Kidney Disease*, 17(4), 302–307.
- West, C.A., Noel, A.A., Bower, T.C., Cherry Jr., K.J., Głowiczki, P., Sullivan, T.M., Kalra, M., Hoskin, T.L., Harrington, J.R. (2006). Factors affecting outcomes of open surgical repair of pararenal aortic aneurysms: A 10-year experience. *Journal of Vascular Surgery*, 43(5), 921–928.
- Williams, L. and Leggett, R. (1989). Reference values for resting blood flow to organs of man. *Clinical Physics and Physiological Measurement*, 10(3), 187.
- Xiao, N., Alastruey, J., Figueroa, C.A. (2014). A systematic comparison between 1-D and 3-D hemodynamics in compliant arterial models. *International Journal for Numerical Methods in Biomedical Engineering*, 30(2), 204–231.

Youssefi, P., Gomez, A., Arthurs, C., Sharma, R., Jahangiri, M., Figueroa, C.A. (2018). Impact of patient-specific inflow velocity profile on hemodynamics of the thoracic aorta. *Journal of Biomechanical Engineering*, 140(1).

3

Vascular Geometric Singularities, Hemodynamic Markers and Pathologies

Valérie DEPLANO and Carine GUIVIER-CURIEN

*CNRS, IRPHE, Ecole Centrale Marseille,
Aix-Marseille University, France*

3.1. Introduction

Vascular pathologies are numerous and varied, and their genesis and development are multifactorial. Nevertheless, it is now known that the characterization and analysis of the fluid dynamics and structures involved in the functioning of certain segments of the vascular system allow their dysfunction to be better understood, and allow correlations to be established between these dynamics and the genesis and development of vascular pathologies.

The purpose of this chapter is to describe flow behaviors in certain geometric singularities of the cardiovascular system, whether they are native or pathological, and to correlate their dynamics with the evolution of cardiovascular pathologies. These correlations can be made using associations between the spatiotemporal distributions of certain hemodynamic markers/indexes and in vivo observation of deleterious clinical events. Certain in silico and in vitro works conducted within the IRPHE Biomechanics team, mostly over the period of the “Biomechanics of fluids and transfers, biological structure-fluid interaction” and “MEChAnics

Biological Flow in Large Vessels,

coordinated by Valérie DEPLANO, José-Maria FULLANA, Claude VERDIER. © ISTE Ltd 2022.

Biological Flow in Large Vessels: Dialog Between Numerical Modeling and In Vitro/In Vivo Experiments,
First Edition. Valérie Deplano; José-Maria Fullana and Claude Verdier.

© ISTE Ltd 2022. Published by ISTE Ltd and John Wiley & Sons, Inc.

of BIOlogical materials and fluids” research groups, will notably serve to illustrate the remarks, which will not necessarily be exhaustive.

3.2. General characteristics of blood flows at the macroscopic scale

Biomechanical models of blood flows in the cardiovascular system at the macroscopic scale form part of a complex geometric, hydrodynamic and mechanical environment. As the heart delivers a pulsatile flow, blood flows are inherently unsteady. These flows occur in three-dimensional, evolving geometries, a specific patient with many singularities. The behavior of blood, which is closely linked to that of red blood cells, may exhibit a Newtonian, shear-thinning, viscoelastic or even thixotropic nature, depending on the vascular segment. Arterial walls, which are heterogeneous living media, have a visco-hyperelastic anisotropic mechanical behavior. The pulsatile character of flow and the viscoelastic nature of the walls lead to the propagation of pressure and velocity waves along the arterial system. In addition, the presence of geometric singularities induces wave reflections and thus contributes to altering the shape of the waves (pressure and velocity) along the cardiovascular system. It should be noted that these alterations are also due to the dispersive nature of the wall and the nonlinear effects of the pressure/diameter relationship of the artery and the fluid. At the same time, given their spatial proximity, these geometric singularities also result in it being impossible to obtain fully developed flows.

If we consider circulation models with distributed parameters (as opposed to global parameters), the location of the vascular segment to be modeled within the cardiovascular system will therefore play a significant role. As the acceleration and deceleration ramps and the maximum and minimum values of the pressure and velocity waves vary from one site to another in the cardiovascular system, the spatiotemporal shapes of the velocity profiles associated with different areas of the arterial tree cannot be considered to be identical. Furthermore, any dysfunction will also result in an alteration of these spatiotemporal shapes.

In macro-circulation two dimensionless numbers, the Reynolds number, Re , and the frequency parameter, α , or Womersley number, $\vartheta = \alpha^2$, allow the classification of blood flow regimes.

During systolic acceleration, the maximum value of the Reynolds number¹, $Re = \frac{Ud}{\nu}$, can reach 5,000 at the outlet of the left ventricle and flow can remain laminar. By contrast, at the beginning of deceleration, certain authors (McDonald 1952, for example) agree that for a critical Reynolds number value and particular values of the frequency parameter, disturbances appear, leading to a transition to turbulence.

The frequency parameter, which characterizes flow unsteadiness, is defined as $\alpha = a \sqrt{\frac{\omega}{\nu}}$, where a is the radius of the artery and $\omega = \frac{2\pi}{T}$ represents the pulsation. T is generally considered to be the cardiac cycle period. In practice, however, the definition of laws for the transition to turbulence, as well as analysis of evolution mechanisms for secondary structures that exist in certain geometric singularities of the cardiovascular system, in fact involves characteristic times that are related to systolic acceleration or deceleration times. It should be noted, for example, that the appearance of turbulence during the deceleration phase and the ensuing relaminarization are strongly dependent on the deceleration ramps. A longer deceleration time allows instabilities created at the wall to propagate toward the tube axis, whereas a shorter time results in a faster relaminarization.

The Womersley number can also be written as the ratio of characteristic times. Thus, $\vartheta = \alpha^2 = \frac{a^2/\nu}{1/\omega}$ represents the viscous diffusion time over the period of motion. If, as a first approach, we consider that blood viscosity and the cardiac period remain constant throughout the cardiovascular system, then only the radius of the artery of the site concerned influences this parameter. Therefore, for arteries with large diameters, of the order of 1 cm, the frequency parameter will be higher than for arteries with smaller dimensions and the viscous diffusion time will be large relative to the period of motion. The boundary layer will be confined to the wall and the velocity profiles will have a somewhat plateau shape, regardless of the effects of inlet, setting in motion or the appearance of a turbulent regime. In coronaries, which are arteries with smaller diameters, ~ 3 mm, the frequency parameter value will be lower, the viscous diffusion time will be low compared to the period of motion, the boundary layer will develop faster and thus the velocity profiles will have a more parabolic shape.

¹ ρ density of blood, ν its kinematic viscosity, U its average velocity, and d the artery diameter.

This analysis is supported by a dimensional study of the thickness of the Stokes layer, $\delta_s = \left(\frac{\nu}{\omega}\right)^{1/2} = \frac{a}{\alpha}$. The thickness of the boundary layer is all the thinner (or more developed, respectively), the larger the frequency parameter is (or smaller, respectively).

Table 3.1 gives several mean values of Re and α encountered in different segments of the arterial tree, considering a constant dynamic viscosity value equal to $3.6 \times 10^{-3} \text{ Pa}\cdot\text{s}$, the density of blood, $\rho = 1,060 \text{ kg/m}^3$, and the cardiac period, $T = 0.8 \text{ s}$.

	Diameter	Re_{ave}	α
Ascending thoracic aorta	~25 mm	1472.2	19
Abdominal aorta	~18 mm	1,060	13.6
Right coronary artery (RCA)	~3.7 mm	261.4	2.8

Table 3.1. Several characteristic values of the Reynolds number and frequency parameter in macrocirculation

The Dean and Strouhal numbers are also used in the characterization of secondary vortical structures (VSSs) that appear downstream of geometric singularities, whether native or pathological. Dean (1928) was one of the first to describe the counter-rotating helical structures existing in the aortic arch. The Dean number, defined as $De = Re \sqrt{H}$, allows consideration of the aspect ratio, H , between the radius of the artery, a , and its radius of curvature, R , $H = \frac{a}{R}$. It measures the ratio of the centrifugal inertial forces to the viscous forces. Within the context of biofluid mechanics, the Strouhal number, $S_t = \frac{f D_r}{U}$, is also used to quantify the frequency, f , of the detachment of vortex rings downstream of the orifice, where D_r is the constriction diameter and U the upstream flow velocity.

The general characteristics of blood flows have been presented succinctly. Nevertheless, these elements make it easier to address one of the main objectives of this chapter, focusing on the analysis of the relationships existing between the dynamics of blood flows in certain geometric singularities, the determination of hemodynamic markers associated with the behavior of these dynamics and the evolution of vascular pathologies. The

physical phenomena and subsequent behaviors of blood flows in the most common macroscopic singularities of the cardiovascular system are presented in the following section. The purpose is not to provide an exhaustive review but to describe the main physical phenomena.

3.3. Several geometric singularities of the cardiovascular system

The physiological singularities that will induce particularities in flow behavior are mainly those correlated with the existence of curvatures and bifurcations, that is, a change in flow direction. The valves also induce hemodynamic specificities linked to a significant dynamic variation in the diameter of the arterial lumen, from approximately 21–22 mm (Oh *et al.* 1999) in systole to 0 mm in diastole through the valve leaflets. The most notable pathological particularities are correlated with cross-section enlargements and constrictions, which are found in many pathologies. The most evident are aneurysms and valve or artery stenoses, regardless of their locations. Other conditions, such as aortic dissection and aortic coarctation, also induce cross-section enlargements and constrictions. These particularities can be combined: notably, cross-section constriction followed by an enlargement or a curvature. We must note that vessel tortuosities, which may be physiological or pathological, are, quite simply, curvatures. Finally, prosthetic particularities also induce alterations in blood flow behavior. Examples include bypass surgery, stents, endoprostheses, mechanical or bioprosthetic valves. Only valve prostheses will be described in this chapter.

3.3.1. Curvatures and bifurcations

The characteristics of the aortic arch mean it is considered to be a duct of great curvature with an average curvature ratio, H , between $\frac{1}{4}$ and $\frac{1}{2}$. In addition, there are many bifurcations in the vascular system, with these feeding adjacent organs. Starting from the aorta, for example: the brachiocephalic arterial trunk, the left primitive carotid and the left and right subclavians irrigate the head, neck and upper limbs, the renal arteries that bifurcate from the abdominal aorta vascularize the kidneys, the iliac bifurcation feeds the lower limbs, etc.

Generically speaking, curved or bifurcated geometries induce a change in fluid direction, initially straight, giving rise to a centrifugal force directed

from the inner wall of the curved duct (or outer of the daughter branch of the bifurcation) to the outer wall. In addition to the viscosity forces, the fluid motion is then governed by the relationship between the centrifugal forces and the transverse pressure gradient, which is in the opposite direction. Flows in bent or bifurcated geometries were extensively studied by Pedley (1980).

To describe the characteristics of this flow type in the center plane of symmetry (r, θ) (Figure 3.1(a)) as simply as possible, let us assume that at inlet there is a plateau-type velocity profile with a thin wall boundary layer corresponding to a high frequency-parameter value. Such a scenario is quite likely in the aortic arch as in the parent branch of the iliac bifurcation, that is, the abdominal aorta. In this case, for most of the tube the flow can be considered as inviscid; the pressure increases upon moving away from the center of curvature and by applying Bernoulli, in the center plane, the maximum axial velocity is initially located toward the inner wall of the curved duct. Then downstream, with the development of the boundary layer toward the center of the curved duct, this maximum velocity is offset toward the outer wall; in the boundary layer the centrifugal force induces a motion of fluid directed toward the outer wall. Boundary layers play an important role in the development of three-dimensional effects.

In the center plane, where the axial velocity amplitudes are highest, the centrifugal forces are predominant on the pressure gradient leading to a motion directed toward the outer wall of the tube. In the lower and upper planes, the decrease in velocity amplitude is accompanied by the domination of the transverse pressure gradient and the fluid motions directed toward the interior wall (Figure 3.1(b)). The composition of these opposing motions gives rise to a secondary flow in the form of two counter-rotating vortices, which develop in planes perpendicular to the axial flow and propagate helically.

It seems important to describe some characteristics associated with bifurcations that depend on geometric factors such as the bifurcation angle, β , or the ratio, R_s , between the daughter branch diameter, D_d , and the radius of the parent branch, a_p as well as the flow regime. In general, recirculating regions appear along the outer walls if the ratio, R_s , is greater than 1. The extent of the recirculating regions is accentuated with the increase in the Re number, but also with the bifurcation angle.

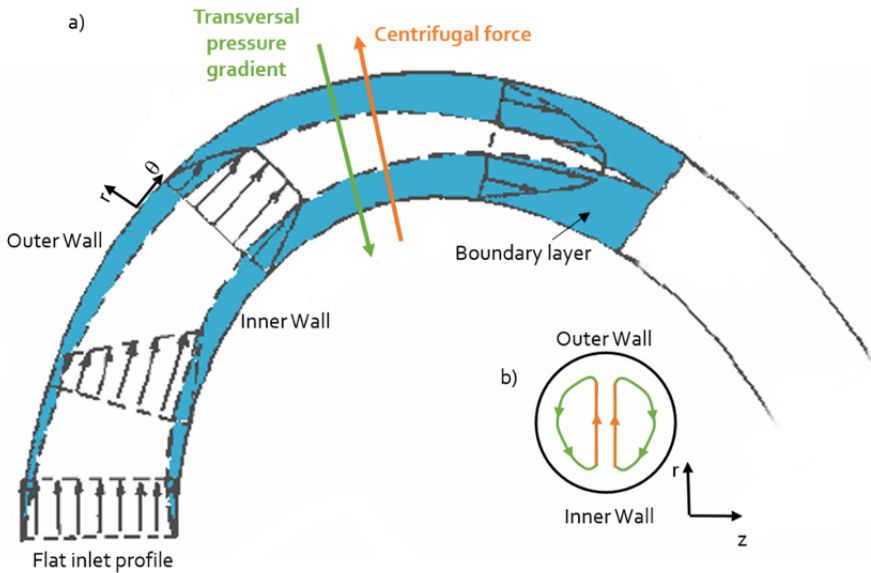


Figure 3.1. Representative diagram of a) main and b) secondary flows in a singularity with change of direction. Steady flow. Adapted from Fung (1996). For a color version of this figure, see www.iste.co.uk/deplano/biological.zip

All of these characteristics evolve during the cardiac cycle. The dynamic evolution of counter-rotating vortices may, for example, be described in different cross-sections, θ , perpendicular to the main flow as a function of the instant considered in the cardiac cycle. It is dependent on the inlet velocity conditions as well as the De and α numbers. Thus, in parallel with the description of these structures with two counter-rotating vortices, works conducted in the 1980s (Masliyah 1980; Dennis and Ng 1982; Cheng and Mok 1986) show that, based on a critical value of the Dean number of the order of 950, a dual solution exists, consisting of four counter-rotating vortices. The existence of secondary flows with two additional vortices, stable or unstable, appears to be due to centrifugal instabilities.

The works, *in vitro* and *in silico*, carried out by Boiron *et al.* (2007) in a bent tube by considering physiological flows, make it possible to illustrate the evolution of secondary structures in an idealized aortic arch model.

For small values of the Dean number, $De = 114$, and the frequency parameter, $\alpha = 8.14$ (Figure 3.2), during systolic acceleration, we observe

the development of two circumferential motions along the side walls. These motions, which remain confined in the viscous layer, are directed from the outer wall to the inner wall. Given the low value of α , the viscous diffusion time is low relative to the period of motion, which induces a viscous layer thickness of the order of one-third of the radius at $\theta = 156^\circ$. At maximum flow ($t = 0.528$ s), these motions impact at the inner wall and give rise to two counter-rotating vortices that move from the inner wall to the outer wall. The development of these vortices may be likened to a “mushroom” shape. At the start of systolic deceleration, $t = 0.79$ s, these vortices extend radially to occupy almost the entire cross-section. Their intensities then decrease.

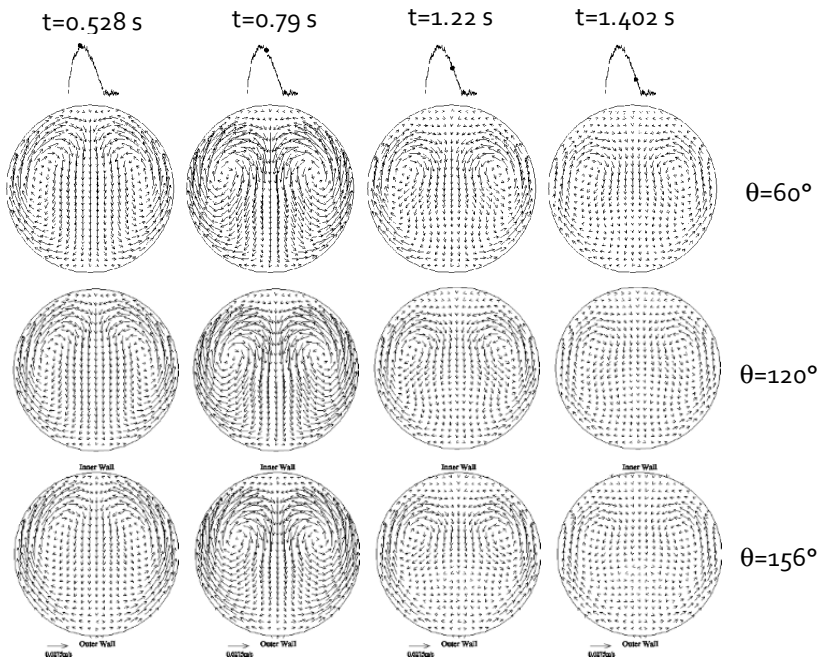


Figure 3.2. Time evolution of velocity vectors in the planes $\theta = 60^\circ$, $\theta = 120^\circ$, $\theta = 156^\circ$, $De = 114$, $\alpha = 8.14$

For the same frequency parameter value, $\alpha = 8.14$, but for a higher value of the Dean number, $De = 210$ (Figure 3.3), the intensity of the counter-rotating vortices is greater but they remain confined to the upper part of the cross-section throughout the acceleration phase, $t < 0.565$ s. When the flow decelerates, 0.79 s $< t < 1.24$ s, the vortices extend toward the outer

wall. For $\theta < 120^\circ$, due to the presence of a radial pressure gradient near the axis of symmetry, they are pushed toward the side walls. These structures, which can be likened to “bean” shapes, belong, according to the Sudo classification (Sudo *et al.* 1992), to structures called deformed Dean circulation. For $\theta = 156^\circ$, two additional counter-rotating vortices, rotating in the opposite direction to the first two, are worth noting. They are associated with structures, which are called intermediate circulation between Dean and Lyne (Lyne 1971).

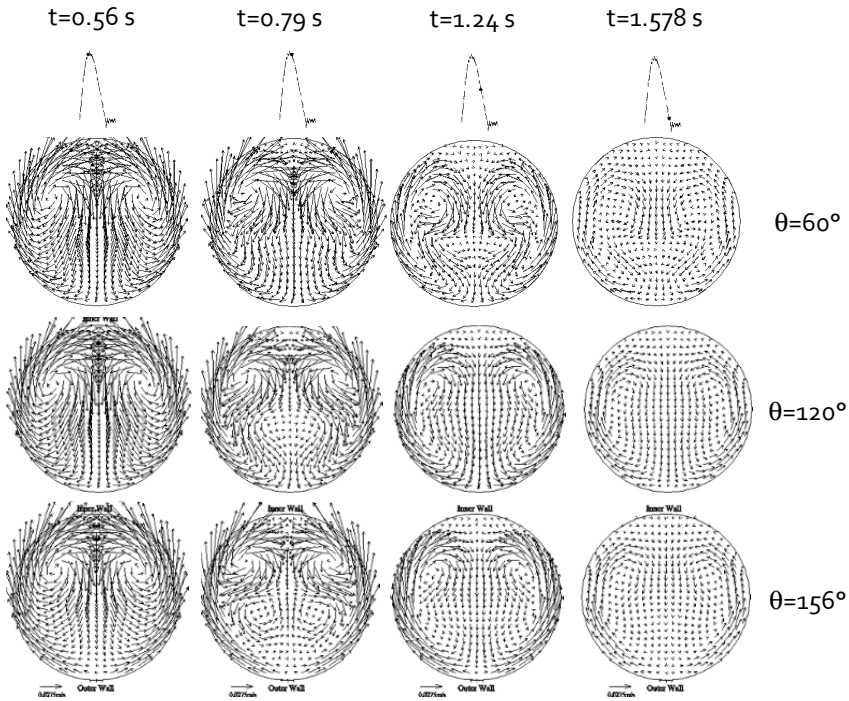


Figure 3.3. Time evolution of the velocity vectors in the planes $\theta = 60^\circ$, $\theta = 120^\circ$, $\theta = 156^\circ$, $De = 210$, $\alpha = 8.14$

These results obtained *in silico* have been confirmed by *in vitro* measurements and visualizations (Boiron *et al.* 2007). The complexity of the spatiotemporal dynamics of these secondary structures according to hydrodynamic conditions offers an indication of the importance for patients of biomechanical models that closely resemble reality.

3.3.2. Cross-section constriction

The flow in a cross-section constriction, representative of arterial stenosis, for example, is equivalent to the flow in a convergent followed by a divergent. Its description in the center plane (Figure 3.4) is facilitated with the use of the rotational transport equation, $\Omega(X, t)$.

$$\frac{\partial}{\partial t}(\Omega) + (\mathbf{V} \cdot \nabla)\Omega = (\Omega \cdot \nabla)\mathbf{V} + \nu \Delta(\Omega)$$

Upstream of the convergent, flow is irrotational. When the fluid arrives in the convergent, it undergoes continuous acceleration and subsequently, rotational convection takes place toward the low-velocity zones. The convection terms of the rotational equation are opposed to the diffusion terms and reduce the viscous layer to an increasingly small thickness along the convergent. This phenomenon is accentuated by the extension term of the vortex lines, which is directed toward the wall. The velocity profiles then show a central plateau whose width increases upon moving toward the convergent throat. At the throat, the area of the minimum cross-section, the flow has the characteristics of a wall boundary layer, which will be thinner, the higher the Reynolds number.

In the convergent, we can observe a cone of potential fluid whose base lies in the vicinity of the throat.

In the divergent, the convection of the rotational, which takes place toward the center of the tube, will add to its diffusion from the wall and to the extension of the vortex lines, which is directed toward the axis. In the case of the free jet, there is therefore a rotational supplement, which penetrates the potential core and reduces its length. In combination with the decrease in mean velocity, the fluid is subjected to an increase in pressure, which induces a detachment of the boundary layer and the creation of recirculating regions at near-wall negative velocities. The position of the reattachment point, downstream of the neck, is a function of the Reynolds number.

The boundary layer is transformed into a free shear layer that separates the potential core from the region with negative velocities near the walls. It is limited downstream of the neck by the reattachment point, which is not

fixed and oscillates constantly over time. The shear layer transforms into a boundary layer again by reattachment to the wall.

Three main regions can thus be differentiated by moving upstream and downstream: the recirculating region, the reattachment area and the recovery area. It is important to note the sensitivity of post-stenotic flows, via the shear layer, to very small disturbances that can generate convective-type instabilities that “self-maintain” through the recirculating regions, as well as the amplifying nature of instabilities of stenosis.

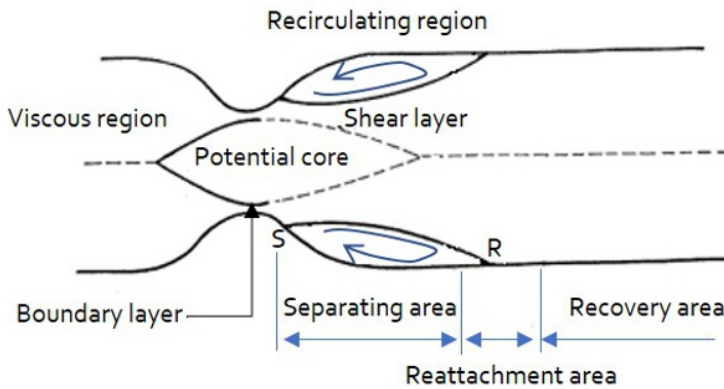


Figure 3.4. Diagram of the main flows in the center plane of a stenosis. *S*, detachment point of the boundary layer; *R*, reattachment point. Adapted from Siouffi (1988)

The Re and α values, the spatiotemporal form of the inlet flow rate and the form and degree of severity of stenosis, have an influence on the dynamics of post-stenotic flows. The characterization of the lesion influence lengths and the temporal and spatial evolutions of vortex shedding in the recirculating regions, reattachment points and detachment can be described using the rotational transport equation in a dimensionless form

$$\alpha^2 \frac{\partial}{\partial t} (\Omega^*) + 2Re_{\max} (\mathbf{V} \cdot \nabla) \Omega^* = 2Re_{\max} (\Omega^* \cdot \nabla) \mathbf{V} + \nu \Delta (\Omega^*)$$

The extension term of the vortex lines $(\Omega^* \cdot \nabla) \mathbf{V}$, as well as the term relating to the convection of the rotational $(\mathbf{V} \cdot \nabla) \Omega^*$, increase with the value

of Re_{\max} . Thus, the longitudinal dimension of the recirculating region increases as the maximum Reynolds value increases. The propagation of the recirculating region is then facilitated by an increase in Re_{\max} . If we also consider the rotational transport time, the longitudinal and radial amplitude of the recirculating region will be greater at the beginning of deceleration. The studies of Siouffi *et al.* (1998), carried out by modifying the value of the frequency parameter, however, show that increasing this value leads to a reduction in the recirculating region.

During the flow deceleration phase, the shear layer bordering the potential core will roll up to form a vortex ring downstream of the stenosis neck. The formation and evolution of this ring will be described in section 3.3.3, devoted to cross-section enlargements. The works of Kim *et al.* (2016) enable it to be viewed by MRI, for example. The studies of Zhu *et al.* (2018), meanwhile, demonstrate the complexities of the flows resulting from the serial combination of a stenosis followed by a curvature.

3.3.3. Cross-section enlargement

The flow in a cross-section enlargement is representative of that occurring in fusiform aneurysms, for example. It has characteristics in common with post-stenotic flow, notably with regard to the creation of a jet and the appearance of VSs in the form of a vortex ring downstream of the neck. However, the pre-constriction convergent effects are not present and the effects of the divergent are more pronounced.

As with other singularities, the flow dynamics in cross-section enlargements will depend on the Re number, the frequency parameter, α , but also on the geometric characteristics of the enlargement, such as its dilatation, length, asymmetry and aspect ratio. Nevertheless, a general description can be given.

The cross-section enlargement associated with the flow acceleration phase leads to an irrotational jet flow that enters the divergent. During this phase, the flow remains attached to the wall. At the beginning of deceleration, the velocity discontinuity at the edge of the jet generates an unstable Kelvin–Helmholtz-type shear layer that rolls into a vortex, which detaches at the neck of the divergent and propagates downstream. During the deceleration phase, recirculating regions appear in the zones furthest from the jet axis. The propagation of the ring may, depending on the

hydrodynamic, geometric and rheological conditions, result in an impact of the structure at the wall in the distal region with the appearance of a stagnation point, but also in a near-wall dislocation. It is also important to note that several rings can coexist during a cardiac cycle, depending on the propagation time of the structures.

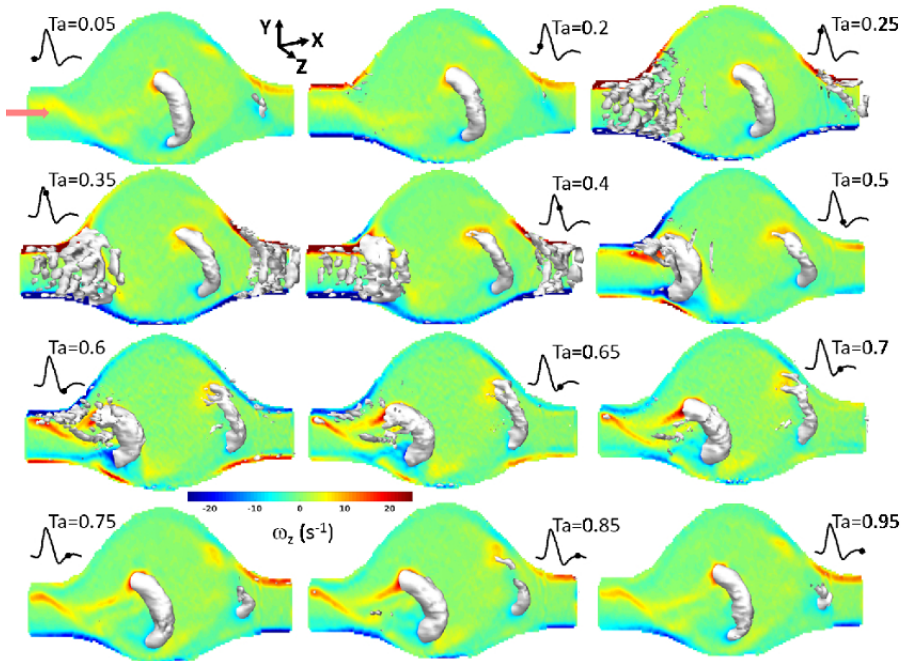


Figure 3.5. 3D temporal evolution of the vortex ring (in gray) overlaid on vorticity maps in the center plane. Adapted from Deplano *et al.* (2016). For a color version of this figure, see www.iste.co.uk/deplano/biological.zip

The *in vitro* works of Deplano *et al.* (2007, 2014, 2016) notably enable the dynamics and propagation of this ring to be quantified by performing velocity measurements using stereo-PIV in a deformable asymmetric aneurysm model for physiological 3D flows and a fluid with shear-thinning behavior. The dynamics of VSs are described and quantified using the criterion λ_{ci} from the works of Zhou *et al.* (1999), which allows structures with local rotation to be extracted from vorticity maps. Figure 3.5 shows the

propagation of vortex rings, identified by 3D isocontours of λ_{ci} overlaid on the vorticity maps in the center plane. These VSs may be involved in the formation of thrombus in the aneurysm sac according to mechanisms, notably associated with the transport of platelet elements (see section 3.5.2.3).

3.3.4. Valves

The aortic valve is the first singularity encountered by the flow in the systemic vascular system. It is located at the aortic root, between the left ventricle and the aorta. This valve is generally composed of three flexible, deformable leaflets (tricuspid valve) but may sometimes have only two leaflets (bicuspid) or even just one (unicuspid) in rare cases (Novaro *et al.* 2003). Behind each of these leaflets, an anatomical bulge, the Valsalva sinus, is present, ending the junction with the aorta. The diameter of the sinotubular junction, downstream of the aortic root, is slightly larger than that of the valve orifice.

The two main characteristics of aortic trans-valvular flows are the formation of a jet through the valve orifice and the presence of vortex structures in the sinuses.

The left ventricular outflow tract ends with the valve orifice, thus creating a constriction. Moreover, the leaflets confine the trans-valvular flow, the streamlines are straight and parallel. Thus, during the systolic phase, a flow in the form of a jet is established through the valve. The opening surface of the valve is quasi-circular, which leads to the formation of a jet centered on the orifice with velocities of the order of 0.8–1.2 m/s. The flow in the ascending aorta is then preferentially aligned with the aortic walls. Generally referred to as symmetric, the jet may nevertheless impact the anterior distal wall of the ascending aorta, according to the latter's curvature in relation to the valve orifice. The downstream cross-section enlargement of the aortic root associated with the curvature of the ascending aorta leads to the development of a secondary helical motion in the ascending aorta from the systolic peak (see section on curvatures and bifurcations) (Kilner *et al.* 1993; Morbiducci *et al.* 2011). This motion is visible during the entire deceleration phase.

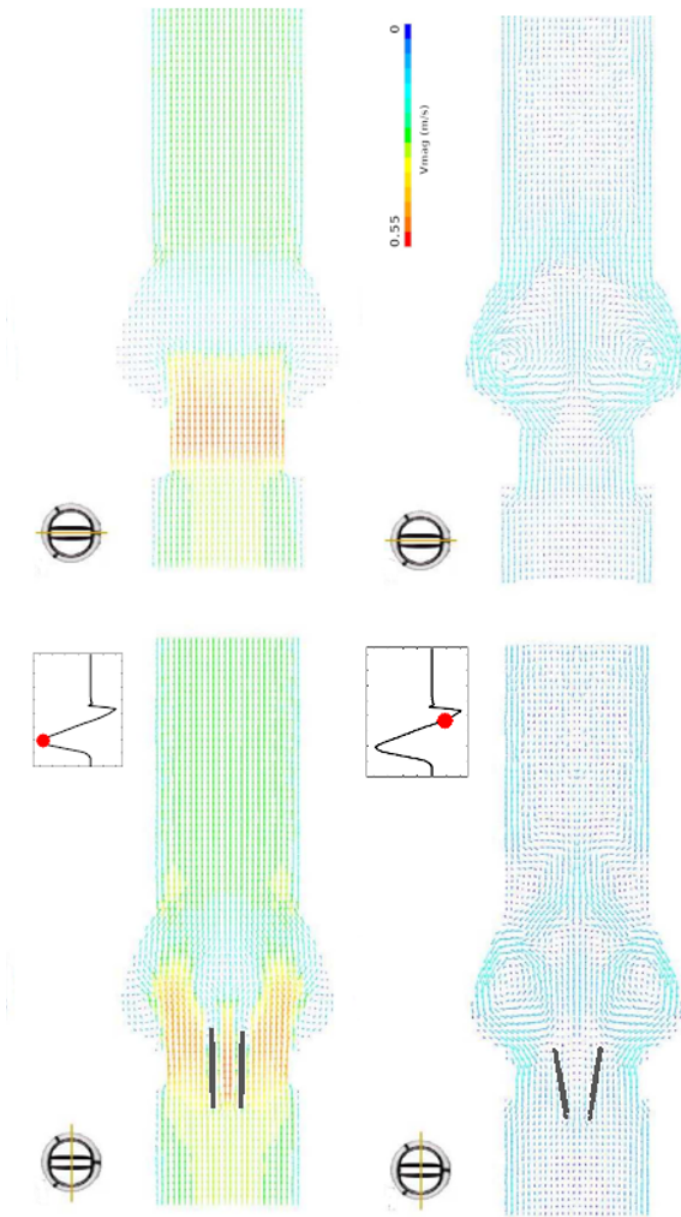


Figure 3.6. Temporal evolution of velocity vectors through a bileaflet prosthetic valve in two perpendicular planes. Adapted from Guivier et al. (2009). For a color version of this figure, see www.iste.co.uk/deplano/biological.zip

In bicuspid cases, two of the three leaflets are fused together, creating an eccentric opening in the aortic root. The dynamics of the transvalvular jet then differ from that observed in the case of a healthy tricuspid valve. The jet is eccentric and asymmetric in the ascending aorta (Hope *et al.* 2011). According to the fused leaflets, the jet directly impacts the anterior wall of the proximal ascending aorta (in the case of a bicuspid with right and left leaflet fusion) or the posterior wall, before being deflected toward the anterior wall (in the case of a bicuspid with right, non-coronary leaflet fusion) (Rodriguez-Palomares *et al.* 2018). Successive deviations and impacts in the curved geometry of the ascending aorta lead to the appearance of a highly helical secondary flow, mainly in patients with a fusion of the right and non-coronary leaflet (Meierhofer *et al.* 2013; Mahadevia *et al.* 2014). Given the geometric angulation of the aorta associated with helical motion, it has been possible to observe retrograde flows in some patients (Barker *et al.* 2010) during the systolic phase.

In case of failure (a problem with closure-regurgitation or with optimal opening – stenosis – calcification, etc.), the aortic valve is replaced with a bioprosthesis or mechanical prosthesis. The design of mechanical valves differs from one prosthesis to another, thus resulting in the behaviors of prosthesis-dependent flows (Dasi *et al.* 2009), whose main characteristics are visible from the systolic peak. In the case of a monoleaflet valve, the orifice is divided into two geometrically asymmetric parts. The result is the formation of two jets of marked, very different amplitudes. The velocity profiles are eccentric in the proximal ascending aorta. In the case of a bileaflet valve, two lateral orifices and one central orifice lead to the formation of three separate jets, also making the flow non-axisymmetric (Figure 3.6). Due to the cross-section constrictions related to the valve design, the recorded velocities are generally higher. At about two diameters downstream of the prosthesis, the velocity profiles become more or less dampened (Yoganathan *et al.* 1986; Hasenkam *et al.* 1988).

During systolic ejection, the free edge of the leaflets of the native or prosthetic aortic valve is not in contact with the wall, given the presence of the sinus behind each of the leaflets. The streamlines are parallel to the leaflets in the valve orifice. Upon reaching the free ends of the leaflets, the streamlines separate to enter the sinuses, resulting in the formation of a recirculating region from the start of the ejection. The vortex structure created is present until the start of diastole. With the closure of the leaflets,

each of the vortex structures gradually extends out of the sinuses, decreasing in intensity. Their presence ensures good cleaning and prevents the post-valvular stasis zones during diastole.

3.4. Hemodynamic markers

Quantified characterizations, *in vitro* or *in silico*, of the flow dynamics in geometric models that are close to vascular pathologies by deploying biomechanical models, taking into account the hydrodynamic conditions of patients, the blood shear-thinning behavior and the wall dilatation capabilities, allow the definition of hemodynamic indexes that are capable of providing relevant response elements in predicting the evolution of these pathologies. Among the most widely-used hemodynamic markers are those derived from the spatiotemporal quantification of wall shear stress and those related to the dynamics of secondary structures. The determination of spatiotemporal mapping of wall shear stress as well as secondary vortical and/or helical structures is notably related to velocity gradients and possible viscosity variations. These two quantities are associated with the geometric singularities that, as we have just shown, significantly influence flow dynamics.

Thus, without quantifying a wall shear stress value, it is important to recall that for curvatures or bifurcations, the location of the maximum velocities, alternately on the inner and/or outer walls, will be associated with regions of high wall shear stress values, and the opposite outer and inner walls, respectively, at lower values; recirculating regions that exist downstream of cross-section constriction (stenosis, coarctation, false lumen of aortic dissection, etc.) but also possibly at the outer walls of bifurcation, as well as within cross-section enlargement (Valsalva sinus, aneurysms, etc.) will lead to low, oscillating wall shear stress values; flow impact zones, such as the apex of a bifurcation or the anterior distal wall of the ascending aorta, will be the site of high wall shear stress values relative to the normal, as will arterial stenosis necks, aortic dissection entry tears or mechanical valve leaflets. VSs, meanwhile, which appear in many singularities, allow for the characterization of complex fluid transport. They will be able to interact with cellular/globular elements – transport them and shear them – and the vascular walls by, for example, impacting them.

3.4.1. Indexes derived from wall shear stress

The indication that we can correlate wall shear stress values with the location of certain vascular pathologies dates back about 50 years. It was mainly dedicated to the analysis of zones prone to the development of atherosclerosis. Although the genesis and development of this pathology depend on many biological factors and involve different spatiotemporal scales, it was noted that there are preferred locations at sites of bifurcations, curvature and constrictions, beyond patient profile – excess lipids in blood (LDL-cholesterol), sedentariness, presence of free radicals due to tobacco, hypertension, diabetes, genetic alteration, stress, etc. As we have seen, these geometric singularities are prone to the appearance of zones of high velocities, recirculation, stases, stagnation points, reattachment points, and helical secondary structures, and these flow particularities induce specificities in wall shear stress behavior.

This indication is currently reflected in the characterization of the spatiotemporal evolution of wall shear stress and its numerous derivative indexes, with associated events involved in a deleterious remodeling of the wall, as we will see in section 3.5.

3.4.1.1. Definitions

Let \mathbf{df} be the elementary shear stress force, τ the viscous stress tensor and \mathbf{n} the external normal to the surface element, ds , on which the elementary wall shear stress force is determined.

\mathbf{df} is defined as $\mathbf{df} = \tau \mathbf{n} ds$

Considering that fluid has a generalized Newtonian behavior, τ is written as:

$\tau = 2\mu(J_2)D$ with D the strain velocity tensor, $D = \frac{1}{2}(\nabla\mathbf{V} + \nabla\mathbf{V}^t)$ and J_2 its second invariant.

The wall shear stress vector thus defined will be noted \mathbf{WSS} for the remainder of this chapter. It depends on t and the geometric coordinates in which the object of study is defined; $\mathbf{WSS}(\mathbf{X},t)$. It is, therefore, important to quantify its amplitude, direction, spatiotemporal evolution and its variations in relation to its average, its average direction and the associated spatial and temporal gradients.

The markers most commonly used in the literature to associate **WSS** with the location of deleterious clinical events, derived from the **WSS** quantification, are listed below.

The time average of the **WSS** norm, TAWSS (Time Average Wall Shear Stress), is an index introduced by Ku *et al.* (1985). It is defined as:

$$\text{TAWSS} = \overline{\mathbf{WSS}} = \frac{1}{T} \int_0^T |\mathbf{WSS}| dt, \text{ with } |\mathbf{WSS}| \text{ the } \mathbf{WSS} \text{ norm.}$$

The oscillatory shear index (OSI) (Ku *et al.* 1985) represents the degree of deviation of wall shear stress from its mean direction. Its value varies between 0 when the **WSS** is unidirectional and 0.5 when the **WSS** is highly oscillating. This index is written as:

$$\text{OSI} = \frac{1}{2} \left(1 - \frac{\left| \int_0^T \mathbf{WSS} dt \right|}{\int_0^T |\mathbf{WSS}| dt} \right)$$

The **WSS** spatial gradient, WSSG, is a concept introduced by Lei *et al.* (1996). Its components, WSSG_{ij}, are written as:

$$\text{WSSG}_{ij} = \frac{\partial \text{WSS}_i}{\partial x_j}$$

Relative residence time (RRT) is an index proposed by Himburg *et al.* (2004); it is proportional to the residence time of blood particles. It is defined as:

$$\text{RRT} = (1 - 2\text{OSI})\text{TAWSS}$$

Some authors suggest combinations of these indexes. The following can be found, for example:

The Holmes (High Oscillatory Low Magnitude Shear) indicator, introduced by Alimohammadi *et al.* in 2016 (Alimohammadi *et al.* 2016), that identifies zones of low TAWSS and high OSI values. HOLMES = TAWSS(0.5 – OSI)

The degree of deviation of the wall shear stress gradient (WSSG) from its mean direction, gradient oscillatory number (GON), is proposed by Shimogonya *et al.* (2009): $\text{GON} = \frac{1}{2} \left(1 - \frac{\left| \int_0^T \text{WSSG} dt \right|}{\int_0^T |\text{WSSG}| dt} \right)$

The transWSS is presented by Peiffer *et al.* (2013a), who identifies the temporal variations of the components of the **WSS** perpendicular to the average principal direction.

3.4.2. Indexes describing VSs

The creation and evolution of secondary VSs can also play an important role in the functioning or dysfunction of the cardiovascular system. Their positive role can be found in the left ventricle, with their involvement in a washing function. Their deleterious effects are described in their participation in the formation of thrombotic material, but also in their involvement in various arterial dilatation processes.

The quantification and identification of these coherent structures are derived from works stemming from fluid mechanics (Zhou *et al.* 1999; Chakraborty *et al.* 2005). Vorticity $\mathbf{\Omega} = \text{rot}(\mathbf{V})$ alone will not suffice to extract them; indeed, in the near-wall, for example, there are high-vorticity zones due to shearing, associated with viscous dissipation and not with local rotation.

Of the many techniques proposed, none achieve unanimity because they are based on velocity and pressure, which are global quantities. Those calculated from the eigenvalues of the velocity gradient tensor, $\nabla\mathbf{V}$, are used in particular because the complex eigenvalues delimit zones where the streamlines are locally circular or spiral in shape (Chong *et al.* 1990).

$\nabla\mathbf{V}$ can be broken down into a symmetric part, D , the strain velocity tensor, and an antisymmetric part, $\mathbf{\Omega}$, the vorticity tensor (or rotation rate): $\nabla\mathbf{V} = D + \mathbf{\Omega}$.

The characteristic equation of eigenvalues, λ , of $\nabla\mathbf{V}$ is written as: $\lambda^3 + P\lambda^2 + Q\lambda + R = 0$

For an incompressible flow, $P = -\text{div}\mathbf{V}$, the first invariant $\nabla\mathbf{V}$ is therefore zero. The second and third invariants, Q and R , are defined as:

$$Q = \frac{1}{2}(\|\mathbf{\Omega}\|^2 - \|D\|^2) \text{ and } R = -\det(\nabla\mathbf{V})$$

Several criteria deriving from the characteristic equation are used in our scope. The criteria Δ , Q and λ_{ci} are presented below.

The eigenvalues of $\nabla\mathbf{V}$ are complex when Δ , the discriminant of the characteristic equation, is strictly positive. Thus, $\Delta > 0$ constitutes the first criterion for extracting a vortex.

When the second invariant, Q , is strictly positive, the vorticity (antisymmetric part of $\nabla\mathbf{V}$) dominates the strain velocity tensor (symmetric part of $\nabla\mathbf{V}$). Hunt *et al.* (1988) propose that the vortices then be identified by regions that fulfill the strictly positive Q-criterion.

Introduced by Zhou *et al.* (1999), the criterion λ_{ci} (swirling strength) is based on the criterion Δ . The eigenvectors associated with the complex eigenvalues of $\nabla\mathbf{V}$ enable the plane in which the flow is locally swirling to be defined. The criterion λ_{ci} then consists of determining the imaginary part of the complex eigenvalues that represents a local quantification of the vortex motion.

These criteria, based on invariants, have the advantage of being objective quantities and are therefore frame-independent. Moreover, being based solely on the calculation of complex eigenvalues they thus eliminate vorticity regions without local rotation motion, such as shear zones.

Some authors use the criterion λ_2 (Biasseti *et al.* 2011; Ab Naim *et al.* 2016). Based on the fact that the value of the pressure induced locally by the presence of a vortex is minimal, Jeong *et al.* (1995) propose evaluating the eigenvalues of the tensor $D^2 + \Omega^2$. This tensor is derived from the gradient of the Navier–Stokes equation, broken down into symmetric and antisymmetric parts and overlooking the viscous and unsteady effects, which can suppress or generate minimum pressure values, respectively.

Thus, under these hypotheses $D^2 + \Omega^2 = -\frac{1}{\rho}\nabla(\nabla\mathbf{p})$. A local minimum pressure appears if $D^2 + \Omega^2$ has two negative eigenvalues. Since this tensor is symmetric, its eigenvalues are all real. By ordering $\lambda_1 > \lambda_2 > \lambda_3$, the criterion becomes $\lambda_2 < 0$ to have a local minimum pressure due to a vortex only.

Other authors use Lagrangian techniques such as the “Finite-Time Lyapunov Exponent” (FTLE) to extract coherent structures (Shadden and Taylor 2008). The review by Haller (2015) details the latest developments. Arzani and Shadden (2012a), Arzani and Shadden (2012b) and Joly *et al.* (2018)

notably deploy them in the context of the study of aneurysms to describe flow topology.

Finally, based on the quantification of velocity and vorticity fields and their scalar product, criteria such as the normalized helicity index (LNH) or the helicity flow index (HFI) (Grigoni *et al.* 2005; Morbiducci *et al.* 2009) have also been proposed to define the helical motions present in the vascular system.

3.5. Correlation between hemodynamic markers and pathologies: some examples

From the 1970s, different hypotheses were presented to correlate wall shear stress values with atherosclerosis. Fry (1968) claimed that high values could damage endothelial cells and subsequently lead to the stripping of the endothelium, which was thought to be the initiator of the pathology. Conversely, Caro *et al.* (1971) proposed a correlation between low wall shear stress values and pathology development by observation of preferred lesion locations.

Fifty or so years later, the hypothesis of low values of wall shear stress prevails in the mechanisms of atherosclerosis development. This initial hypothesis suggested that low wall shear stress values could lead to prolonged residence times (RRTs) of LDL lipoproteins and/or monocytes and thus promote their local adhesion and infiltration into the arterial wall, characteristic of the pathology (Hermann *et al.* 1994). This increased permeability was seen as responsible for a cascade of deleterious events leading to a remodeling of the wall, such as intimal thickening. This reasoning was also extended to an effect on mass transfers resulting in the local accumulation of growth factors in the proximity of the intimal surface. However, these concepts consider rheological issues to be critical determinants and consider the arterial wall to be relatively passive. Another hypothesis, linking wall shear stress with atherosclerosis, emerged in the 2000s in light of various works (Gimbrone 1998; Ross *et al.* 2004) on the active participation of arterial-wall cells in pathology processes.

It is now clearly established that hemodynamic factors, in the form of mechanical stimuli of endothelial cells lining the intimal layer of the vascular wall, regulate many of the physiological responses of the healthy arterial wall and are also involved in the development of pathologies of the

arterial wall, such as atherosclerosis, intimal hyperplasia, dilatations and even ruptures. Endothelial cells are primary sensors of wall shear stress and function as sensors of mechanical loads in the wall's biological responses (Tarbell *et al.* 2014). This concept of mechanotransducing endothelium indicates that any change in mechanical stimuli of the endothelial surface – values, orientations, variations, etc. – can cause dysfunction and hence initiate the different processes of development of pathologies in the vascular wall.

In healthy humans, the instantaneous wall shear stress values can vary from 10 to 70 dyn/cm² (1–7 Pa) in the straight arteries of the vascular system (Malek *et al.* 1999). Thus, the order of magnitude of the mean physiological values commonly found in the literature for straight arteries is 15–20 dyn/cm² (Malek *et al.* 1999). These values, called reference values, are classified as atheroprotective and/or conform with the wall stresses to which vascular endothelial cells may be subjected without expressing “corrective” responses to return to the reference value.

Wall shear stress values, however, whether at reference values or above or below reference values, are subject to debate. At present, there is no sufficiently accurate *in vivo* methodology for measuring deformable-wall velocity gradients in the thickness of unsteady boundary layers. MRI measurements, for example, cannot be performed with a resolution finer than 1.5 mm. Numerical simulations, meanwhile, which enable quantification of physical quantities as near as necessary to the wall, depend on the fluid models and structures used to reproduce the vascular segment under investigation, the geometries retained to represent those segments and the boundary conditions deployed. Finally, *in vitro* measurements can present the same disadvantages as *in silico* models, and near-wall quantifications are difficult to implement.

Beyond the difficulty in establishing precise yield values above or below which deleterious processes are possible, the following sections take stock of the trends and controversies combining geometric singularities, low, high and very high values of wall shear stress and its derived indexes, their spatio-temporal variations and pathologies. The dynamics of VSs, representative of fluid transport, are also being investigated as a hemodynamic marker that can be associated with the development of vascular pathologies.

It is essential to underline that although *in vitro* and *in silico* models serve to establish and analyze hemodynamic indexes, the correlations between these markers and vascular pathologies can only be confirmed *in fine* through *in vivo* clinical studies.

3.5.1. WSS and pathologies

If we consider the wall shear stress values between 15 and 20 dyn/cm² as reference values in a healthy human, it is now commonly accepted that values below or equal to 5 dyn/cm² are low WSS values (Sho *et al.* 2004), values greater than 30 dyn/cm² are high values (Dolan *et al.* 2011) and values greater than or equal to 120 dyn/cm² are very high values that act on circulating cells (Moake *et al.* 1988). As we saw in section 3.4, the downstream of cross-section constrictions, bifurcations, curvatures and enlargements of cross-section result in near-wall separation zones occupied by low-velocity flows that can cause low wall shear stress values. In contrast, accelerated flow in the form of a jet results in velocity gradients and, as a result, high near-wall shear stress values and very high values at the cross-section constriction neck. Fluid shear rates are also high.

3.5.1.1. Low WSS values

Having demonstrated the roles played by high residence times (RRTs) of circulating particles and increased endothelial wall permeability subjected to low wall shear stress values in pathologies such as atherosclerosis, new concepts have emerged to better understand the link between hemodynamic markers and pathology. For example, the introduction of the unsteady nature of flows in the different *in vitro* and *in silico* models led to the appearance of the criterion of high oscillating WSS, that is, a high OSI index, as an additional predictive indicator of arterial remodeling (Ku *et al.* 1985). The low WSS hypothesis then evolved into a combined low WSS and high OSI hypothesis. This criterion is now widely used and has been identified as a predictor of zones promoting the development of intimal thickening, either from *in vivo* animal models (Cheng *et al.* 2006; Thim *et al.* 2012), or in experimental models (Moore *et al.* 1994; Ding *et al.* 2001) and in *in silico* models (Steinman *et al.* 2002; Ene-Irodache and Remuzzi 2012), who directly correlate their measurements with clinical observations.

In parallel, DePaola *et al.* (1992), in an experimental study on endothelial cells of bovine aorta, also demonstrate the importance of spatial wall shear stress gradients, WSSG, promoting stretching (WSSG > 0) or compression

(WSSG < 0) of endothelial cells and subsequently influencing their shape, migration and division capacity. Depending on the WSSG level, the wall permeability can also be altered, as discussed by Lei *et al.* (1996), Herrmann *et al.* (1994) or Buchanan *et al.* (1999). In addition, the zones, subject to low and oscillating wall shear stress values, extend or reduce due to flow pulsatility, resulting in strong temporal WSS gradients at the cardiac cycle scale. The works of White *et al.* (2001), Haidekker *et al.* (2001), or Soulis *et al.* (2006) suggest that this temporal variation plays a role in the increase in intimal proliferation.

Thus, the theory of low and oscillating wall shear stress appears to potentially minimize a more complex reality of the links between hemodynamic markers and arterial remodeling. In line with the works of Peiffer *et al.* (2013a) and based on studies by Wang *et al.* (2013), showing that endothelial cells are sensitive to flow multidirectionality, Morbiducci *et al.* (2015) combine the complexity of the links between markers and pathology by exploring the role played by the multi-directionality of wall shear stress. Recent reviews of the literature (Barakat 2013; Peiffer *et al.* 2013b) also question both the systematic generalization of the criterion “low and oscillating wall shear stress” and its universally predictive nature. Indeed, whatever the vascular pathology, it is difficult to compare similar geometric characteristics (curvature, dilatation, constriction, etc.) presenting significant local variabilities from one arterial site to another, from one patient to another, from one study time to another, or indeed from one animal model to another.

3.5.1.2. High WSS values

In the general case of arterial dilatations – aneurysms of the thoracic or abdominal aorta, intracranial and dissection – there are two opposing theories – high and low wall shear stress values – to explain the same development of the pathology.

In *in vivo* studies based on human MRI measurements, Hope *et al.* (2011), Mahavedia *et al.* (2014) and Rodriguez-Palomares *et al.* (2018) highlight an increase in the maximum value of wall shear stress in the dilated ascending aorta downstream of a bicuspid valve relative to the values encountered in healthy cases downstream of a tricuspid valve. High WSS values are also reported in studies correlating measurements *in silico* and clinical patient monitoring for sacciform intracranial aneurysms (Castro *et al.* 2009), or indeed during the aneurysmal evolution of the false lumen of

dissections (Shang *et al.* 2015). The effects of high WSS were also explored *in vitro* on bovine aortic endothelial cells in conjunction with the application of a WSSG, showing that the addition of a positive WSSG exacerbates cell dysfunction, significantly altering their alignment and increasing cell death (Dolan *et al.* 2011).

In contrast, low wall shear stresses are observed *in vivo* in the dilated ascending aorta (Burk *et al.* 2012) and in *in silico* studies with patient-specific geometry, correlating measurements and the patients' clinical profile, in the false lumen of dissections (Karmonik *et al.* 2013; Doyle *et al.* 2014), in intracranial aneurysms (Boussel *et al.* 2008; Zhou *et al.* 2017) or abdominal aneurysms (Boyd *et al.* 2016). In the case of aneurysms, it should be noted that the morphology is generally fusiform.

This low/high wall shear stress controversy is discussed by Meng *et al.* (2014). The differentiated activation of the channels of the biological cascade in the mechanical transduction, notably with an inflammatory pathway – associated with low WSS – and an increase in metalloproteinase expression and activity – correlated with high WSS – seems to be at the origin of the differences observed. Moreover, *in vitro* studies confirm these two pathways: Anidjar *et al.* (1992) show a correlation between aortic enlargement and activation of the inflammatory system using an animal (rat) model of arterial enlargement. Sho *et al.* (2002), meanwhile, confirm, on another animal model (rabbit), an increasing activity of metalloproteinases following the exposure of the wall to strong WSS. Fedak *et al.* (2003) show, in samples of dilated ascending aorta collected from patients with a bicuspid valve, an increase in metalloproteinase activity that is correlated with aortic diameter. Finally, thanks to 4D flow MRI measurements, Guzzardi *et al.* (2015) also report that downstream of a bicuspid valve, ascending aorta dilatation is associated with high WSS values corresponding to extracellular matrix deregulation, the degeneration of elastin fibers and an increase in metalloproteinase expression.

In light of the sometimes divergent conclusions of these different studies putting forward a hypothesis of low or high WSS in the dilatation process, it will, without a doubt, be necessary to question the role of biological and biochemical mechanisms taking place at the cellular or molecular scale and intervening in mechanotransduction: a change of scale for a change of paradigm.

3.5.2. Hemodynamic markers and thrombus

The thrombus can roughly be described as a blood clot forming in various pathologies such as atherosclerosis, aneurysms of the abdominal aorta, dissections, etc. Its presence participates in an alteration of the pathological process. We will not discuss its protective or deleterious role with regard to pathologies here, but we will discuss the mechanisms of its formation that are linked to the hemodynamics. Platelets and circulating blood cells contribute to thrombus formation through their activation, aggregation and adhesion to the arterial wall; these three steps are complementary.

3.5.2.1. Thrombus and high WSS values

In accelerated flow in the form of a jet, such as at the neck of an arterial stenosis or at an aortic dissection entry tear, high near-wall velocity gradients appear and give rise to high WSS values (of the order of 125 dyn/cm^2 (Deplano and Siouffi 1999) and 100 dyn/cm^2 (Khannous *et al.* 2019), respectively) as well as very high fluid shear values (of the order of $5,000 \text{ s}^{-1}$; Casa *et al.* 2015).

This configuration draws platelets and blood proteins such as von Willebrand factor² (vWF) towards the walls. This is known as the margination phenomenon (Zhao *et al.* 2007). In the presence of thrombogenic surfaces such as subendothelial collagen fibers, exposed as a result of endothelium stripping, vWFs will rapidly colonize these surfaces. Given high fluid shear rates, (i) vWFs distort and stretch to form nets, multiplying platelet adhesion contacts and sites, and (ii) platelets will bind to these proteins rather than to fibrinogen, another coagulation factor; platelets rapidly adhere and aggregate even before their activation, as shown in vitro by Ruggeri *et al.* (2006) and in silico by Wellings *et al.* (2012). High shear rates also allow rapid platelet accumulation and activation, as observed in vitro by Bark *et al.* (2012). In addition, high WSS values also cause platelet activation (Moake *et al.* 1988). During the activation phase, platelets release proteins, notably vWF proteins and fibrinogen. In the case where platelets have already adhered, this release will allow thrombus growth. By constricting the cross-section of the arterial lumen slightly further, shear rates increase and the process self-maintains, to the extent of possibly occluding the vessel (Casa *et al.* 2015).

² von Willebrand factor is a protein that allows platelet adhesion to the arterial wall.

Thrombi that adhere in zones of high WSS are generally more unstable than those formed in zones of low WSS, given the bonds involved for platelet aggregation (Shi *et al.* 2016). The instability of thrombi formed in this way may lead to partial or total detachment of the thrombus, which gives rise to risks of the occlusion of a downstream artery with a smaller diameter.

3.5.2.2. *Thrombus and low WSS values*

Low WSS values found in zones of recirculation, for example, aneurysm, or other zones presenting cross-section enlargement, appear to favor adhesion of platelets preferentially via the fibrinogen present, as shown in vitro by Savage *et al.* (1996), in a study conducted on blood from human donors. Back in the 1970s, Blackshear *et al.* (1971), as well as Karino and Goldsmith (1977), demonstrated that the recirculation regions, the site of low WSS values, were favorable for thrombus formation. Other, more recent, studies have also correlated the presence of low wall TAWSS with the presence of thrombus, notably in the false lumen of aortic dissection. Zones of flow recirculating at low velocities (Chen *et al.* 2013; Cheng *et al.* 2015) or even of stagnant flow (Rinaudo and Pasta 2014), essentially dominated, as we have seen, by low TAWSSs and RRTs of fairly high circulating particles (Cheng *et al.* 2013; Cheng *et al.* 2015), therefore represent regions favorable to thrombus development (Meng *et al.* 2014; Menichini and Xu 2016).

It should be noted that, again, differences may appear here, underlining the complexity of the process: the in silico study by Di Achille *et al.* (2014) correlates, with clinical observations, low WSS and high OSI values with zones of the aneurysm sac of the abdominal aorta presenting thrombus in the patients under consideration. O'Rourke *et al.* (2012), meanwhile, also suggest, through in silico measurements, a combination of low WSS and low OSI values to correlate with thrombus growth zones based on two-stroke clinical imaging for patient follow-up.

3.5.2.3. *Thrombus and coherent structures*

In parallel to the concept of shear yield values within the fluid and/or at the wall as a platelet-stress mechanism acting on thrombus formation, several research groups have taken an interest in the role played by VSs, whether concerning aneurysms or aortic dissections (TAD) (Basciano *et al.* 2011; Biasetti *et al.* 2011; Ab Naim *et al.* 2016; Menichini *et al.* 2018). Through in silico models and using the criterion λ_2 to identify VSs, the

retained mechanisms clearly presented by Biasetti *et al.* (2011) in the case of abdominal aortic aneurysms (AAA) can be summarized in four phases: (i) platelets are trapped in VSs formed at the proximal throat of an aneurysm or at the entry tear of the false lumen of a TAD. (ii) The platelets, trapped in the VSs, are activated by the high shear values existing at the periphery of VSs and/or by the high WSS values that exist at the TAD entry tears. (iii) The VSs transport and convect the activated platelets downstream. (iv) In the deceleration phase, the VSs impact at the distal wall or dislocate near-wall, releasing activated platelets that aggregate and/or adhere to the wall in zones of low WSS.

The multiphysics model for modeling thrombus formation and growth, proposed by Biasetti *et al.* (2012), confirms the concept of activation/convection/release/aggregation of platelet elements.

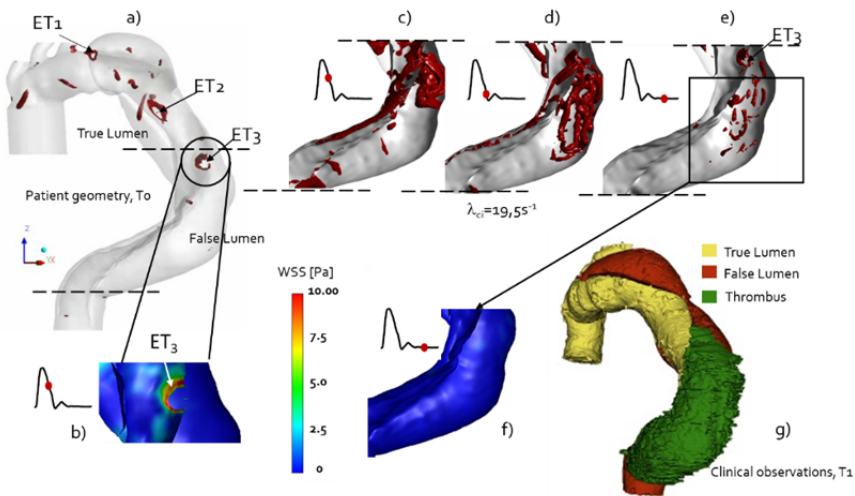


Figure 3.7. a) Geometry of a patient with type-A aortic dissection treated at T_0 by a prosthesis on the ascending-aorta segment and having residual type-B dissection. Three entry tears (ET_1) are present. b) WSS at the neck of ET_3 presenting values $>100 \text{ dyn/cm}^2$. c–e) Evolution of coherent structures in the false lumen. f) Low WSS values in coherent structure dislocation zones. g) Clinical findings 1 year after T_0 , showing thrombus formation in the false lumen. Adapted from Khannous *et al.* (2019). For a color version of this figure, see www.iste.co.uk/deplano/biological.zip

The works carried out by Khannous *et al.* (2019) within a residual type-B aortic dissection model enable this concept to be illustrated (Figure 3.7). In this unsteady 3D *in silico* model of a fluid with shear-thinning behavior, the criterion λ_{ci} is used as an identifier of coherent structures in a geometry of a patient at T_0 , presenting an unfavorable evolution one year later (T_1). Analysis performed at T_0 of the evolution of coherent structures in the false lumen and the spatiotemporal mapping of WSS shows that all of the ingredients are combined to initiate thrombus formation in the false lumen of the dissection. This result is confirmed by clinical observations made one year later at T_1 .

3.6. Conclusion and perspectives

In vitro and/or *in silico* models are implementing increasingly complex multi-physical models to closely approximate the pathophysiological reality of vascular pathologies. Thanks to advances in medical imaging, the focus in recent years is on *in vivo* validation and even inter-validation. Indeed, *in vivo* measurements validate *in vitro* and/or *in silico* modeling, but the accuracy of *in vivo* assessments of hemodynamic markers based on 4D flow MRI acquisitions, for example, must be validated by *in vitro* and/or *in silico* models. Thus, these non-invasive *in vivo* assessments at the patient's bed are of particular relevance as a diagnostic aid or in patient follow-up.

However, the understanding of the mechanisms for the initiation and development of vascular pathologies needs to be further improved. This is demonstrated by the controversies discussed in this chapter on the links between hemodynamic markers and pathologies. As such, multi-scale, growth and remodeling aspects must be included long term in the models developed. The recent technological advances in observations and measurements at the microscopic scale are enabling an ever greater understanding of the multi-scale aspect, and consequently, models are better equipped to take into account mechanisms at the cellular or indeed molecular scale. The mechanical-biological and biochemical mechanisms of arterial wall growth and remodeling are complex and their modeling remains only partial. Without being trite, the new possibilities linked to deep learning and processing by large databases will no doubt enable analysis of the correlations made between pathologies and hemodynamic indexes (or any other markers) on a large number of patients, and deduce associations that are useful to patient care.

3.7. References

- Ab Naim, W.N., Ganesan, P.B., Sun, Z., Liew, Y.M., Qian, Y., Lee, C.J., Jansen, S., Hashim, S.A., Lim, E. (2016). Prediction of thrombus formation using vortical structures presentation in Stanford type B aortic dissection: A preliminary study using CFD approach. *Appl. Math. Model.*, 40(4), 3115–3127.
- Alimohammadi, M., Pichardo-Almarza, C., Agu, O., Diaz-Zuccarini, V. (2016). Development of a patient-specific multi-scale model to understand atherosclerosis and calcification locations: Comparison with in vivo data in an aortic dissection. *Front. Physiol.*, 7, 238.
- Anidjar, S., Dobrin, P.B., Eichorst, M., Graham G.P., Chejfec, G. (1992). Correlation of inflammatory infiltrate with the enlargement of experimental aortic aneurysms. *J. Vasc. Surg.*, 16(2), 139–147.
- Arzani, A. and Shadden, S.C. (2012a). Flow topology in patient-specific abdominal aortic aneurysms during rest and exercise. *APS Division of Fluid Dynamics Meeting Abstracts, APS Meeting Abstracts*, G16.001.
- Arzani, A. and Shadden, S.C. (2012b). Characteristics of the transport topology in patient-specific abdominal aortic aneurysm models. *Phys. Fluids*, 24, 081901.
- Barakat, A.I. (2013). Blood flow and arterial endothelial dysfunction: Mechanisms and implications. *C.R. Physiques*, 14, 479–496.
- Bark, D.L., Para, A.N., Ku, D.N. (2012). Correlation of thrombosis growth rate to pathological wall shear rate during platelet accumulation. *Biotechnol. Bioeng.*, 109, 2642–2650.
- Barker, A.J., Lanning, C., Shandas, R. (2010). Quantification of hemodynamic wall shear stress in patients with bicuspid aortic valve using phase-contrast MRI. *Ann. Biomed. Eng.*, 38(3), 788–800.
- Basciano, C., Kleinstreuer, C., Hyun, S., Finol, E.A. (2011). A relation between near-wall particle-hemodynamics and onset of thrombus formation in abdominal aortic aneurysms. *Ann. Biomed. Eng.*, 39(7), 2010–2026.
- Biasetti, J., Hussain, F., Gasser, T.C. (2011). Blood flow and coherent vortices in the normal and aneurysmatic aortas: A fluid dynamical approach to intraluminal thrombus formation. *J. R. Soc. Interface*, 8, 1449–1461.
- Blackshear, P.L., Forstrom, R.J., Lorberbaum, M., Gott, V.L., Sovilj, R. (1971). A role of flow separation and recirculation in thrombi formation on prosthetic surfaces. *AIAA 9th Aerospace Meeting Paper*, 71–103.

- Boiron, O., Deplano, V., Pelissier, R. (2007). Experimental and numerical studies on the starting effect on the secondary flow in a bend. *J. Fluid Mech.*, 574, 109–129.
- Boussel, B., Rayz, V., McCulloch, C., Martin, A., Acevedo-Bolton, G., Lawton, M., Higashida, R., Smith, W.S., Young, W.L., Saloner, D. (2008). Aneurysm growth occurs at region of low wall shear stress. *Interface*, 39, 2997–3002.
- Boyd, A.J., Kuhn, D.C.S., Lozowy, R.J., Kulbisky, G.P. (2016). Low wall shear stress predominates at sites of abdominal aortic aneurysm rupture. *J. Vasc. Surg.*, 63(6), 1613–1619.
- Buchanan J.R., Kleinstreuer C., Truskey G., Lei M. (1999). Relation between non-uniform hemodynamics and sites of altered permeability and lesion growth at the rabbit aorto-celiac junction. *Atherosclerosis*, 143, 27–40.
- Bürk, J., Blanke, P., Stankovic, Z., Barker, A., Russe, M., Geiger, J., Frydrychowicz, A., Langer, M., Markl, M. (2012). Evaluation of 3D blood flow patterns and wall shear stress in the normal and dilated thoracic aorta using flow-sensitive 4D CMR. *J. Cardiovasc. Magn. Reson.*, 14, 84.
- Caro, C.G., Fitz-Gerald, J.M., Schroter, R.C. (1971). Atheroma and arterial wall shear – Observation, correlation and proposal of a shear dependent mass transfer mechanism for atherogenesis. *Proc. Roy. Soc. Land. B*, 177, 109–133.
- Casa, L.D.C., Deaton, D.H., Ku, K.N. (2005). Role of high shear rate in thrombosis. *J. Vasc. Surg.*, 61(4), 1068–1080.
- Castro, M.A., Putman, C.M., Sheridan, M.J., Cebal, J.R. (2009). Hemodynamic patterns of anterior communicating artery aneurysms: A possible association with rupture. *Am. J. Neuroradiol.*, 30(2), 297–302.
- Chakraborty, P., Balachandar, S., Adrian, R.J. (2005). On the relationships between local vortex identification schemes. *J. Fluid Mech.*, 535, 189214.
- Chen, D., Müller-Eschner, M., Kotelis, D., Böckler, D., Ventikos, Y., von Tengg-Kobligk, H. (2013). A longitudinal study of type-B aortic dissection and endovascular repair scenarios: Computational analysis. *Med. Eng. Phys.*, 35, 320–330.
- Cheng, K.C. and Mok, S.Y. (1986). Flow visualization studies on secondary flow patterns and centrifugal instability phenomena in curved tubes. *Fluid Control and Measurement*, 2, 765–773.
- Cheng, C., Tempel, D., Haperen, R., Baan, A., Grosveld, F., Daemen, M., Krams, R., Crom, R. (2006). Atherosclerotic lesion size and vulnerability are determined by patterns of fluid shear stress. *Circ.*, 113, 2744–2753.

- Cheng, Z., Riga, C., Chan, J., Hamady, M., Wood, N.B., Cheshire, N.J., Xu, Y., Gibbs, R.G.J. (2013). Initial findings and potential applicability of computational simulation of the aorta in acute type B dissection. *J. Vasc. Surg.*, 57, 35–43.
- Cheng, Z., Wood, N.B., Gibbs, R.G., Xu, X.Y. (2015). Geometric and flow features of type B aortic dissection: Initial findings and comparison of medically treated and stented cases. *Ann. Biomed. Eng.*, 43(1), 177–189.
- Chong, M.S., Perry, A.E., Cantwel, B.J. (1990). A general classification of three-dimensional flow fields. *Phys. Fluid. A*, 2, 765–777.
- Dasi, L.P., Simon, H.A., Sucusky, P., Yoganathan, A.P. (2009). Fluid mechanics of artificial heart valves. *Clin. Exp. Pharmacol. P.*, 36, 225–237.
- Dean, W.R. (1928). The streamline motion of fluid in a curved pipe. *Phil. Mag.*, 7, 673–695.
- Dennis, S.C.R. and Ng, M. (1982). Dual solutions for steady laminar flow through a curved tube. *Quart. J. Mech. Appl. Math.*, 35, 305–324.
- DePaola, N., Gimbrone M.A., Davies, P.F., Dewey C.F. (1992). Vascular endothelium responds to fluid shear stress gradients. *Arterioscler. Thromb.*, 12, 1254–1257.
- Deplano, V. and Siouffi, M. (1999). Experimental and numerical study of pulsatile flows through stenosis: Wall shear stress analysis. *J. Biomech.*, 32, 1081–1090.
- Deplano, V., Knapp, Y., Bertrand, E., Gaillard, E. (2007). Flow behaviour in an asymmetric compliant experimental model for abdominal aortic aneurysm. *J. Biomech.*, 40(11), 2406–2413.
- Deplano, V., Knapp, Y., Bailly, L., Bertrand, E., (2014). Flow of a blood analogue fluid in a compliant abdominal aortic aneurysm model: Experimental modelling. *J. Biomech.*, 47(6), 1262–1269.
- Deplano, V., Guivier-Curien, C., Bertrand, E. (2016). 3D analysis of vortical structures in an abdominal aortic aneurysm by stereoscopic PIV. *Exp. Fluids*, 57, 167.
- Di Achille P., Tellides, G., Figueroa, C.A., Humphrey J.D. (2014). A haemodynamic predictor of intraluminal thrombus formation in abdominal aortic aneurysms. *Proc. R. Soc. A.*, 470, 20140163.
- Ding, Z., Wang, K., Li, J., Cong, X. (2001). Flow field and oscillatory shear stress in a tuning-fork-shaped model of the average human carotid bifurcation. *J. Biomech.*, 34(12), 1555–1562.

- Dolan, J.M., Meng, H., Singh, S., Paluch, R., Kolega, J. (2011). High fluid shear stress and spatial shear stress gradients affect endothelial proliferation, survival, and alignment. *Ann. Biomed. Eng.*, 39, 1620–1631.
- Doyle, B.J. and Norman, P.E. (2016). Computational biomechanics in thoracic aortic dissection: Today's approaches and tomorrow's opportunities. *Ann. Biomed. Eng.*, 44, 71–83.
- Ene-Iordache, B. and Remuzzi, A. (2012). Disturbed flow in radial-cephalic arteriovenous fistulae for haemodialysis: Low and oscillating shear stress locates the sites of stenosis. *Nephrol. Dial. Transpl.*, 27(1), 358–368.
- Fedak, P.W.M., De Sa, M.P.L., Verma, S., Nili, N., Kazemian, P., Butany, J., Strauss, B.H., Weisel, R.D., David, T.E. (2003). Vascular matrix remodeling in patients with bicuspid aortic valve malformations: Implications for aortic dilatation. *J. Thorac. Cardiovasc. Surg.*, 126(3), 797–805.
- Fry, D.L. (1968). Acute vascular endothelial changes associated with increased blood velocity gradients. *Circ. Research*, 22, 165–197.
- Fung, Y.C. (1996). *Biomechanics: Circulation*, 2nd edition. Springer-Verlag, New York.
- Gimbrone Jr., M.A. and Topper, J.N. (1998). Biology of the vessel wall: Endothelium. In *Molecular Basis of Heart Diseases*, Chien, K.R. (ed). Harcourt Brace, Troy, MO.
- Grigioni, M., Daniele, C., Morbiducci, U., Del Gaudio, C., D'Avenio, G., Balducci, A., Barbaro, V. (2005). A mathematical description of blood spiral flow in vessels: Application to a numerical study of flow in arterial bending. *J. Biomech.*, 38(7), 1375–1386.
- Guivier, C., Deplano, V., Bertrand, E. (2009). Validation of a numerical 3-D fluid–structure interaction model for a prosthetic valve based on experimental PIV measurements. *Med. Eng. Phys.*, 31, 986–993.
- Guzzardi, D.G., Barker, A.J., van Ooij, P., Malaisrie, S.C., Puthumana, J.J., Belke, D.D., Mewhort, H.E.M., Svystonyuk, D.A., Kang, S., Verma, S., Collins, J., Carr, J., Bonow, R.O., Markl, M., Thomas, J.D., McCarthy, P.M., Fedak, P.W.M. (2015). Valve-related hemodynamics mediate human bicuspid aortopathy. *J. Am. Coll. Cardiol.*, 66(8), 892–900.
- Haidekker, M.A., White, C.R., Frangos, J.A. (2001). Analysis of temporal shear stress gradients during the onset phase of flow over a backward-facing step. *J. Biomech Eng.*, 123, 455–463.

- Haller, G. (2015). Lagrangian coherent structures. *Annu. Rev. Fluid Mech.*, 47(1), 137–162.
- Hasenkam, J.M., Giersiepen, M., Reul, H., (1988). Three-dimensional visualization of velocity fields downstream of six mechanical aortic valves in a pulsatile flow model. *J. Biomech.*, 21, 647–661.
- Hermann, R.A., Malinauskas, R.A., Truskey, G.A. (1994). Characterization of sites with elevated LDL permeability at intercostal, celiac, and iliac branches of the normal rabbit aorta. *Arterioscler. Thromb.*, 14, 313–323.
- Himburg, H.A., Grybowski, D.M., Hazel, A.L., LaMarck, J.A., Li, X.M., Friedman, M.H. (2004). Spatial comparison between wall shear stress measures and porcine arterial endothelial permeability. *Am. J. Phys. – Heart Circ. Phys.*, 286, 1916–1922.
- Hope, M.D., Hope, T.A., Crook, S.E., Ordovas, K.G., Urbania, T.H., Alley, M.T., Higgins, C.B. (2011). 4D flow CMR in assessment of valve-related ascending aortic disease. *JACC Cardiovasc. Imaging*, 4, 781–787.
- Hunt, J.C.R., Wray, A.A., Moin, P. (1988). Eddies, stream, and convergence zones in turbulent flows. *Center for Turbulence Research Report*. CTR-S88, 193–208.
- Jeong, J., Hussain, F., Schoppa, W., Kim, J. (1997). Coherent structures near the wall in a turbulent channel flow. *J. Fluid Mech.*, 332, 185–214.
- Joly, F., Soulez, G., Garcia, D., Lessard, S., Kauffmann, C. (2018). Flow stagnation volume and abdominal aortic aneurysm growth: Insights from patient-specific computational flow dynamics of Lagrangian-coherent structures. *Comput. Biol. Med.*, 92, 98–109.
- Karino, T. and Goldsmith, H.L. (1977). Flow behaviour of blood cells and rigid spheres in an annular vortex. *Phil. Trans. R. Soc. Lond. B*. 279, 413–445.
- Karmonik, C., Müller-Eschner, M., Partovi, S., Geisbüsch, P., Ganten, M.-K., Bismuth, J., Davies, M.G., Böckler, D., Loebe, M., Lumsden, A.B., von Tengg-Kobligk, H. (2013). Computational fluid dynamics investigation of chronic aortic dissection hemodynamics versus normal aorta. *Vasc. Endovasc. Surg.*, 47(8), 625–631.
- Khannous, F., Gaudry, M., Guivier-Curien, C., Piquet, P., Deplano, V. (2019). How can flow dynamics predict clinical evolution of residual type B aortic dissection? *Comput. Meth. Biomech. Biomed. Eng.*, 22(1), S99–S101.
- Kilner, P.J., Yang, G.Z., Mohiaddin, R.H., Firmin, D.N., Longmore, D.B. (1993). Helical and retrograde secondary flow patterns in the aortic arch studied by three-directional magnetic resonance velocity mapping. *Circ.*, 88, 2235–2247.

- Kim, G.B., Hojin, H., Kweon, J., Lee, S.J., Kim Y., Yang, D.H., Kim, N. (2016). Post-stenotic plug-like jet with a vortex ring demonstrated by 4D flow MRI. *Magn. Reson. Imaging*, 34, 371–375.
- Ku, D.N., Giddens, D.P., Zarins, C.K., Glagov, S. (1985). Pulsatile flow and atherosclerosis in the human carotid bifurcation. Positive correlation between plaque location and low oscillating shear stress. *Arteriosclerosis*, 5, 293–302.
- Lei, M., Kleinstreuer, C., Truskey, G.A. (1996). A focal stress gradient-dependent mass transfer mechanism for atherogenesis in branching arteries. *Med. Eng. Phys.*, 18(4), 326–332.
- Lyne, W.H. (1971). Unsteady viscous flow in a curved pipe. *J. Fluid Mech.*, 45, 13.
- Mahadvia, R., Barker, A.J., Schnell, S., Entezari, P., Kansal, P., Fedak, P.W.M., Malaisrie, C., McCarthy, P., Collins, J., Carr, J., Marki, M. (2014). Bicuspid aortic cusp fusion morphology alters aortic three-dimensional outflow patterns, wall shear stress, and expression of aortopathy. *Circ.*, 129(6), 673–682.
- Malek, A.M., Alper, S.L., Izumo, S. (1999). Hemodynamic shear stress and its role in atherosclerosis. *JAMA*, 282(21), 2035–2042.
- Masliyad, J.H. (1980). On laminar flow in curved semicircular ducts. *J. Fluids Mech.*, 99(3), 469–479.
- McDonald, D.A. (1952). The velocity of blood flow in the rabbit aorta studied with high-speed cinematography. *J. Physiol.*, 118, 328–339.
- Meierhofer, C., Schneider, E.P., Lyko, C., Hutter, A., Martinoff, S., Markl, M., Hager, A., Hess, J., Stern, H., Fratz, S. (2013). Wall shear stress and flow patterns in the ascending aorta in patients with bicuspid aortic valves differ significantly from tricuspid aortic valves: A prospective study. *Eur. Heart J. – Cardiovasc. Imag.*, 14(8), 797–804.
- Meng, H., Tutino, V.M., Xiang, J., Siddiqui, A. (2014). High WSS or low WSS? Complex interactions of hemodynamics with intracranial aneurysm initiation, growth, and rupture: Toward a unifying hypothesis. *Am. J. Neuroradiol.*, 35(7), 1254–1262.
- Menichini, C. and Xu, X.Y. (2016). Mathematical modeling of thrombus formation in idealized models of aortic dissection: Initial findings and potential applications. *J. Math. Biol.*, 73, 1205–1226.
- Menichini, C., Cheng, Z., Gibbs, R.G.J., Xu, X.Y. (2016). Predicting false lumen thrombosis in patient-specific models of aortic dissection. *J. R. Soc. Interface*, 13, 20160759.

- Moake, J.L., Turner, N.A., Statopoulos, N.A., Nolasco, L., Hellums, J.D. (1988). Shear-induced platelet aggregation can be mediated by vWF released from platelets, as well as by exogenous large or unusually large vWF multimers, requires adenosine diphosphate and is resistant to aspirin. *Blood*, 71(5), 1366–1374.
- Moore, J.E., Xu, C., Glagovb, S., Zarinsc, C.K., Ku, D.N. (1994). Fluid wall shear stress measurements in a model of the human abdominal aorta: Oscillatory behavior and relationship to atherosclerosis. *Atherosclerosis*, 10(2), 225–240.
- Morbiducci, U., Ponzini, R., Rizzo, G., Cadioli, M., Esposito, A., De Cobelli, F., Del Maschio, A., Montevecchi, F.M., Redaelli, A. (2009). In vivo quantification of helical blood flow in human aorta by time-resolved three-dimensional cine phase contrast magnetic resonance imaging. *Ann. Biomed. Eng.*, 37(3), 516–531.
- Morbiducci, U., Ponzini, R., Rizzo, G., Cadioli, M., Esposito, A., Montevecchi, F.M., Redaelli, A. (2011). Mechanistic insight into the physiological relevance of helical blood flow in the human aorta: An in vivo study. *Biomech. Model. Mechanobiol.*, 10, 339–355.
- Morbiducci, U., Gallo, D., Cristofanelli, S., Ponzini, R., Deriu, M.A., Rizzo, G., Steinman, D.A. (2015). A rational approach to defining principal axes of multidirectional wall shear stress in realistic vascular geometries, with application to the study of the influence of helical flow on wall shear stress directionality in aorta. *J. Biomech.*, 48(6), 899–906.
- Novaro, G.M., Mishra, M., Griffin, B.P. (2003). Incidence and echocardiographic features of congenital unicuspid aortic valve in an adult population. *J. Heart Valve Dis.*, 12, 674–678.
- Oh, J.K., Seward, J.B., Tajik, A.J. (1999). Valvular heart disease. In *The Echo Manual*, 2nd edition. Lippincott Williams & Wilkins, Philadelphia.
- O'Rourke, M.J., McCullough, J.P., Kelly, S. (2012). An investigation of the relationship between hemodynamics and thrombus deposition within patient-specific models of abdominal aortic aneurysm. *Proceedings of the Institution of Mechanical Engineers, Part H: J. Eng. Med.*, 226(7), 548–564.
- Pedley, T. (1980). *The Fluid Mechanics of Large Blood Vessels*. Cambridge University Press, Cambridge.
- Peiffer, V., Sherwin, S.J., Weinberg, P.D. (2013a). Computation in the rabbit aorta of a new metric – the transverse wall shear stress – to quantify the multidirectional character of disturbed blood flow. *J. Biomech.*, 46(15), 2651–2658.

- Peiffer, V., Sherwin, S.J., Weinberg, P.D. (2013b). Does low and oscillatory wall shear stress correlate spatially with early atherosclerosis? A systematic review. *Cardiovasc. Res.*, 99(2), 242–250.
- Rinaudo, A. and Pasta, S. (2014). Regional variation of wall shear stress in ascending thoracic aortic aneurysms. *Proceedings of the Institution of Mechanical Engineers, Part H: J. Eng. Med.*, 228(6), 627–638.
- Rodríguez-Palomares, J.F., Dux-Santoy, L., Guala, A., Kale, R., Maldonado, G., Teixidó-Turà, G., Galian, L., Huguet, M., Valente, F., Gutiérrez, L., González-Alujas, T., Johnson, K.M., Wieben, O., García-Dorado, D., Evangelista, A. (2018). Aortic flow patterns and wall shear stress maps by 4D-flow cardiovascular magnetic resonance in the assessment of aortic dilatation in bicuspid aortic valve disease. *J. Cardiovasc. Magn. R.*, 20, 28.
- Ross, K.A., Pyrak-Nolte, L.J., Campanella, O.H. (2004). The use of ultrasound and shear oscillatory tests to characterize the effect of mixing time on the rheological properties of dough. *Food Res. Int.*, 37(6), 567–577.
- Ruggeri, Z.M., Orje, J.N., Habermann, R., Federici, A.B., Reininger, A.J. (2006). Activation-independent platelet adhesion and aggregation under elevated shear stress. *Blood*, 108(6), 1903–1910.
- Savage, B., Saldívar, E., Ruggeri, Z.M. (1996). Initiation of platelet adhesion by arrest onto fibrinogen or translocation on Von Willebrand factor. *Cell*, 84(2), 289–297.
- Shadden, S.C. and Taylor, C.A. (2008). Characterization of coherent structures in the cardiovascular system. *Ann Biomed Eng.*, 36(7), 1152–1162.
- Shang, E.K., Nathan, D.P., Fairman, R.M., Bavaria, J.E., Gorman, R.C., Gorman, J.H., Jackson, B.M. (2015). Use of computational fluid dynamics studies in predicting aneurysmal degeneration of acute type B aortic dissections. *J. Vasc. Surg.*, 62(2), 279–284.
- Shi, X., Yang, J., Huang, J., Long, Z., Ruan, Z., Xiao, B., Xi, X. (2016). Effects of different shear rates on the attachment and detachment of platelet thrombi. *Mol. Med. Rep.*, 13, 2447–2456.
- Shimogonya, Y., Ishikawa, T., Imai, Y., Matsuki, N., Yamaguchi, T. (2009). Can temporal fluctuation in spatial wall shear stress gradient initiate a cerebral aneurysm? A proposed novel hemodynamic index, the gradient oscillatory number (GON). *J. Biomech.*, 42(11), 550–554.
- Sho, E., Sho M., Singh, T.M., Nanjo, H., Komatsu, M., Xu, C., Masuda, H., Zarins, C.K. (2002). Arterial enlargement in response to high flow requires early expression of matrix metalloproteinases to degrade extracellular matrix. *Exp. Mol. Pathol.*, 73(2), 142–153.

- Siouffi, M. (1988). Analyse des effets instationnaires sur les caractéristiques de l'écoulement en aval d'un rétrécissement local de section. PhD Thesis, University of Aix-Marseille II.
- Siouffi, M., Deplano, V., Pélissier, R. (1998). Experimental analysis of unsteady flows through a stenosis. *J. Biomech.*, 31, 11–19.
- Soulis, J.V., Giannoglou, G.D., Chatzizisis, Y.S., Farmakis, T.M., Giannakoulas, G.A., Parcharidis, G.E., Louridas, G.E. (2006). Spatial and phasic oscillation of non-Newtonian wall shear stress in human left coronary artery bifurcation: An insight to atherogenesis. *Coronary Artery Dis.*, 17(4), 351–358.
- Steinman, D.A., Thomas, J.B., Ladak, H.M., Milner, J.S., Rutt, B.K., Spence, J.D. (2002). Reconstruction of carotid bifurcation hemodynamics and wall thickness using computational fluid dynamics and MRI. *Magn. Reson. Med.*, 47, 149–159.
- Sudo, K., Sumida, M., Yamane, R. (1992). Secondary motion of fully developed oscillatory flow in a curved pipe. *J. Fluid Mech.*, 237, 189–208.
- Tadros, T.M., Klein, M.D., Shapira, O.M. (2009). Ascending aortic dilatation associated with bicuspid aortic valve. *Circ.*, 119(6), 880–890.
- Tarbell, J.M., Shi, Z.D., Dunn, J., Jo, H. (2014). Fluid mechanics, arterial disease, and gene expression. *Ann. Rev. Fluid Mech.*, 46(1), 591–614.
- Thim, T., Hagensen, M.K., Hørlyck, A., Kim, W.Y., Niemann, A.K., Thrysøe, S.A., Drouet, L., Paaske, W.P., Bøtker, H.E., Falk, E. (2012). Wall shear stress and local plaque development in stenosed carotid arteries of hypercholesterolemic minipigs. *J. Cardiovasc. Dis. Res.*, 3(2), 76–83.
- Wang, C., Baker, B.M., Chen, C.S., Schwartz, M.A. (2013). Endothelial cell sensing of flow direction. *Arterioscler. Thromb. Vasc. Biol.*, 33, 2130–2136.
- Wellings, P.J. and Ku, D.N. (2012). Mechanisms of platelet capture under very high shear. *Cardiovasc. Eng. Tech.*, 3, 161–170.
- White, C.R., Haidekker, M., Bao X., Frangos, J.A. (2001). Temporal gradients in shear, but not spatial gradients stimulate endothelial cell proliferation. *Circ.*, 103, 2508–2513.
- Yoganathan, A.P., Woo, Y.R., Sung, H.W. (1986). Turbulent shear stress measurements in the vicinity of aortic heart valve prostheses. *J. Biomech.*, 19, 433–442.
- Zhao, R., Kameneva, M.V., Antaki, J.F. (2007). Investigation of platelet margination phenomena at elevated shear stress. *Biorheology*, 44, 161–177.

- Zhou, J., Adrian, R.J., Balachandar, S., Kendall, T.M. (1999). Mechanisms for generating coherent packets of hairpin vortices in channel flow. *J. Fluid Mech.*, 387, 353–396.
- Zhou, G., Zhu, Y., Yin, Y., Su, M., Li, M. (2017). Association of wall shear stress with intracranial aneurysm rupture: Systematic review and meta-analysis. *Sci. Rep.*, 7, 5331.
- Zhu, C., Seo, J.H., Mitta, R. (2018). Computational modelling and analysis of haemodynamics in a simple model of aortic stenosis. *J. Fluid Mech.*, 851, 23–49.

4

Role of Arterial Blood Flow in Atherosclerosis

Guillermo VILAPLANA and Abdul I. BARAKAT

Ecole Polytechnique, Palaiseau, France

The pathological complications of atherosclerosis, namely heart attacks and strokes, remain the leading cause of mortality and morbidity worldwide. Atherosclerosis is a disease of medium and large arteries, and it involves the accumulation of lipids, lipoproteins, and blood cells within the arterial wall. These deposits ultimately develop into plaques that can either directly obstruct blood flow or rupture to induce very rapid occlusive thrombosis. A key feature of early atherosclerosis is that it is a focal disease, with lesions developing preferentially near branches and bifurcations where arterial blood flow is highly disturbed. However, despite nearly five decades of study, the nature of the flow disturbance that best correlates with atherosclerotic lesions remains a matter of controversy. In this chapter, we review what we know about the role of fluid mechanical factors in the development of atherosclerosis. Furthermore, to concretely illustrate the complexity of arterial flow fields, we provide a specific example of a computational study of fluid mechanical interactions between two adjacent arterial branches. We conclude with a short section that describes the limitations of current studies and evokes strategies for future investigations.

4.1. Introduction

Atherosclerosis is the arterial disease whose pathological complications, namely heart attacks and strokes, are the leading cause of mortality

Biological Flow in Large Vessels,

coordinated by Valérie DEPLANO, José-Maria FULLANA, Claude VERDIER. © ISTE Ltd 2022.

Biological Flow in Large Vessels: Dialog Between Numerical Modeling and In Vitro/In Vivo Experiments,
First Edition. Valérie Deplano; José-Maria Fullana and Claude Verdier.

© ISTE Ltd 2022. Published by ISTE Ltd and John Wiley & Sons, Inc.

worldwide. While the development of atherosclerosis involves a myriad of complex biochemical and biological events, fluid mechanical considerations associated with arterial blood flow also play a central part. This chapter focuses on these biophysical considerations.

This chapter is divided into two distinct parts. The first part (section 4.2) provides a rapid review of the initiation and development of atherosclerosis, before focusing on what we know about the role of arterial flow in the genesis and progression of the disease. The second part of the chapter (section 4.3) presents new results on a specific question in biofluid mechanics, namely how fluid dynamic interactions between two adjacent arterial branches affect the structure of the flow field. These results are based on three-dimensional, time-dependent computational fluid dynamics (CFD) simulations, and are intended as an illustrative example of the complexity of arterial flow field and the exquisite sensitivity of the flow field to what may appear as small changes in arterial geometry. The implications of the results to atherosclerosis also are discussed.

4.2. Role of arterial fluid mechanics in atherosclerosis

4.2.1. Atherosclerosis initiation and progression

Atherosclerosis develops exclusively in medium and large arteries with particular prevalence in the coronary arteries, the carotid arteries, the aorta and parts of the cerebral arterial network. The disease can also develop in peripheral arteries where it is commonly referred to as “peripheral artery disease”.

Why atherosclerosis develops in arteries but not in veins remains poorly understood. As illustrated in Figure 4.1, there are several important differences between arteries and veins. First, the blood pressure in arteries is significantly higher than that in veins, with a mean arterial pressure of ~ 100 mm Hg and a mean venous pressure of 10–20 mm Hg. Second, arteries transport oxygen-rich blood, whereas veins carry oxygen-poor blood. Third, veins contain valves that prevent backflow during diastole, a feature that is absent in arteries. Finally, arterial walls are significantly thicker and more muscular than those of veins of comparable size. It is unknown if one or more of these differences underlies the different predisposition of the two vessel types to atherosclerosis. Interestingly, when a venous section is implanted in an arterial setting, which occurs, for instance, during coronary

bypass surgery, the venous section undergoes progressive remodeling, assumes an arterial phenotype and becomes predisposed to atherosclerotic disease development.

As detailed elsewhere (Tedgui and Mallat 2001; Libby 2002; Libby *et al.* 2011) and illustrated in Figure 4.2, the development of atherosclerosis is a complex multi-step process that typically lasts decades and involves many different players in both the bloodstream and the arterial wall. It is widely accepted today that atherosclerosis is triggered by chronic inflammation of the vascular endothelium, the cellular monolayer that lines the inner surfaces of all blood vessels. This inflammation may be initiated by a variety of factors including oxidized low-density lipoprotein in the bloodstream, viral and/or bacterial infection, smoking and ionized radiation. In addition, and of particular relevance here, endothelial inflammation can also be induced by disturbances in arterial blood flow, as will be described in more detail below.

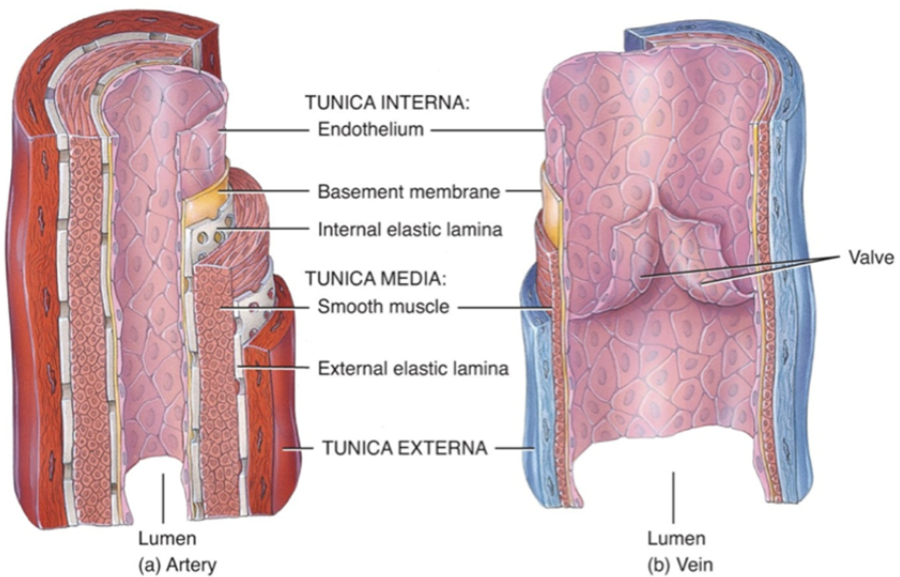


Figure 4.1. Differences in structure between arteries and veins (see: www.haikudeck.com/cardiovascular-system-science-and-technology-presentation-4AkIbF7Dtff#slide8). For a color version of this figure, see www.iste.co.uk/deplano/biological.zip

Under normal physiological conditions, the vascular endothelium serves a number of critical functions, as follows: (1) regulation of vascular

permeability to both small and large molecules, (2) vasoregulation, that is, control of arterial diameter through the release of vasoactive agents that exert their effect on smooth muscle cells within the arterial wall, (3) provision of a non-thrombogenic surface and (4) maintenance of a contractile smooth muscle cell phenotype. In the context of atherosclerosis, the permeability regulation function of the endothelium is particularly critical because it prevents excessive transport of blood-borne macromolecules into the arterial wall. A normally functioning endothelium has tight cell–cell junctions that are able to effectively exclude macromolecules larger albumin (Stokes–Einstein hydrodynamic radius of ~ 4 nm) from entering the arterial wall through the non-specific intercellular pathway.

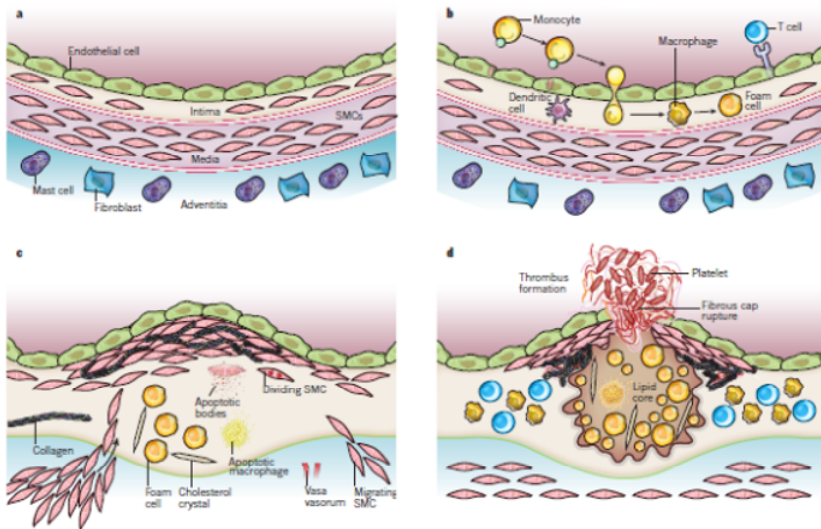


Figure 4.2. Progressive development of atherosclerotic lesions. a) A normal artery consists of three distinct layers: the tunica intima, which is lined by a monolayer of endothelial cells (in green); the tunica media, which contains a high concentration of smooth muscle cells, and the adventitia, which has important structural functions. b) Atherosclerosis is triggered by chronic inflammation of the endothelium, leading to the recruitment and transmigration of monocytes that eventually differentiate into foam cells. c) Lesion development involves the migration of smooth muscle cells from the media into the intima and the increased production of extracellular matrix, most notably collagen. d) The largest risk is plaque rupture that disrupts the endothelial layer and can cause rapid obstructive thrombosis. Reproduced with permission from Libby et al. (2011). For a color version of this figure, see www.iste.co.uk/deplano/biological.zip

When arterial endothelial cells (ECs) become chronically inflamed, which occurs during atherogenesis, their permeability regulation function becomes compromised because inflammation leads to the loosening of cell–cell junctions. As a result, there is a greatly enhanced influx of blood-derived macromolecules, most notably low-density lipoproteins, into the arterial wall. If the extent of macromolecular influx into the arterial wall overwhelms the ability of the wall to eliminate these macromolecules through metabolic and/or efflux pathways, then there is net accumulation of these macromolecules within the arterial wall, which contributes to the development of fatty streaks that constitute the early form of atherosclerotic lesions.

A chronically inflamed endothelium also triggers an immune response facilitated by the increased expression on the EC surface of adhesion molecules, such as intercellular adhesion molecule-1 (ICAM-1) and vascular cell adhesion molecule-1 (VCAM-1). Consequently, leukocytes, most notably monocytes, adhere to the arterial wall, transmigrate across the endothelium and become trapped in the subendothelial space where they transform into macrophages, and upon excessive uptake of lipids, ultimately differentiate into lipid-laden foam cells that form a central component of the nascent atherosclerotic lesion.

Concomitant with the events described above, smooth muscle cells and collagen fibers are recruited to the intimal layer of the arterial wall where they serve to thicken and structurally stabilize the atherosclerotic plaque. While certain plaques remain relatively soft, others become calcified over time and thus develop much higher rigidity. The greatest pathological risk arises from a plaque rupture which, when it occurs, leads to very rapid thrombosis that can cause a myocardial infarction if it occurs in a coronary artery, or a stroke if it occurs in a cerebral artery.

4.2.2. Role of arterial flow in atherosclerosis

The primary reason for implicating arterial fluid mechanics in the development of atherosclerosis is that the disease in its early stages is highly focal in nature. It has long been known that early atherosclerotic lesions do not develop randomly within the arterial system. Rather, they localize preferentially near branches and bifurcations where blood flow patterns are highly disturbed due to the complex arterial geometry at those locations.

A key question is what type of flow disturbance actually correlates with atherosclerotic lesions. This question has been the subject of numerous investigations over the past four decades. However, despite the fact that a plethora of studies have focused on this issue, the answer remains unclear. Most of the investigations focus on wall shear stress as the most relevant parameter because it is thought that ECs are more sensitive to changes in shear stress than they are to changes in other flow-derived forces, including pressure and stretch.

The earliest investigations suggested that atherosclerotic lesions develop in arterial regions where the wall shear stress is particularly high (Fry 1968) because it was thought that high shear stress would induce endothelial damage and thus promote lesion development. This concept has, however, fallen out of favor for two reasons: (1) detailed histological studies demonstrated that the endothelium remains intact (i.e. not damaged) during early atherosclerosis and (2) the wall shear stresses required to induce endothelial damage *in vivo* (>35 Pa) are much higher than values encountered physiologically. Instead, subsequent work has suggested that atherosclerosis correlates best with areas of low wall shear stress (below ~0.5 Pa) (Caro *et al.* 1969, 1971), which would occur in zones of boundary layer separation and flow recirculation that are commonly observed at arterial branches and bifurcations. The physical argument here was that regions of low wall shear stress would lead to a longer residence time for blood-borne macromolecules, such as low-density lipoproteins near the arterial wall, which would increase the probability of their uptake and accumulation.

The low shear hypothesis was subsequently expanded to include temporal oscillations in shear when it was realized that in the presence of pulsatile flow, the flow recirculation zones periodically grow and shrink, thereby subjecting underlying ECs to oscillations in blood flow (Ku *et al.* 1985). Although this remains the most widely accepted fluid dynamic atherosclerosis correlate today, several recent studies have raised questions about its universal validity. For instance, more recent studies on rabbits have indicated that atherosclerotic lesions are more likely to correlate with regions of high shear stress than low shear stress (Peiffer *et al.* 2012). Other studies have implicated gradients of shear stress, both spatial and temporal, as the likely culprits (DePaola *et al.* 1992; White *et al.* 2005).

In summary, despite four decades of detailed experimental and computational studies, there is no consensus today as to whether a single fluid mechanical parameter correlates with atherosclerotic lesions. This rather confusing picture is attributable at least in part to the following

reasons: (1) the difficulty of making accurate measurements of wall shear stress *in vivo*, (2) the fact that the data in the literature are derived from different species that exhibit significant differences in the topography of atherosclerotic lesions and (3) the sensitivity of arterial flow fields to inter-individual variations in arterial geometry.

To illustrate this last point about how seemingly small changes in arterial geometry have a significant impact on the flow field, the following section focuses on CFD simulations of fluid mechanical interactions between two arterial branches.

4.3. An illustrative example of the complexity of arterial flow fields: fluid dynamic interactions between two arterial branches

4.3.1. The specific problem addressed

As already mentioned, during the past few decades, a large body of work has been devoted to elucidating the link between arterial blood flow and the localized genesis of atherosclerosis (Karino and Goldsmith 1979; Ku *et al.* 1985; Karino *et al.* 1990; Barakat *et al.* 1992, 1997; Cheer *et al.* 1998; Friedman and Giddens 2005). While the low and oscillating wall shear stress hypothesis is very commonly cited (Ku *et al.* 1985; Wentzel *et al.* 2005; Chien 2008), other hemodynamic parameters such as spatial gradients of wall shear stress (DePaola *et al.* 1992) and spatial angular gradients of wall shear stress have also been related to the focal nature of the early disease (Buchanan *et al.* 1999, 2003).

The complex wall shear stress patterns affecting the endothelium are a consequence of important flow disturbances occurring in regions of arterial curvature or around branches. These disturbances can take the form of periodically appearing and disappearing boundary layer separation areas, intense flow recirculation zones, and extensive secondary flow structures that develop and evolve during the course of the cardiac cycle. Despite an extensive body of work devoted to advanced statistical cross-correlations of hemodynamic parameters to precise lesion locations (Buchanan *et al.* 1999, 2003), a deep understanding of the precise dependence of arterial flow fields on various geometric, mechanical and fluid mechanical parameters is lacking. This is important in view of changes in these parameters for different species, individuals, ages and activity levels (Barakat *et al.* 1997; O'Flynn *et al.* 2010; Al-Musawi *et al.* 2004).

Steady flow in single T-junctions has been widely studied in glass models (Karino and Goldsmith 1979), *ex vivo* geometries (Karino *et al.* 1990; Barakat *et al.* 1997) and numerical simulations (Cheer *et al.* 1998; Buchanan *et al.* 1999). Separation zones have been consistently found laterally to the ostium for large ranges of Reynolds numbers, flow rate ratios and geometries (Karino *et al.* 1990; Cheer *et al.* 1998). It has also been shown that these recirculating zones are filled with particular streamlines that loop along the lateral walls of mother vessels before entering the branch (Karino and Goldsmith 1979; Karino *et al.* 1990; Barakat *et al.* 1997). These looping streamlines and the subsequent disturbed reversal flow are potentially very important in early atherosclerotic development.

The present study aims to understand how these disturbances around T-junctions are affected when two branches are in close interaction, such as the aorto-celiac and superior-mesenteric junctions. The variability of the separation between these branches among species and individuals has motivated our interest in the dependence on this particular parameter.

4.3.2. Materials and methods

Laminar three-dimensional blood flow was simulated in two successive T-junctions. Geometry and boundary conditions (whose details are provided below) were chosen to model a generic rabbit abdominal aorta with celiac and superior mesenteric branches. Since the main goal of the study is to show a general result concerning two interacting junctions, it was not necessary to capture the geometrical details that are particular to every animal, and a very simplified geometry was therefore considered. Both steady and unsteady simulations were conducted: the steady flow simulations were used to identify the consequences of the interaction of two branches, while the pulsatile flow simulations allowed us to show the implications of the observed phenomena under pulsatile flow.

4.3.2.1. Geometry and mesh

The geometry and mesh used are presented in Figure 4.3, where the flow comes from left to right. The different arteries are rigid straight tubes and the dimensions are inspired by rabbit measurements (Barakat *et al.* 1997): the aortic diameter is $D_a = 4$ mm, and each of the two branches has a diameter that is half that of the aorta. The separation distance L between the two branches is a parameter of our study and was varied from 1.5 to 13 aortic diameters, $5D_a$ being considered as the reference case since it is roughly

close to a mean value for rabbit abdominal aortic branches. The variation of L is large but is motivated by the fact that in other species and particularly in humans, this distance is very different from that in rabbits. To reproduce experimental observations (Karino and Goldsmith 1979; Barakat *et al.* 1997), the proximal lip of each orifice was gently rounded while the distal orifice was made more sharp. No taper effects were considered.

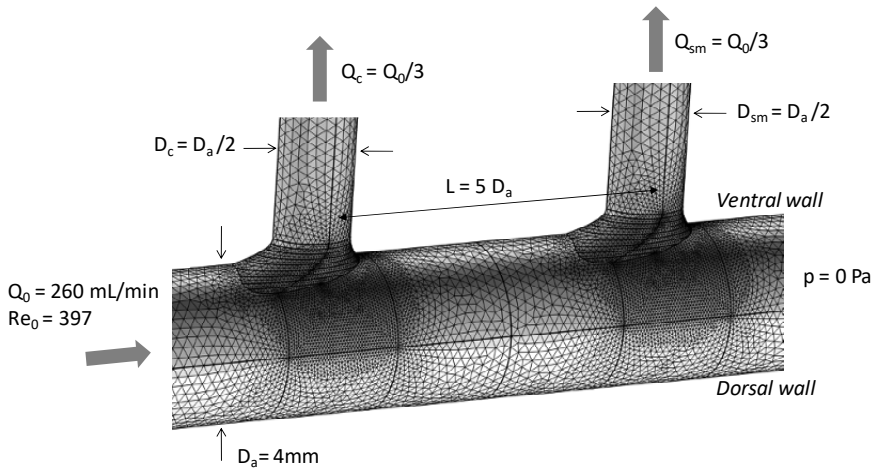


Figure 4.3. Geometry, mesh and boundary conditions used in the simulations. Note that the separation distance L between branches and the Reynolds number are parameters of the study; the base case is shown

We used a free tetrahedral mesh combined with a boundary layer mesh, and mesh independence was verified using the recommended procedure by the *Journal of Fluids Engineering* (2008): the mesh size used ensured a relative error in wall shear stress at the regions of interest not greater than 3%. For the base case (Figure 4.3), the consistency of the results was also verified for a mesh that was twice as fine. As noted by Praskash and Ethier (2001), mesh independence for spatial shear stress gradients was far more difficult to obtain, and no maps of wall shear stress gradients will be shown in this study.

4.3.2.2. Equations and solver

Blood was assumed to behave as a Newtonian fluid with a density $\rho = 1,055 \text{ kg/m}^3$ and a dynamic viscosity $\mu = 0.00348 \text{ Pa}\cdot\text{s}$. The full

three-dimensional incompressible Navier–Stokes equations in a rigid geometry were considered:

$$\nabla \cdot \vec{u} = 0 \text{ and } \rho \left[\frac{\partial \vec{u}}{\partial t} + (\vec{u} \cdot \nabla) \vec{u} \right] = -\nabla p + \mu \nabla^2 \vec{u}$$

where \vec{u} is the velocity vector and p is the pressure field. No-slip conditions were assumed at the walls, a Poiseuille velocity profile ($\vec{u}_0 = 8 \frac{Q_0}{D^2} (1 - \frac{r^2}{(D/2)^2})$) was assumed at the inlet and at the outlet of the two daughter arteries, and zero pressure was imposed at the aortic outlet. To avoid artificial interactions between the imposed velocity profiles and the computed flow around both junctions, tube extensions were added to extend the arteries. For the base case, the assumed inlet flow rate was $Q_0 = 260$ mL/min, as determined from experimental measurements (Barakat *et al.* 1997). The corresponding Reynolds number was $Re_0 = \frac{\rho_B U_0 D_a}{\mu_B} = 397$. For unsteady flow, a time-dependent profile (shown later) was imposed at the aortic inlet with a Womersley number $W_0 = \frac{D_a}{2} \sqrt{\frac{\omega \rho}{\mu}} = 5.3$. Flow rate ratios were fixed for the study and inspired by the same experimental data (Barakat *et al.* 1997): $Q_{\text{celiac}}/Q_0 = Q_{\text{superior mesenteric}}/Q_0 = 1/3$. The solver used was the commercial code COMSOL, and convergence was achieved when the momentum residual term was $\varepsilon < 10^{-4}$. All of the presented results are made non-dimensional using the aortic diameter $D_a = 4$ mm, the base-case mean inlet velocity $U_0 = 334.8$ mm/s and the corresponding upstream wall shear stress $\tau_0 = 20.1$ dyne/cm². We will denote $WSS = \frac{|\vec{\tau}|}{\tau_0}$ as the normalized wall shear stress.

4.3.3. Results

4.3.3.1. Steady flow

4.3.3.1.1. Effect of branch interactions on the flow structure

Steady results at $Re_0 = 397$ are first presented for different distances between branches. The flow rate ratios used are slightly above the geometrical ratio: $Q_c/Q_0 = 1/3 > (D_c/D_a)^2 = 1/4$ for the aorto-celiac junction and $Q_{\text{sm}}/(Q_0 - Q_c) = 1/2 > (D_{\text{sm}}/D_a)^2 = 1/4$ for the superior mesenteric branch.

As reported in a number of previous studies performed under largely similar conditions (Karino and Goldsmith 1979; Barakat *et al.* 1997; Cheer *et al.* 1998), a thin separation zone with reversal flow is observed in the aorta, lateral to the first branch. The zone is filled with streamlines coming from a middle lateral region of the aortic lumen, which are highly deflected toward the branch but not enough to enter it directly. They first impact the aortic ventral wall near the distal lip before looping back close to the side, they form the separation region (Figure 4.4, red and magenta streamlines), and then enter the branch with a complex movement. Although we can estimate that the maximum size of the observed loops around the first branch is around 75% of the aortic diameter, we will provide a more accurate estimate later of the size of the recirculation zone based on the structure of the wall shear stress streamlines.

Figure 4.4(a) shows the base case, where $L/D_a = 5$, which we compare to the situation of $L/D_a = 2.5$ in Figure 4.4(b). In both configurations, the structure of the flow around the first junction is quite similar. This, in fact, is the case for the entire range of L/D_a values explored (1.5–12). In contrast, the flow around the second branch is strongly influenced by the wake of the first branch. When the branches are close to one another with L/D_a in the range of 1.5–3 (see Figure 4.4(b)), the same looping streamlines are observed at both junctions. Interestingly, however, for $L/D_a > 3$ (see Figure 4.4(a)), the interaction is such that the looping streamlines at the second branch are abolished. This means that the typical recirculation zone lateral to the ostium that we described above is absent at the second junction due to the interaction of the two branches. Note that another type of streamlines that loop along the dorsal wall before entering the branch is present at the second junction (see Figure 4.4(a) in magenta), showing that a recirculation region exists opposite to the branch, but is positioned along the dorsal wall rather than along the lateral walls. As expected, when the spacing between the branches is increased further, the flow around the second junction begins to recover its natural form with looping streamlines along the lateral walls of both branches (not shown), indicating that the two branches have now become sufficiently far apart so as to behave as independent (non-interacting) branches. This occurs around $L/D_a = 5.2$, meaning, in conclusion, that there is a wide range of L/D_a values (from 3–5.2 in our configuration of Reynolds number Re_0 , flow rate ratios and geometry) where the interaction between the two branches radically changes the flow structure lateral to the second ostium.

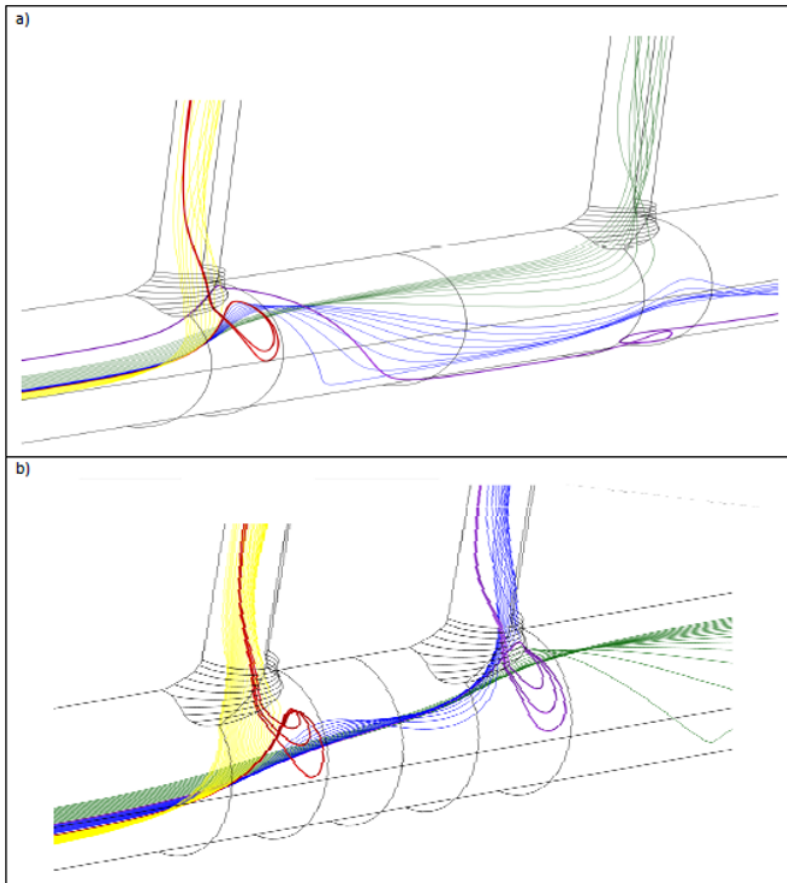


Figure 4.4. Steady flow streamlines. a) Base case with $L/Da = 5$. b) $L/Da = 2.5$. Note the difference in the localization of the looping streamlines (magenta) at the second branch between the two cases. For a color version of this figure, see www.iste.co.uk/deplano/biological.zip

4.3.3.1.2. Effect of branch interactions on wall shear stress

A separated flow zone with flow recirculation and reversing streamlines, as shown above, is also characterized by low wall shear stress and disturbed wall shear stress directions. Figure 4.5 depicts the wall shear stress patterns associated with different values of inter-branch spacing ($L/D_a = 5$, 2.5 and 1.5 for panels a, b, and c, respectively). The vectors show the direction of the

wall shear stress field, and the surface color maps correspond to the shear stress magnitude normalized by the baseline wall shear stress ($\tau_0 = 20.1 \text{ dyne/cm}^2$) (*WSS* hemodynamic parameter). Next to each color map is a depiction of the wall shear stress streamlines on a view of half of the aortic wall, with the aorta ventrally cut open and pinned flat so as to look up on the endothelial surface *en face*. Our primary interest here is the lateral region of the aorta close to both ostia, where we have observed the looping streamlines. Those regions are found to always correspond to a low wall shear stress zone very close to the ostium, at around one aortic diameter streamwise from the proximal lip. From there, this zone extends to the dorsal wall and in both directions downstream and upstream. This wall shear stress pattern is consistent with previous numerical results (Cheer *et al.* 1998; Buchanan *et al.* 1999).

Figure 4.5(a) shows the base case (see also Figure 4.3(a)), where the flow entering the second branch does not show any looping streamlines. Although they have similar wall shear stress values, the wall shear stress vectors around the first and second junctions are very different. As we can see from the wall shear stress streamlines in the insets, the structure of these fields are not topologically equivalent (Lighthill 1963; Ghil *et al.* 2001): the structure near the first ostium corresponds to a separated recirculation region, while near the second ostium the flow is laminar and stays streamwise. As defined in literature (Legendre 1956; Lighthill 1963; Déleroy 2001) and using the terminology of Legendre, the separated region is delimited by wall shear stress streamlines that merge in singular points. In this case, the singular points are two saddle points located opposite the branch, and we can therefore say that the separated region near the first ostium extends up to the dorsal wall. This situation was also observed experimentally by Karino and Goldsmith (1979), where looping flow streamlines extended to the dorsal wall. This regime was called the “fully disturbed regime”. On the contrary, in the immediate vicinity of the second ostium, the wall shear stress streamlines do not exhibit any separation, and they either enter the branch or simply proceed on to the downstream portion of the aorta. Note that another structure develops opposite to the second branch, corresponding to a separated region stacked to the dorsal wall (see also the magenta streamline in Figure 4.4(a)). This separated zone is typical in bifurcations and particularly in two-dimensional T-junctions, but the disturbance generated is positioned far from the regions where early atherosclerotic lesions localize; therefore, we will not focus on this structure.

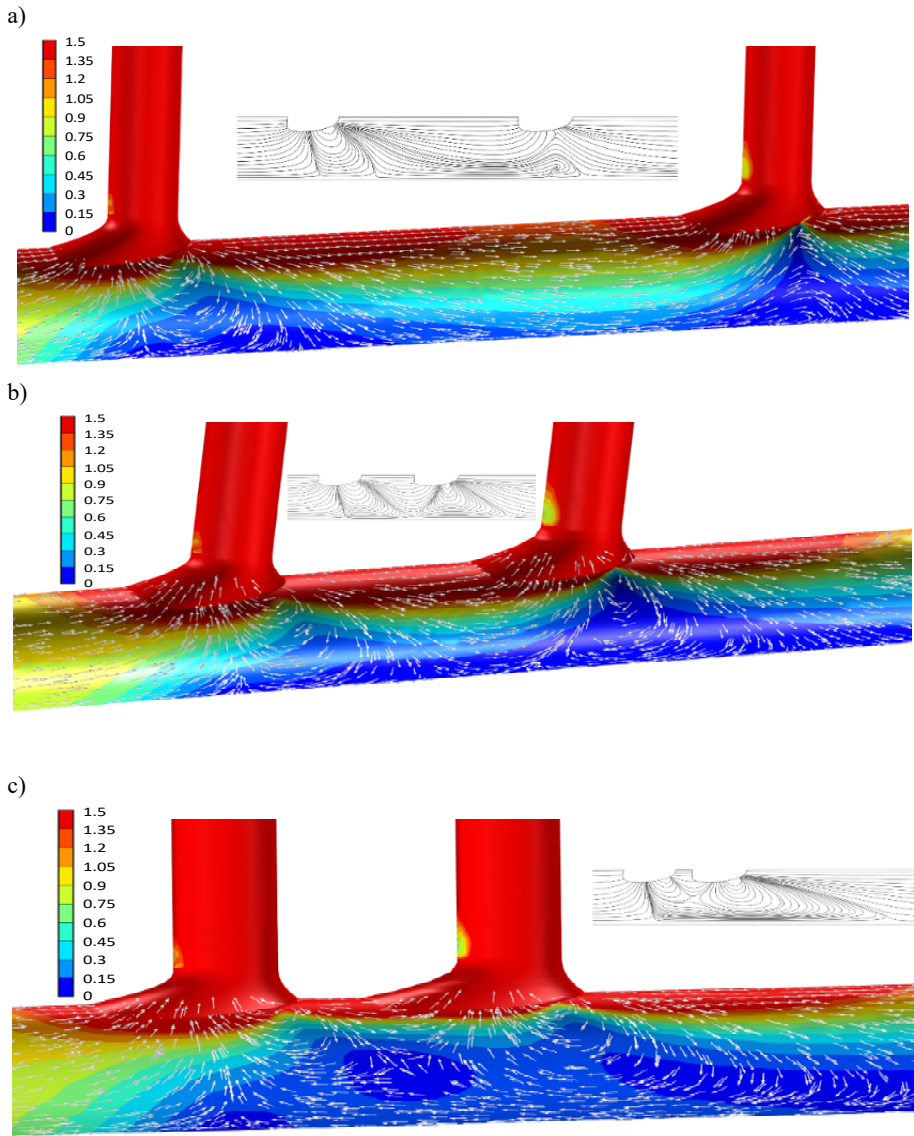


Figure 4.5. Comparison of wall shear stress for different inter-branch spacing at the baseline Reynolds number ($Re_0 = 400$). The arrows show the direction of the wall shear stress, while the color map denotes its magnitude. The inset next to each color map depicts the topology of the wall shear stress field. a) Base case $L/Da = 5$, b) $L/Da = 2.5$ and c) $L/Da = 1.5$. For a color version of this figure, see www.iste.co.uk/deplano/biological.zip

When the branches are closer to one another (see Figures 4.5(b) and (c)), the wall shear stress structure at the second bifurcation is radically different from the base case (see Figure 4.5(a)) and becomes topologically equivalent to the structure seen at the first branch. When the branches are close to one another, we thus have flow separation near both ostia and a so-called fully disturbed flow regime at both junctions. In the case where $L/D_a = 1.5$, the recirculating regions of both branches overlap, leading to a large disturbed flow zone. It must also be noted that the wall shear stress patterns for the first branch are fairly similar among all configurations; it is the pattern for the second branch that is altered from one configuration to another.

Immediately upstream and for a longer region downstream of each branch, the wall shear stress is elevated, and the spatial gradients of shear stress are equally high. This is consistent with other published studies (Cheer *et al.* 1998; Buchanan *et al.* 2003, 1999). A low wall shear stress zone corresponding to a possible separation is also observed along the proximal wall of the bifurcating artery. This observation is common in T-junctions, but there is paucity of experimental data on early atherosclerotic lesion development inside aortic branches; thus, we will not focus on this part of the junction.

4.3.3.1.3. Dependence on Reynolds number

Figure 4.6 presents the results for the base case geometry ($L/D_a = 5$) at different upstream Reynolds numbers ranging from $0.2 \cdot Re_0$ to $2 \cdot Re_0$ (corresponding to $Re = 80, 200, 400$ and 800 , respectively). In every image, we show streamlines of wall shear stress and a color map of the WSS parameter on a view of the aorta cut open and pinned flat. At low velocity (see Figure 4.6(a), $Re < 100$), no separation is observed, the flow is completely laminar and it enters both branches smoothly. Upon increasing the velocity to $Re_1 = 100 \pm 8$, a first bifurcation of the structure of the wall shear stress field occurs and leads to separation in both branches at the same time. For $Re \in [100; 384]$, the separated lateral region is similar in both branches, and there is reversed and disturbed flow lateral to both branches (see Figure 4.6(b)). At around $Re_2 = 384 \pm 8$, the looping wall shear stress pattern at the second junction shrinks at its middle, and a second bifurcation occurs. The flow entering the second branch is reorganized and no more separation is observed in the vicinity of the second ostium (see Figure 4.6(c)), corresponding to the base case Re_0 where no looping streamlines enter the

second branch). However, as mentioned earlier, a separated flow zone remains, at the dorsal wall, isolated from the second ostium. For $Re > 384$ and at least up to 800, the absence of looping streamlines at the second branch persists, and the wall shear stress structure is maintained (see Figure 4.6(d)). It should be noted that at high Reynolds number, we observe a small zone of low wall shear stress and even flow recirculation immediately distal to the second branch along the ventral wall (see Figure 4.6(d)). However, this is highly dependent on the shape of the distal lip. The WSS maps are similar in both branches and for the different Reynolds numbers, showing high WSS proximal and distal to each branch and low WSS lateral to the ostium. Therefore, the two bifurcations of the structure of the flow mentioned above do not have any influence on the WSS parameter; they only affect the directions of the shear stress vectors.

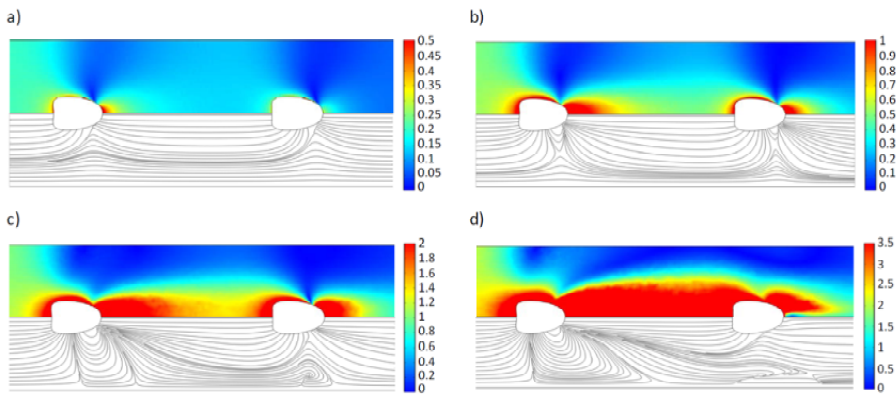


Figure 4.6. Effect of the inlet Reynolds number on the wall shear stress. In each panel, the top half (color map) represents the magnitude of the normalized wall shear stress (WSS; normalization is relative to $\tau_0 = 20.1 \text{ dyne/cm}^2$), while the bottom half shows wall shear stress streamlines. a) $Re = 80$, b) $Re = 200$, c) $Re = 400$ and d) $Re = 800$. For a color version of this figure, see www.iste.co.uk/deplano/biological.zip

The dependence of the flow field on Reynolds number was then studied for different spacings between the two branches (i.e. different L/D_a values). The two Reynolds number thresholds mentioned above are depicted in the phase diagram in Figure 4.7, which summarizes all of the observations made for steady flow. The lower part of the diagram corresponds to the fully

laminar regime, where no separation is observed (see the structure shown in Figure 4.6(a)). Note that the first bifurcation at $Re_1 \approx 100 \pm 20$ is independent of L , showing that the interaction between branches has little effect at a low Reynolds number. For the intermediate region, labeled the “disturbed flow region”, separation is observed lateral to both ostia (as shown in Figure 4.6(b)). The second threshold is also computed with the same precision (± 20) and limits the upper region where the flow entering the first branch remains disturbed and the flow around the second ostium becomes laminar again. Note that the convex shape of the Re_2 curve is consistent with the results mentioned above (and shown in Figure 4.5) for different L values at fixed Reynolds numbers.

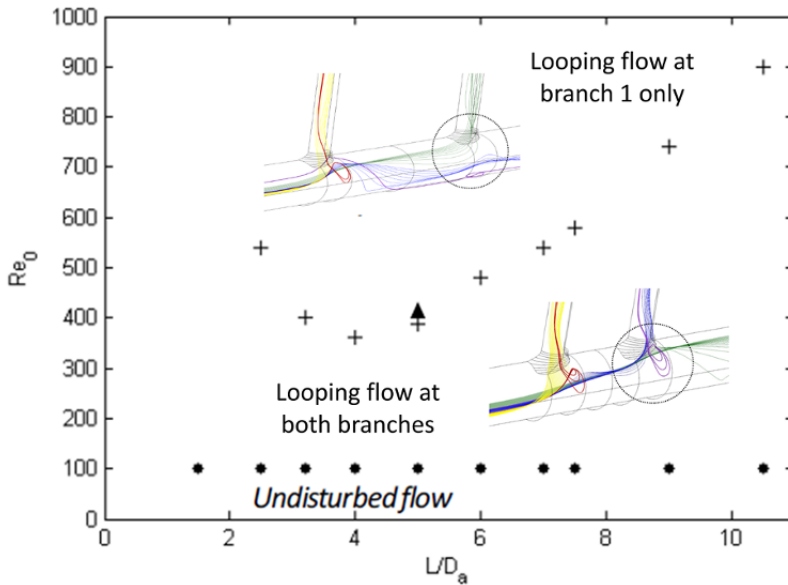


Figure 4.7. Phase diagram for the flow structure as a function of both the Reynolds number and the inter-branch spacing L/D_a . For a color version of this figure, see www.iste.co.uk/deplano/biological.zip

4.3.3.2. Pulsatile flow

4.3.3.2.1. Flow structure and wall shear stress

In the case of unsteady flow, a separated flow region shows highly oscillating wall shear stress due to the periodic growth and the motion of the

separated streamlines. Unsteady simulations were conducted using the pulse waveform shown in Figure 4.8 on the base case geometry with $L/D_a = 5$ (similar to that in Figures 4.3, 4.4(a), 4.5(a) and 4.6). The waveform is a sinusoid that oscillates between Reynolds numbers of 80 and 800 ($0.2Re_0$ and $2Re_0$), without retrograde flow, consistent with what would be expected in the rabbit abdominal aorta. Figure 4.9 illustrates color maps of the normalized wall shear stress WSS magnitude, with the vectors indicating the wall shear stress directions at the four different time points during the pulsatile cycle indicated in Figure 4.8 ($0.25T$, $0.5T$, $0.75T$ and T , where T is the period of the cycle).

The WSS color maps are fairly similar throughout the pulsatile cycle, showing the same characteristics as in the case of steady flow: broadly lower WSS values lateral to the branches and higher values proximal and distal to each ostium. During diastole at $t = 0.75T$, we observe that the dorsal wall maintains an elevated WSS, even though the WSS value upstream of the first branch is lower. This is due to the skewness of the velocity profile downstream of the first branch, as we will demonstrate below.

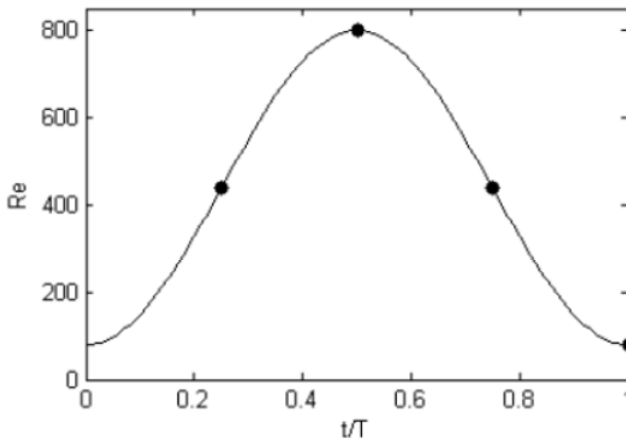


Figure 4.8. Non-reversing sinusoidal waveform used in the pulsatile flow simulations. The black dots correspond to the time points of $0.25T$, $0.5T$, $0.75T$, and T , where T is the pulse period, at which flow behavior is subsequently shown. The minimum and maximum Reynolds numbers are 80 and 800, respectively

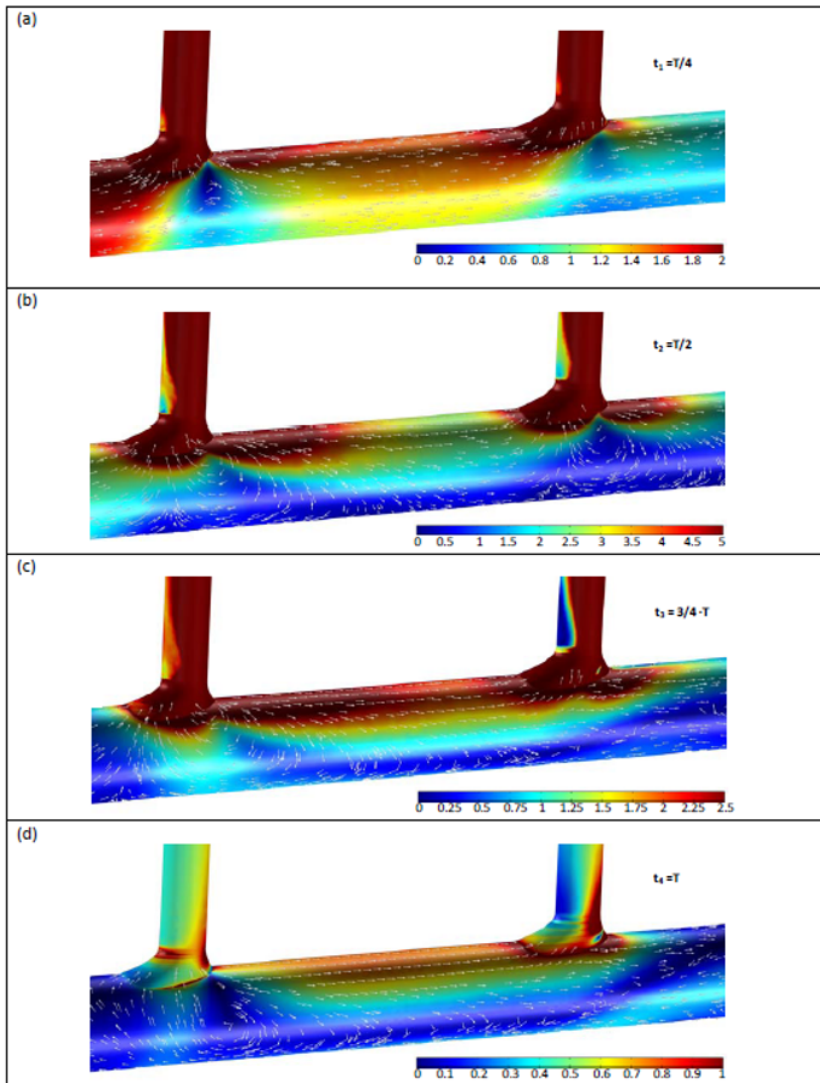


Figure 4.9. Wall shear stress variation during the pulsatile cycle at the four time points indicated by the black dots in Figure 4.8. The colors denote the magnitude of the normalized wall shear stress (WSS; normalization is relative to $\tau_0 = 20.1 \text{ dyne/cm}^2$), while the vectors depict the direction of the wall shear stress. a) T , b) $0.75T$, c) $0.5T$, and d) $0.25T$, where T is the pulse period. For a color version of this figure, see www.iste.co.uk/deplano/biological.zip

In the instantaneous snapshots in Figure 4.9, we also recognize the different wall shear stress structures described in the steady flow case (see Figure 4.7). At $0.25T$, no separation is observed, and the flow enters smoothly into the branches. Flow separation occurs lateral to both ostia later in the cycle as seen at $t = 0.5T$, and the last structure is observed at $t = 0.75T$ where the flow loops before entering the first branch, but no separation and no looping is observed in the vicinity of the second ostium. At the end of the cycle, complex structures remain, but very low WSS values are registered. During the cycle, the flow undergoes similar bifurcations to the ones described in the steady flow simulations, but the successive critical Reynolds numbers are modified due to the accelerating and decelerating inertia terms. Note that the second bifurcation leading to the structure observed at $t = 0.75T$, where no looping is found at the second ostium, occurs even during diastole at a lower Reynolds number. As already mentioned in other studies (Cheer *et al.* 1998; Buchanan *et al.* 2003, 1999), a deceleration in inertia leads to an amplification of secondary flows and therefore also leads to the second structural bifurcation observed here. Also note that the structures observed in unsteady flow around the dorsal wall are more complex than the ones observed in the steady flow simulations.

In the region lateral and near the ostium where early atherosclerotic lesions have been reported, this succession of separated and non-separated flow structures that we have observed has a very important consequence under pulsatile flow. Around the first ostium, the wall shear stress is streamwise during approximately half of the cycle (t_1) and reversed during the other half (t_2 and t_3). Around the second ostium, however, the wall shear stress is streamwise during part of the cycle (t_1), and reverses similar to the first ostium (t_2), but then reverts back to being streamwise (t_3). Therefore, the wall shear stress lateral to the second ostium oscillates more strongly than at the first ostium.

4.3.3.2.2. Hemodynamic indices

We wish to explore if there are hemodynamic indices that are capable of capturing the differences between the two branches in flow structure and directional oscillations along the lateral walls, as described above. A hemodynamic index encountered in the literature is the time-averaged wall shear stress. Figure 4.10(a) depicts a map of the time-averaged WSS:

$\langle WSS \rangle = \frac{1}{T} \int_0^T \frac{|\vec{\tau}|}{\tau_0} dt$ on half of the aortic wall, with the aorta cut open and pinned flat. As can be clearly seen, this index shows largely similar results for both ostia, with low WSS at the sides of the junctions and elevated WSS proximal and distal to each ostium. The one exception is the already mentioned small zone immediately downstream of the second branch. It is clear from these results that this index fails to capture the differences between the two ostia.

We then turned our attention to the commonly used oscillatory shear index (OSI), which is defined as: $OSI = \frac{1}{2} \left[1 - \frac{\left| \int_0^T \vec{\tau} dt \right|}{\int_0^T |\vec{\tau}| dt} \right]$ and which represents a time-averaged parameter that assesses the oscillatory character of the wall shear stress during a cycle. The OSI for this simulation is depicted in Figure 4.10(b) and shows a particularly oscillating region along the dorsal wall, which corresponds to the region where large structures develop during diastole. However, around both ostia, which are our zones of primary interest, not much oscillating shear stress is observed apart from a small zone lateral to the second ostium, where we have precisely found that the structure of the flow changes up to two times during the cycle.

Because the OSI appears incapable of fully capturing the steepness of the oscillations, we have considered another averaged hemodynamic parameter that uses the time derivative of the wall shear stress, which we call the “time derivative oscillating shear index” (DtOSI):

$$DtOSI = T \frac{\int_0^T \left| \frac{\partial \vec{\tau}}{\partial t} \right| dt}{\int_0^T |\vec{\tau}| dt}$$

Figure 4.10(c) depicts a map of this quantity, where we observe that a lateral region close to the second ostium undergoes steep oscillating shear stress, while the region near the first ostium is largely spared. A small region with high DtOSI is also noted immediately downstream of the second ostium, which corresponds to the small recirculating region observed in Figure 4.6(d). Again, the ventral wall is far less prone to steep oscillations than the dorsal wall.

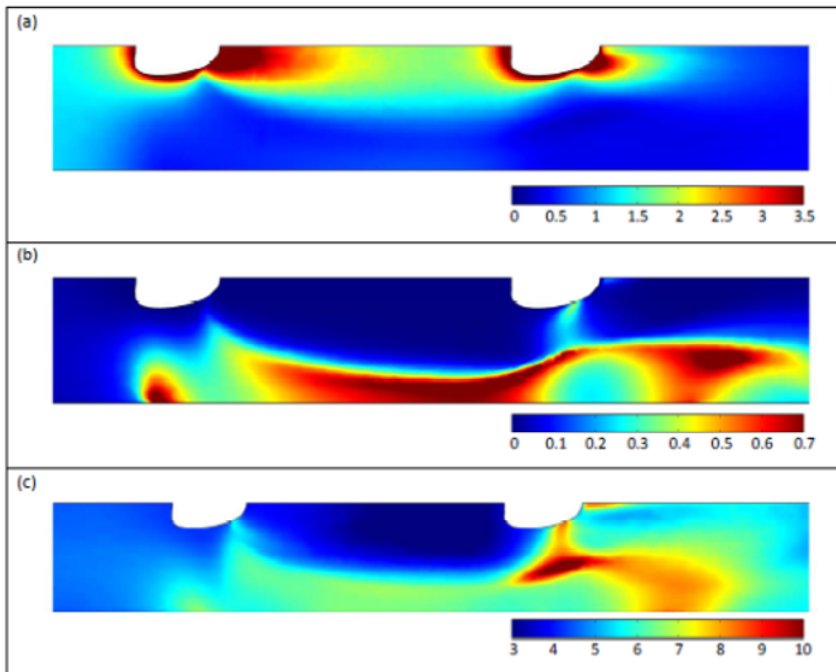


Figure 4.10. Hemodynamic shear indices. a) The time-averaged wall shear stress. b) The oscillatory shear index (OSI). c) The “time derivative oscillating shear index” (DtOSI). For a color version of this figure, see www.iste.co.uk/deplano/biological.zip

4.3.3.2.3. Wake of the first branch is a critical factor

As we have shown, when two T-junctions are placed successively, the flow and the wall shear stress around the second ostium are highly modified. It should be noted that the suppression of flow separation and looping streamlines found at the second junction is strictly a consequence of the interaction between the two branches, since an isolated second branch under the corresponding inlet conditions ($Re=2/3Re_0$ and $Q_s/Q_0 = 0.5$) gives the classical looping streamlines and an extended separation region. Thus, the wake of the first branch plays a key role in the new wall shear stress behavior that we have observed around the second ostium. This wake is described as a combination of a skewed velocity profile in the streamwise direction and induced secondary flows in the transverse plane. Here, the secondary flows are a pair of counter-rotating streamwise vortices, a consequence of the deflection of the flow toward the ventral wall when passing the first branch

(see Figure 4.11, base case under steady flow conditions). Note that the velocity profile is skewed toward the ventral wall and the streamwise rotation is from the ventral to the dorsal side near the wall and opposite to the midplane.

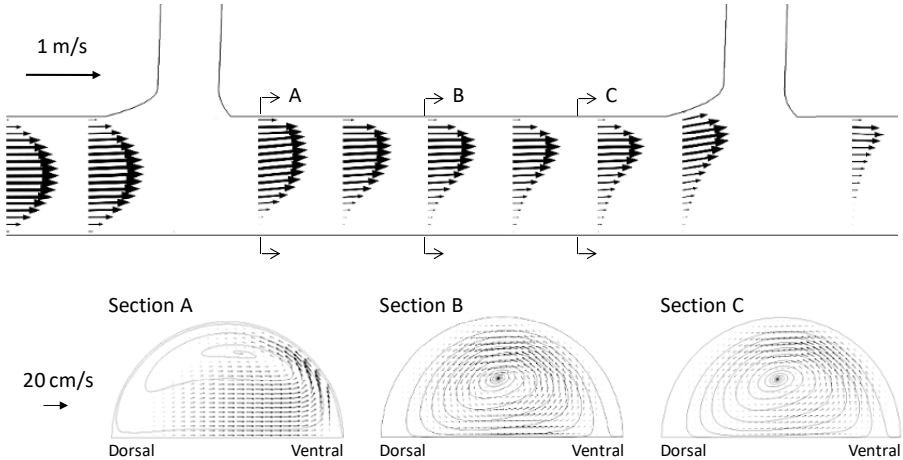
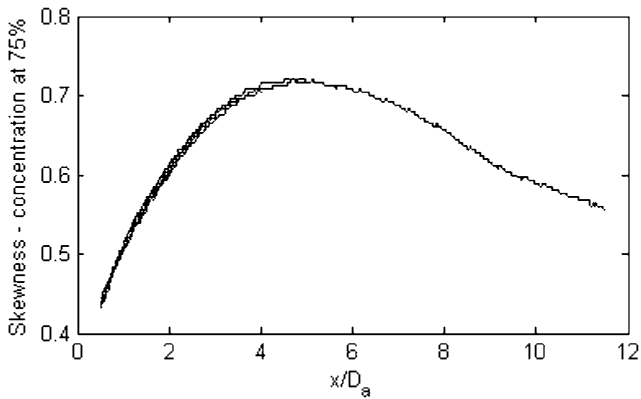


Figure 4.11. Top: velocity profile in the midplane of the geometry, demonstrating the skewness of the streamwise velocity profile downstream of the first branch toward the ventral wall. Bottom: Transverse plane velocity at three different locations between the two branches, demonstrating the presence of secondary flow patterns that take the form of two counter-rotating vortices. The simulations are for steady flow and the baseline conditions

In order to explore the spatial evolution of the skewness downstream of the first branch under steady flow conditions, we define a simple skewness index as a concentration of the flow around the peak: $\text{Skewness} = 1 - \frac{\Delta y}{D_a}$, where Δy is the size of the transverse segment where the velocity is above 75% of the peak velocity. This index ranges from 0 to 1, with larger values denoting increased profile skewness. The evolution of the skewness downstream of the first branch as a function of the streamwise distance from the first branch x/D_a is shown in Figure 4.12(a) for different inter-branch spacing L/D_a ranging from 2.5 to 12.5. Interestingly, almost no difference is found among the different L/D_a values, suggesting that the presence of the second branch does not have a significant effect on the skewness of the

velocity profile between the two branches. Also note that the skewness increases initially due to the nature of the secondary flows in the transverse plane (vortices bringing fluid to the ventral wall) and then decreases naturally due to viscous effects.

a)



b)

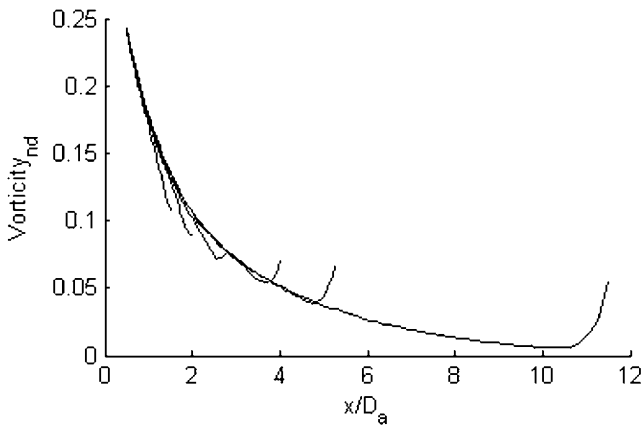


Figure 4.12. a) Assessment of the extent of velocity profile skewness as a function of the distance from the first branch. b) Non-dimensional vorticity as a function of the distance from the first branch. In both panels, multiple curves are shown corresponding to inter-branch spacing L/D_a ranging from 2.5 to 12.5. The simulations are for steady flow under the baseline conditions

A similar analysis can be conducted for the evolution of the secondary flow between the branches. Figure 4.12(b) shows the evolution of the non-dimensional vorticity as a function of x/D_a for inter-branch spacing L/D_a ranging from 2.5 to 12.5. To avoid the negative vorticity generated by the boundary layer near the wall, we simply integrate the positive values (Jeong and Hussain 1995), or more formally, the non-dimensional computed quantity is:

$$Vorticity_{nd}(x) = \frac{1}{D_a u_0} \iint_{\Sigma(x)} \max(\omega, 0) dS$$

where $\Sigma(x)$ is the transverse surface at the streamwise x coordinate and ω is the streamwise component of the vorticity. In Figure 4.12(b), it is important to note that each curve is stopped one D_a before the second branch. Therefore, we observe that the decrease in the vorticity is independent of the presence of a second branch until $1.5D_a$ above the center of the second branch.

The presence of a second branch does not appear to influence the wake of the first branch, which means that the flow around the second branch and in particular, the phenomenon of suppression of looping streamlines and flow separation along the lateral walls observed above, can only be studied in terms of a skewed and rotating inlet flow (streamwise and transverse disturbances). We thus isolated the second branch for the baseline case and artificially eliminated one of the two components – skewness or secondary flow – of the disturbed inlet at $1.5D_a$ upstream of the second branch. Interestingly, when only the skewness is included at the inlet of the second branch (see Figure 4.13(a)), the resulting wall shear stress structure is very different from the natural situation (see Figure 4.5(a)), and a large flow separation region is observed. The same occurs when only the secondary flows are included at the inlet with an unskewed (Poiseuille) streamwise velocity profile (see Figure 4.13(b)). These results show that both skewness and secondary flows are necessary to obtain the suppression of looping streamlines around the second ostium observed in Figure 4.5(a).

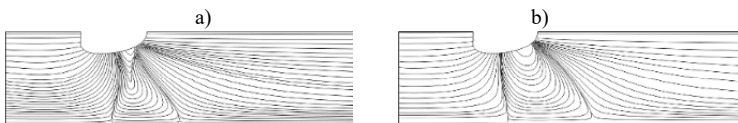


Figure 4.13. Wall shear stress streamlines for steady flow under the baseline conditions a) in the presence of velocity profile skewness, but without secondary flow and b) in the presence of secondary flow, but without velocity profile skewness

4.3.4. Discussion

In the present work, we have studied the flow patterns at two successive T-junctions by performing a series of computational simulations on a rigid model of generic abdominal aorta with model celiac and superior mesenteric arteries. Motivated by the differences observed among species, a major parameter of interest was the distance between the two branches. We specifically wished to understand how this distance influences the fluid dynamic interactions between the two branches.

For single isolated branches, a prominent feature of the flow field is the presence of separated flow and looping streamlines along the lateral wall of the aorta in the vicinity of the branch. In the case of a two-branch geometry, however, the results demonstrated that for a large range of both the Reynolds number and the spacing between the two branches, flow separation and looping streamlines do not develop in the vicinity of the second branch, while they do systematically in the vicinity of the first branch. The consequences for the WSS patterns were studied in terms of the structure of the wall shear stress field, and this has allowed us to identify the absence of separation around the second branch as a bifurcation of the structure of the flow field: as the Reynolds number grows, starting from zero, two structural bifurcations are obtained. The first one leads to separation around both ostia, and the second one leads to the relaminarization of the flow entering the second branch. The practical consequence of this is that although in steady flow the regions near both branches experience similar magnitudes of wall shear stress, the directions of the stresses near the ostia are opposite (reversed for the first branch and streamwise for the second).

For sinusoidal pulsatile flow, this change in wall shear stress direction has major consequences for the underlying endothelium in the vicinity of the ostia. Since the separation zone appears and disappears more rapidly at the second junction, ECs along the lateral walls of the second ostium undergo steeper oscillations throughout the cardiac cycle. This is well translated by a newly proposed averaged parameter, the DtOSI, defined to take into account the steepness of oscillations.

Some light has been shed on the reasons for this change in direction between the two branches; however, more work is needed for complete understanding. Our results have shown that the disturbed flow downstream of the first branch is virtually insensitive to the position of the second branch, which means that the relaminarization phenomenon can be studied in

terms of disturbed flow at the inlet of the second branch. We were able to demonstrate that both disturbances (skewness and secondary flow patterns) found downstream of the first branch are necessary for the relaminarization to occur. The same kind of observations are expected to be made around junctions placed just after curved sections of the aorta, since these flows are both skewed and possess significant secondary flow patterns.

The present simulations were conducted under highly simplified conditions including rigid arterial walls, a Newtonian fluid and idealized geometries that neglected minor curvature and vessel taper. Therefore, whether or not the flow structures observed here would also be seen in vivo remains to be established. High resolution in vivo flow imaging would help in this regard.

Finally, the potential implications of the results obtained here for endothelial dysfunction and the development of atherosclerosis remain to be elucidated. It is now well established that ECs are exquisitely responsive to fluid dynamic shear stress (Hahn and Schwartz 2009; Barakat 2013). The development of experimental systems that can reproduce the types of flow patterns observed here and the investigation of these flow patterns on EC structure and function would certainly merit future study.

4.4. Concluding remarks

This chapter is divided into two complementary sections. The first is a general review of the role of arterial fluid mechanics in the development of atherosclerosis. The second section provides an illustrative example of the complexity of arterial flow fields, even under highly simplified and idealized geometric and flow conditions.

The possible link between arterial fluid mechanics and atherogenesis was evoked over five decades ago. However, despite a very large number of theoretical, computational and experimental studies that have certainly greatly expanded our understanding of arterial flow fields, we still have not been able to establish definitively what type of flow corresponds to and correlates with the localization of atherosclerotic lesions. This lack of definitive conclusions is attributable to a number of considerations. One such consideration is the complexity of arterial flow fields and the difficulty of measuring wall shear stress in vivo, due to both resolution limitations and the movement of the arterial wall. Another complicating factor is that in

addition to studies on human subjects, different animal models are used in atherosclerosis research, including pigs, rabbits and mice, and the localization of lesions is different in all of these different species. Finally, in light of the fact that atherosclerosis is triggered by endothelial inflammation, as already described, linking fluid mechanics to atherosclerosis requires understanding of how disturbances in blood flow can induce endothelial dysfunction. This falls within the realm of the field of mechanobiology, a very active research field, where progress promises to ultimately unlock the secrets of fluid mechanical involvement in the development and progression of atherosclerosis.

4.5. References

- Al-Musawi, S.L., Bishton, J., Dean, J., Williams, S., Cremers, S.G., Weinberg, P.D. (2004). Evidence for a reversal with age in the pattern of near-wall blood flow around aortic branches. *Atherosclerosis*, 172, 79–84.
- Barakat, A.I. (2013). Blood flow and arterial endothelial dysfunction: Mechanisms and implications. *Comptes rendus physique*, 14, 479–496.
- Barakat, A.I., Uhthoff, P.A.F., Colton, C.K. (1992). Topographical mapping of sites of enhanced HRP permeability in the normal rabbit aorta. *Journal of Biomechanical Engineering*, 114, 283–292.
- Barakat, A.I., Karino, T., Colton, C.K. (1997). Microcinematographic studies of flow patterns in the excised rabbit aorta and its major branches. *Biorheology*, 34, 195–221.
- Buchanan Jr., J.R., Kleinstreuer, C., Truskey, G.A., Lei, M. (1999). Relation between non-uniform hemodynamics and sites of altered permeability and lesion growth at the rabbit aorto-celiac junction. *Atherosclerosis*, 143, 27–40.
- Buchanan Jr., J.R., Kleinstreuer, C., Hyun, S., Truskey, G.A. (2003). Hemodynamics simulation and identification of susceptible sites of atherosclerotic lesion formation in a model of abdominal aorta. *Journal of Biomechanics*, 36, 1185–1196.
- Caro, C.G., Fitz-Gerald, J.M., Schroter, R.C. (1969). Arterial wall shear and distribution of early atheroma in man. *Nature*, 223, 1159–1161.
- Caro, C.G., Fitz-Gerald, J.M., Schroter, R.C. (1971). Atheroma and arterial wall shear. Observation, correlation and proposal of a shear dependent mass transfer mechanism for atherogenesis. *Proceedings of the Royal Society of London B*, 177, 109–133.

- Cheer, A.Y., Dwyer, H.A., Barakat, A.I., Sy, E., Bice, M. (1998). Computational study of the effect of geometric and flow parameters on the steady flow field at the rabbit aorto-celiac bifurcation. *Biorheology*, 35, 415–435.
- Chien, S. (2008). Effects of disturbed flow on endothelial cells. *Annals of Biomedical Engineering*, 36, 554–562.
- Délery, J.M. (2001). Robert Legendre and Henri Werlé: Toward the elucidation of three-dimensional separation. *Annual Review of Fluid Mechanics*, 33, 129–154.
- DePaola, N., Gimbrone Jr., M.A., Davies, P.F., Dewey Jr., C.F. (1992). Vascular endothelium responds to fluid shear stress gradients. *Arteriosclerosis and Thrombosis*, 12, 1254–1257.
- Friedman, M.H. and Giddens, D.P. (2005). Blood flow in major blood vessels – Modeling and experiments. *Annals of Biomedical Engineering*, 33, 1710–1713.
- Fry, D.L. (1968). Acute vascular endothelial changes associated with increased blood velocity gradients. *Circulation Research*, 22, 165–197.
- Ghil, M., Ma, T., Wang, S. (2001). Structural bifurcation of 2-D incompressible flows. *Indiana University Mathematics Journal*, 50, 159–180.
- Hahn, C. and Schwartz, M.A. (2009). Mechanotransduction in vascular physiology and atherogenesis. *Nature Reviews Molecular Cell Biology*, 10, 53–62.
- Jeong, J. and Hussain, F. (1995). On the identification of a vortex. *Journal of Fluid Mechanics*, 285, 69–94.
- Karino, T. and Goldsmith, H.L. (1979). Particle flow behavior in models of branching vessels I: Vortices in 90° T-junctions. *Biorheology*, 16, 231–248.
- Karino, T., Motomiya, M., Goldsmith, H.L. (1990). Flow patterns at the major T-junctions of the dog descending aorta. *Journal of Biomechanics*, 23, 537–548.
- Ku, D.N., Giddens, D.P., Zarins, C.K., Glagov, S. (1985). Pulsatile flow and atherosclerosis in the human carotid bifurcation: Positive correlation between plaque location and low oscillating shear stress. *Arteriosclerosis*, 5, 293–302.
- Legendre, R. (1956). Séparation de l'écoulement laminaire tridimensionnel. *La recherche aéronautique*, 54, 3–8.
- Libby, P. (2002). Inflammation in atherosclerosis. *Nature*, 420, 868–874.
- Libby, P., Ridker, P.M., Hansson, G.K. (2011). Progress and challenges in translating the biology of atherosclerosis. *Nature*, 473, 317–325.
- Lighthill, M.J. (1963). Attachment and separation in three-dimensional flow. In *Laminar Boundary Layers*, volume 2.6, Rosenhead, L. (ed). Oxford University Press, Oxford.

- O'Flynn, P.M., O'Sullivan, G., Pandit, A.S. (2010). Geometric variability of the abdominal aorta and its major peripheral branches. *Annals of Biomedical Engineering*, 38, 824–840.
- Peiffer, V., Rowland, E.M., Cremers, S.G., Weinberg, P.D., Sherwin, S.J. (2012). Effect of aortic taper on patterns of blood flow and wall shear stress in rabbits: Association with age. *Atherosclerosis*, 223, 114–121.
- Prakash, S. and Ethier, C.R. (2001). Requirements for mesh resolution in 3D computational hemodynamics. *Journal of Biomechanical Engineering*, 123, 134–144.
- Tedgui, A. and Mallat, Z. (2001). Anti-inflammatory mechanisms in the vascular wall. *Circulation Research*, 88, 877–887.
- Wentzel, J.J., Corti, R., Fayad, Z.A., Wisdom, P., Macaluso, F., Winkelman, M.O., Fuster, V., Badimon, J.J. (2005). Does shear stress modulate both plaque progression and regression in the thoracic aorta? Human study using serial magnetic resonance imaging. *Journal of the American College of Cardiology*, 45, 846–854.
- White, C.R., Stevens, H.Y., Haidekker, M.A., Frangos, J.A. (2005). Temporal gradients in shear, but not spatial gradients, stimulate ERK1/2 activation in human endothelial cells. *American Journal of Physiology*, 289, H2350–H2355.

5

Patient-specific Hemodynamic Simulations: Model Parameterization from Clinical Data to Enable Intervention Planning

Irene E. VIGNON-CLEMENTEL¹ and Sanjay PANT²

¹Inria Saclay Ile-de-France Research Center, France

²Swansea University, Wales

5.1. Introduction

In normal systemic circulation, oxygenated blood flows out of the pumping heart (left ventricle), through an architecture of branching trees from larger to smaller conduits in the arterial network, to the micro-vasculature of each organ. Here, it exchanges oxygen to enable appropriate organ function, subsequently returning to the heart (right atrium) through the smaller to larger conduits of the venous network. A similar network architecture is present in pulmonary circulation where blood flows out of the heart (right ventricle) to the lungs for oxygenation, and goes back

For a color version of all the figures in this chapter, see www.iste.co.uk/deplano/biological.zip.

Biological Flow in Large Vessels,

coordinated by Valérie DEPLANO, José-Maria FULLANA, Claude VERDIER. © ISTE Ltd 2022.

Biological Flow in Large Vessels: Dialog Between Numerical Modeling and In Vitro/In Vivo Experiments,
First Edition. Valérie Deplano; José-Maria Fullana and Claude Verdier.

© ISTE Ltd 2022. Published by ISTE Ltd and John Wiley & Sons, Inc.

to the heart (left atrium). Blood thus moves essentially forward in a closed-loop system, due to pressure generated in the heart ventricles, in which the flow rate is distributed according to the different subsystems' need and resistance to flow, and with a velocity that decreases from larger to smaller vessels. In geometric multi-scale (or multi-domain) modeling, the larger vessels, that is, the region of interest where the pathophysiology exists or where an intervention is to be performed, are represented in full 3D forms (reconstructed from medical images) while the remaining circulation is represented by reduced order models, 1D or 0D lumped parameter models. This approach (Formaggia *et al.* 2009; Vignon-Clementel *et al.* 2010a, 2010b; Quarteroni *et al.* 2016). Blood flow in a 3D domain Ω is modeled by the Navier–Stokes equations (partial differential equations, PDE), as an incompressible and often Newtonian fluid, taking into account the interaction with the (visco)elastic vessel wall (fluid–solid interaction, FSI) or not (rigid walls). In the latter case,

$$\begin{cases} \rho \frac{\partial \mathbf{u}}{\partial t} + \rho (\mathbf{u} \cdot \nabla) \mathbf{u} - \operatorname{div} \boldsymbol{\sigma} = \mathbf{f} & \text{in } \Omega, \\ \operatorname{div} \mathbf{u} = 0 & \text{in } \Omega, \end{cases} \quad [5.1]$$

with

$$\boldsymbol{\sigma}(\mathbf{u}, p) = -p\mathbf{I} + 2\mu\mathbf{D}(\mathbf{u}) \quad \text{and} \quad \mathbf{D}(\mathbf{u}) = \frac{1}{2} \left(\nabla \mathbf{u} + \nabla \mathbf{u}^T \right) \quad [5.2]$$

where ρ and μ denote the density and dynamic viscosity, respectively, p and \mathbf{u} denote pressure and the velocity vector, respectively, \mathbf{f} represents the external body forces such as gravity, $\boldsymbol{\sigma}$ represents the stress tensor, \mathbf{I} is an identity matrix, and \mathbf{D} is the strain-rate tensor. A no-slip boundary condition is imposed on the surfaces Γ_{wall} representing the vessel walls. At inlet surface(s) Γ_{in} , a Dirichlet boundary condition is typically imposed through a measured mean flow rate and an assumed velocity profile (parabolic, Womersley, or plug) but multiscale or multi-domain coupling (Vignon-Clementel *et al.* 2006; Esmaily Moghadam *et al.* 2013; Quarteroni *et al.* 2016) can also be done there. At the outlet surface(s) Γ_{out} , a pressure boundary condition is typically imposed: for non-multiscale models, the pressure values are either measured or imposed, and for multiscale models, this pressure is derived from the coupled 1D or 0D models (hence enforcing a relationship between pressure at this outlet and the rest of the system, rather than fixing the pressure). The pressure boundary condition is usually imposed

as a Neumann boundary condition on the traction $\boldsymbol{\sigma} \cdot \mathbf{n}$ (where \mathbf{n} is the normal vector) defined through equation [5.2].

By integration of FSI models on the cross-section of each vessel under certain assumptions, one can obtain the 1D Euler equations (mass and momentum balance equations), which contain wave propagation phenomena:

$$\begin{cases} \frac{\partial A}{\partial t} + \frac{\partial(Av)}{\partial x} = 0, \\ \frac{\partial v}{\partial t} + v \frac{\partial v}{\partial x} + \frac{1}{\rho} \frac{\partial p}{\partial x} = \frac{f}{\rho A} + g \end{cases} \quad [5.3]$$

where A represents the cross-sectional area at a location x along a vessel centerline, v represents the average uniaxial velocity, f represents the friction force per unit length, which depends on the assumptions made on velocity profile and blood viscosity, and g denotes gravity along the longitudinal direction. Equation [5.3] is closed with a pressure–area relationship through the material properties of the vessel walls, which typically is:

$$p = p_{\text{ext}} + \beta \left(\sqrt{A} - \sqrt{A_0} \right) \quad [5.4]$$

where p_{ext} is the external pressure, A_0 is the area at zero transmural pressure, and β is a material parameter which depends on the Young's modulus, Poisson ratio and thickness of the vessel wall. Finally, an integration of the 1D equations along the x -direction results in a set of ordinary differential equations (lumped parameter models or 0D models). These 0D models are conveniently described as a combination of several electrical elements, connected in series or in parallel, to describe various segments of the circulation (pressure is considered analogous to electrical voltage and flow rate is considered analogous to electric current). The electrical analogy and the relationships between pressure and flow for the commonly used elements are described in Table 5.1.

0D models are often designed to represent heart subparts or circulatory subsystems with just a few components. These reduced models enable computational tractability (Shi *et al.* 2011). For patient-specific predictions, multiscale models require tuning of the model parameters (typically the 0D part of the model) to individual patients. To this end, clinical measurements/data are required, and parameters are estimated such that the model reproduces the clinical data within the bounds of measurement errors

and model fidelities. This chapter presents some strategies on how such parameter estimation may be performed given the type of clinical data available and the importance of the 3D part. Note that such strategies can also be used in multiscale ventilation simulations, such as air flows in the lung through the trachea connected to the airway branching tree and terminal regions (Oakes *et al.* 2015).

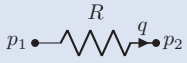
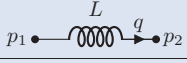
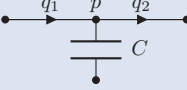
Phenomenon	Electrical analogy	Component	Pressure–flow relation
Viscous losses	Resistance		$p_1 - p_2 = R q$
Inertial losses	Inductance		$p_1 - p_2 = L \dot{q}$
Vessel compliance	Capacitance		$q_1 - q_2 = C \dot{p}$

Table 5.1. Pressure (p) and flow rate (q) relationship in 0D models

5.2. Multiscale models: do we need patient-specific data?

While it is clear that patient-specific measurements are important, some thought on when such data are indispensable is required. The utilities of hemodynamic models can be broadly classified into three categories: (i) generic assessment of a novel medical device, for example a valve, or surgical/interventional procedure, for example creation of a shunt; (ii) optimizing the design of a medical device or surgical/interventional procedure to an individual patient for target hemodynamic indicators (pressure, flow rate, wall shear stress); and (iii) studies where an overall analysis for a population is required. These three scenarios are discussed next.

5.2.1. Assessing function of a new procedure/device

Clinical practitioners (interventional cardiologists, surgeons, etc.) devise novel procedures or devices to tackle particular pathophysiologies based on experience. For example, the concept of a percutaneous pulmonary valve reducer was proposed as an alternative to surgical valve replacement in order to alleviate the right ventricle suffering from pulmonary valve regurgitation in the enlarged right ventricular outflow tract of tetralogy of Fallot patients. Caiazzo *et al.* (2015) proposed to study the effect of this novel device on

patient hemodynamics through a multiscale model. The aims were to study the device function (change in mean flow generated by the device, pressure drop induced by the reducer, generated forces, etc.) and to compare two variations of device implantation (the pulmonary reducer alone and when it is augmented with a valve). In such a typical design study, patient hemodynamic measurements may not be necessary. Before a new device is implanted in patients, by design there are no data available, let alone for the geometry. In such cases, a representative model of the pathophysiology before treatment would suffice. Boundary conditions should be chosen such that they are not expected to change with the device. For example, 0D Windkessel models representing the distal circulation at each outlet can be taken from the literature, or tuned such that typical pressure and flow rate averages or cardiac-cycle variations of that part of the cardiovascular system are reproduced (see Caiazzo *et al.* (2015) for a more specific example, and section 5.3 but taking typical information instead of patient-specific information for parameter tuning). The device geometry or surgical anastomosis should be designed with the medical expert, and virtually implanted in a typical patient geometry. The effects of the device can then be simulated.

5.2.2. Optimizing the procedure/device for an individual patient

Once a particular procedure or device is being tested in clinical feasibility study or has been established to be clinically beneficial, surgical connection or device design may require optimization to provide maximal benefit to the patient or to understand failing cases, given their specific unique vessel geometry and hemodynamic conditions. This can be particularly important when the margins of acceptable hemodynamic ranges in post-operative hemodynamics may be low. As an example, Yang *et al.* (2013) proposed multiscale modeling to optimise the design of a Y-graft in Fontan circulation so that hepatic flow distribution was improved. In this case, since the device design is specific to patient anatomy and the optimization is done for one individual patient, multiscale model personalization through preoperative patient-specific clinical measurements is indispensable.

5.2.3. Population studies

To go further in the understanding of a pathophysiology and its alleviation and treatment options, population studies are desirable from a scientific point of view. Such studies can build on patient-specific multiscale simulations, as in the previous section but be performed for many patients such that

statistically meaningful conclusions can be drawn. To date, such an approach is rare due to the fact that it is difficult to have access to the patient-specific data necessary to establish individualized flow simulations: such necessary data are often acquired for research protocols only, for ethical and cost reasons, and it is tedious to retrieve them, post-process them and perform the entire chain of simulation (Vignon-Clementel *et al.* 2010a). Thus, “population” studies that involve patient-specific hemodynamic data are typically restricted to half a dozen or a dozen cases (Yeung *et al.* 2006; LaDisa *et al.* 2011; Yang *et al.* 2012; Arbia *et al.* 2015). However, this is the clinical number of cases needed for feasibility or prospective studies. Most often, population studies are based on patient-specific anatomy and average hemodynamics of the normal population (sometimes scaled by BSA) (Cebral *et al.* 2005, Joly *et al.* 2020). The rare large population studies are conducted under simplified assumptions (steady, not multiscale, etc.) to describe a state rather than to be predictive (Haggerty *et al.* 2014). For normal physiology, as the different organs and circulation subsystem parameters are documented in the literature, a model (such as 1D-0D of a large number of arteries) can be run spanning a range of parameter population priors to generate hemodynamic waveforms (pressure and flow rate) at different locations of the cardiovascular system that are representative of the population (Willemet *et al.* 2015). If population priors can be known for disease cases, this approach can be extended to pathophysiologies; however, these parameter priors are not generally known for pathophysiologies. If enough hemodynamic data are gathered for a given pathology, then by parameter estimation of the whole population (most probably on a reduced model), we could derive such disease parameter population priors.

5.3. How do we include patient-specific data?

When patient-specific data need to be integrated into the model (multiscale or purely 0D), strategies should be devised according to the available measurements, that is, their implementation and computational complexity need to be coherent with the amount of information. Thus parameter identification can be done on purely 0D models, and for multiscale models, on loosely coupled 3D-0D models (meaning only a few 3D-0D simulations are required), or on strongly-coupled 3D-0D models (in the sense that each parameter identification simulation includes the 3D part).

In what follows, the types of clinical data that are typically available and the associated challenges in their inclusion are first described. Then, a broad categorization of model and measurements features, from which a suitable

parameter estimation strategy can be devised, is presented along with examples where such strategies have been employed.

5.3.1. *Type of clinical data available and associated challenges*

In multiscale models, reduced models constitute boundary conditions for the 3D part and drive most of its dynamics. They are thus crucial for the model. In closed-loop 0D models, the dynamics are defined by their many parameters. Yet, in all of these cases, their parameters are *a priori* unknown: they need to be identified in order to reflect hemodynamic measurements. Depending on the considered application, available measurements besides imaging data to build the 3D geometry vary. Direct or surrogate measurements of flow and/or pressure are considered (see Figure 5.1):

1) phase-contrast magnetic resonance imaging (PC-MRI) can provide flow rate over time on a surface and if the spatial resolution is fine enough even a velocity profile over a surface and its time evolution;

2) catheterization leads to pressure over time at a given location (direct or wedge as a surrogate);

3) Doppler ultrasound can provide maximum (in a small volume) velocity over time, typically interpreted as a flow rate over time assuming a certain flow profile on a surface or by direct integration by the machine.

Depending on the acquisition method, either mean values (in time and possibly within a certain region), min/max values or full time-varying curves are trusted. We thus present several challenges in this topic:

1) measurements are not necessarily taken at boundaries of the 3D domain;

2) they are often too few to identify all parameters, and thus need to be complemented by modeling assumptions or literature data;

3) they are usually not taken simultaneously and are thus not synchronized in time;

4) computational complexity is often an issue for parameter identification.

Each section is addressing these challenges in its own way. The question of identifiability (see for example Miao *et al.* (2011), Pant and Lombardi (2015) and the references therein) is not addressed here in the formal mathematical sense (see Boulakia *et al.* (2013) for Robin parameter estimation in the Stokes system), but rather a practical approach is proposed: either the model chosen is

simple enough to ensure identifiability (section 5.3.3.1) or sensitivity analysis tools give numerical feedback (section 5.3.3.2). There are certainly different ways to address these questions, and we propose here practical strategies based on experience: the main idea of the procedure is sketched in Figure 5.2. For the sake of clarity, here unless otherwise stated, we will consider that the inlet flow rate is known, on average (for steady simulations) or over time (for pulsatile simulations). It can either come from measurement or from the literature; in such cases, scaling with the patient's body surface area (BSA) as often done in the clinics or following allometric scaling laws (across species) with the subject mass to the power $3/4$ (West *et al.* 1997) is recommended. Even if the inlet is coupled to a 0D model or has a pressure boundary condition imposed, the philosophy is similar.

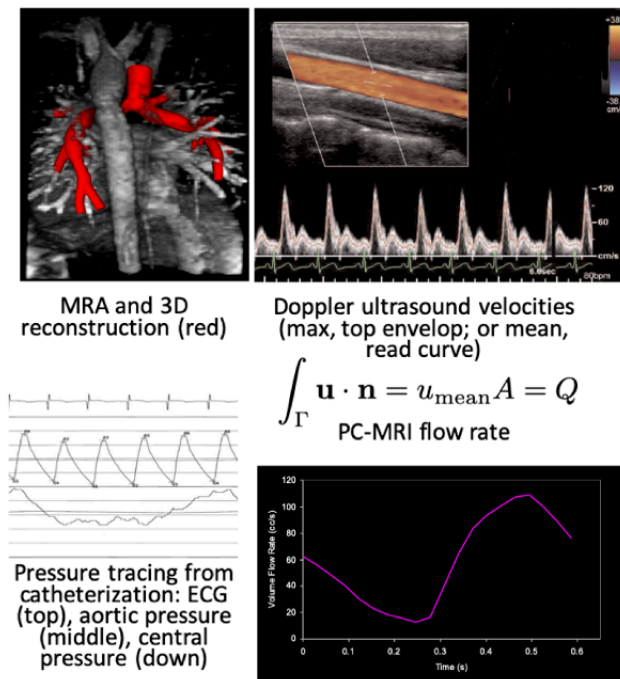


Figure 5.1. Examples of clinical data. MRA for the geometry (top left). Pressure tracings over a few cardiac cycles (bottom left). Doppler velocity over seven cardiac cycles (top right) and PC-MRI flow rate over one cardiac cycle (bottom right)

5.3.2. Establishing if the resistance of the 3D part is negligible or not, and parameterization in case it is

The resistance of developed flow in a pipe is given by the Poiseuille law, which states that the resistance $R = \frac{8\mu l}{\pi r^4}$ is proportional to the pipe length l and inversely proportional to the pipe radius r to the power 4. Hence, for most large vessels, their resistance is small compared to the overall system: in many pathophysiologies, almost all resistance to flow is due to downstream micro-vasculature. In such cases, if no major nonlinearities are estimated to exist in the 3D part of the multiscale model, such as those arising due to stenoses, for example, then for the purpose of parameter estimation, the 3D region may be neglected, thereby significantly reducing the computational cost of parameter estimation. The main idea of the different tuning options presented below is shown in Figure 5.2.

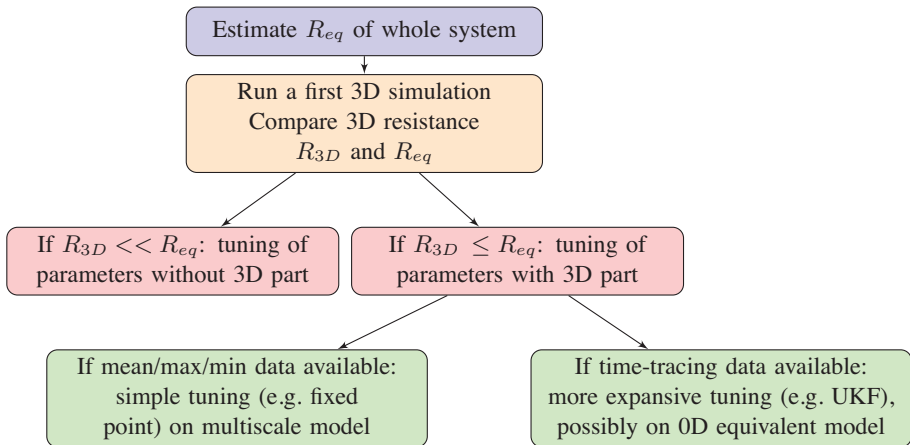


Figure 5.2. Scheme to choose a multiscale parameter tuning method appropriate for the 3D effects and type of available clinical hemodynamic data

In any case, let us start with an initial steady simulation on a 3D multi-branch geometry, which has one inlet and N outlets (cases with a single vessel or with multiple inlets can be considered in a similar manner). The precise pressure or flow rate is rarely known at each inlet and outlet (Vignon-Clementel *et al.* 2006, 2010b). The minimum required information is then to know the mean flow rate that goes through the model (Q_{in}), a representative mean target pressure P^T in this area of the cardiovascular system and a reference pressure P_{ref} that represents the pressure at the distal part of the 3D-0D model (typically the capillary pressure or the right atrium

pressure for systemic simulations, and the left atrium pressure for pulmonary simulations). The latter is often neglected in systemic arterial models. These data can come from measurements or from the literature (Avolio 1980, Nichols and O'Rourke 2005, Vignon-Clementel *et al.* 2006, 2010a). These values enable us to define the total equivalent resistance of the branching network, $R_{eq} = \frac{P^T - P_{ref}}{Q_{in}}$. A first simulation can then be run, imposing the following set of boundary conditions (see section 5.1): $\{Q_{in}$ at the inlet, zero outlet pressures $\}$. The output determines a first estimation of the resistance of the 3D geometry $R_{3D} = \frac{P_{3D}^{3D}}{Q_{in}}$. If $R_{3D} \ll R_{eq}$, then the 3D part of the model represents *a priori* a negligible portion of the overall resistance of the multiscale model, and most of the dynamics and flow distribution among branches are expected to be driven by the choice of inlet and outlet boundary conditions respectively.

In hemodynamic multiscale models, 3D outlets are coupled to 0D parts which, prior to connecting together to the common pressure P_{ref} , consist for each outlet i from 1 to N in a resistance, a Windkessel RCR model (resistance, capacitance and resistance) or more complex models (RLCR, RCRCR, impedances from fractal trees...) (Vignon-Clementel *et al.* 2006, Alastruey *et al.* 2008, Vignon-Clementel *et al.* 2010b, Arbia *et al.* 2015, Pant *et al.* 2016). In all of these cases, the total resistance R_i determines the average relationship between pressure and flow at this outlet i , and thus the flow distribution among the different branches on average over a cardiac cycle, assuming periodicity of the solution. This average flow distribution is a modeling choice that should represent the physiological needs of the distal vasculature and/or organs connected to that branch. Such flow distribution thus depends on the application. Either distributions are known from the patient data (see LaDisa *et al.* (2011), Pant *et al.* (2014a) for examples in the aorta) or patient data in combination with assumptions of flow distribution proportional to 3D outlet surface area to a certain power (see Troianowski *et al.* (2011), Arbia *et al.* (2015) for examples in pulmonary circulation) determine this average flow distribution $\alpha^T = (\alpha_i)_{1 \leq i \leq N}$, $\alpha_i = Q_i / Q_{in}$.

This thus sets the total resistance of each outlet reduced model $R_i = R_{eq} / \alpha_i$. Another steady simulation can be run with the same inlet flow and the $R_{i, 1 \leq i \leq N}$ as outlet boundary conditions. Post-processing of the solution leads to a comparison of the resulting inlet pressure to P^T and flow distribution to the target one α^T . If the differences are negligible, then we need to define based on these R_i s the rest of the 0D parameters (see section

5.3.3.1) and verify that this is still the case on a pulsatile multiscale simulation. The multiscale model is then parameterized as best as possible given the available information: local flow features, wall shear stress or other post processing to study the pathophysiology can be performed, or virtual changes in the 3D geometry or the inlet conditions can be investigated (Vignon-Clementel *et al.* 2010a). If the differences are not negligible, then the 3D part is in fact non-negligible in the setting of the multiscale parameters, and we need to consider other strategies explained below. These strategies must also be devised if $R_{3D} \sim R_{eq}$ or if more complex measurements (target data) are available.

5.3.3. Resistance of the 3D part is not negligible

In many pathophysiologies, particularly those involving aneurysms/stenoses or very complex anatomies, the 3D resistance may not be neglected. Measurements to be matched or target data may also not be as simple as the ones presented above. These cases are addressed in this section with two sub-categories: (i) cases where only mean values of key hemodynamic indicators such as pressure and flow-rate are available; and (ii) cases where full time-varying measurement curves are available.

5.3.3.1. Only mean values of flow/pressure are available

When only mean values of pressure and flow are available at a few locations, there is clearly too little information to identify dynamical components, such as compliances (capacitances) and inertial (inductance) components, in the 0D model. As a first approximation, we can neglect their influence on mean pressures and flow rates. Therefore, while only total outlet resistances can be identified through steady-state multiscale simulations, the latter are computationally less expensive than full pulsatile simulations. Iterative strategies can thus be employed in the full multiscale model. Moreover, the following approach tackles cases where measurements are not taken at boundaries of the 3D domain. Examples are average flow over one subpart (e.g. one side of the pulmonary arterial tree), and time-average pressure for which the exact location has not been recorded but clinical experts define it as being the minimum, maximum or average over a certain number of branches – thereafter called non-local target pressure P^T (Figure 5.3). Such an approach is illustrated in a case of single ventricle physiology where more details can be found (Arbia *et al.* 2015).

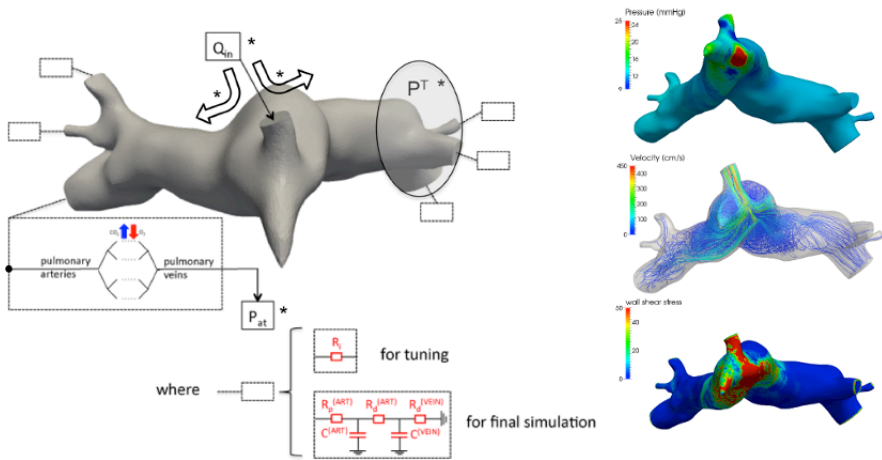


Figure 5.3. Left: multiscale model set-up for pre-stage 2 single ventricle physiology with the 3D domain, its inlet face on which the inflow Q_{in} is prescribed, and the distal pulmonary circulation for each outlet which all merge in the single atrium defined by its pressure P_{at} . Clinically measured quantities are marked with a star. At each outlet (dashed rectangle), the pulmonary arteries, capillaries and veins are represented either by a single total resistance for tuning, or by a more complete five-parameter reduced model for predictions. Right: example of simulation results (pressure, velocity streamline, wall shear stress). Images adapted from Arbia *et al.* (2015)

Several stages of palliative surgery are required to connect the systemic and pulmonary circulations in single ventricle physiology. Arbia *et al.* (2015) performed patient-specific multiscale simulations, identifying parameters based on preoperative measurements, with the aim of studying the pre-stage 2 and virtual stage-2 treatment options. The multiscale model is shown in Figure 5.3 where the inlet face represents the systemic-to-pulmonary shunt that feeds into the left and right pulmonary arteries. Since only mean values of inlet flow (Q_{in}), flow-split (ratio of right pulmonary artery flow to total flow) f_s , atrial pressure (P_{at}) and non-local pulmonary artery pressure (P^T), in which localization and type are defined differently for each patient, are available for parameter estimation, only total resistances can be identified. Therefore, each pulmonary outlet is coupled to a single total resistance for parameter estimation. As opposed to the previous case, the 3D anatomy cannot, in general, be neglected in this model. An alternative strategy is hence devised based on the following principles:

1) the measured Q_{in} is imposed directly at the inlet and the measured atrial pressure P_{at} is imposed at the ends of the model defining P_{ref} ;

2) the target values to be reproduced by the model are P^T and f_s ;

3) to alleviate the ill-posed nature of the inverse problem of identifying all (6–20 depending on the patient anatomy) terminal total resistances from just two measurements, a further assumption is made: the total flow of the right/left pulmonary artery outlets is partitioned into the individual outlets in proportion to the individual outlet surface areas. This defines with Q_{in} and f_s a certain flow repartition α^T , as defined in section 5.3.2;

4) the above assumptions lead to a fixed-point iterative method for total resistance identification which, starting from a guess of total resistance values (e.g. as defined in section 5.3.2), typically converges in 5–10 iterations.

The total resistances $R_{i,1 \leq i \leq N}$ are then split to RCRCR boundary conditions (see Figure 5.3) based on a morphometric approach and scaling rules (e.g. relative role of arterial and venous vascular beds) presented in the literature. The iterative scheme can also be used with pulsatile inlet and RCRCR boundary conditions. The resulting multiscale model has then been coupled to larger closed-loop models or used for surgical planning. More generally, $R_{i,1 \leq i \leq N}$ can be the basis for RCR (LaDisa *et al.* 2011, Vignon-Clementel *et al.* 2010b), RCRCR (Arbia *et al.* 2015, Pant *et al.* 2016), RLCR Alastruey *et al.* (2008) or more complex impedances (Vignon-Clementel *et al.* 2006).

5.3.3.2. *Time-varying curves of flow/pressure are available*

When full time-varying measurements are available, while the measurement data are quite rich and allow for identification of the dynamical components as well, the forward models (unsteady models that need to be run for multiple cardiac cycles) can be prohibitively expensive for parameter estimation. In such cases, one strategy is to employ a reduced order model for parameter estimation that can capture the essential features of the fluid-flow in the 3D regions. This strategy is illustrated in a case of aortic coarctation (CoA).

CoA is a disease characterized by the narrowing of the aorta. The clinical evaluation of coarctation severity, which determines whether or not corrective surgery is required, is based on the threshold of 20 mm Hg pressure-drop across the coarctation under exercise conditions. Measuring this pressure

drop under stress conditions is difficult in a clinical setup and hence it is thought that multiscale computational modeling can predict this pressure drop and therefore aid in decision-making. The multiscale model proposed by Pant *et al.* (2014a, 2014b) is shown in Figure 5.4 (left panel) where the outlets are coupled to RCR Windkessel models and an inlet capacitance is used to characterize compliance effects in the ascending aorta. The inlet flow rate is measured and is imposed as a Dirichlet boundary condition before the capacitance, and the target is to match the measured pressure in the proximal plane (close to the 3D inlet, Figure 5.4), the measured flow rate in the descending aorta and the measured mean flow rates in the supra-aortic branches. Since time-varying measurement curves are available, Pant *et al.* proposed to use a data-assimilation method, the unscented Kalman filter (UKF), for parameter estimation.

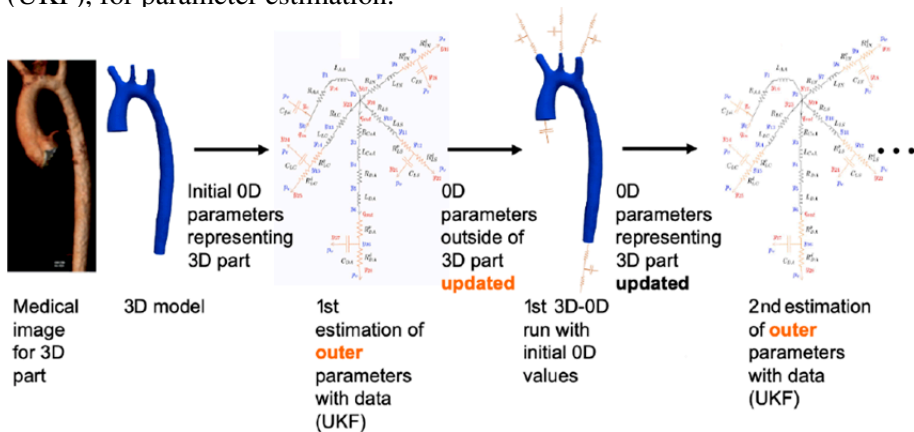


Figure 5.4. Left: the image of the CoA region of interest. Iterations for parameter estimation of the 3D region for CFD and the lumped boundary conditions and the 0D equivalent where the 3D part has also been replaced by a lumped parameter model (black). Outer parameters (inlet capacitance and outlet Windkessel boundary elements) are represented in orange

Two challenges were found: first, the pressure and flow-rate measurements were not synchronized in time; and second, only mean flow rates were available in the supra-aortic branches when the UKF method requires full time-varying curves. The authors addressed the former issue by introducing a time-lag parameter between pressure and flow-rate measurements, which was also to be estimated, and the latter creating pseudo-measurement curves for the supra-aortic branches by redistributing the difference between ascending and descending aorta flow-rates in proportion to the mean-flow rates. Since UKF methodology allows for

specification of confidence in each measurement, the pseudo-measurement curves were assigned a relatively low confidence when compared to the true measurements. As coarctation is characterized by narrowing of the aorta, a change in anatomical feature in the 3D geometry, the 3D resistance may not be neglected. Furthermore, as opposed to the previous case of single ventricle physiology, where only mean measurements were available and hence only steady-state simulations (relatively inexpensive), here full unsteady simulations (computationally expensive) would have been required even if an iterative estimation method had been chosen. Therefore, the authors chose to employ the UKF strategy not on the multiscale model but on a reduced order model based on the following procedure (see Figure 5.4):

- 1) a 0D representation of the 3D geometry is created, whose parameters are initialized by geometrical considerations. For the outer 0D parameters, they can be initialized based on total resistances estimated as in section 5.3.2 and common RCR derivation (section 5.3.3.1);
- 2) UKF procedure is used on the 0D representation to estimate all 14 outer parameters;
- 3) multiscale simulations are run from the above estimated parameters;
- 4) from the multiscale results, the 0D representation of the 3D geometry is improved by linear regression analysis;
- 5) steps 2–3 are repeated until convergence.

The essential idea is that, in order to be computationally efficient, parameter estimation is performed on a 0D representation of the 3D model, and at each iteration the 0D representation is improved by the results of the multiscale simulations, but requiring overall only a few 3D-0D simulations (Pant *et al.* 2014a). Another approach to circumvent the high computational cost of 3D simulations is to utilize a surrogate model. In this approach, a few 3D simulations, scattered so that they fill the parametric space, can be run to create a surrogate model (often referred to as a meta model) that interpolates or regresses the 3D model's response. This fast-running surrogate model can then be used in lieu of the higher fidelity 3D model for parameter estimation, uncertainty quantification (Schiavazzi *et al.* 2016) and sensitivity analysis (Quicken *et al.* 2016). Typical surrogate modeling approaches are Kriging (Gaussian Process modeling), methods based on polynomial chaos expansion and machine learning methods such as neural networks.

5.4. When models fall short of expectations: toward adaptation

An important aspect that requires attention is model validation. It serves two purposes: (i) when model validation is successful, it provides further confidence in the model results so that the unique insights provided by the model can be trusted; and (ii) when model validation fails, it points to shortcomings in the coherence of the clinical data (Arbia *et al.* 2015) or in the model, thereby paving the way for further development and adaptation to account for important physical phenomenon. In what follows, two cases where validation led to model adaptation and significantly improved results are presented.

5.4.1. Liver hepatectomy and blood loss

Partial liver hepatectomy (resection) is widely performed to treat liver disease or for liver donor transplantation. The resected liver is expected to regenerate over a few weeks post-hepatectomy, but in some cases function is poorly restored. Audebert *et al.* (2017) adopted a 0D modeling approach (Figure 5.5) to gain insights into liver hepatectomy. They represented three distinct lobes of liver to be able to simulate removal of one or more lobes during hepatectomy. Parameters of the model were estimated for 12 pigs individually through measurements of arterial and venous pressures, portal vein pressure and flow rate, and hepatic artery flow rate. These were further augmented by assumptions that liver lobe resistances and compliances were inversely and directly proportional, respectively, to lobe mass. With these assumptions, excellent agreement between the measurements and model results was obtained pre-hepatectomy (which reflected the good tuning of the parameters). On the other hand, while the simulations of hepatectomy correctly predicted the general trend (increase or decrease) in the variation of key hemodynamic indicators, the magnitudes were either over- or under-estimated. The key phenomenon missing in the model was the fact that significant blood loss occurred during the hepatectomy procedures, while the model only accounted for loss of liver mass. When the authors took this blood loss into consideration by introducing a variable $Q_{i,b}$, they were able to obtain significantly better post-hepatectomy predictions through the model. Mechanisms that explained these non-trivial quantitative increases and decreases in key hemodynamic factors could thus be elucidated. This example shows how model adaptation is necessary for reliable understanding or predictions in different pathophysiologicals, as opposed to adopting a one-size-fits-all approach.

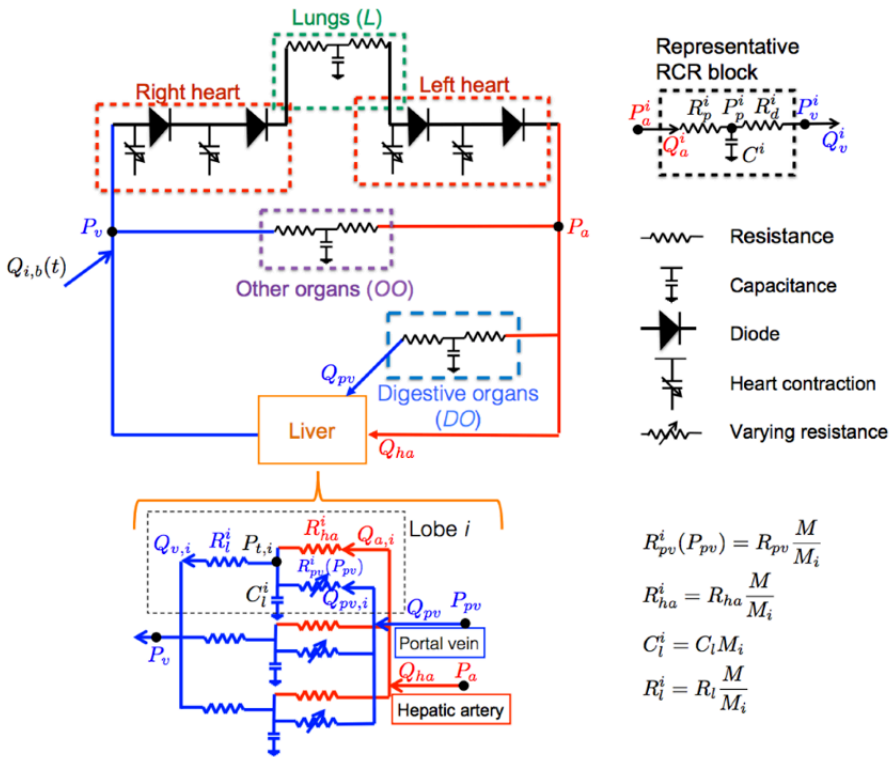


Figure 5.5. Schematic representation of the 0D closed-loop cardiovascular and liver blood circulation. The pig liver model consists of three distinct lobes. $Q_{i,b}$ accounts for blood loss during surgery (Audebert et al. 2017)

5.4.2. Pulmonary stenosis alleviation and vascular adaptation

Peripheral pulmonary artery stenosis is a disease characterized by narrowing of the branched pulmonary artery segments. Yang *et al.* (2016) developed a multiscale model with three-element Windkessel boundary conditions to predict post-operative, i.e. when stenoses were virtually surgically removed, hemodynamics to aid surgical planning between different options (which, by nature, cannot all be tested on a given patient). They estimated the Windkessel parameters by first identifying the total resistances and then distributing the total resistance to RCR Windkessel components based on a morphometry-based tree approach (Spilker *et al.* 2007). The post-operative results, however, showed a deviation of $\sim 20\%$ with respect to the gold-standard clinical measure of flow to the right lung. The most likely

reason for this deviation was that the pulmonary vasculature has an ability to change its resistance through vascular dilatation and contraction, which the model did not account for. Therefore, the authors hypothesized that a target for such an adaptation could be maintenance of constant shear stress in the pulmonary vasculature. It is, however, not straightforward to determine how shear-stress-related dilatation/contraction will result in changes in parameter value of the Windkessel model. Therefore, to model adaptation, the authors constructed an equivalent structured pulmonary tree (see Figure 5.6), with branches of successively decreasing radii. With the acute post-operative results from the Windkessel multi-scale model, it was possible to change the radii in the structured trees with the constant shear hypothesis. These adapted structured trees were then converted back to Windkessel models to simulate the post-operative and post-adaptation hemodynamics. This resulted in a reduction from $\sim 20\%$ error to $\sim 4\%$ error with respect to the measurements. This example shows how classical multiscale models, when they fail on straightforward application, can be adapted to include key physical phenomenon to improve their predictive power.

5.5. Conclusion

In this chapter, we have presented the challenges in devising patient-specific model simulations and, in particular, presented an overall strategy to choose a 0D parameter tuning method based on the type of available data and the importance of the 3D flow features compared to the overall system. When time-tracings of hemodynamic data are available, the UKF has been shown to be a good option for such hemodynamic cases. Besides multiscale simulations, it has been successfully used in a 0D closed-loop model of the entire circulation for severe pathologies (Pant *et al.* 2016), including when pressure and flow rate data were acquired at different heart rates (Pant *et al.* 2017). Although progress has been made in patient-specific hemodynamic simulations and the combination of modeling and machine learning seems promising (Joly *et al.* 2020), to date large population studies with patient-specific hemodynamic data are lacking, and validation of such simulations remains a challenge. Both facts are due to the complexity of gathering patient-specific hemodynamic data from multiple modalities, preoperatively or more often post-operatively to validate a prediction based on preoperative data and virtual surgery planning (Vignon-Clementel *et al.* 2010a). Furthermore, circulation changes due to surgery, adaptation, growth or remodeling are largely yet to be better understood and integrated into models (Corsini *et al.* 2015, Yang *et al.* 2016, Audebert *et al.* 2017).

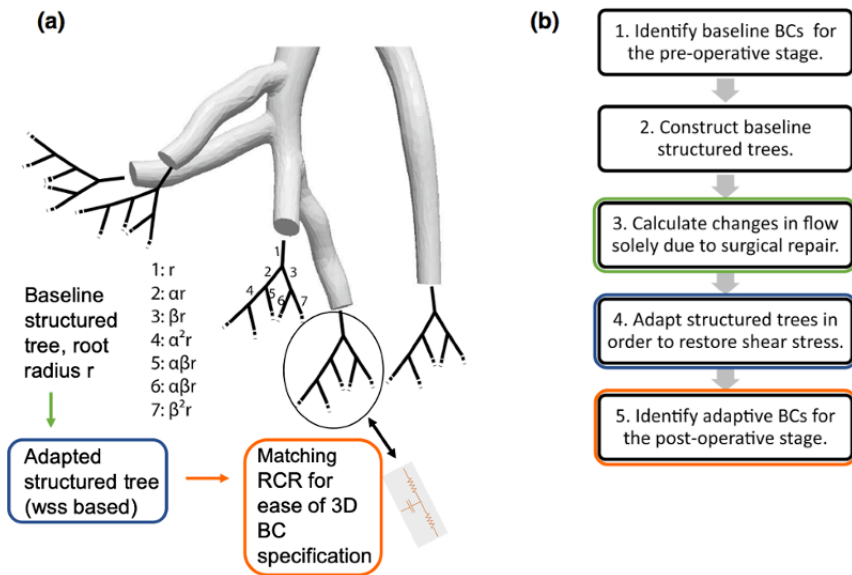


Figure 5.6. a) Illustration of structured trees for the PAs. If a root segment has a radius of r , the size for the daughter segments is scaled by α and β . For each 3D outlet, a structured tree is created such that the total resistance of the structured tree is equal to the resistance of the three-element Windkessel model used for the same 3D outlet in simulations. b) Algorithm of structured tree adaptation for post-operative outflow boundary conditions. Figures adapted from Yang et al. (2016)

5.6. Acknowledgments

The authors would like to thank collaborators whose work on model parameterization has formed the basis of this chapter. In particular, they thank Gregory Arbia, Chloe Audebert, Benoit Fabreges, Jean-Frederic Gerbeau and Weiguang Yang. This material is based upon work supported by the Leducq Foundation (Transatlantic Network of Excellence for Cardiovascular Research on Multi-scale modeling of single ventricle hearts for clinical decision support), the French National Agency for Research ANR-13-TECS-0006, EPSRC UK grant EP/R010811/1 and the European Research Council (ERC) under the European Unions Horizon 2020 research and innovation programme (Grant agreement No. 864313).

5.7. References

- Alastruey, J., Parker, K., Peiró, J., Sherwin, S. (2008). Lumped parameter outflow models for 1-D blood flow simulations: Effect on pulse waves and parameter estimation. *Communications in Computational Physics*, 4(2), 317–336.
- Arbia, G., Corsini, C., Baker, C., Pennati, G., Hsia, T.-Y., Vignon-Clementel, I.E. (2015). Pulmonary hemodynamics simulations before stage 2 single ventricle surgery: Patient-specific parameter identification and clinical data assessment. *Cardiovasc. Eng. Technol.*, 6(3), 268–280.
- Audebert, C., Bekheit, M., Bucur, P., Vibert, E., Vignon-Clementel, I.E. (2017). Partial hepatectomy hemodynamics changes: Experimental data explained by closed-loop lumped modeling. *J. Biomech.*, 50, 202–208.
- Avolio, A. (1980). Multi-branched model of the human arterial system. *Med. Biol. Eng. Comput.*, 18(6), 709–718.
- Boulakia, M., Egloffé, A.-C., Grandmont, C. (2013). Stability estimates for the unique continuation property of the Stokes system and for an inverse boundary coefficient problem. *Inverse Problems*, 115001.
- Caiazzo, A., Guibert, R., Boudjemline, Y., Vignon-Clementel, I.E. (2015). Blood flow simulations for the design of stented valve reducer in enlarged ventricular outflow tracts. *Cardiovascular Engineering and Technology*, 6(4), 485–500.
- Cebral, J.R., Castro, M.A., Burgess, J.E., Pergolizzi, R.S., Sheridan, M.J., Putman, C.M. (2005). Characterization of cerebral aneurysms for assessing risk of rupture by using patient-specific computational hemodynamics models. *American Journal of Neuroradiology*, 26(10), 2550–2559.
- Corsini, C., Baker, C., Baretta, A., Biglino, G., Hlavacek, A., Hsia, T., Kung, E., Marsden, A., Migliavacca, F., Vignon-Clementel, I., Pennati, G., Hearts, M.C. (2015). Integration of clinical data collected at different times for virtual surgery in single ventricle patients: A case study. *Annals of Biomedical Engineering*, 43(6), 1310–1320.
- Esmaily Moghadam, M., Vignon-Clementel, I.E., Figliola, R., Marsden, A.L. (2013). A modular numerical method for implicit 0D/3D coupling in cardiovascular finite element simulations. *Journal of Computational Physics*, 244, 63–79.
- Formaggia, L., Quarteroni, A., Veneziani, A. (2009). Multiscale models of the vascular system. *Cardiovascular Mathematics*, 1, 395–446.
- Haggerty, C.M., Restrepo, M., Tang, E., de Zélicourt, D.A., Sundareswaran, K.S., Mirabella, L., Bethel, J., Whitehead, K.K., Fogel, M.A., Yoganathan, A.P. (2014). Fontan hemodynamics from 100 patient-specific cardiac magnetic resonance studies: A computational fluid dynamics analysis. *The Journal of Thoracic and Cardiovascular Surgery*, 148(4), 1481–1489.

- Joly, F., Soulez, G., Lessard, S., Kauffmann, C., Vignon-Clementel, I.E. (2020) A cohort longitudinal study identifies morphology and hemodynamics predictors of abdominal aortic aneurysm growth. *Annals of Biomedical Engineering*, 48(2), 606–623.
- LaDisa Jr., J.F., Dholakia, R.J., Figueroa, C.A., Vignon-Clementel, I.E., Chan, F.P., Samyn, M.M., Cava, J.R., Taylor, C.A., Feinstein, J.A. (2011). Computational simulations demonstrate altered wall shear stress in aortic coarctation patients treated by resection with end-to-end anastomosis. *Congenital Heart Disease*, 6(5), 432–443.
- Miao, H., Xia, X., Perelson, A.S., Wu, H. (2011). On identifiability of nonlinear ODE models and applications in viral dynamics. *SIAM Rev.*, 53(1), 3–39.
- Nichols, W. and O'Rourke, M. (2005). *McDonald's Blood Flow in Arteries*. Hodder Arnold, London.
- Oakes, J.M., Marsden, A.L., Grandmont, C., Darquenne, C., Vignon-Clementel, I.E. (2015). Distribution of aerosolized particles in healthy and emphysematous rat lungs: Comparison between experimental and numerical studies. *J. Biomech.*, 48(6), 1147–1157.
- Pant, S. and Lombardi, D. (2015). An information-theoretic approach to assess practical identifiability of parametric dynamical systems. *Math. Biosci.*, 268, 66–79.
- Pant, S., Fabrèges, B., Gerbeau, J.-F., Vignon-Clementel, I. (2014a). A methodological paradigm for patient-specific multi-scale CFD simulations: From clinical measurements to parameter estimates for individual analysis. *International Journal for Numerical Methods in Biomedical Engineering*, 30(12), 1614–1648.
- Pant, S., Fabrèges, B., Gerbeau, J.-F., Vignon-Clementel, I.E. (2014b). A multiscale filtering-based parameter estimation method for patient-specific coarctation simulations in rest and exercise. In *Statistical Atlases and Computational Models of the Heart*, Camara, O., Mansi, T., Pop, M., Rhode, K., Sermesant, M., Young, A. (eds). Springer, Cham.
- Pant, S., Corsini, C., Baker, C., Hsia, T.-Y., Pennati, G., Vignon-Clementel, I.E., Modeling of Congenital Hearts Alliance (MOCHA) Investigators (2016). Data assimilation and modelling of patient-specific single-ventricle physiology with and without valve regurgitation. *Journal of Biomechanics*, 49(11), 2162–2173.
- Pant, S., Corsini, C., Baker, C., Hsia, T.-Y., Pennati, G., Vignon-Clementel, I.E. (2017). Inverse problems in reduced order models of cardiovascular haemodynamics: Aspects of data assimilation and heart rate variability. *Journal of The Royal Society Interface*, 14(126), 20160513.
- Quarteroni, A., Veneziani, A., Vergara, C. (2016). Geometric multiscale modeling of the cardiovascular system, between theory and practice. *Computer Methods in Applied Mechanics and Engineering*, 302, 193–252.

- Quicken, S., Donders, W.P., van Disseldorp, E.M., Gashi, K., Mees, B.M., van de Vosse, F.N., Lopata, R.G., Delhaas, T., Huberts, W. (2016). Application of an adaptive polynomial chaos expansion on computationally expensive three-dimensional cardiovascular models for uncertainty quantification and sensitivity analysis. *Journal of Biomechanical Engineering*, 138(12), 121010.
- Schiavazzi, D., Arbia, G., Baker, C., Hlavacek, A.M., Hsia, T.-Y., Marsden, A., Vignon-Clementel, I., Modeling of Congenital Hearts Alliance (MOCHA) Investigators (2016), Uncertainty quantification in virtual surgery hemodynamics predictions for single ventricle palliation. *International Journal for Numerical Methods in Biomedical Engineering*, 32(3), e02737.
- Shi, Y., Lawford, P., Hose, R. (2011). Review of zero-D and 1-D models of blood flow in the cardiovascular system. *BioMedical Engineering OnLine*, 10(1), 33.
- Spilker, R.L., Feinstein, J.A., Parker, D.W., Reddy, V.M., Taylor, C.A. (2007). Morphometry-based impedance boundary conditions for patient-specific modeling of blood flow in pulmonary arteries. *Annals of Biomedical Engineering*, 35(4), 546–559.
- Troianowski, G., Taylor, C.A., Feinstein, J.A., Vignon-Clementel, I.E. (2011). Three-dimensional simulations in Glenn patients: Clinically based boundary conditions, hemodynamic results and sensitivity to input data. *Journal of Biomechanical Engineering*, 133, 111006.
- Vignon-Clementel, I.E., Figueroa, C.A., Jansen, K.E., Taylor, C.A. (2006). Outflow boundary conditions for three-dimensional finite element modeling of blood flow and pressure in arteries. *Computer Methods in Applied Mechanics and Engineering*, 195(29–32), 3776–3796.
- Vignon-Clementel, I.E., Marsden, A.L., Feinstein, J.A. (2010a). A primer on computational simulation in congenital heart disease for the clinician. *Prog. Pediatr. Cardiol.*, 30(1), 3–13.
- Vignon-Clementel, I.E., Figueroa, C.A., Jansen, K.E., Taylor, C.A. (2010b). Outflow boundary conditions for 3D simulations of non-periodic blood flow and pressure fields in deformable arteries. *Computer Methods in Biomechanics and Biomedical Engineering*, 13(5), 625–640.
- West, G.B., Brown, J.H., Enquist, B.J. (1997). A general model for the origin of allometric scaling laws in biology. *Science*, 276(5309), 122–126.
- Willemet, M., Chowienczyk, P., Alastruey, J. (2015). A database of virtual healthy subjects to assess the accuracy of foot-to-foot pulse wave velocities for estimation of aortic stiffness. *American Journal of Physiology-Heart and Circulatory Physiology*, 309(4), H663–H675.

- Yang, W., Vignon-Clementel, I.E., Troianowski, G., Reddy, V.M., Feinstein, J.A., Marsden, A.L. (2012). Hepatic blood flow distribution and performance in conventional and novel Y-graft Fontan geometries: A case series computational fluid dynamics study. *Journal of Thoracic and Cardiovascular Surgery*, 143(5), 1086–1097.
- Yang, W., Feinstein, J.A., Shadden, S.C., Vignon-Clementel, I.E., Marsden, A.L. (2013). Optimization of a y-graft design for improved hepatic flow distribution in the fontan circulation. *Journal of Biomechanical Engineering*, 135(1), 011002.
- Yang, W., Feinstein, J.A., Vignon-Clementel, I.E. (2016). Adaptive outflow boundary conditions improve post-operative predictions after repair of peripheral pulmonary artery stenosis. *Biomechanics and Modeling in Mechanobiology*, 15(5), 1345–1353.
- Yeung, J.J., Kim, H.J., Abbruzzese, T.A., Vignon-Clementel, I.E., Draney-Blomme, M.T., Yeung, K.K., Perakash, I., Herfkens, R.J., Taylor, C.A., Dalman, R.L. (2006). Aortoiliac hemodynamic and morphologic adaptation to chronic spinal cord injury. *Journal of Vascular Surgery*, 44(6), 1254–1265.

6

Reduced-order Models of Blood Flow: Application to Arterial Stenoses

**Jeanne VENTRE¹, José-Maria FULLANA¹, Pierre-Yves LAGRÉE¹,
Francesca RAIMONDI² and Nathalie BODDAERT²**

¹*Institut Jean Le Rond d'Alembert, CNRS UMR 7190,
Sorbonne University, Paris, France*

²*Hôpital Necker Enfants Malades, APHP, Centre M3C, Paris, France*

6.1. Introduction

Blood flow models in arteries are based on the Navier–Stokes fluid equations and to solve the complete problem they have to be coupled to the mechanics of the displacement of the arterial wall in a three-dimensional (3D) domain. Coupling blood dynamics with wall displacements is a challenging research topic due to the complexity of the problem. Because of the technical difficulties, 3D modeling is usually restricted to small regions of the systemic circulatory system such as arterial bifurcations, aneurysms (Kim *et al.* 2010, Vignon-Clementel *et al.* 2010) and only in a few cases applied to the entire circulation (Xiao *et al.* 2013). Nevertheless, it is clear and acknowledged that 3D models can provide relevant information on the blood flow behavior in patient-specific configurations. However, the drawback is the time required for computations, which is far above real medical application needs. Fortunately, it is possible to derive reduced-order models that circumvent the computational time and resource problems by making

Biological Flow in Large Vessels,

coordinated by Valérie DEPLANO, José-Maria FULLANA, Claude VERDIER. © ISTE Ltd 2022.

Biological Flow in Large Vessels: Dialog Between Numerical Modeling and In Vitro/In Vivo Experiments,
First Edition. Valérie Deplano; José-Maria Fullana and Claude Verdier.

© ISTE Ltd 2022. Published by ISTE Ltd and John Wiley & Sons, Inc.

some assumptions about the geometry of arteries and the flow symmetries. Reduced models have been developed in the past and it is interesting to compare their behavior in medical configurations.

We present four reduced blood flow models, each with different degrees of complexity and compare them on a real medical configuration, a stenosis. Stenosis is a narrowing of a blood vessel and can originate from aortic coarctation, a congenital heart disease, frequently located in large arteries (Warnes *et al.* 2008). Arterial stenoses can also result from the formation of fat plaques on the arterial wall of the coronaries (Benjamin *et al.* 2017). Regardless of the causes, the obstruction of the vessel affects the hemodynamics, which is why we use the reduced-order models to analyze the flow in such a configuration.

Section 6.2 presents the four reduced models for blood flow modeling: the steady RNSP model, the multi-ring model, the one-dimensional (1D) model and a zero-dimensional (0D) model. All of these models derive from the Navier–Stokes equations, with the assumption of axisymmetric blood flow and the classical long-wavelength hypothesis, that is, axial wavelength greater than the arterial radius, leading to the reduced Navier–Stokes Prandtl (RNSP) equation. To take into account the fluid–structure interactions, the mechanics of the arterial wall are modeled by a relation called pressure law that can either be elastic (Ghigo *et al.* 2017), hyper-elastic, viscoelastic (Alastruey *et al.* 2011) or rigid (Lagrée and Lorthois 2005). Starting from the Navier–Stokes equations, we obtain :

- the RNSP model which is coupled to elastic or rigid walls and can lead to two specific models:

- the steady RNSP model,
- the multi-ring model;

- next, by averaging the RNSP model over the cross-section of the vessel, we recover the classical one-dimensional model (Alastruey *et al.* 2012, Ventre *et al.* 2019). The 1D model also requires coupling with a wall pressure law (Quarteroni *et al.* 2016) to take into account the fluid–structure interactions, and an additional hypothesis on the velocity profile to compute the wall shear stress (WSS);

- finally, by averaging the 1D equations over the length of the artery, we obtain the 0D model, also referred to as the algebraic model (Young and Tsai 1973a,b).

To validate the reduced models, in section 6.3 we propose two classical configurations: a numerical one based on the development of the boundary layer of a flow entering a straight rigid channel where the reduced models (steady RNSP model, multi-ring model and Poiseuille solution) are compared to a complete 2D axisymmetric simulation of the Navier–Stokes equations; and a theoretical one by computing the analytical Womersley solution for unsteady flows, in this case using the multi-ring model.

Finally in section 6.4, we present a comparison between the reduced models over a stenosis configuration and against invasive and in vivo experimental data of pressure drops (Young *et al.* 1975).

6.2. Blood flow modeling

The dynamics of blood flow in arteries are governed by the 3D Navier–Stokes equations

$$\rho \left(\frac{\partial \mathbf{u}}{\partial t} + (\mathbf{u} \cdot \nabla) \mathbf{u} \right) = -\nabla p + \mu \nabla^2 \mathbf{u} \quad [6.1]$$

where \mathbf{u} is the 3D velocity vector, p is the pressure, ρ is the fluid density and μ is the dynamic viscosity. In a cylindrical system, the components of the velocity vector \mathbf{u} are (u_r, u_θ, u_x) . The dynamic viscosity is constant because in large arteries the average shear rate $\dot{\gamma}$ is high enough to consider the fluid homogeneous and Newtonian. Because the velocity in the arteries never exceeds a few meters per second, the Mach number is small and we can thus consider that blood flow is incompressible, that is, $\nabla \cdot \mathbf{u} = 0$.

Most arterial wall models consider the artery as an axisymmetric thin cylinder. In physiological conditions, the wall displacement is small compared to the typical arterial radius R_0 , that is, the small perturbation assumption is then valid. The simplest way to describe the arterial wall is with a homogeneous, isotropic, isothermal, linear elastic material, therefore the stress and strain tensors are related through Hooke's law.

These hypotheses allow for simplifying the Navier–Lamé equations into a simple law of the behavior of the arterial wall, which links the pressure to the cross-section of the artery. This law can be elastic (Quarteroni *et al.* 2016) or more complex, such as a viscoelastic (Alastruey *et al.* 2011) or hyperelastic law. The elastic model follows:

$$p(x, t) = K(x) \left(\sqrt{A(x, t)} - \sqrt{A_0(x)} \right) \quad [6.2]$$

where p is the fluid pressure, $A(x)$ is the cross-section, $A_0(x)$ is the reference cross-section and the parameter K characterizes the elastic behavior of the arterial wall and is of the following form:

$$K(x) = \frac{E}{1 - \nu^2} \frac{\sqrt{\pi}h}{A_0(x)} \quad [6.3]$$

where E is Young's modulus, h is the wall thickness and ν is the Poisson coefficient.

6.2.1. Two-dimensional axisymmetric model

The Navier–Stokes equations [6.1] simplify by considering the geometry of an artery as axisymmetric, leading to the mathematical condition of symmetry $\partial/\partial\theta = 0$ and assuming that the azimuthal velocity u_θ is negligible by mass conservation.

To perform an asymptotic analysis, we introduce a small parameter $\epsilon_\lambda = \frac{R_0}{\lambda} \ll 1$ that measures the ratio between the characteristic arterial radius and the wavelength. In the large arteries, the wavelength λ of the pulse wave is much larger than the characteristic radius: the elastic wave velocity c is of order 10^2 cm/s (Moens 1878, Korteweg 1878), and the heart period T_c is around 1 s. The axial wavelength of the pulse wave is then $\lambda = cT_c \approx 10^2$ cm, which is much larger than $R_0 \sim 1 - 0.5$ cm, the characteristic radius of a large artery.

We re-write equations [6.1] introducing the following dimensionless variables:

$$t = \frac{\lambda}{c} \bar{t}, r = R_0 \bar{r}, x = \lambda \bar{x}, u_r = U_r \bar{u}_r, u_x = U_x \bar{u}_x, p = p_0 + \Pi \bar{p}$$

Two dimensionless numbers appear naturally and characterize blood flows in the arteries: (1) the Shapiro number $Sh = \frac{U_x}{c}$ which assesses the nonlinear effects and (2) the Womersley number $\alpha = R_0 \sqrt{\omega/\nu}$ which compares the pulsatile and viscous effects and the kinematic viscosity ($\omega = 2\pi/T_c$ and $\nu = \mu/\rho$). In large arteries, the Shapiro number ranges between 0 and 1 and the Womersley number between 0 and 25.

According to the principle of least degeneracy (Van Dyke 1964), the leading order terms should remain in equations [6.1]. It leads to $U_r = \epsilon_\lambda U_x$

in the mass conservation equation and, similarly, the principle states that the pressure gradient must balance the inertial terms giving $\Pi = \rho U_x c$.

Finally, in the 2D cylindrical coordinate system (r, x) , the RNSP equations are given as

$$\left\{ \begin{array}{l} \frac{1}{r} \frac{\partial r u_r}{\partial r} + \frac{\partial u_x}{\partial x} = 0, \\ 0 = -\frac{1}{\rho} \frac{\partial p}{\partial r}, \\ \frac{\partial u_x}{\partial t} + u_r \frac{\partial u_x}{\partial r} + u_x \frac{\partial u_x}{\partial x} = -\frac{1}{\rho} \frac{\partial p}{\partial x} + \nu \left(\frac{1}{r} \frac{\partial}{\partial r} \left(r \frac{\partial u_x}{\partial r} \right) \right) \end{array} \right. \quad [6.4]$$

The set of equations [6.4] can be written in the dimensionless form with the Shapiro number Sh in front of the inertial term and $1/\alpha^2$ instead of ν in the diffusion term of the x -momentum equation (Lagrée and Lorthois 2005).

We define two particular models from the RNSP equations by: (a) removing the unsteady term from the x -momentum of equation [6.4], supposing a rigid wall similar to Lagrée and Lorthois (2005), which we refer to as the steady RNSP model in the following; and (b) coupling equation [6.4] with an elastic arterial wall similar to Ghigo *et al.* (2017), which we refer to as the multi-ring model.

For solving the steady RNSP model, we use an implicit finite difference scheme. More details can be found in Lagrée and Lorthois (2005).

6.2.2. Multi-ring model

The multi-ring model was derived in Ghigo *et al.* (2017) to include the elasticity of the arterial wall into the RNSP equations [6.4]. The model was originally inspired by the multilayer model of Audusse *et al.* (2011) for the Saint-Venant equations in shallow water flows.

The flow is solved by decomposing the fluid domain into concentric rings. Each ring n is characterized by a width $h_n = R_{n+\frac{1}{2}} - R_{n-\frac{1}{2}}$. The cross-section of each ring A_n and the average flow rate in the ring Q_n are defined by

$$\left\{ \begin{array}{l} A_n = \int_0^{2\pi} \int_{R_{n-\frac{1}{2}}}^{R_{n+\frac{1}{2}}} r dr d\theta, \\ Q_n = \int_0^{2\pi} \int_{R_{n-\frac{1}{2}}}^{R_{n+\frac{1}{2}}} u_x r dr d\theta \end{array} \right. \quad [6.5]$$

We re-write the equations [6.4] in terms of the averaged quantities A_n and Q_n on each ring n

$$\left\{ \begin{array}{l} \frac{\partial A_n}{\partial t} + \frac{\partial Q_n}{\partial x} = G_{n+\frac{1}{2}} - G_{n-\frac{1}{2}}, \\ \frac{\partial Q_n}{\partial t} + \frac{\partial}{\partial x} \left[\psi_n \frac{Q_n^2}{l_n A} \right] + \frac{A_n}{\rho} \frac{\partial p}{\partial x} = S_{M,n} + S_{\nu,n}, \end{array} \right. \quad [6.6]$$

coupled to the elastic pressure law (equation [6.2]). The parameter ψ_n is the nonlinear shape factor that we set to 1.

The term $G_{n+\frac{1}{2}}$ (respectively, $G_{n-\frac{1}{2}}$) in equation [6.6] represents the radial mass exchange at the interface of $R_{n+\frac{1}{2}}$ (respectively, $R_{n-\frac{1}{2}}$), the source term $S_{M,n}$ characterizes the momentum associated with the radial mass exchanges in the ring n and the source term $S_{\nu,n}$ describes the viscous dissipation.

By coupling the system of equation [6.6] with the pressure law [6.2], we obtain

$$\left\{ \begin{array}{l} \frac{\partial A}{\partial t} + \frac{\partial F_A}{\partial x} = 0, \\ \frac{\partial Q_n}{\partial t} + \frac{\partial F_{Q_n}}{\partial x} = S_{M,n} + S_{\nu,n} + l_n S_T \quad \text{for } n = 1, \dots, N_r, \end{array} \right. \quad [6.7]$$

where the source term S_T corresponds to the geometrical and mechanical source terms and

$$\left\{ \begin{array}{l} F_A = \sum_{i=0}^{N_r} Q_i, \\ F_{Q_n} = \psi_n \frac{Q_n^2}{l_n A} + l_n \frac{K}{3\rho} A^{\frac{3}{2}}. \end{array} \right. \quad [6.8]$$

The system of equation [6.7] is solved using a finite volume approach. We split the system of equations into a convective subproblem that accounts for the transport and a reaction subproblem for the friction source term. We treated the convective subproblem with an explicit method using a kinetic scheme for the flux (Audebert *et al.* 2017). We solved the viscous subproblem using an implicit numerical scheme. More details can be found in Ghigo *et al.* (2017).

6.2.3. One-dimensional model

The 1D equations result from averaging the RNSP equations [6.4] over the cross-section. In the averaging process, we lose information about the velocity profile and thus require an assumption on the profile to compute the friction. The 1D equations are written in terms of the flow rate Q and the cross-section A :

$$\begin{cases} \frac{\partial A}{\partial t} + \frac{\partial Q}{\partial x} = 0, \\ \frac{\partial Q}{\partial t} + \frac{\partial}{\partial x} \left(\psi \frac{Q^2}{A} \right) + \frac{A}{\rho} \frac{\partial p}{\partial x} = -C_f \frac{Q}{A}. \end{cases} \quad [6.9]$$

The shape factor ψ is set to 1, following the literature. The friction coefficient C_f is set to $2(\xi + 2)\mu\pi$ (Sherwin *et al.* 2003) where the parameter ξ determines the friction depending on the hypothesis on the velocity profile. For instance, $\xi = 2$ for a Poiseuille velocity profile, whereas $\xi = 9$ for a flat velocity profile.

In our numerical computations, we use the same elastic pressure law (equation [6.2]) to couple the motion of the wall to the flow, which corresponds to equation [6.7] with $n = 1$. The same finite volume approach of the previous section is used to solve the problem (Ghigo *et al.* 2017, Delestre *et al.* 2015).

6.2.4. Zero-dimensional model

The last level of simplifications leads to algebraic, lumped parameter, or 0D models. The models are obtained from averaging the 1D equations [6.9] over the longitudinal variable. Several 0D models were derived for specific applications which explain the variety in the literature (Young and Tsai 1973b, Seeley and Young 1976, Stergiopoulos *et al.* 1992, Liang *et al.* 2009).

For the comparison section 6.4, we present the generalization of Bernoulli's principle, or a balance of mechanical energy proposed by Young and Tsai (1973b) for the pressure drop assessment in a stenosis:

$$\Delta P = \frac{K_v \mu}{D_0} U(t) + K_u \rho L_{st} \frac{dU(t)}{dt} + \frac{K_t}{2} \left(\left(\frac{A_0}{A_{st}} \right)^2 - 1 \right) \rho |U(t)| U(t), \quad [6.10]$$

where ΔP is the pressure drop across the length of the stenosis L_{st} , D_0 is the diameter and A_0 is the reference cross-section, A_{st} is the cross-section at the throat of the stenosis, and K_v , K_u and K_t are empirical coefficients. The velocity $U(t)$ is the instantaneous input velocity and $|\cdot|$ stands for the absolute value. The Poiseuille viscous loss depends on the coefficient K_v , the inertial effect of blood flow in a constriction on an inertial coefficient K_u and, finally, the nonlinear effects on the coefficient K_t .

These expressions are considered in the literature as the gold standard for model comparison and are used by physicians to roughly estimate the pressure drop across an arterial stenosis, in cases where they do not have access to invasive measurement.

In the following, we show two analytical cases that enable the models to be validated against one another.

6.3. Validation of the models

6.3.1. The entry effect

The first comparison case is called the entry effect, as shown in Figure 6.1. We investigate the development of the boundary layer of a flow entering a straight rigid channel of radius R_0 and length L , and we expect the velocity profile to go from a flat to a fully developed Poiseuille profile.

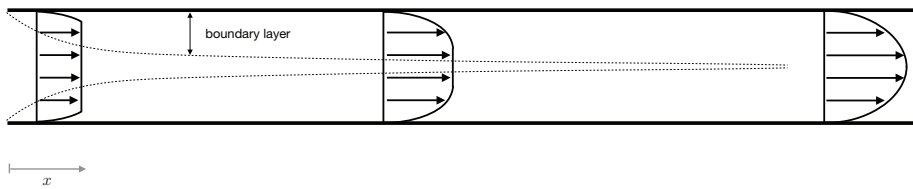


Figure 6.1. Developing and fully developed flows in a channel. The flow is fully developed after the two boundary layers have merged

The parameters of the simulation are presented in Table 6.1. A full 2D axisymmetric Navier–Stokes computation is used as a target and compared to the steady RNSP, the multi-ring and the Poiseuille solution.

In Figure 6.2, we plot the dimensionless pressure and the dimensionless velocity at the centerline for the different models. We note that the numerical results are similar. As predicted, we observe in Figure 6.2a that the dimensionless center velocity goes from 1, which is the magnitude of the flat

profile, to 2, the magnitude of the Poiseuille profile. When the boundary layer is fully developed, all models fit the analytic solution for the pressure (Figure 6.2b).

R_0	L	Re_R	U_0	ρ	$\frac{\rho U_0 R_0}{Re_R}$	K
1	25	100	100	1	1	1e7

Table 6.1. Characteristic scales of the entry effect problem. R_0 : initial radius, L : artery length, Re_R : Reynolds number, U_0 : entrance velocity, ρ : density, μ : dynamic viscosity, K : elasticity. All values are in CGS units

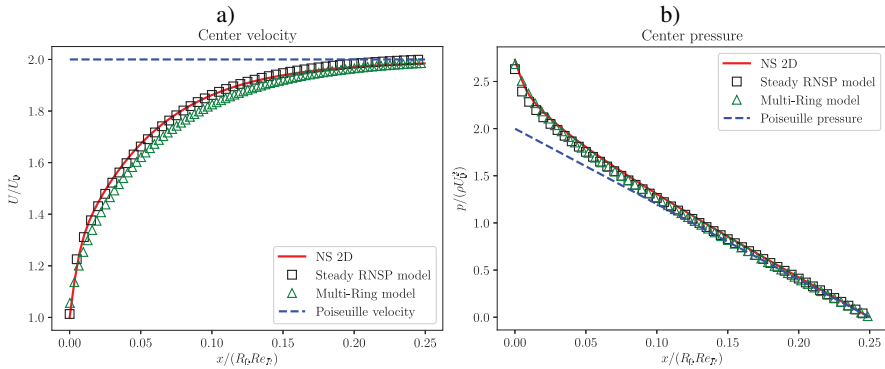


Figure 6.2. Comparison of (—) the 2D axisymmetric Navier–Stokes, (□) the steady RNSP model, (△) the multi-ring model and (---) the Poiseuille solution for the entry effect. Dimensionless velocity (a) and pressure (b) at the centerline as a function of the position in the tube. For a color version of this figure, see www.iste.co.uk/deplano/biological.zip

6.3.2. The Womersley solution in an elastic artery

The second comparison case is the Womersley velocity profile in a straight elastic tube. Womersley (1955) gives the analytic solution of the equations [6.4] for $Sh = 0$, depending on the Womersley number α . For the velocity, the solution is

$$u_x = \hat{u}_x(r) e^{i(\omega t - kx)} \quad [6.11]$$

with $\hat{u}_x = \frac{\hat{p}}{\rho c} \left(1 - \frac{J_0 \left(i^{3/2} \alpha \frac{r}{R_0} \right)}{J_0 \left(i^{3/2} \alpha \right)} \right)$, where J_0 is the Bessel function and

$\hat{p} = \sqrt{\pi} K \hat{R}$ is the amplitude of the inlet oscillating pressure, imposed as a boundary condition.

The configuration is a straight elastic tube with the properties reported in Table 6.2. We compute the multi-ring model, which can account for the elasticity of the arterial wall, and compare it to the analytic solution [6.11]. We use $N_r = 32$ rings.

R_0	L	ρ	μ	K	\hat{R}	R_t	T_c	t_f	α
1	200	1	$2\pi \frac{\rho}{T_c} \frac{R_0^2}{\alpha^2}$	10^4	10^{-3}	0	0.5	$12T_c$	{5,20}

Table 6.2. Characteristic parameters of the Womersley velocity profile. R_0 : initial radius, L : tube length, ρ : density, μ : dynamic viscosity, K : elastic coefficient [6.3], \hat{R} : inlet boundary condition, R_t : reflection coefficient, T_c : period, t_f : final time of the simulation, α : Womersley number. All values are in CGS units

We show a comparison between the multi-ring model and the analytic solution [6.11] for a small Womersley number $\alpha = 5$ (Figure 6.3a) and a large Womersley number $\alpha = 20$ (Figure 6.3b). We observe that the multi-ring model accurately reproduces the analytic solution [6.11] for both Womersley numbers. For $\alpha = 5$, the viscous effects dominate over the inertial effects, and we thus obtain a slightly deformed oscillating Poiseuille profile. On the other hand, for $\alpha = 20$, the boundary layer is very small and we obtain a flatter velocity profile that tends to look like the slip condition at the wall.

Womersley (1955) also gives an analytic solution for the flow rate Q and the WSS τ_w . We compute these quantities with the multi-ring model and show the comparison in Figure 6.4. Again, we obtain very good agreement between the multi-ring model and the analytic solution.

In the following section, we compare the reduced models on a real medical configuration, a stenosis.

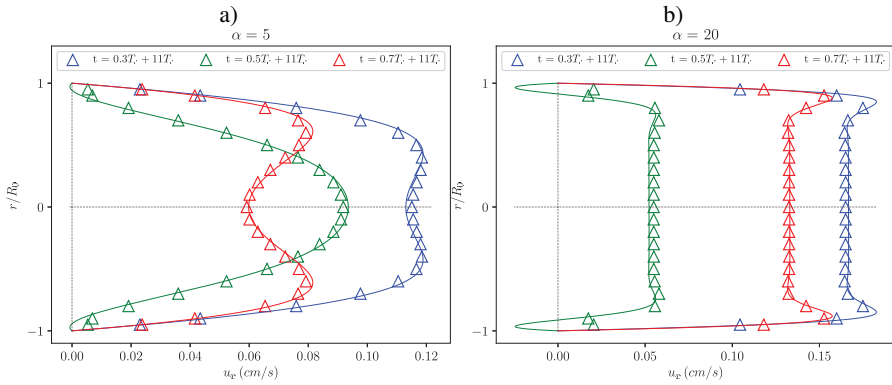


Figure 6.3. Womersley velocity profiles in an elastic tube for a) $\alpha = 5$ and b) $\alpha = 20$. Triangles correspond to the multi-ring model computation, and solid lines correspond to the analytic solution [6.11]. Blue is $t = 0.3T_C + 11T_c$, green is $t = 0.5T_C + 11T_c$ and red is $t = 0.7T_C + 11T_c$. For a color version of this figure, see www.iste.co.uk/deplano/biological.zip

6.4. Application to arterial stenoses

The configuration is an idealized stenosed artery of length L , radius R_0 , stenosis length L_{st} and stenosis degree β , as shown in Figure 6.5. At the inlet of the vessel, we impose a steady input flow, that is, at $x = 0$, $U(t) = U_0$. At the outlet of the vessel, we impose a zero pressure, that is, at $x = L$, $p = 0$. The properties of the configuration are reported in Table 6.3. The shape of the radius of the artery $R(x)$ is

$$R(x) = R_0 \left(1 + \beta \exp \left(-\frac{(x - x_{st})^2}{x_l} \right) \right) \quad [6.12]$$

where x_{st} is the axial position of the throat of the stenosis and x_l is related to the length of the stenosis L_{st} .

We compare the steady RNSP, multi-ring and 1D models in the rigid stenosed artery against the Poiseuille center velocity, center pressure and WSS, as shown in Figures 6.6 a–c, respectively.

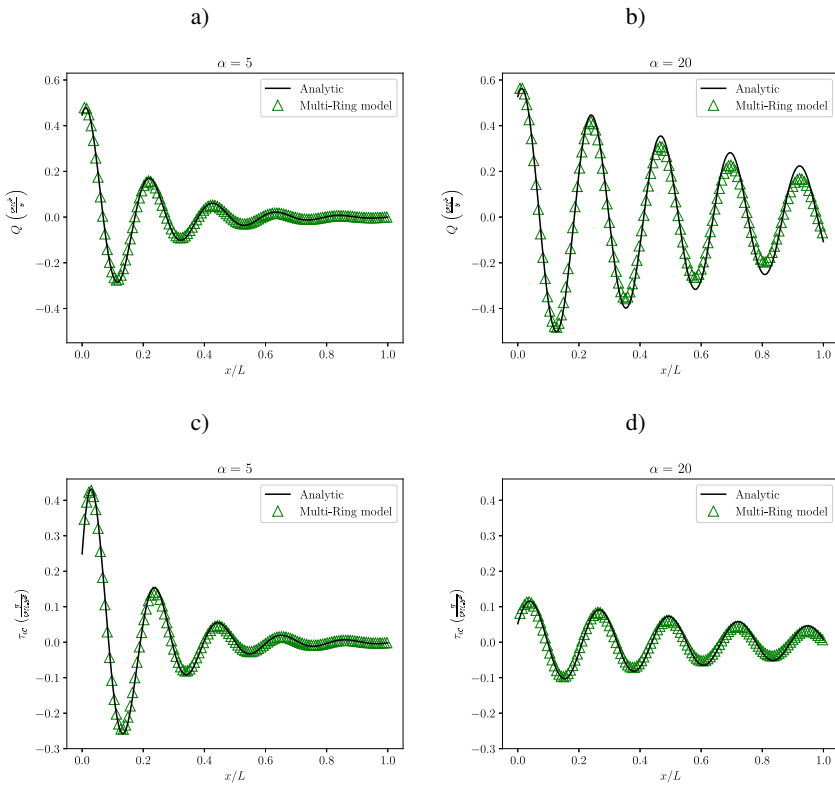


Figure 6.4. Center flow rate Q and WSS τ_w comparison between the multi-ring model (\triangle) and the analytic solution ($—$) for $\alpha = 5$ (a and c) and $\alpha = 20$ (b and d) at $t = 0.3T_c + 11T_c$. For a color version of this figure, see www.iste.co.uk/deplano/biological.zip

R_0	β	L	L_{st}	Re_R	U_0	ρ	$\frac{\mu}{\rho U_0 R_0}$	K
1	-0.4	40	10	100	100	1	$\frac{\mu}{\rho U_0 R_0}$	10^7

Table 6.3. Properties of the stenosed artery. R_0 : initial radius, β : degree of stenosis, L : artery length, L_{st} : stenosis length, Re_R : Reynolds number based on the radius, U_0 : input velocity, ρ : fluid density, μ : dynamic viscosity, K : elastic coefficient [6.3]. All values are in CGS units

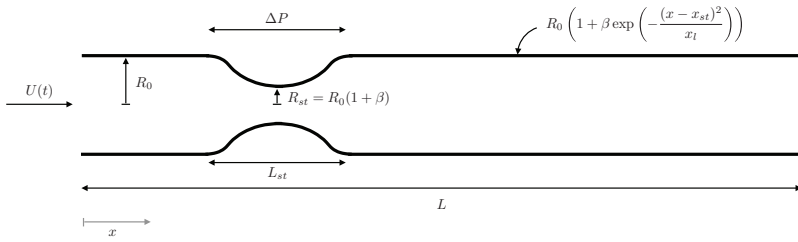


Figure 6.5. Geometry of the stenosed artery of length L , radius R_0 , stenosis length L_{st} and stenosis degree β ($\beta < 0$). The shape of the radius of the wall is equation [6.12], with x_{st} the position of the throat of the stenosis and x_l related to L_{st} . The pressure drop over the length of the stenosis is ΔP

We observe in Figure 6.6b that the center pressure drop between the beginning and the throat of the stenosis is similar in all models. However, the center pressure downstream of the stenosis is different in the 1D model compared to the steady RNSP and the multi-ring. Indeed, the 1D model does not account for the recirculation near the walls and the jet formation in the center of the artery after the stenosis, as can also be seen in Figure 6.6a. One of the assumptions of the 1D model is on the shape of the velocity profile, therefore, the downstream flow is not impacted by the constriction in the 1D model, as opposed to the steady RNSP and multi-ring models. We observe in Figure 6.6b that the steady RNSP and multi-ring models account for the jet and recirculation after the stenosis, which is confirmed by Figure 6.7, in which we show the velocity profiles at different locations in the artery.

Figure 6.6c shows that the WSS computed with the multi-ring and RNSP models is maximal at the throat of the stenosis. Downstream of the constriction, the WSS becomes negative before going back to the Poiseuille value, which characterizes a backflow near the walls downstream of the stenosis.

We verify the presence of this back-flow by plotting the velocity profile in the stenosis using the multi-ring model. The shape of the velocity profile changes when entering the constriction (Figure 6.7d): the magnitude increases and the profile becomes plug-like. The magnitude of the profile is maximal at the throat of the stenosis (Figure 6.7e), that is, at $x = 10$ cm from the entrance. After the throat (Figures 6.7f and g), we observe the formation of a jet in the center. Far from the stenosis (Figure 6.7h), the velocity profile is no longer affected by the constriction and goes back to the initial entry Poiseuille velocity profile, as shown in Figure 6.7a.

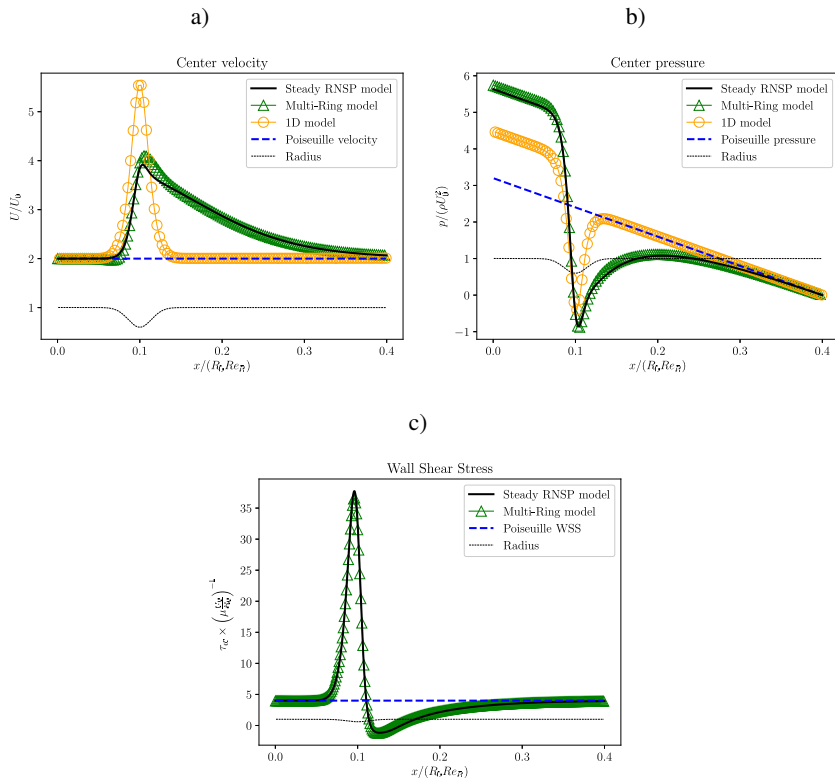


Figure 6.6. Dimensionless center velocity (a), center pressure (b) and WSS along the stenosis (c) represented in Figure 6.5 with properties of Table 6.3. The black solid line (—) corresponds to the steady RNSP model, the green triangles (Δ) to the multi-ring model, the orange circles (\circ) to the 1D model and the dashed blue line (---) to the Poiseuille pressure along a straight tube. The black dotted line ($\cdot \cdot \cdot$) represents the radius $R(x)$ of the artery. For a color version of this figure, see www.iste.co.uk/deplano/biological.zip

The models presented in section 6.2 allow for computing the velocity and pressure fields in the entire domain. However, the relevant indicator for medical diagnosis is the pressure drop ΔP evaluated across the length of the stenosis. Therefore, we compute the pressure drop with the algebraic model from Young and Tsai (1973a), the 1D model, the multi-ring model and the steady RNSP model.

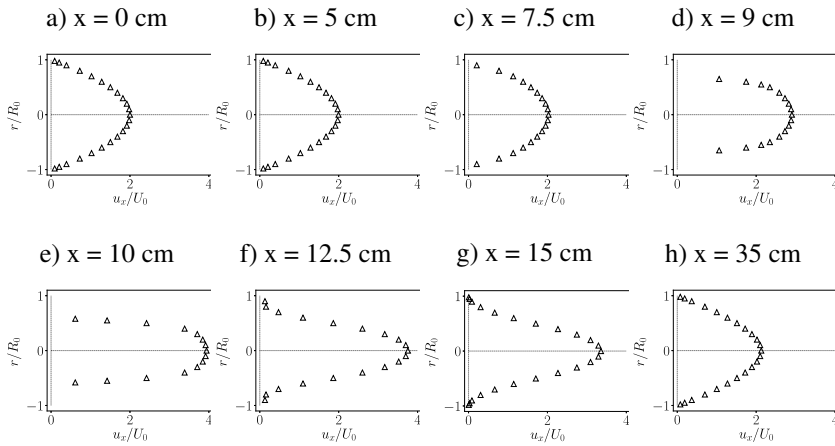


Figure 6.7. Velocity profiles at different locations in the rigid stenosed artery, represented in Figure 6.5 with the properties in Table 6.3, computed with the multi-ring model

We compare our reduced-order models to two sets of in vivo data extracted from two patients with aortic coarctation. We determine geometric properties of the stenosis and the velocity mapping of the aorta using 4D flow MRI (Stankovic *et al.* 2014), carried out with the 1.5-T system (Signa CV/i; GE Healthcare, Milwaukee, USA, Necker Hospital in Paris), knowing already the invasive measurement of pressure gradient across the stenosis (both patients had invasive catheterization during their follow up before MRI study). The characteristics of the invasive data are reported in Table 6.4.

n°	R_0	β	L_{st}	U_0	HR	ΔP
IM1	0.55	-0.28	3	115	61	20
IM2	0.55	-0.47	3.65	79	92	30

Table 6.4. Characteristics of the invasive pressure drop measurements. R_0 : arterial radius, β : degree of stenosis, L_{st} : stenosis length, U_0 : velocity, HR: heart rate in BPM, ΔP : pressure drop between upstream and downstream of the stenosis in mm Hg. All other values are in CGS units

We also compare our models with in vivo pressure drop measurements in animals from Young *et al.* (1975).

In Figure 6.8, we show the dimensionless upstream to downstream pressure drop computed with our four models as a function of the degree of

stenosis. The comparison between the models and the invasive measurements shows that the steady RNSP and multi-ring model are the most accurate in predicting the pressure drop. The 1D model gives a lower estimation, whereas the multi-ring model gives an upper estimation. However, the 1D model remains a relevant first approximation for mild stenoses.

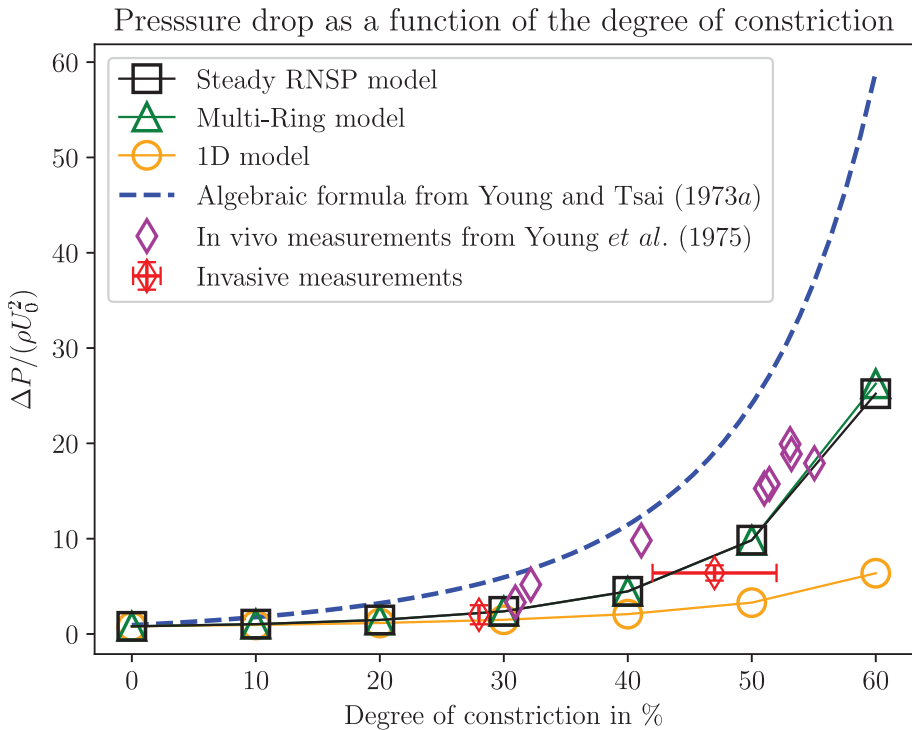


Figure 6.8. Comparison of the dimensionless pressure drop as a function of the degree of constriction expressed in % (i.e. -100β , $\beta < 0$) for the algebraic model from Young and Tsai (1973a), the 1D model (○), the multi-ring model (△), the steady RNSP model (□), in vivo measurements from Young *et al.* (1975) (◇) and arterial catheter invasive measurements (◇). For a color version of this figure, see www.iste.co.uk/deplano/biological.zip

The comparison with in vivo measurements from Young *et al.* (1975) also shows that the steady RNSP and multi-ring are the most accurate models to estimate the pressure drop across the stenosis. However, we can also observe that for mild stenosis, the 1D model gives a reasonable agreement with the in vivo measurements. Even if the 1D model might underestimate the pressure

drop, it is a better starting point than the current algebraic formula with the empirical coefficients of the literature.

6.5. Conclusion

We have described four reduced-order models to compute blood flows, all of them derived from the Navier–Stokes equations and of differing complexity, from 2D to 0D approaches. For the validation, we proposed two classical configurations (entry effect) and Womersley solutions and we compared the models and found an excellent agreement.

As shown by detailed numerical results, the multi-ring model is a relevant approach to be applied on blood flows: first, it reproduced two well-known analytical cases; second, it accounted for the elasticity of the arterial wall and solved the flow with more accuracy than the 1D model but was less computationally expensive than a 3D fluid–structure interaction mode; and third, it accounted for the unsteady effects, unlike the steady RNSP model.

In vivo pressure drop measurements in arterial stenoses provide us with a framework to evaluate the models on a real medical application. We have shown that the multi-ring model is the most accurate compared to the real invasive data.

6.6. References

- Alastruey, J., Khir, A., Matthys, K., Segers, P., Sherwin, S., Verdonck, P., Parker, K., Peiró, J. (2011). Pulse wave propagation in a model human arterial network: Assessment of 1-D visco-elastic simulations against in vitro measurements. *Journal of Biomechanics*, 44, 2250–2258.
- Alastruey, J., Parker, K., Sherwin, S. (2012). Arterial pulse wave hemodynamics. *Proceedings of the 11th International Conference on Pressure Surges*, 30, 401–443, Lisbon, Portugal.
- Audebert, C., Bucur, P., Bekheit, M., Vibert, E., Vignon-Clementel, I.E., Gerbeau, J.-F. (2017). Kinetic scheme for arterial and venous blood flow, and application to partial hepatectomy modeling. *Computer Methods in Applied Mechanics and Engineering*, 314, 102–125.
- Audusse, E., Bristeau, M.-O., Perthame, B., Sainte-Marie, J. (2011). A multilayer Saint-Venant system with mass exchanges for shallow water flows. Derivation and numerical validation. *ESAIM: Mathematical Modelling and Numerical Analysis*, 45(1), 169–200.

- Baumgartner, H., Bonhoeffer, P., De Groot, N.M., de Haan, F., Deanfield, J.E., Galie, N., Gatzoulis, M.A., Gohlke-Baerwolf, C., Kaemmer, H., Kilner, P., Meijboom, F., Mulder, B.J., Oechslin, E., Olivier J.M., Serraf, A., Szatmari, A., Thaulow, E., Vouhe, P.R., Walma, E. (2010). ESC guidelines for the management of grown-up congenital heart disease. *European Heart Journal*, 31(23), 2915–2957.
- Benjamin, E.J., Blaha, M.J., Chiuve, S.E., Cushman, M., Das, S.R., Deo, R., Floyd, J., Fornage, M., Gillespie, C., Isasi, C., Jiménez, M.C., Jordan, L.C., Judd, S.E., Lackland, D., Lichtman, J.H., Lisabeth, L., Liu, S., Longenecker, C.T., Mackey, R.H., Matsushita, K., Mozaffarian, D., Mussolino, M.E., Nasir, K., Neumar, R.W., Palaniappan, L., Pandey, D.K., Thiagarajan, R.R., Reeves, M.J., Ritchey, M., Rodriguez, C.J., Roth, G.A., Rosamond, W.D., Sasson, C., Towfighi, A., Tsao, C.W., Turner, M.B., Virani, S.S., Voeks, J.H., Wiley, J.Z., Wilkins, J.T., Wu, J.H.Y., Alger, H.M., Wong, S.S., Muntner, P. (2017). Heart disease and Stroke statistics – 2017 update: A report from the American Heart Association. *Circulation*, 135(10), e146–e603.
- Delestre, O., Ghigo, A., Fullana, J.-M., Lagrée, P.-Y. (2015). A shallow water with variable pressure model for blood flow simulation. *Networks & Heterogeneous Media*, 11(1), 69–87.
- Ghigo, A.R., Delestre, O., Fullana, J.-M., Lagrée, P.-Y. (2017). Low-Shapiro hydrostatic reconstruction technique for blood flow simulation in large arteries with varying geometrical and mechanical properties. *Journal of Computational Physics*, 331, 108–136.
- Ghigo, A.R., Fullana, J.-M., Lagrée, P.-Y. (2017). A 2D nonlinear multiring model for blood flow in large elastic arteries. *Journal of Computational Physics*, 350, 136–165.
- Kim, H., Vignon-Clementel, I., Coogan, J., Figueroa, C.A., Jansen, K., Taylor, C. (2010). Patient-specific modeling of blood flow and pressure in human coronary arteries. *Annals of Biomedical Engineering*, 38(10), 3195–3209.
- Korteweg, D. (1878). Ueber die fortpflanzungsgeschwindigkeit des schalles in elastischen röhren. *Annalen der Physik*, 241(12), 525–542.
- Lagrée, P.-Y. and Lorthois, S. (2005). The RNS/Prandtl equations and their link with other asymptotic descriptions: Application to the wall shear stress scaling in a constricted pipe. *International Journal of Engineering Science*, 43(3), 352–378.
- Liang, F., Takagi, S., Himeno, R., Liu, H. (2009). Multi-scale modeling of the human cardiovascular system with applications to aortic valvular and arterial stenoses. *Medical & Biological Engineering & Computing*, 47(7), 743–755.
- Moens, A.I. (1878). *Die Pulscurve*. E.J. Brill, Leiden.

- Quarteroni, A., Veneziani, A., Vergara, C. (2016). Geometric multiscale modeling of the cardiovascular system, between theory and practice. *Computer Methods in Applied Mechanics and Engineering*, 302, 193–252.
- Seeley, B.D. and Young, D.F. (1976). Effect of geometry on pressure losses across models of arterial stenoses. *Journal of Biomechanics*, 9(7), 439–448.
- Sherwin, S.J., Franke, V., Peiró, J., Parker, K. (2003). One-dimensional modelling of a vascular network in space-time variables. *Journal of Engineering Mathematics*, 47(3–4), 217–250.
- Stergiopoulos, N., Young, D., Rogge, T. (1992). Computer simulation of arterial flow with applications to arterial and aortic stenoses. *Journal of Biomechanics*, 25(12), 1477–1488.
- Van Dyke, M. (1964). *Perturbation Methods in Fluid Mechanics*. Academic Press, New York.
- Ventre, J., Politi, M.T., Fernández, J., Ghigo, A., Gaudric, J., Wray, S., Lagaert, J., Armentano, R., Capurro, C., Fullana, J., Lagree, P.Y. (2019). Parameter estimation to study the immediate impact of aortic cross-clamping using reduced order models. *International Journal for Numerical Methods in Biomedical Engineering*, e3261.
- Vignon-Clementel, I.E., Marsden, A.L., Feinstein, J.A. (2010). A primer on computational simulation in congenital heart disease for the clinician. *Progress in Pediatric Cardiology*, 30(1–2), 3–13.
- Warnes, C.A., Williams, R.G., Bashore, T.M., Child, J.S., Connolly, H.M., Dearani, J.A., del Nido, P., Fasules, J.W., Graham Jr., T.P., Hijazi, Z.M., Hunt, S.A., King, M.E., Landzberg, M.J., Miner, P.D., Radford, M.J., Walsh, E.P., Webb, G.D. (2008). ACC/AHA 2008 guidelines for the management of adults with congenital heart disease: Executive summary. *Journal of the American College of Cardiology*, 52(23), 1890–1947.
- Womersley, J.R. (1955). XXIV. Oscillatory motion of a viscous liquid in a thin-walled elastic tube I: The linear approximation for long waves. *The London, Edinburgh, and Dublin Philosophical Magazine and Journal of Science*, 46(373), 199–221.
- Xiao, N., Humphrey, J.D., Figueroa, C.A. (2013). Multi-scale computational model of three-dimensional hemodynamics within a deformable full-body arterial network. *Journal of Computational Physics*, 244, 22–40.
- Young, D.F. and Tsai, F.Y. (1973a). Flow characteristics in models of arterial stenoses I. Steady flow. *Journal of Biomechanics*, 6(4), 395–402.

- Young, D.F. and Tsai, F.Y. (1973b). Flow characteristics in models of arterial stenoses II. Insteady flow. *Journal of Biomechanics*, 6(5), 547–559.
- Young, D.F., Cholvin, N.R., Roth, A.C. (1975). Pressure drop across artificially induced stenoses in the femoral arteries of dogs. *Circulation Research*, 36(6), 735–743.

YALES2BIO: A General Purpose Solver Dedicated to Blood Flows

**Simon MENDEZ¹, Alain BÉROD^{1,2}, Christophe CHNAFA^{1,2},
Morgane GARREAU^{1,3}, Etienne GIBAUD¹, Anthony LARROQUE¹,
Stephanie LINDSEY¹, Marco MARTINS AFONSO¹,
Pascal MATTÉOLI¹, Rodrigo MENDEZ ROJANO¹,
Dorian MIDOU¹, Thomas PUISEUX^{1,3}, Julien SIGÜENZA^{1,2},
Pierre TARACONAT^{1,4}, Vladeta ZMIJANOVIC¹ and
Franck NICOUD¹**

¹IMAG, CNRS, University of Montpellier, France

²Sim&Cure, Montpellier, France

³ALARA Expertise, Strasbourg, France

⁴Horiba Medical, Grabels, France

Many cardiovascular diseases are related to blood flow features, and are able to predict how blood flows could open a door toward better diagnostic and treatment capabilities. To this respect, computational physics is complementary to theoretical, experimental and medical imaging techniques used to address questions related to either microscopic or macroscopic blood flows.

Many (medical) questions related to blood flows are relevant to the biggest arteries/veins of the cardiovascular system. The typical length scale ranges from 1 mm to a few centimeters and the typical Reynolds number can be as high as a few thousands. At these scales, blood is practically considered

For a color version of all the figures in this chapter, see www.iste.co.uk/deplano/biological.zip.

Biological Flow in Large Vessels,

coordinated by Valérie DEPLANO, José-Maria FULLANA, Claude VERDIER. © ISTE Ltd 2022.

Biological Flow in Large Vessels: Dialog Between Numerical Modeling and In Vitro/In Vivo Experiments,
First Edition. Valérie Deplano; José-Maria Fullana and Claude Verdier.

© ISTE Ltd 2022. Published by ISTE Ltd and John Wiley & Sons, Inc.

as a homogeneous fluid with either constant viscosity (typically $\mu = 3 \times 10^{-3}$ Pa.s) or characterized by a shear-thinning behavior. Typical issues that must be properly handled are then related to the highly complex and deformable geometry of the domain where blood flows, the transitional nature of the wall-bounded blood flow, the interaction with thin and highly deformable membranes (e.g. valve leaflets), thrombus formation due to the presence of biomedical materials and, of course, validation.

Blood is actually not homogeneous, but a dense (volume fraction in the range 20–50%) suspension of particles, ranging from 2 (platelets) to 20 μm (white blood cells) in size. More than 95% of the cells flowing in plasma are actually red blood cells, which are non-spherical (equivalent diameter 6 μm) particles. Because their reduced volume is only 0.65, red blood cells are highly deformable, their dynamics resulting from the coupling between the inner fluid (cytosol), the membrane of the cell and the outer fluid (plasma). In flow regimes typical of the micro-circulation, hemodynamics is dominated by suspension-related phenomena such as the non-inertial migration of red blood cells toward the center of the vessels.

This chapter describes some achievements and current modeling efforts based on the YALES2BIO solver (see: imag.umontpellier.fr/~yales2bio/) developed at IMAG (Montpellier, France). A short account about the numerical strategy is provided in section 7.1, where some validation test cases are also described. Examples of simulations performed to support modeling efforts are then provided in section 7.2, while section 7.3 gathers two industrial applications. Eventually, some on-going developments are described in section 7.4.

7.1. Methods and validation

YALES2BIO is a massively parallel multiphysics solver based on the YALES2 solver (see: www.coria-cfd.fr/index.php/YALES2) developed at CORIA (Rouen, France). YALES2BIO is dedicated to the simulation of blood flows at the macroscopic and microscopic scales. The base is a solver for the incompressible Navier–Stokes equations. The equations are discretized using a finite-volume fourth-order scheme, adapted to unstructured meshes (Moureau *et al.* 2011a,b). The divergence-free property of the velocity field is ensured thanks to the projection method introduced by Chorin (1968). The velocity field is first advanced in time using a low-storage fourth-order Runge–Kutta scheme (Moureau *et al.* 2011b, Chnafa *et al.* 2014) in a prediction step. This predicted field is then corrected by a pressure

gradient, obtained by solving a Poisson equation to calculate pressure. This equation is solved using the Deflated Preconditioned Conjugate Gradient algorithm (Malandain *et al.* 2013). For turbulence modeling, large-eddy simulations (LESs) are performed using the so-called sigma subgrid scale model (Nicoud *et al.* 2011), which guarantees that no eddy viscosity is applied for canonical laminar flows, and is well-suited to wall-bounded, as well as transitional flows (Nicoud *et al.* 2018). Computations may be performed with moving meshes, with an arbitrary Lagrangian–Eulerian formulation being used in such cases (Chnafa *et al.* 2014, 2016).

Several YALES2BIO simulations involve fluid–structure interaction, both at the macroscopic (Sigüenza *et al.* 2018) and microscopic scales (Lanotte *et al.* 2016, Mendez and Abkarian 2018). For fluid–structure coupling, YALES2BIO relies on Peskin’s immersed boundary method (IBM) (Peskin 2002) for massless structures. The action of the structure is seen by the fluid as a force density applied in the prediction step. Forced Navier–Stokes equations are solved as described in the former paragraph. Once the flow velocity is calculated, the structure is simply convected by the flow, after the interpolation of the fluid velocity on the structure. The deformed structure being massless, it is always at equilibrium, which enables the calculation of forces at the nodes of the structure mesh. These forces are then regularized (or spread) over the fluid mesh. The original IBM, developed for Cartesian meshes has been adapted to unstructured meshes to comply with the data structure of YALES2BIO. This has been performed using the reproducing kernel particle method, which guarantees that the regularization and interpolation operators are coherent and reproduce a number of mathematical moments of the regularized/interpolated functions (Liu *et al.* 1995, Pinelli *et al.* 2010, Mendez *et al.* 2014). The cellular membrane mechanics are modeled by combining different models representing either the in-plane or out-of-plane resistances of the membrane (Skalak *et al.* 1973, Helfrich 1973). More details may be found in Mendez and Abkarian (2019). The method, originally developed for infinitely thin membranes, has also been extended to finite-size yet thin structures (Sigüenza *et al.* 2016, 2018). Numerous validation test cases have been presented in 2D (Mendez *et al.* 2014) and 3D (Sigüenza *et al.* 2016), in particular for the fluid–structure interaction coupling.

Our aim in confronting numerical results to reference data is not only to confirm the quality of the solver, but also to provide new understanding on the configuration. As an example, we developed new analytical solutions for the case of an inertial relaxation of a membrane immersed in fluid (Martins Afonso *et al.* 2014). Three other examples of advanced validation cases are

discussed in the remainder of this section to illustrate how simulating for validation may actually shed new light on the computed case itself.

7.1.1. Food and Drug Administration case

The configuration is the one proposed by the Food and Drug Administration (FDA) as a benchmark for computational fluid dynamics (CFD) in the context of biomedical engineering. It has been studied both experimentally and numerically by several independent research groups worldwide (Hariharan *et al.* 2011, Stewart *et al.* 2012). The geometry is axisymmetric with a long inlet section, a convergent nozzle, a throat section (10 diameters long) and a sudden expansion at the downstream end. The jet generated into the sudden expansion section may break down and become turbulent sooner or later depending on the flow regime. Five flow regimes were considered experimentally, ranging from fully laminar to fully turbulent and corresponding to $Re_{th} = 500; 2000; 3500; 5000; 6500$ (Re_{th} is the Reynolds number based on the bulk velocity and throat diameter). From a turbulence modeling point of view, LES is better suited than the RANS approach to deal with flow situations at a moderate Reynolds number. It turns out that none of the 28 blinded, RANS-based CFD studies led to a good comparison with the FDA experimental results (Stewart *et al.* 2012), while more successful LES-based computations were achieved after the experimental results were released (Passerini *et al.* 2013, Delorme *et al.* 2013, Bhushan *et al.* 2013, Janiga 2014). This observation and the absence of sensitivity analysis in the successful, not-blinded studies question the actual predictive character of these simulations. YALES2BIO was thus used to address the robustness of the FDA simulation (Zmijanovic *et al.* 2017, Nicoud *et al.* 2018). The main outcome of this study is that a proper LES strategy can indeed reproduce the experimental results with good accuracy and for all of the flow regimes (from laminar to turbulent), as soon as small perturbations are superimposed to the inlet velocity profile. In the absence of inlet perturbations, the results are extremely sensitive (and thus neither robust nor predictive) to any numerical parameters, such as the numerical scheme, mesh topology and refinement or time step (see Figure 7.1 for an illustration). The necessity to inject perturbations at inlet in order to obtain robust and predictive simulations of the FDA configuration was recently demonstrated by another research group using a different numerical tool (Bergersen *et al.* 2019).

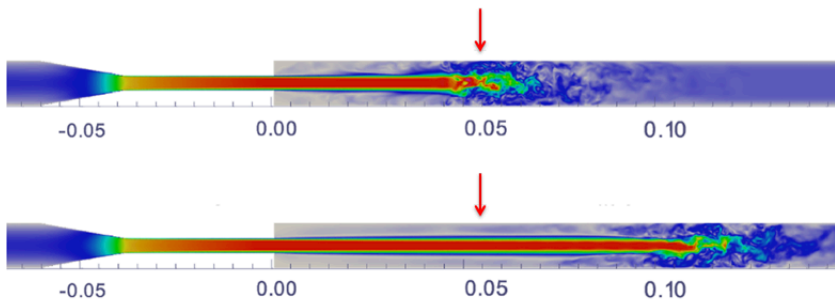


Figure 7.1. Velocity map in the FDA nozzle showing the jet generated in the downstream pipe. The location of the jet breakdown (transition from laminar to turbulent) is well captured when a small time step is used ($CFL = 0.1$, top view), but not when a larger, yet numerically admissible, value is selected ($CFL = 0.6$, bottom view). The red arrow shows the position of the jet breakdown as observed in the experiment (Hariharan *et al.* 2011)

7.1.2. Optical tweezers

The validation of a solver dedicated to the dynamics of red blood cells (RBCs) is a challenge as it mixes physical complexity with biological complexity. In general, the validation includes fluid–structure interaction test cases with simpler particles such, as vesicles or spherical capsules (Yazdani *et al.* 2011, Barthès-Biesel 2009, 2016). It also relies on static cases in which the membrane mechanics alone are probed. This explains the success of the optical tweezers experiment (Dao *et al.* 2003, Mills *et al.* 2004) for validation (Li *et al.* 2005, Dao *et al.* 2006, Pivkin and Karniadakis 2008, Le *et al.* 2009, Fedosov *et al.* 2010a,b, Klöppel and Wall 2011, Chen and Boyle 2014, Farutin *et al.* 2014, Sinha and Graham 2015). In this configuration, two microbeads are attached on opposite sides of the RBC rim. One is fixed to a glass slide and the other one is controlled by a laser beam, which allows it to be displaced. The intensity of the laser beam allows the maximum force applied on the microbead to be fixed. The RBC is thus stretched by displacing the second beam with different forces. The sizes of the deformed RBC are measured in the direction of the stretching and in the normal direction, so that force-deformation curves can be obtained.

Simulations of a RBC stretched by optical tweezers have been performed using the YALESBIO solver (Sigüenza *et al.* 2017), with excellent comparisons with the experimental data from Mills *et al.* (2004). In addition, we clarified the meaning of this validation. It had been clearly shown that RBC simulations of the optical tweezers stretching are very sensitive to the

membrane shear modulus (Mills *et al.* 2004). However, the dependence to other deformation modes of the membrane was unclear. We first performed simulations with and without bending resistance (not shown) and changing the resistance to area stretching (see Figure 7.2(a)). We showed that results were rather insensitive to such parameters. As a result, this means that this validation test case can only assess the accuracy of the model representing the resistance to shear deformations of the membrane, and not the whole membrane model.

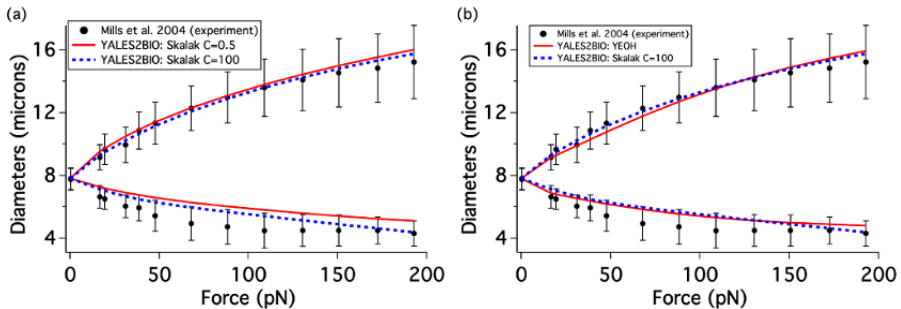


Figure 7.2. Comparison of long and small diameters in the plane of view of an RBC stretched by optical tweezers, between simulations and experiments. a) Simulations with the same in-plane Skalak model using different values of C , the ratio between the area modulus and the shear modulus and b) simulations with the Skalak model with $C = 100$ and the Yeoh model (Mills *et al.* 2004)

In addition, we showed that very different models could yield similar results, as shown in Figure 7.2(b), where results using either the Skalak model or the Yeoh model (see Mills *et al.* (2004), Sigüenza *et al.* (2017)) are compared. Both models align well. However, with the Yeoh model, the area of the RBC membrane increases by 30% (see Sigüenza *et al.* (2017)), which is impossible in RBCs. In addition, in order to obtain this fair comparison, the shear modulus of the Yeoh model has to be twice as large than that used with the Skalak model. The results presented by Sigüenza *et al.* (2017) thus show how cautious we have to be when using the optical tweezers for validation or assessment of the membrane mechanics. As detailed by Dimitrakopoulos (2012), this experiment focuses on large deformations of the cell. It is thus not a good configuration for assessing the shear modulus of the membrane, which is characteristic of small deformations: the value of the shear modulus inferred by the simulations depends on the model used. If the same membrane model is used, it is a good configuration to compare the resistance of different cells, but not the resistances to bending or area changes. Note, however, that the 3D shape of the RBC depends on such parameters, so that

more detailed 3D data from the experiment could yield a more thorough validation case for simulations (Sigüenza *et al.* 2017).

7.1.3. Red blood cell self-organization

The YALESBIO solver can also be run with multiple cells. The validation of this capability has been demonstrated by Iss *et al.* (2019), where the self-organization of RBCs in a rectangular channel has been computed. Iss *et al.* (2019) have shown that in microfluidic channels of height $9\ \mu\text{m}$ and width 30 and $60\ \mu\text{m}$, RBCs self-organize in trains and lines at preferred distances from the lateral walls. Numerical simulations of RBC suspensions at different hematocrit values were performed in a periodic channel until convergence was reached in terms of structure, and compared to experimental images captured at the end of a 5-mm-long channel (see Figure 7.3). Simulations predict how RBCs organize in one, two or three files with increasing hematocrit well, as in the experiment. The essential role of deformability and lateral walls was also proved by numerical simulations. More details can be found in Iss *et al.* (2019).

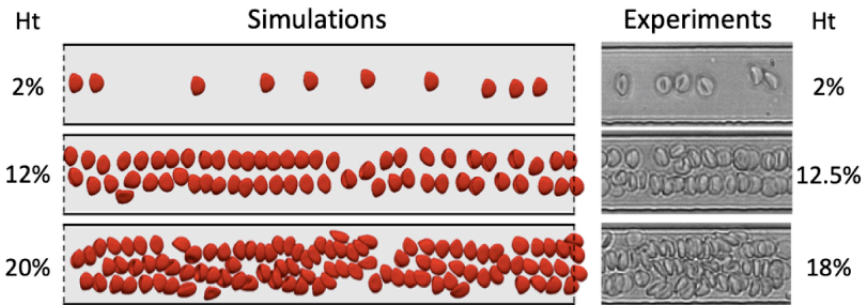


Figure 7.3. Example of the structure of the flow in one, two or three lines for RBC suspensions at different hematocrits in a channel of height $9\ \mu\text{m}$ (direction normal to the image) and width $30\ \mu\text{m}$ (vertical direction). RBCs flow from left to right. Figure adapted from Iss *et al.* (2019)

7.2. Simulation as support of modeling efforts

An interesting use of a flow solver is the generation of reference data as part of a modeling effort. With the increase in computing resources, more and more computationally demanding simulations become feasible, but the need for simplified models remains. In this context, numerical simulations may provide well-controlled data for building new low-order models to either

understand a particular phenomenon, account for some effect at a moderate cost in simulations or validate data reconstruction algorithms. This section provides some examples of the use of YALES2BIO simulations to support modeling.

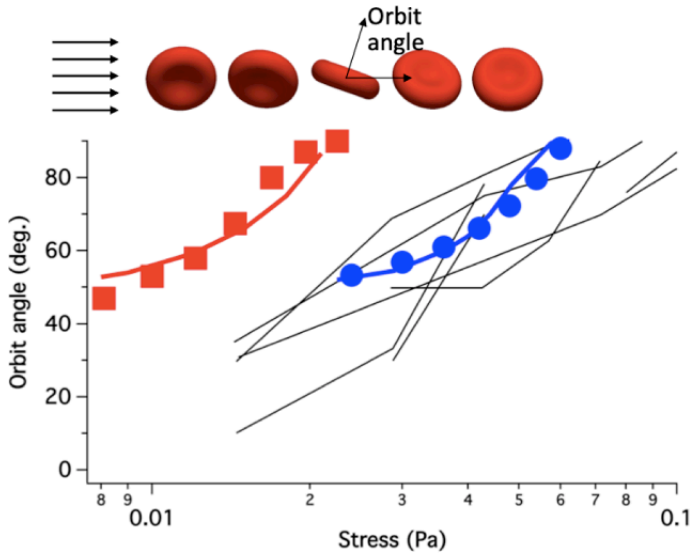


Figure 7.4. Orbit angles of RBCs flipping under shear flow, as a function of the shear rate, at viscosity contrast 1.0. Black lines: experiments from Dupire *et al.* (2012). Symbols: YALES2BIO simulations for different stress-free shapes (red: quasi-sphere of reduced volume 0.997; blue: ellipsoid of reduced volume 0.96). Bold continuous lines: reduced-order model (Mendez and Abkarian 2018) changing the energy barrier to mimic the change of stress-free shape. The definition of the orbit angle is provided in the sequence of images extracted from a top view of the dynamics of a RBC flipping over an orbit

7.2.1. Single cell dynamics

One fascinating aspect of the dynamics of red blood cells in shear flow (Mendez and Abkarian 2019) is their behavior at low shear stresses, for which RBCs exhibit very different motions without major deformations (Dupire *et al.* 2012). The absence of RBC deformations actually led to the consideration that their movement could be described by models developed for the motion of rigid objects, and in particular the model of Jeffery (1922), which predicts the motion of a rigid ellipsoid in shear flow. However, recent experiments have shown that contrary to rigidified RBCs, healthy RBCs flip

under shear over a specific orbit that depends on the shear rate. While the in-plane elasticity associated with the cytoskeleton was suspected to be a key element in the orbital selection and orbital drift, it was demonstrated for the first time by numerical simulations (Mendez and Abkarian 2018), by changing the stress-free shape of the cytoskeleton, which in turn controls the energy barrier that has to be overcome for the membrane to tank-tread (Abkarian *et al.* 2007). The effect is illustrated in Figure 7.4, which shows how the orbital drift (change of angle with shear rate) depends on the stress-free shape. This motivated the development of a low-order model reproducing all of the motions of RBCs at low shear rates (Mendez and Abkarian 2018). This model considers a fixed-shaped ellipsoid with a membrane that is able to tank-tread around it. By providing the appropriate modeling for the membrane elasticity, it displays all of the expected features of RBCs at low stresses, where deformation remains small: an example is the orbital drift predicted by such a model and displayed in Figure 7.4. This model opens the door to new theoretical developments in terms of RBC dynamics and blood flows.

7.2.2. Flow diverters

An intracranial aneurysm is an abnormal deformation of the arterial wall occurring in 3.6–6% of the general population, according to the systematic review by Rinkel *et al.* (1998). Since the prognosis¹ of subarachnoid hemorrhage is still very low, preventive surgery prior to rupture is considered as a therapeutic option by physicians (Hackenberg *et al.* 2018). Among all of the available treatments, flow-diverting type of devices are widely used due to their high rate of success (76%), low procedure-related morbidity (5%) and mortality (4%) (Brinjikji *et al.* 2013). The aim of these devices is to isolate the aneurysm from the parent artery blood flow, in order to promote a stable environment for thrombus formation (D’Urso *et al.* 2011). CFD has been extensively used to extract relevant indices that could discriminate successful and unsuccessful treatments (Ouaed *et al.* 2016). To simulate the hemodynamic effect of a deployed flow-diverter inside patient-specific arterial geometries, two major techniques arise in the literature: *conformal* and *porous*. The first one subtracts the volume taken by the struts of the device from the arterial mesh. As struts are small compared to the size of the aneurysm, this leads to heavy computational costs. In order to reduce these costs, the porous method originally developed in Augsburg *et al.* (2010) uses a homogeneous approach by approximating the device as a porous

¹ Predicting the likelihood of a person’s survival.

material that imposes calibrated pressure losses through its surface via volumetric source terms added to the Navier–Stokes equations. Despite being computationally less expensive, the porous method requires an initial calibration and does not reproduce the effect of each strut on the flow. To circumvent these issues, a novel technique that is halfway between the conformal and porous methods has been developed and implemented in YALES2BIO (Alain *et al.* 2021). This framework has been compared to a “gold-standard” conformal computation of a steady flow through a patient-specific aneurysm. The results depicted in Figure 7.5 show that the implemented model compares reasonably well to the conformal results both locally near the wires and globally in the intra-aneurysmal recirculating region. The effort is currently geared toward validating this strategy using other conformal computations with different patient-specific and device geometries.

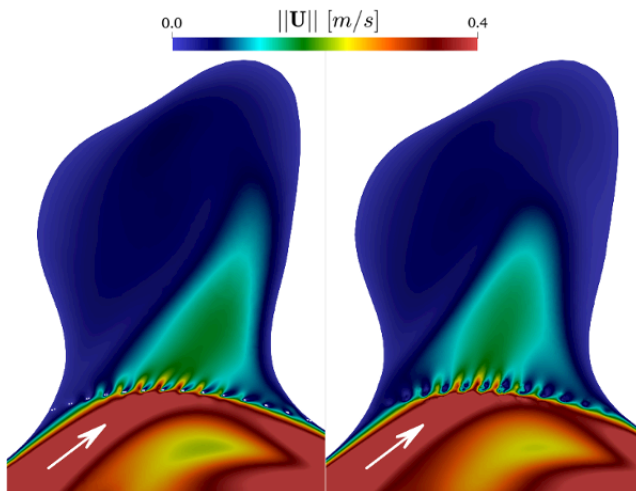


Figure 7.5. Blood velocity magnitude in an aneurysm treated by a flow diverter, accounting for the device using a conformal approach (left) or a model (right). The white arrows show the mean flow direction

7.2.3. Echocardiography

YALES2BIO was used to produce the intra-cardiac flow compatible with the time-evolving geometry observed from either the computed tomography of an actual patient (Chnafa *et al.* 2014) or magnetic resonance imaging of a normal volunteer (Chnafa *et al.* 2016). In both cases, the computational

domain extends from the four pulmonary veins to the root of the aorta and includes the left atrium and ventricles, as well as rough models of the mitral and aortic valves. The LESs were based on a subgrid scale model well suited to represent wall-bounded transitional flows (Nicoud *et al.* 2011) and performed over more than 50 cardiac cycles. The analysis revealed that turbulence is periodically generated in the left ventricle at the end of the diastole and washed out during systole (Chnafa *et al.* 2015). Moreover, the large vortex observed from advanced medical imaging techniques (Markl *et al.* 2011) at late diastole is well retrieved in the phase-averaged computational results. This flow feature is of particular interest from a medical point of view (it helps to redirect blood momentum toward the outlet of the ventricle and facilitates ejection) and being able to characterize it from routine echocardiography would be a useful feature for cardiologists. This requires being able to reconstruct the intra-ventricular velocity field from the knowledge of the radial component measured in color Doppler mode. The numerical database for the intraventricular flow (Chnafa *et al.* 2014) was used to support the development of a reconstruction algorithm based on an optimization procedure (Assi *et al.* 2017). As illustrated in Figure 7.6, the CFD recirculation zone is fairly well retrieved.

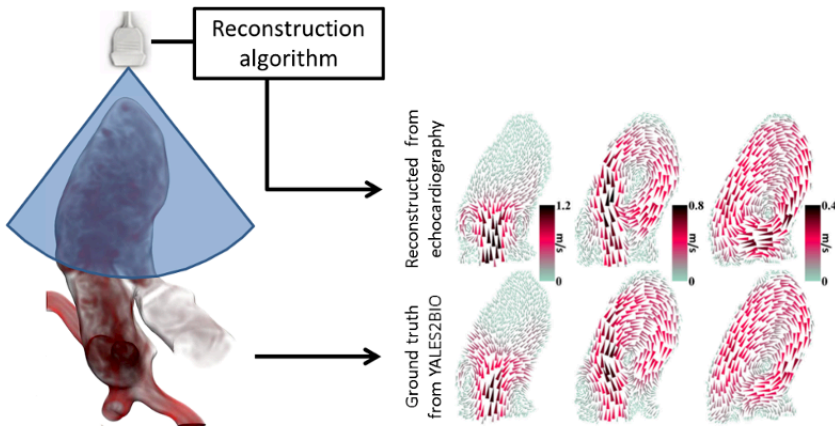


Figure 7.6. Left: a virtual echocardiography exam is made on the numerical intra-cardiac flow. Right: the flow structure reconstructed from the virtual echocardiography image (top) is compared to the exact flow structure from the numerical database (bottom) at three different instants

7.3. Simulations for industrial applications

7.3.1. Flow in the Carmat artificial heart

Since YALES2BIO relies on fully unstructured and parallelized numerical methods, it has the potential to tackle complex industrial configurations. A typical example is the total artificial heart developed by Carmat (see: www.carmat.com), which, from a fluid mechanics point of view, relies on the interaction between a biomimetic membrane and a working fluid operated by two rotating pumps to alternatively suck and push blood as an actual heart would do. Of course, the complexity of this blood-wetted device goes beyond the fluid–structure interaction problem, and ensuring the reliability of the control system and keeping the thrombogenic risk at a low level are other paramount issues to deal with when developing such a device. Still, handling the three elements (working oil, membrane, blood) fluid–structure problem in a complex geometry under pulsatile conditions is already quite challenging and was done using YALES2BIO (Larroque 2015). As an illustration, the membrane shape is shown at two instants in Figure 7.7. Note that the actual flow domain was truncated in this case (the casing where the two rotating pumps are located was not represented) and that the membrane dynamics were computed thanks to the LMGC90 software (Radjai and Dubois 2011) coupled with YALES2BIO, as detailed in Sigüenza *et al.* (2016). The ability of the YALES2BIO-LMGC90 coupling to handle macroscopic fluid–structure interaction problems accurately was demonstrated elsewhere (Sigüenza *et al.* 2016, 2018).

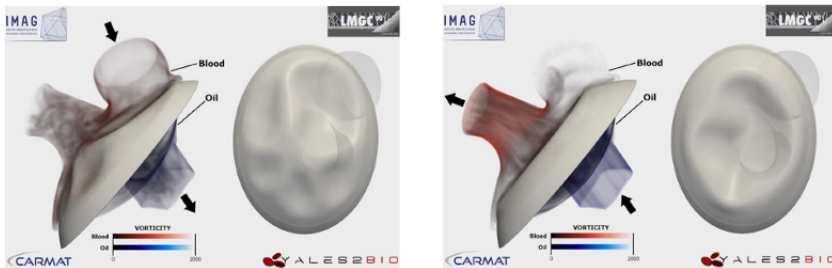


Figure 7.7. 3D view of the flow and membrane shape in a geometry inspired by the Carmat artificial heart during diastole (left) and systole (right). The black arrows show the mean flow direction. The red and blue color scales denote blood and oil (working fluid) vorticity renderings, respectively

7.3.2. Red blood cell dynamics in Horiba Medical's blood analyzers

In a collaborative work between HORIBA Medical and IMAG, the impedance measurement of red blood cells in an industrial hematology analyzer was investigated (Taraconat *et al.* 2019). The configuration consists of a polarized micro-orifice in which RBCs are aspirated one at a time. This constriction generates a high electrical field in the aperture so that the presence of the RBC induces an increase in electrical resistance that can be detected as voltage pulse. Numbering the electrical prints provides a count of cells that crossed the micro-orifice, and the amplitudes of the perturbations are assumed to be proportional to the particles size. Also known as the “Coulter counter” (Coulter 1953), this system thus yields measurements of the RBCs volumes and concentration. Coulter counters have been implemented in blood analyzers for decades, but some measurement artifacts are still misunderstood. In the neighborhood of the aperture walls, inhomogeneities of the electrical field and complex RBCs dynamics lead to measurement errors. Studying the dynamics of particles in the detection area to understand these edge-effects is an intricate task because industrial systems suffer from accessibility issues. This is why numerical simulation was preferred for investigations.

Handling the simulation of deforming cells in a Coulter counter involves a challenge that is multi-scale in nature, and has been overcome by a specific sequence of simulations, as proposed by Taraconat *et al.* (2019). The proposed method was compared with experimental measurements obtained from a healthy blood sample and a latex bead sample (see Figure 7.8). Numerical results not only reproduce the experimental observations, but also provide indications for the understanding of the complex signatures that arise when particles evolve in the wall vicinity. On the one hand, electrical edge-effects occur when particles encounter regions of highly heterogeneous electrical fields, near the aperture corner (see the blue circles in Figure 7.8). On the other hand, dynamical edge-effects consist of a cell rotation induced by substantial velocity shear located near the aperture walls (see the black arrows in Figure 7.8). Both types of artifacts impact the electrical prints, but they may be stratified thanks to the simulations (Taraconat *et al.* 2021).

7.4. Current developments

Most of the current challenges involve multi-physics and/or multi-scale situations. Three examples are provided in this section: modeling developments for the prediction of thrombotic events, modeling of the

velocity measurement by 4D flow magnetic resonance imaging (MRI) and the extension of YALES2BIO to dense suspensions of RBCs.

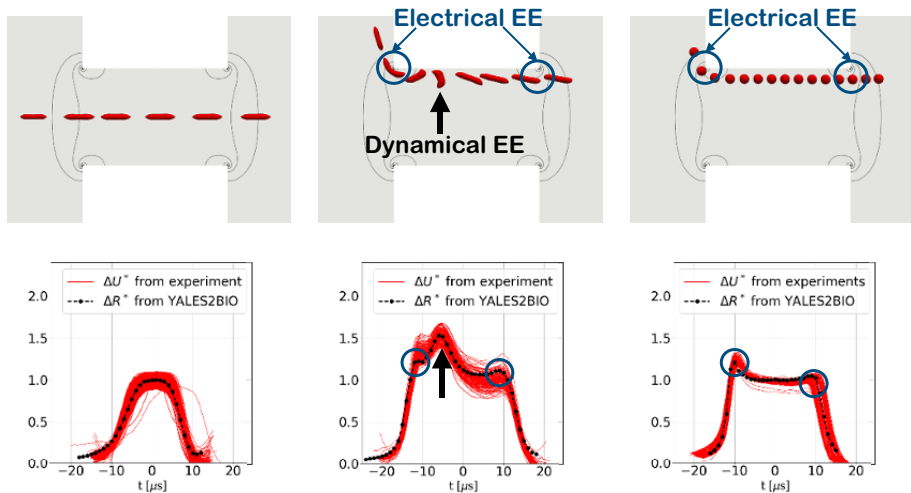


Figure 7.8. The top row illustrates the simulated RBC dynamics in the micro-orifice, while the associated electrical perturbations are displayed in the bottom row. Electrical pulses arising from simulations are superimposed with experimental observations in the bottom row. The left, middle and right columns correspond to an RBC on a centered path, a RBC on a near-wall path and a rigid sphere on a near-wall path, respectively. Electrical field isolines are shown over the cut view of the fluid domain in the particle dynamics pictures in the top row. Electrical and dynamical edge-effects (EE) are highlighted by blue circles and black arrows, respectively

7.4.1. Thrombosis

A major issue with blood-coated medical devices is their trend to produce extra blood coagulation (thrombosis) that may lead to device malfunction or thromboembolism (Manning *et al.* 2021). The adsorption/activation of the coagulation factor XII (Hageman factor) by the artificial surfaces of the devices is thought to be a key mechanism in this respect. A biochemical scheme (Chatterjee *et al.* 2010) was recently implemented in YALES2BIO to model thrombin generation by contact activation of factor XII with the device wall. To reflect mass conservation, a proper boundary condition was introduced that relates the species diffusive wall flux to the surface reaction rate of factor XII activation:

$$D\nabla_n[XII_a] + k_s[XII] = 0 \quad [7.1]$$

In this equation, $[\cdot]$ is a molar fraction, ∇_n is the gradient operator along the direction normal to a solid boundary, XII_a is the activated form of factor XII , D stands for the species diffusivity in whole blood and k_s is a material property (surface reaction rate). This boundary condition contrasts with what is used in conventional in vivo models, in which the coagulation cascade is initiated at user-defined and arbitrary injury sites. This strategy was applied to a backward facing step geometry (Mendez Rojano *et al.* 2018) and a significant amount of thrombin was generated in the recirculation zone, as expected. Coupled to an existing model that represents platelet activity and thrombus growth (Taylor *et al.* 2016), the approach developed leads to a predictive pipeline for device-related thrombosis. This is illustrated in Figure 7.9, which shows that the generation of the thrombus is well captured, as well as its growth. Interestingly, this result was obtained without *a priori* knowledge of the regions prone to thrombosis: Equation 7.1 was prescribed in the same way everywhere and the appearance (or not) of a thrombus is controlled locally by the chemical-to-flow time scales ratio (a thrombus may only form if the fluid flow is slow enough to allow thrombin generation). Current research efforts are devoted to the reduction of the biochemical scheme (Chatterjee *et al.* 2010) used to predict thrombin formation (Mendez Rojano *et al.* 2019).

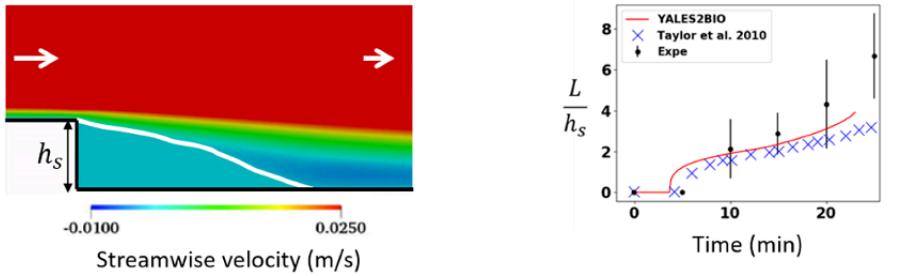


Figure 7.9. Left: velocity map and boundary of the thrombus (thick white line). The white arrows show the mean flow direction. Right: time evolution of the length of the thrombus that appears behind the step, as observed in the experiment (Taylor *et al.* 2014)

7.4.2. In Silico MRI

Time-resolved 3D phase-contrast MRI (3D PCMRI, also called 4D flow MRI) is a promising tool for non-invasive blood flow quantification in vivo. As it relies on complex physical principles and the multi-modal acquisition

process, different types of velocity measurement errors arise, which might impair the diagnosis. A way to identify the origins of these measurement errors consists of numerically simulating the MRI experiment, governed by the Bloch equations (Bloch 1946), in order to reconstruct synthetic images that are exempt from experimental errors. However, the large variety of time scales generally induced by coupling the MRI equations to the flow motion, as well as the considerable acquisition times to simulate (of order 1000 s, say), results in prohibitive computational costs and largely contributes to making the simulations infeasible.

An Eulerian-Lagrangian 4D flow MRI simulation pipeline was developed, which benefits from the massively parallel capabilities of the YALES2BIO solver to solve the Bloch equations on Lagrangian particles with “on the fly” coupling to the CFD flow solver (Puisseux 2021). A semi-analytic formulation of the Bloch equations was proposed to accelerate the computations, and a specific particle injection strategy was implemented that uses the periodic removal of the transverse magnetization (RF-spoiling) to keep the particle distribution homogeneous and avoid zones of spurious signal. The coupling with the YALES2BIO solver was validated in several configurations (Puisseux 2021). A cardiovascular-like in vitro flow phantom was designed and integrated to a MRI-compatible experimental test bench (Puisseux *et al.* 2019). Several PC-MRI experiments were carried out and post-corrected from imaging artifacts. The compatible image-based CFD analysis was performed, prescribing the PC-MRI measurements as inlet velocity profiles. The CFD velocity field was downsampled to match the MRI spatiotemporal resolution, and compared to the experimental MRI velocity, resulting in 97% velocity correlations (Puisseux *et al.* 2019). Finally, coupled 4D flow MRI simulation was performed and the corresponding in silico velocity images were reconstructed and compared to the input CFD velocity field to validate the full simulation pipeline (see Figure 7.10). Both the experimental and simulated MRI velocity fields were compared with the downsampled CFD velocity field. As shown in Figure 7.10, the sites of largest velocity error seem well reproduced by the MRI simulation, although a systematically higher error is reported in the experimental MRI. We suggest that the large error site at the collateral-descending tube junction is a direct consequence of neglecting the acceleration in 4D flow MRI sequences. The remaining systematic error can be attributed to the experimental noise due to magnetic field inhomogeneities and off-resonance effects that are not accounted for in the MRI simulations.

7.4.3. Multi-cells

YALES2BIO is also extended to perform multi-cells simulations, as illustrated by the simulations of suspensions in microfluidic channels (Iss *et al.* 2019) already mentioned in the validation section. The aim is now to understand the relationship between single-cell behavior in shear flow, the motions of the cells in suspension and the macroscopic outcome, such as blood rheology, for instance. In particular, we have shown that RBCs in plasma subjected to increasing shear stress become more and more folded and compact (Mauer *et al.* 2018), which has beneficial effects on blood rheology, as demonstrated experimentally (Lanotte *et al.* 2016). Simulations may provide the explanation for this effect. In addition, our interpretation of blood dynamics is often driven by the knowledge on single cells. Systematic studies of the effect of increasing the concentration are still needed to determine to which extent single cell dynamics can be used to explain blood results. With this in mind, YALES2BIO now has the capability of performing multi-cells simulations, and computation in pure shear flow is currently being performed (see Figure 7.11) at various hematocrit levels.

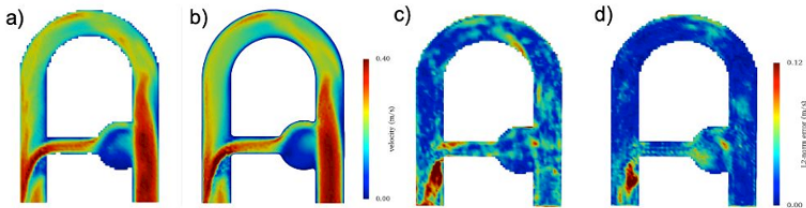


Figure 7.10. Left: magnitude of the velocity a) reconstructed by MRI simulation and b) predicted by CFD at peak systole. Right: velocity L2-norm error reported for c) experimental MRI and d) simulated MRI, as compared to CFD

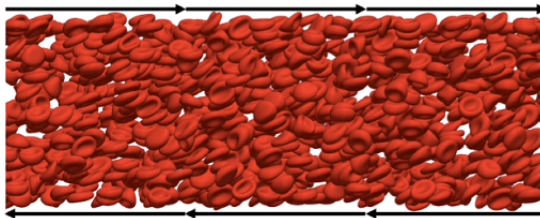


Figure 7.11. RBC suspension under shear flow, at physiological viscosity contrast and shear rate 100 s^{-1} . Hematocrit is 12.5%

7.5. Acknowledgments

The authors thank the ANR, the I-SITE Muse and the BPI for their support through the Laboratory of Excellence NUMEV (ANR-10-LABX-20), the FORCE (ANR-11-JS09-0011), the GLOBULE and the DAT@DIAG (ISI-I1112018W) projects. Dr. Moureau, Dr. Lartigue (CORIA, UMR 6614) and the SUCCESS scientific group are gratefully acknowledged for giving access to the YALES2 solver. This work was performed using HPC resources from GENCI-CINES (grants c2014037194 to c2016037194, A0020307194, A0040307194, and A0060307194) and from the platform MESO@LR.

7.6. References

- Abkarian, M., Faivre, M., Viallat, A. (2007). Swinging of red blood cells under shear flow. *Physical Review Letters*, 98, 188302.
- Alain, B., Chnafa, C., Mendez, S., Nicoud, F. (2021). A heterogeneous model of endovascular devices for the treatment of intracranial aneurysms. *International Journal for Numerical Methods in Biomedical Engineering* (in press) [Online]. Available at: <https://doi.org/doi.org/10.1002/cnm.3552>.
- Assi, K., Gay, E., Chnafa, C., Mendez, S., Nicoud, F., Abascal, J., Lantelme, P., Tournoux, F., Garcia, D. (2017). Intraventricular vector flow mapping a Doppler-based regularized problem with automatic model selection. *Physics in Medicine & Biology*, 62(17), 7131–7147.
- Augsburger, L., Reymond, P., Rufenacht, D.A., Stergiopulos, N. (2010). Intracranial stents being modeled as a porous medium: Flow simulation in stented cerebral aneurysms. *Annals of Biomedical Engineering*, 39(11), 850–863.
- Barthès-Biesel, D. (2009). Capsule motion in flow: Deformation and membrane buckling. *Comptes rendus physique*, 10(8), 764–774.
- Barthès-Biesel, D. (2016). Motion and deformation of elastic capsules and vesicles in flow. *Annual Review of Fluid Mechanics*, 48, 25–52.
- Bergersen, A.W., Mortensen, M., Valen-Sendstad, K. (2019). The FDA nozzle benchmark: In theory there is no difference between theory and practice, but in practice there is. *International Journal for Numerical Methods in Biomedical Engineering*, 35(1), 1–10.
- Bhushan, S., Walters, D., Burgreen, G. (2013). Laminar, turbulent, and transitional simulations in benchmark cases with cardiovascular device features. *Cardiovascular Engineering and Technology*, 4(4), 408–426.
- Bloch, F. (1946). Nuclear induction. *Phys. Rev.*, 70(7–8), 460–474.

- Brinjikji, W., Murad, M.H., Lanzino, G., Cloft, H.J., Kallmes, D.F. (2013). Endovascular treatment of intracranial aneurysms with flow diverters. *Stroke*, 44(2), 442–447.
- Chatterjee, M.S., Denney, W.S., Jing, H., Diamond, S.L. (2010). Systems biology of coagulation initiation: Kinetics of thrombin generation in resting and activated human blood. *PLoS Computational Biology*, 6(9), e1000950.
- Chen, M. and Boyle, F.J. (2014). Investigation of membrane mechanics using spring networks: Application to red-blood-cell modelling. *Materials Science and Engineering C*, 43, 506–516.
- Chnafa, C., Mendez, S., Nicoud, F. (2014). Image-based large-eddy simulation in a realistic left heart. *Computers and Fluids*, 94, 173–187.
- Chnafa, C., Mendez, S., Moreno, R., Nicoud, F. (2015). Using image-based CFD to investigate the intracardiac turbulence. In *Modeling the Heart and the Circulatory System. MS&A, Volume 14*, Quarteroni, A. (ed.). Springer International Publishing, New York.
- Chnafa, C., Mendez, S., Nicoud, F. (2016). Image-based simulations show important flow fluctuations in a normal left ventricle: What could be the implications? *Annals of Biomedical Engineering*, 44(11), 3346–3358.
- Chorin, A. (1968). Numerical solution of the Navier–Stokes equations. *Mathematics of Computation*, 22, 745–762.
- Coulter, W.H. (1953). Means for counting particles suspended in a fluid. Patent #US2656508A.
- Dao, M., Lim, C.T., Suresh, S. (2003). Mechanics of the human red blood cell deformed by optical tweezers. *Journal of the Mechanics and Physics of Solids*, 51, 2259–2280.
- Dao, M., Li, J., Suresh, S. (2006). Molecularly based analysis of deformation of spectrin network and human erythrocyte. *Materials Science and Engineering C*, 26, 1232–1244.
- Delorme, Y., Anupindi, K., Frankel, S. (2013). Large eddy simulation of FDA’s idealized medical device. *Cardiovascular Engineering and Technology*, 4(4), 392–407.
- Dimitrakopoulos, P. (2012). Analysis of the variation in the determination of the shear modulus of the erythrocyte membrane: Effects of the constitutive law and membrane modeling. *Physical Review E*, 85, 041917.
- Dupire, J., Socol, M., Viallat, A. (2012). Full dynamics of a red blood cell in shear flow. *Proceedings of the National Academy of Sciences USA*, 109(51), 20808–20813.

- D'Urso, P.I., Lanzino, G., Cloft, H.J., Kallmes, D.F. (2011). Flow diversion for intracranial aneurysms. *Stroke*, 42(8), 2363–2368.
- Farutin, A., Biben, T., Misbah, C. (2014). 3D numerical simulations of vesicle and inextensible capsule dynamics. *Journal of Computational Physics*, 275, 539–568.
- Fedosov, D.A., Caswell, B., Karniadakis, G. (2010a). Systematic coarse-graining of spectrin-level red blood cell models. *Computer Methods in Applied Mechanics and Engineering*, 199, 1937–1948.
- Fedosov, D.A., Caswell, B., Karniadakis, G.E. (2010b). A multiscale red blood cell model with accurate mechanics, rheology, and dynamics. *Biophysical Journal*, 98, 2215–2225.
- Hackenberg, K.A., Hänggi, D., Etminan, N. (2018). Unruptured intracranial aneurysms. *Stroke*, 49(9), 2268–2275.
- Hariharan, P., Giarra, M., Reddy, V., Day, S., Manning, K., Deutsch, S., Stewart, S., Myers, M., Berman, M., Burgreen, G., Paterson, E., Malinauskas, R. (2011). Multilaboratory particle image velocimetry analysis of the FDA benchmark nozzle model to support validation of computational fluid dynamics simulations. *Journal of Biomechanical Engineering*, 133(4), 041002.
- Helfrich, W. (1973). Elastic properties of lipid bilayers: Theory and possible experiments. *Z. Naturforsch*, 28, 693–703.
- Iss, C., Midou, D., Moreau, A., Held, D., Charrier, A., Mendez, S., Viallat, A., Helfer, E. (2019). Self-organization of red blood cell suspensions under confined 2D flows. *Soft Matter*, 15, 2971–2980.
- Janiga, G. (2014). Large eddy simulation of the FDA benchmark nozzle for a Reynolds number of 6500. *Computers in Biology and Medicine*, 47(April), 113–119.
- Jeffery, G.B. (1922). The motion of ellipsoidal particles immersed in a viscous fluid. *Proceedings of the Royal Society of London, Series A*, 102(715), 161–179.
- Klöppel, T. and Wall, W.A. (2011). A novel two-layer, coupled finite element approach for modeling the nonlinear elastic and viscoelastic behavior of human erythrocytes. *Biomechanics and Modeling in Mechanobiology*, 10, 445–459.
- Lanotte, L., Mauer, J., Mendez, S., Fedosov, D.A., Fromental, J.-M., Claveria, V., Nicoud, F., Gompper, G., Abkarian, M. (2016). Red cells' dynamic morphologies govern blood shear thinning under microcirculatory flow conditions. *Proceedings of the National Academy of Sciences USA*, 113(47), 13289–13294.
- Larroque, A. (2015). Haemodynamic simulations in a total artificial heart. Technical report, Université Paris-Sud & IMAG, Université de Montpellier.
- Le, D.V., White, J., Péraire, J., Lim, K.M., Khoo, B.C. (2009). An implicit immersed boundary method for three-dimensional fluid-membrane interactions. *Journal of Computational Physics*, 228, 8427–8445.

- Li, J., Dao, M., Lim, C.T., Suresh, S. (2005). Spectrin-level modeling of the cytoskeleton and optical tweezers stretching of the erythrocyte. *Biophysical Journal*, 88, 3707–3719.
- Liu, W.K., Jun, S., Zhang, Y.F. (1995). Reproducing kernel particle methods. *International Journal for Numerical Methods in Fluids*, 20, 1081–1106.
- Malandain, M., Maheu, N., Moureau, V. (2013). Optimization of the deflated conjugate gradient algorithm for the solving of elliptic equations on massively parallel machines. *Journal of Computational Physics*, 238, 32–47.
- Manning, K.B., Nicoud, F., Susan, M.S. (2021). Mathematical and computational modeling of device-induced thrombosis. *Current Opinion in Biomedical Engineering*, 20, 100349 [Online]. Available at: <https://doi.org/10.1016/j.cobme.2021.100349>.
- Markl, M., Kilner, P.J., Ebberts, T. (2021). Comprehensive 4D velocity mapping of the heart and great vessels by cardiovascular magnetic resonance. *J. Cardiovasc. Magn. Reson.*, 13(1), 7.
- Martins Afonso, M., Mendez, S., Nicoud, F. (2014). On the damped oscillations of an elastic quasi-circular membrane in a two-dimensional incompressible fluid. *Journal of Fluid Mechanics*, 746, 300–331.
- Mauer, J., Mendez, S., Lanotte, L., Nicoud, F., Abkarian, M., Gompper, G., Fedosov, D.A. (2018). Flow-induced transitions of red blood cell shapes under shear. *Physical Review Letters*, 121, 118103.
- Mendez, S. and Abkarian, M. (2018). In-plane elasticity controls the full dynamics of red blood cells in shear flow. *Physical Review Fluids*, 3, 101101(R).
- Mendez, S. and Abkarian, M. (2019). Single red blood cell dynamics in shear flow and their role in hemorheology. In *Dynamics of Blood Cell Suspensions in Microflows*, Mendez, S., Abkarian, M. (eds). CRC Press, Boca Raton.
- Mendez, S., Gibaud, E., Nicoud, F. (2014). An unstructured solver for simulations of deformable particles in flows at arbitrary Reynolds numbers. *Journal of Computational Physics*, 256, 465–483.
- Mendez Rojano, R., Mendez, S., Nicoud, F. (2018). Introducing the pro-coagulant contact system in the numerical assessment of device-related thrombosis. *Biomechanics and Modeling in Mechanobiology*, 17(3), 815–826.
- Mendez Rojano, R., Mendez, S., Lucor, D., Ranc, A., Giansily-Blaizot, M., Schved, J.-F., Nicoud, F. (2019). Biomechanics and modeling in mechanobiology kinetics of the coagulation cascade including the contact activation system: Sensitivity analysis and model reduction. *Biomechanics and Modeling in Mechanobiology*, 18(4), 1139–1153.

- Mills, J.P., Qie, L., Dao, M., Lim, C.T., Suresh, S. (2004). Nonlinear elastic and viscoelastic deformation of the human red blood cell with optical tweezers. *Mechanics & Chemistry of Biosystems*, 1(3), 169–180.
- Moureau, V., Domingo, P., Vervisch, L. (2011a). Design of a massively parallel CFD code for complex geometries. *Comptes rendus mécanique*, 339(2–3), 141–148.
- Moureau, V., Domingo, P., Vervisch, L. (2011b). From large-eddy simulation to direct numerical simulation of a lean premixed swirl flame: Filtered laminar flame-PDF modelling. *Combustion and Flame*, 158, 1340–1357.
- Nicoud, F., Baya Toda, H., Cabrit, O., Bose, S., Lee, J. (2011). Using singular values to build a subgrid-scale model for large eddy simulations. *Physics of Fluids*, 23(8), 085106.
- Nicoud, F., Chnafa, C., Siguenza, J., Zmijanovic, V., Mendez, S. (2018). Large-eddy simulation of turbulence in cardiovascular flows. In *Biomedical Technology. Lecture Notes in Applied and Computational Mechanics, Volume 84*, Wriggers, P., Lenarz, T. (eds). Springer, Cham [Online]. Available at: https://doi.org/10.1007/978-3-319-59548-1_9.
- Ouared, R., Larrabide, I., Brina, O., Bouillot, P., Erceg, G., Yilmaz, H., Lovblad, K.O., Mendes Pereira, V. (2016). Computational fluid dynamics analysis of flow reduction induced by flow-diverting stents in intracranial aneurysms: A patient-unspecific hemodynamics change perspective. *Journal of NeuroInterventional Surgery*, 8, 1288–1293.
- Passerini, T., Quaini, A., Villa, U., Veneziani, A., Canic, S. (2013). Validation of an open source framework for the simulation of blood flow in rigid and deformable vessels, 29(11), 1192–1213.
- Peskin, C.S. (2002). The immersed boundary method. *Acta Numerica*, 11, 479–517.
- Pinelli, A., Naqavi, I.Z., Piomelli, U., Favier, J. (2010). Immersed-boundary methods for general finite-difference and finite-volume Navier–Stokes solvers. *Journal of Computational Physics*, 229, 9073–9091.
- Pivkin, I.V. and Karniadakis, G.E. (2008). Accurate coarse-grained modeling of red blood cells. *Physical Review Letters*, 101, 118105.
- Puiseux, T., Sewonu, A., Meyrignac, O., Rousseau, H., Nicoud, F., Mendez, S., Moreno, R. (2019). Reconciling PC-MRI and CFD: An in-vitro study. *NMR in Biomedicine*, 32(5), e4063 [Online]. Available at: <https://hal.archives-ouvertes.fr/hal-01962356>. [Accessed 12 February 2019].
- Puiseux, T., Sewonu, A., Moreno, R., Mendez, S., Nicoud, F. (2021). Numerical simulation of time-resolved 3D phase-contrast magnetic resonance imaging. *PLoS ONE*, 16(3), e0248816 [Online]. Available at: <https://doi.org/10.1371/journal.pone.0248816>. [Accessed 12 February 2019].

- Radjai, F. and Dubois, F. (2011). *Discrete Numerical Modeling of Granular Materials*. ISTE Ltd, London, and John Wiley and Sons, New York.
- Rinkel, G.J.E., Djibuti, M., Algra, A., van Gijn, J. (1998). Prevalence and risk of rupture of intracranial aneurysms. *Stroke*, 29(1), 251–256.
- Sigüenza, J., Mendez, S., Ambard, D., Dubois, F., Jourdan, F., Mozul, R., Nicoud, F. (2016). Validation of an immersed thick boundary method for simulating fluid-structure interactions of deformable membranes. *Journal of Computational Physics*, 322, 723–746.
- Sigüenza, J., Mendez, S., Nicoud, F. (2017). How should the optical tweezers experiment be used to characterize the red blood cell membrane mechanics? *Biomechanics and Modeling in Mechanobiology*, 16(5), 1645–1657.
- Sigüenza, J., Pott, D., Mendez, S., Sonntag, S., Kaufmann, T., Steinseifer, U., Nicoud, F. (2018). Fluid-structure interaction of a pulsatile flow with an aortic valve model: A combined experimental and numerical study. *International Journal for Numerical Methods in Biomedical Engineering*, 34(4), 1–19.
- Sinha, K. and Graham, M.D. (2015). Dynamics of a single red blood cell in simple shear flow. *Physical Review E*, 92, 042710.
- Skalak, R., Tozeren, A., Zarda, R.P., Chien, S. (1973). Strain energy function of red blood cell membranes. *Biophysical Journal*, 13, 245–264.
- Stewart, S., Paterson, E., Burgreen, G., Hariharan, P., Giarra, M., Reddy, V., Day, S., Manning, K., Deutsch, S., Berman, M., Myers, M., Malinauskas, R., Berman, M., Malinauskas, R. (2012). Assessment of CFD performance in simulations of an idealized medical device: Results of FDA’s first computational interlaboratory study. *Cardiovascular Engineering and Technology*, 3(2), 139–160.
- Taraconat, P., Gineys, J.-P., Isèbe, D., Nicoud, F., Mendez, S. (2019). Numerical simulation of deformable particles in a Coulter counter. *International Journal for Numerical Methods in Biomedical Engineering* [Online]. Available at: <https://onlinelibrary.wiley.com/doi/10.1002/cnm.3243>. [Accessed 2 August 2019].
- Taraconat, P., Gineys, J.-P., Isèbe, S., Nicoud, F., Mendez, S. (2021). Detecting cells rotations for increasing the robustness of cell sizing by impedance measurements, with or without machine learning. *Cytometry*, 99(10), 977–86 [Online]. Available at: <https://doi.org/10.1002/cyto.a.24356>.
- Taylor, J.O., Witmer, K.P., Neuberger, T., Craven, B.A., Meyer, R.S., Deutsch, S., Manning, K.B. (2014). In vitro quantification of time dependent thrombus size using magnetic resonance imaging and computational simulations of thrombus surface shear stresses. *Journal of Biomechanical Engineering*, 136(7), 1–11.

- Taylor, J.O., Meyer, R.S., Deutsch, S., Manning, K.B. (2016). Development of a computational model for macroscopic predictions of device-induced thrombosis. *Biomechanics and Modeling in Mechanobiology* [Online]. Available at: <http://link.springer.com/10.1007/s10237-016-0793-2>.
- Yazdani, A.Z.K., Kalluri, R.M., Bagchi, P. (2011). Tank-treading and tumbling frequencies of capsules and red blood cells. *Physical Review E*, 83, 046305.
- Zmijanovic, V., Mendez, S., Moureau, V., Nicoud, F. (2017). About the numerical robustness of biomedical benchmark cases: Interlaboratory FDA's idealized medical device. *International Journal for Numerical Methods in Biomedical Engineering*, 33(1), 1–17 e02789.

8

Capsule Relaxation Under Flow in a Tube

**Bruno SARKIS¹, Anne-Virginie SALSAC² and
José-Maria FULLANA³**

¹*Sorbonne University, Paris and Université de Technologie de Compiègne, France*

²*Université de Technologie de Compiègne, France*

³*Institut Jean Le Rond d'Alembert, CNRS UMR 7190,
Sorbonne University, Paris, France*

8.1. Introduction

A capsule is a mixed object consisting of a solid envelope surrounding an internal substance at its core. A wide variety of materials, both natural and bio-artificial, can be used for encapsulation purposes to create the envelope and protect the internal medium. Depending on the materials constituting it and its thickness, the capsule wall can range from a simple membrane that is thin (as thin as a few nanometers for lipid layers), ultra-flexible and fragile, to a rigid shell. Its ability to protect the internal medium from the inner environment will depend on its mechanical strength and permeability. Indeed, the membrane plays the triple role of vector for the capsule core, protective barrier and controller of the exchanges between the internal substance and the outer medium.

Capsules are ubiquitous and extremely varied in their natural state. In the viral kingdom, the genetic material of most viruses is enclosed in a protective shell called a capsid, obtained by the structured assembly of sets of proteins

Biological Flow in Large Vessels,

coordinated by Valérie DEPLANO, José-Maria FULLANA, Claude VERDIER. © ISTE Ltd 2022.

Biological Flow in Large Vessels: Dialog Between Numerical Modeling and In Vitro/In Vivo Experiments,
First Edition. Valérie Deplano; José-Maria Fullana and Claude Verdier.

© ISTE Ltd 2022. Published by ISTE Ltd and John Wiley & Sons, Inc.

called capsomeres. In multicellular organisms, capsules are used, for example, in reproduction, in the form of spores and eggs, or in blood circulation, in the form of circulating cells such as red and white blood cells and platelets, which are cells fragments. Other forms of encapsulation are also found in the circulation, such as cholesterol transport by lipoproteins.

In most examples, the primary role of capsules is to allow vectorization, which consists of modulating and controlling the distribution of an active principle to a specific target. The control may be spatial, temporal or quantitative. Many studies have focused on the encapsulation of active principles, such as anti-cancer drugs for targeted chemotherapy (Desai *et al.* 2010, Singh *et al.* 2010, Sato *et al.* 2011, Henning *et al.* 2012, Zhang *et al.* 2013, Yan *et al.* 2016). Capsules also have a wide variety of industrial applications, in the food, textile, cosmetic, hygiene, mechanical and automotive sectors, but also in environmental applications, for instance, for depollution. The number of applications for artificial capsules continues to increase, but decades of work to develop artificial red blood cells, and, more generally, artificial blood, demonstrate the difficulty in developing vectors capable of withstanding hydrodynamic stresses in the circulation.

Understanding the flow dynamics of microcapsules in a confined environment and being able to determine and control the mechanical properties of the membrane are of great importance in the context of encapsulation and controlled release of active agents. Despite the inherent difficulty in characterizing the elastic properties of these small fragile objects, different experimental approaches have been designed to deform microcapsules under a known force. These are divided into two groups: techniques such as atomic force microscopy (Dubreuil *et al.* 2003, Ivanovska *et al.* 2004), micropipette aspiration (Fery and Weinkamer 2007), compression between two parallel plates (Carin *et al.* 2003, Bando and Yamaguchi 2017) and stretching with optical tweezers (Helfer *et al.* 2000) are applied on individual microcapsules, while other techniques are used to test entire capsule populations: generally, these consist of placing capsule suspensions under flow in microfluidic channels (Hu *et al.* 2013, Loubens *et al.* 2014) or under extension flows (Loubens *et al.* 2015). But these studies only enable quantification of the elastic properties of the membrane. In order to trace back to viscoelastic properties, the transient behavior of capsules needs to be studied. Gires *et al.* (2016) studied the flow of microcapsules through a microfluidic channel with a step and a cross-section that suddenly changed from square to rectangular. They demonstrated that it is possible to identify the elastic properties from the steady shape that the capsule takes in the square part of the channel, and the membrane viscosity from the

relaxation time once it enters the rectangular part. But no complete model of the relaxation of a capsule in such a channel can be found in the literature.

The purpose of this work is to propose a numerical method of fluid–structure coupling to characterize the relaxation of a microcapsule as it flows through a channel with a change in cross-section for comparison with the measurements from Gires *et al.* (2016), but also to extend the study to the Navier–Stokes inertial regime. The capsule is modeled as a droplet enclosed in a zero-thickness membrane with hyperelastic behavior. The fluid–structure interactions are solved by coupling a finite-volume fluid solver (Popinet 2009) with a finite-element solid solver performing Lagrangian tracking of the position of the capsule membrane material points (Walter *et al.* 2010). Coupling is performed using the immersed boundary method (IBM) (Peskin 2002b).

After detailing the numerical method and validating the results, we will study the temporal evolution of capsule deformation and the fluid flow structure induced by capsule relaxation in the step cross-section. We will consider the case of Stokes flows, and then the case where internal and external fluid inertia is taken into account. Finally, we will show that indicators of the capsule relaxation after the step can be predicted by reduced models of the inertial Kelvin–Voigt type.

8.2. Overview of the physical problem

Let us consider an initially spherical liquid-core capsule with a radius a_0 , suspended in a fluid of the same density ρ and viscosity μ as the inner fluid. The capsule membrane has an elastic resistance characterized by a surface shear modulus G_s . The membrane is assumed to be without thickness, and devoid of bending stiffness and membrane viscosity.

The capsule is placed in a microchannel composed of a squared cross-section $2l \times 2l$ of length L ($L/l = 16$) connected to a co-axial portion with a rectangular cross-section $2l \times 4l$ along axes Oy and Oz , respectively, and of length L according to Ox (Figure 8.1). The capsule is initially positioned at a distance of $2l$ from the channel inlet. For aspect ratios $a_0/l > 0.9$, the capsule is pre-deformed into an ellipsoid of revolution before being inserted into the channel (Hu *et al.* 2012, 2013). In the study, we focus on a capsule with an aspect ratio $a_0/l = 1.1$, pre-deformed into an ellipsoid of half-major axis $1.5a_0$ and half-minor axes $a_0/\sqrt{1.5}$. The coordinate system, whose axis Ox is oriented in the direction of flow, is centered on the

initial position of the capsule center of gravity. The step is located at $x/l = 14$.

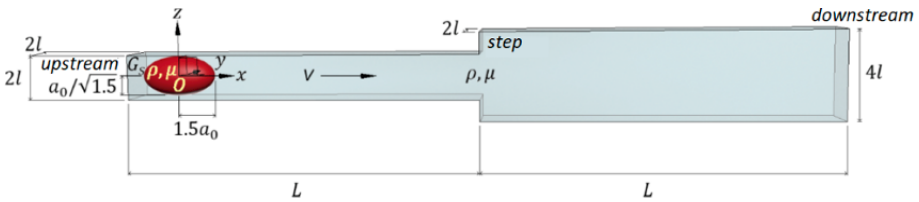


Figure 8.1. Geometry of the micro-channel composed of a square cross-section ($2l \times 2l$) opening onto a co-axial portion with a rectangular cross-section ($4l \times 2l$). For a color version of this figure, see www.iste.co.uk/deplano/biological.zip

The capsule is set in motion by a Poiseuille flow of mean velocity V , imposed at the inlet. The characteristic time scale is therefore l/V , giving the dimensionless time $\tilde{t} = tV/l$. For numerical simulations under Stokes conditions, the pressure scale is $\mu V/l$, giving the dimensionless pressure $\tilde{p} = pl/\mu V$.

The dimensionless numbers controlling the flow of the capsule into the square channel are

- the aspect ratio a_0/l ;
- the capillary number $Ca = \mu V/G_s$, the ratio between elastic and viscous forces;
- the Reynolds number $Re = \rho V l/\mu$.

8.2.1. Fluid solver

The fluid solver, detailed in Popinet (2009), numerically solves the dimensionless incompressible Navier–Stokes equation given by

$$\begin{cases} \partial_t \mathbf{v} + (\mathbf{v} \cdot \nabla) \mathbf{v} = -\nabla p + \frac{1}{Re} \Delta \mathbf{v} + \mathbf{f} \\ \nabla \cdot \mathbf{v} = 0 \end{cases} \quad [8.1]$$

where \mathbf{v} is the velocity and p is the pressure. The Reynolds number, $Re = \rho V l/\mu$, is the dimensionless number that characterizes the ratio between inertial and viscous forces. The density ρ and viscosity μ are assumed to be constant. The source term \mathbf{f} is used to pass the capsule

deformation forces, which are solutions of the solid solver described in section 8.2.2.

The Stokes equations are obtained by neglecting the nonlinear inertia term. Formally, we multiply [8.1] by Re , and non-dimensionalize time and pressure by their respective viscous scale ($T_\mu = \mu l^2 / \rho = Re T_V$ et $P_\mu = \mu V / l = P_V / Re$) to obtain the unsteady Stokes equation.

$$\begin{cases} \partial_t \mathbf{v} = -\nabla p + \Delta \mathbf{v} + \mathbf{f} \\ \nabla \cdot \mathbf{v} = 0 \end{cases} \quad [8.2]$$

The boundary conditions imposed at the inlet and outlet of the channel (Figure 8.1) are a Dirichlet condition for velocity and a Neumann condition for pressure at the inlet, and vice versa for the outlet.

Equation [8.1] (much like equation [8.2]) is solved from instants $0 = t_0 < \dots < t_{n\Delta t} = t_f$, where Δt is the (dimensionless) time step and n is the number of time steps. The time step is adjusted to satisfy the CFL (Courant–Friedrich–Levy) stability condition

$$\Delta t < C \frac{\Delta x}{V_{\max}}, \quad [8.3]$$

where $V_{\max} = \|\mathbf{v}(t)\|_\infty$ is the maximum velocity in the entire fluid domain at the instant t and C is set by default to 0.8 in the study.

System [8.1] semi-discretized at time step t_n is written as

$$\begin{cases} \frac{\mathbf{v}_{n+1} - \mathbf{v}_n}{\Delta t} + \left(\mathbf{v}_{n+\frac{1}{2}} \cdot \nabla \right) \mathbf{v}_{n+\frac{1}{2}} = -\nabla p_{n+1/2} \\ \quad + \frac{1}{Re} \nabla \cdot (\mathbb{D}_n + \mathbb{D}_{n+1}) + \mathbf{f}_n \\ \nabla \cdot \mathbf{v}_{n+1} = 0, \end{cases} \quad [8.4]$$

where \mathbb{D} is the strain velocity tensor defined by $\mathbb{D} = \frac{1}{2} (\nabla \mathbf{v} + \nabla \mathbf{v}^T)$.

In the case of an incompressible fluid, pressure p is a dual velocity variable that ensures the divergence of the velocity is nil. We therefore use an auxiliary velocity field \mathbf{v}_* according to the Hodge decomposition. The system then becomes (Chorin 1969)

$$\mathbf{v}_{n+1} - \mathbf{v}_n = (\mathbf{v}_{n+1} - \mathbf{v}_*) + (\mathbf{v}_* - \mathbf{v}_n) \quad [8.5]$$

$$\mathbf{v}_* = \mathbf{v}_{n+1} + \Delta t \nabla p_{n+\frac{1}{2}} \quad [8.6]$$

By injecting [8.4] in [8.5], and replacing \mathbb{D}_{n+1} by \mathbb{D}_* , we obtain

$$\begin{cases} \frac{\mathbf{v}_* - \mathbf{v}_n}{\Delta t} + \left(\mathbf{v}_{n+\frac{1}{2}} \cdot \nabla \right) \mathbf{v}_{n+\frac{1}{2}} = \frac{1}{Re} \nabla \cdot (\mathbb{D}_n + \mathbb{D}_*) + \mathbf{f}_n \\ \mathbf{v}_* = \mathbf{v}_{n+1} + \Delta t \nabla p_{n+\frac{1}{2}} \\ \nabla \cdot \mathbf{v}_{n+1} = 0 \end{cases} \quad [8.7]$$

Finally, we can rewrite the system [8.7] by placing the second line beneath the divergence operator and considering the last line of [8.7]. We obtain

$$\begin{cases} \frac{\mathbf{v}_* - \mathbf{v}_n}{\Delta t} + \left(\mathbf{v}_{n+\frac{1}{2}} \cdot \nabla \right) \mathbf{v}_{n+\frac{1}{2}} = \frac{1}{Re} \nabla \cdot (\mathbb{D}_n + \mathbb{D}_*) \mathbf{f}_n \\ \Delta p_{n+\frac{1}{2}} = \frac{1}{\Delta t} \nabla \cdot \mathbf{v}_* \\ \mathbf{v}_{n+1} = \mathbf{v}_* - \Delta t \nabla p_{n+\frac{1}{2}} \end{cases} \quad [8.8]$$

The nonlinear term $\left(\mathbf{v}_{n+\frac{1}{2}} \cdot \nabla \right) \mathbf{v}_{n+\frac{1}{2}}$ is estimated using the second-order offset Godunov scheme by Bell–Collela–Glaz (Bell *et al.* 1989). Next, the auxiliary velocity \mathbf{v}_* is solved implicitly. The pressure $p_{n+1/2}$ of the second line is solved by using the Poisson multi-grid solver on an Eulerian mesh (\mathcal{E}) at each node defined by $x \in \mathcal{E}$. Finally, the third equation gives the velocity field at the next time step, \mathbf{v}_{n+1} . The velocity field \mathbf{v}_{n+1} defined for $x \in \mathcal{E}$ is used in the IBM coupling procedure to move the Lagrangian points defining the structure of the capsule. The Basilisk numerical scheme is accurate to the second order in time because of the offset discretization of pressure.

8.2.2. Solid solver

The forces exerted by the membrane on the fluid are calculated by the solid solver of the Caps3D fluid–structure solver from the reference Lagrangian and the current Lagrangian \mathcal{L} . It is based on a finite element approach and a Lagrangian following of the capsule nodes. Finite elements are third-order accurate in space, and in some couplings they can give fourth-order spatial accuracy (Walter *et al.* 2010). They present a certain numerical stiffness that ensures stability in compression. Based on a given reference to configuration \mathbf{X}_0 of the membrane, the solid equations are solved to deduce the internal elastic forces of its membrane, and finally the stress exerted on the neighboring fluid (Walter 2009). The IMB coupling method described below transfers the stress to the Eulerian fluid (\mathcal{E}).

To define the parameters that characterize the solid, the lengths are non-dimensionalized by the initial radius of the capsule a_0 , the tensions and

energies per unit surface by the surface shear modulus G_s , the stresses by G_s/a_0 , the forces by $G_s a_0$ and the energies by $G_s a_0^2$.

Knowing the Lagrangian configuration (\mathcal{L}) containing the position \mathbf{X} of the capsule nodes, which were at \mathbf{X}_0 in the reference configuration at time $t = 0$, we compute the surface gradient of the transformation \mathbf{F} , as well as the Cauchy–Green (dilatation) tensor \mathbf{C} defined by

$$\mathbf{C} = \mathbf{F}^T \cdot \mathbf{F} \quad [8.9]$$

From the principal dilatations, we obtain the deformation invariants I_1 and I_2 that allow the membrane constituent laws to be defined from the free energy of deformation per unit of undeformed surface area, $w_s(I_1, I_2)$. We use Skalak’s law (Sk) that has a stiffening behavior (Skalak *et al.* 1973)

$$w_s^{\text{Sk}} = \frac{G_s^{\text{Sk}}}{4} (I_1^2 + 2I_1 - 2I_2 + CI_2^2) \quad [8.10]$$

The strain energy function links the Cauchy stress tensor \mathbf{T} to the transformation gradient \mathbf{F} and the Green–Lagrange stress tensor $\mathbf{e} = \frac{1}{2}(\mathbf{F}^T \cdot \mathbf{F} - 1)$ by $\mathbf{T} = \frac{1}{J_s} \mathbf{F} \cdot \frac{\partial w_s^{\text{Sk}}}{\partial \mathbf{e}} \cdot \mathbf{F}^T$, where the Jacobian J_s represents the ratio between deformed and undeformed surfaces. Once the Cauchy tensor \mathbf{T} is known, the membrane elastic load per unit of deformed surface area \mathbf{q} is determined by solving the weak form of the wall equilibrium equation

$$\nabla_s \cdot \mathbf{T} + \mathbf{q} = \mathbf{0}$$

where ∇_s is the surface gradient operator on the deformed configuration. Further details can be found in Walter *et al.* (2010) and Barthès-Biesel *et al.* (2010). The elastic load \mathbf{q} is passed to the fluid solver in the term \mathbf{f} by the IBM method described below.

8.2.3. Fluid–structure coupling by the IBM method

We present the fundamentals of the IBM method. The IBM method is designed to couple a Cartesian mesh (\mathcal{E} for fluid) to a Lagrangian mesh (\mathcal{L} for solid) (Peskin 1972, 2002, Mittal and Iaccarino 2005). The IBM method utilizes a transfer function used for both the volume dispersion of elastic

forces in the fluid ($\mathcal{L} \rightarrow \mathcal{E}$) and approximation of advection rates of the solid ($\mathcal{E} \rightarrow \mathcal{L}$). We propose the IBM filter defined by Beyer and Leveque (1992)

$$\begin{cases} \delta_{\text{BL}}(s) = 1 - s^2, & |s| \leq 1 \\ \delta_{\text{BL}}(s) = 2 - 3|s| + s^2, & 1 < |s| \leq 2 \\ \delta_{\text{BL}}(s) = 0, & 2 < |s| \end{cases} \quad [8.11]$$

The two transfer processes are as follows:

– ($\mathcal{L} \rightarrow \mathcal{E}$): to be injected into the fluid solver, the membrane elastic load per unit surface \mathbf{q} , calculated by the solid solver, is converted into a fluid source term, \mathbf{f} , defined in the Navier–Stokes equation in section 8.2.1. It is first integrated on the surface of the nearest neighbors at each Lagrangian node $\mathbf{X} \in \mathcal{L}$. The integration scheme uses three Hammer points, which guarantees that the force on the finite element is maintained. The forces $\mathbf{F}(\mathbf{X})$ on the Lagrangian node are distributed on the Eulerian grid \mathcal{E} used by the fluid solver using the IBM proposed in Peskin (2002), thus providing the force density

$$\mathbf{f}(\mathbf{x}) = \sum_{\mathbf{X} \in \mathcal{L}} \frac{\mathbf{F}(\mathbf{X})}{(\Delta)^3} \prod_{i=1}^3 \delta_{\text{BL}}\left(\frac{x_i - X_i}{\Delta}\right), \quad [8.12]$$

where Δ is the spatial size of the Eulerian grid \mathcal{E} .

– ($\mathcal{E} \rightarrow \mathcal{L}$): at the end of the integration step of the fluid solver with the new force \mathbf{f} , the new Eulerian velocity field $\mathbf{v}(\mathbf{x}, t_{n+1})$ is used to find the new configuration, $\mathcal{L}(t_{n+1})$, of the Lagrangian nodes $\mathbf{X}(t_{n+1})$ determined by an explicit Euler method. The IBM method approximates the advection velocity $\mathbf{V}(\mathbf{X}(t_n))$ of the solid at the node \mathbf{X} by the local average of the surrounding fluid velocities, via

$$\frac{\mathbf{X}(t_{n+1}) - \mathbf{X}(t_n)}{\Delta t} = \Delta^3 \sum_{\mathbf{x} \in \mathcal{E}} \mathbf{v}(\mathbf{x}) \prod_{i=1}^3 \delta_{\text{BL}}(x_i - X_i(t_n)), \quad \mathbf{X} \in \mathcal{L} \quad [8.13]$$

A volume correction is applied to each time step according to the Lagrange multiplier method used by Mendez *et al.* (2014). The volume correction maintains a relative error on the volume below 6×10^{-4} throughout the simulation, which must be compared to values between 10^{-3} and 10^{-2} without applying the correction.

8.3. Transient flow of a microcapsule into a microfluidic channel with a step

In this study, the capillary number is set to $Ca = 0.05$, and the Reynolds number has a value of $Re = 0$ for Stokes flows and varies from 1 to 15 for Navier–Stokes flows. The mean velocity of the inlet flow is increased linearly from zero velocity to the reference value V between $t = 0$ and the dimensionless time $\tilde{t} = 1$. This time is chosen to guarantee that the capsule has reached its steady form at a minimum distance of $2a_0$ from the step. For steady state, we check that the surface area variation of the capsule membrane with respect to the reference configuration varies by less than 5×10^{-4} for cases $Re = 0$ and $Re = 1$ and by less than 2×10^{-3} for $Re = 15$ on a time interval $\tilde{t} = 1$.

8.3.1. Capsule flow in the Stokes regime

We will start by validating the simulations for a capsule flowing in a channel with a step in the Stokes regime, which was studied experimentally in Gires *et al.* (2016), and for a capsule in a straight channel under Stokes flow, which was studied by Hu *et al.* (2012), Hu *et al.* (2013), Krüger *et al.* (2014), Kusters *et al.* (2014) and Wang *et al.* (2016). The results obtained in the Stokes regime are compared with those obtained by Hu *et al.* (2013) using the Caps3D fluid–structure solver coupling the boundary-integral (BIM) and finite-element (FEM) methods (Walter *et al.* 2010). The evolution of the capsule shape in the plane xOz to $\tilde{t} = 9$ is shown in Figure 8.2.

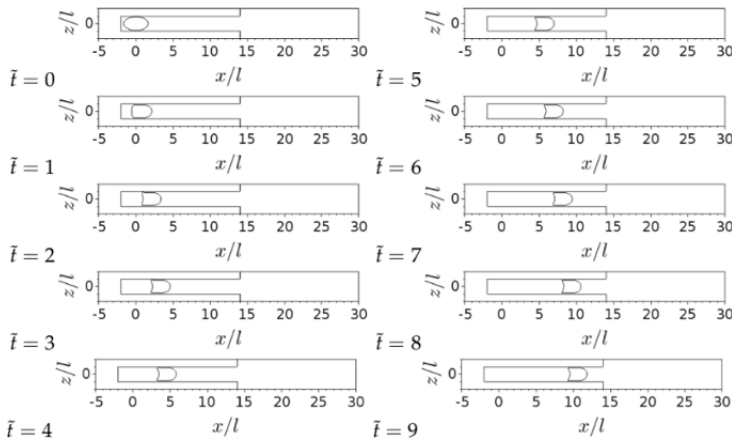


Figure 8.2. Evolution of the capsule shape in the square channel: capsule profile in the xOz plane at different instants, spanning $\tilde{t} = 0$ to $\tilde{t} = 9$

We can observe that steady state is reached shortly before $\tilde{t} = 8$. The temporal evolution of the relative variation of the membrane surface area and the comparison of the steady solution with that of the references (Hu *et al.* 2012, 2013, Gires *et al.* 2016) are represented in Figure 8.3.

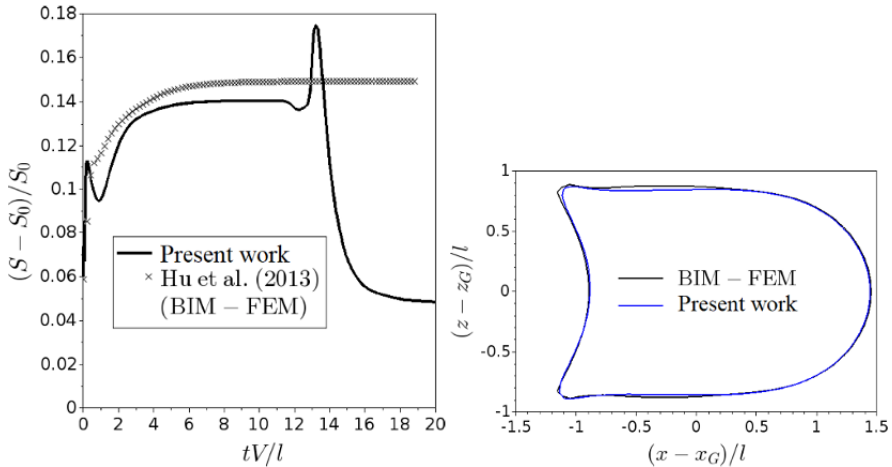


Figure 8.3. a) Temporal evolution of the relative variation of membrane area $(S(\tilde{t}) - S_0)/S_0$ and comparison with the results of Hu *et al.* (2013). b) Profile of the capsule in the xOz plane in steady state at $\tilde{t} = 8$ and comparison of the simulation with the Caps3D results (Hu *et al.* 2013). For a color version of this figure, see www.iste.co.uk/deplano/biological.zip

Figure 8.3(a) shows the temporal evolution of the membrane area through its relative variation with respect to the reference configuration. Note that the area stabilizes shortly before $\tilde{t} = 8$, at a value close to that obtained in the infinite straight channel by Hu *et al.* (2012) and Hu *et al.* (2013). Figure 8.3(b) compares, for $\tilde{t} = 8$, the capsule shape given by the full simulation with that of the previous studies (Hu *et al.* 2012, 2013) (Gires *et al.* 2016). The results are consistent across almost the entire membrane, with the modified Hausdorff distance calculated using the projection method being equal to $d_{H,m,p} \approx 8 \times 10^{-3}$, which validates the steady state of the full simulation. For the evolution of the surface, good concordance is obtained, the variation being 14.1% in the present simulations and 14.9% in the simulation by Hu *et al.* (2012) and Hu *et al.* (2013). The steady state is reached before the capsule reaches a distance $2a_0$ from the step, which ensures that the crossing of the step by the capsule will be independent of the initial conditions. From the area variations shown in Figure 8.3(a), one can note that the membrane at steady state is around 2.4

times more deformed than the initial ellipsoidal state, for which the relative area variation is only 6%.

The complex dynamics of the variation of the capsule shape when passing through the step is well illustrated in Figure 8.4, where it is compared with the experimental data from Gires *et al.* (2016). Four cross-sections of the capsule during the different stages of its flow are shown: one approaching the step, the other during its crossing and the remaining two during relaxation. The blue/pink cross-sections represent the results of our simulations and the images from the Gires *et al.* (2016) experiment are in gray, in the background.

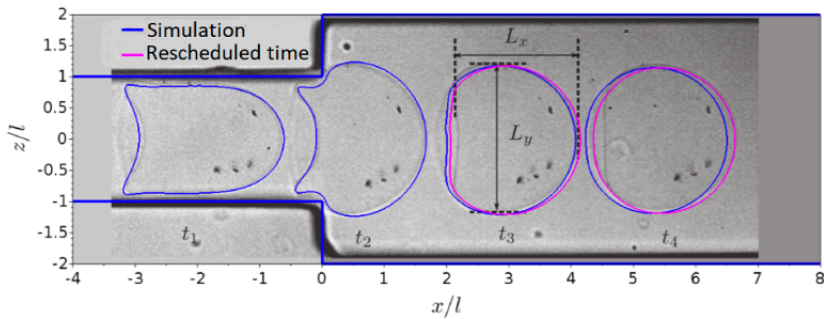


Figure 8.4. Shape of the capsule under flow at different instants around the passage of the step, and overlaying Figure 2 from Gires *et al.* (2016). The capsule cross-sections from the numerical simulation are in blue. The cross-sections at numerical times corrected to correspond to the slower dynamics of the experiment are in pink. For a color version of this figure, see www.iste.co.uk/deplano/biological.zip

Note that the simulated capsule has higher maximum curvatures, which indicates the presence of a bending stiffness in the experimental case. Finally, we note that the membrane from Gires *et al.* (2016) has a membrane viscosity, which is reflected in a slower adoption of a convex rear shape than in our simulations. The authors themselves have made this finding and estimated the membrane viscosity after comparison with the results from Diaz *et al.* (2001).

8.3.2. Relaxation dynamics in the Stokes regime

When the capsule exits the step, the dynamics of its structure are complex and result from the interactions between the fluid flow and the membrane mechanics. The capsule extends rapidly in the vertical direction with an increase in L_z . But because the temporal variation in length is slower in the

flow direction, which was noted by Gires *et al.* (2016), the length L_x is more relevant to characterize the mechanical behavior of the membrane. If the capsule shape and the lengths L_x and L_z are observable experimentally and numerically, the interest of numerical simulation lies in accessing hydrodynamic data, such as velocity (including streamlines) and pressure, as well as quantities related to membrane deformation, such as elastic energy.

Figure 8.5 represents the temporal evolution of the longitudinal length L_x of the capsule. After a rapid decrease when the capsule passes through the step, it asymptotically approaches the length $L_{x,\infty}$, which differs from that of Gires *et al.* (2016) by only $0.02 l$. With regard to the final width of the capsule according to Oz , L_z differs by only $0.004 l$ from the numerical simulations of Gires *et al.* (2016), which is an excellent level of agreement.

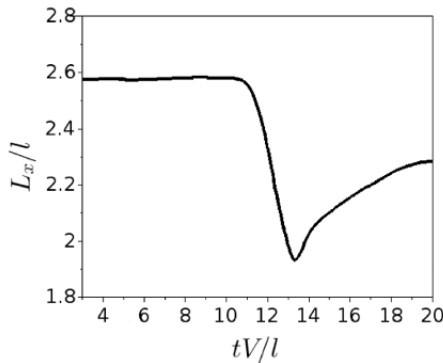


Figure 8.5. Temporal evolution of the length L_x of the capsule in Stokes regime

Figure 8.6 shows the streamlines in the plane xOz : (a) without the capsule and (b) just after the instant when the capsule passes through the step. Note that the tightening of the streamlines due to the presence of the capsule accelerates flow and therefore the capsule. Capsule acceleration is a fairly subtle fluid–structure coupling phenomenon identifiable through numerical simulation.

The velocity field for the longitudinal component v_x at time $\tilde{t} = 13.17$ (Figure 8.7) gives important additional information: it presents a local maximum on the inner side of the capsule edges.

Figure 8.8 presents the evolution of the velocity of the capsule center of gravity. Note that at the steady state, the capsule velocity has a value of $V_{\text{caps}} = 1.21V$, which is in very good agreement with the value

$V_{\text{caps}} = 1.2V$ of the BIM-FEM square-channel simulation from Hu *et al.* (2012). We can observe the sudden acceleration due to the capsule-flow interaction, as explained previously.

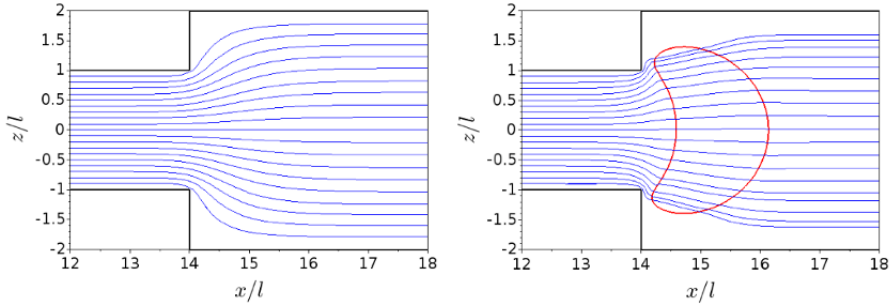


Figure 8.6. Streamlines (blue line) in the sectional plane xOz in the vicinity of the step under Stokes conditions: (a) without the capsule and (b) in the presence of the capsule (red line), at time $\tilde{t} = 13.17$

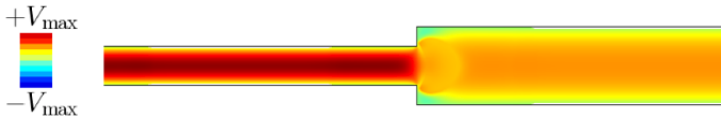


Figure 8.7. Velocity field in the plane xOz under Stokes conditions at time $\tilde{t} = 13.17$. For a color version of this figure, see www.iste.co.uk/deplano/biological.zip

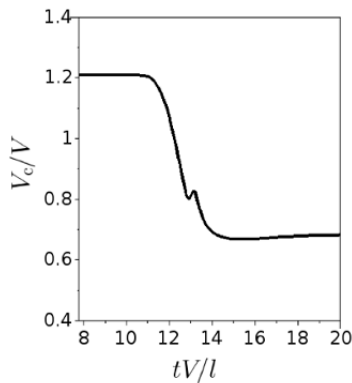


Figure 8.8. Temporal evolution of the capsule velocity in the Stokes regime. For a color version of this figure, see www.iste.co.uk/deplano/biological.zip

We present the capsule (Figure 8.9) at the instant studied, $\tilde{t} = 13.17$. In Figure 8.9(a), we can observe the negative stress values $T_{\text{neg}} \triangleq \min(T_{\text{min}}, 0)$, where $T_{\text{min}} \leq T_{\text{max}}$ are the two eigenvalues of the stress tensor \mathbf{T} . The stresses are normalized by G_s . We can see that $|T_{\text{neg}}|/G_s \ll 1$ everywhere, except on the rear part of the capsule edges, located close to the plane xOy . As the membrane is, at this instant, in large deformations (i.e. $\max\{|T_{\text{min}}|, |T_{\text{max}}|\}/G_s = \mathcal{O}(1)$), we have $T_{\text{max}}/G_s = \mathcal{O}(1)$. The membrane is therefore under stress almost everywhere; in one or two directions, the compression zones being quasi-inexistent. Figure 8.9(b) shows the normal load q_n . We can observe that $q_n < 0$ at the center of the capsule. By contrast, we have $q_n > 0$ on the part near the plane xOz and at this location, $|q_n|$ is maximum. This suggests that the external fluid is overpressurized near the center of the capsule, and under low pressure near its edges.

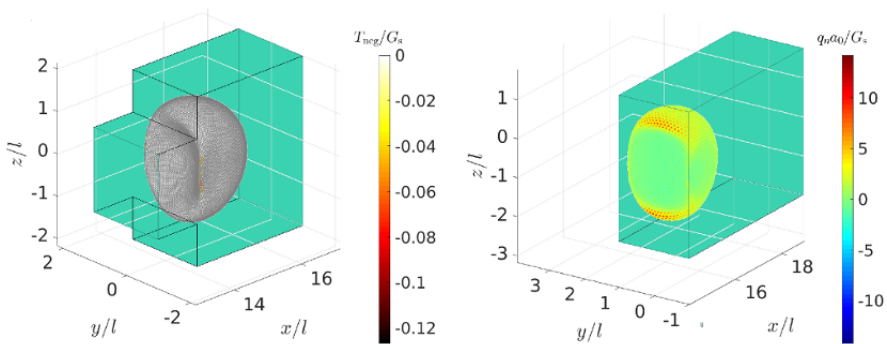


Figure 8.9. 3D representation of membrane state at $\tilde{t} = 13.17$: (a) normalized negative stresses T_{neg}/G_s and (b) normalized normal loads $q_n a_0/G_s$. For a color version of this figure, see www.iste.co.uk/deplano/biological.zip

The deformation at each instant t offers a complementary vision of the dynamics of relaxation. Figure 8.10 presents the strain energy over time. Note that the membrane loses 85% of its energy as it passes through the step, passing from $E_m/G_s a_0^2 \approx 0.74$ to $E_m/G_s a_0^2 \approx 0.11$. The energy stored by the capsule during the deformation imposed by hydrodynamic stresses is released at the crossing of the step, when the velocity of the basic flow is divided by 2. The transition is not monotonous, however, as the fluid flow transmits mechanical energy to the membrane upon expansion along the z axis. The energy then reaches a local maximum of E_m/G_s . In the case of a Stokes flow, this energy transfer gives monotonous relaxation in terms of

lengths (Figure 8.5), which allows the capsule mechanics to be characterized using a simple model of a damped RLC circuit damped, as in Gires *et al.* (2016). We will see that these relaxation dynamics are different for a capsule in Navier–Stokes regime.

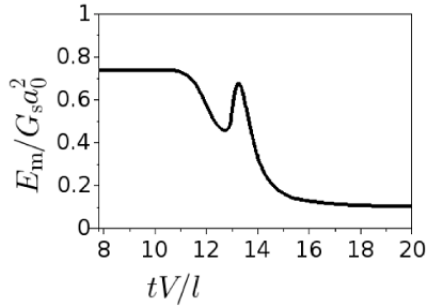


Figure 8.10. Temporal evolution of the membrane energy resulting from the simulation in Stokes regime

8.3.3. Relaxation dynamics in the Navier–Stokes regime

The transient regime is studied in this section within the context of the Navier–Stokes equation for Reynolds numbers of 1 and 15, and is compared with the results of the Stokes regime.

Figure 8.11 presents the evolution of the relative variation of membrane surface $(S - S_0)/S_0$. The line corresponding to $Re = 1$ merges with that of the Stokes regime ($Re = 0$), which indicates that the inertial term is not yet large enough to change the capsule dynamics. However, the behavior of $(S - S_0)/S_0$ for $Re = 15$ is different, with a higher maximum value and offset over time.

The dynamics of relaxation in the Navier–Stokes regime are better understood if one looks at energy exchanges. Figure 8.12 represents the evolution of the energy and the length L_x of the capsule for the different Reynolds numbers. For a Reynolds number $Re = 1$, we have an evolution close to the Stokes regime ($Re = 0$). As for relaxation in a fluid at rest, we find that inertia causes additional exchanges of energy between the fluid flow and the membrane. The oscillation observed for $Re = 15$ is characteristic of an energy exchange, as demonstrated in the case of a capsule at rest (Sarkis 2018).

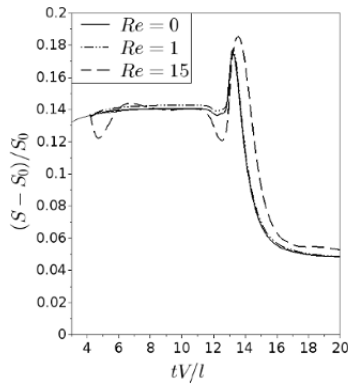


Figure 8.11. Influence of inertia on the temporal evolution of the relative variation of membrane area $(S - S_0)/S_0$

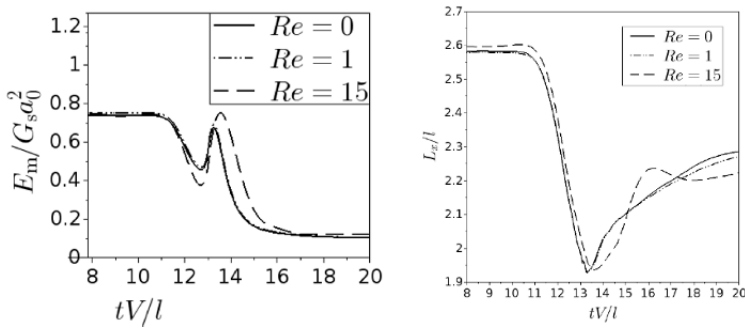


Figure 8.12. Comparison between Stokes and Navier–Stokes regimes: a) evolution of the mechanical energy of the membrane; b) temporal evolution of the capsule length L_x for different Reynolds numbers: $Re = 0, 1$ and 15

The temporal evolution of the longitudinal half-length L_x of the capsule evokes the dynamics of a damped mass-spring system. We propose a Kelvin–Voigt inertial model to predict its evolution. The purpose is to use the reduced model to adjust the results of 3D simulations to identify the values of the model constants and quantify the importance of the contributions of inertia and viscosity to the relaxation of the capsule. The differential equation driving the temporal evolution of its longitudinal half-length L_x is

$$m \frac{d^2 L_x}{dt^2} + \varphi \frac{dL_x}{dt} + k(L_x - a_0) = 0 \quad [8.14]$$

where the stiffness k is associated with the Young surface modulus of the membrane, the shear stress coefficient φ corresponds to a drag coefficient acting on the capsule and the mass m is a measure of the inertia of the system. Further details are provided in Sarkis (2018).

Figure 8.13 shows the results of the Kelvin–Voigt model after adjustment of the parameters for $Re = 1$ and $Re = 15$. This method allows us to deduce the characteristic times of the capsule oscillation, and thus trace back to its physical characteristics. It also shows that the transition from a purely damped system to an oscillating system occurs for $Re \sim 8$.

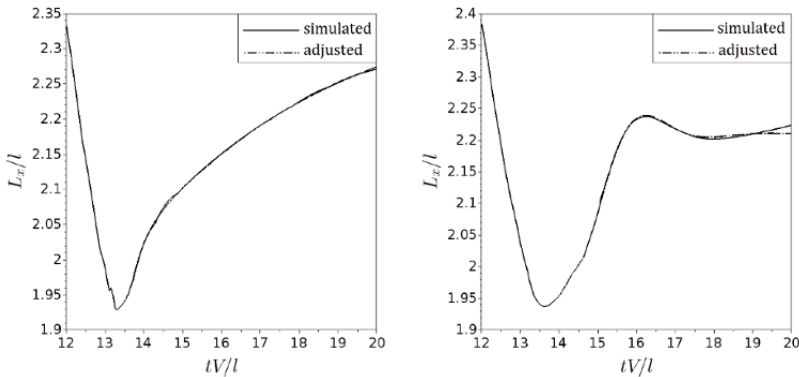


Figure 8.13. Adjustment of L_x curves of simulations by the Kelvin–Voigt inertial model for (a) $Re = 1$ and (b) $Re = 15$

8.4. Discussion and conclusion

We presented a fluid–structure solver coupling a finite–volume fluid solver and a finite–element solid solver using an IBM. The approach was validated in the Stokes regime by comparing the numerical results with the existing results on the flow of a spherical microcapsule in a square cross-section microfluidic channel.

We extended the approach to the Navier–Stokes regime and studied how inertia affects the evolution of the capsule shape and the internal and external flow structures. The detailed study of fluid flow is inaccessible experimentally and it is because of numerical simulations that we can analyze the coupled system. The new coupled fluid–structure solver allowed us to determine two relaxation regimes: a damped regime where the capsule dynamics are in linear regime, and a damped oscillatory regime dominated by

inertia. In this configuration, the system dynamics depend on the Reynolds number Re and the transition from a purely damped system to an oscillating system occurs for $Re \sim 8$.

Because the numerical tool has the ability to investigate the fluid field and capsule state in detail, the analysis focused on a specific instant, at the moment when the capsule exits the step. Access to hydrodynamic data allows us to study the interaction between the streamlines and the shape of the capsule that highlights the deceleration mechanism of the capsule after the passage of the step.

To better understand the physical phenomena that govern the dynamics of capsule relaxation, we studied the interaction between membrane deformation free energy, kinetic energy and viscous dissipation. The analysis of the system from an energy point of view has highlighted the role of energy exchanges between the solid and fluids, and how it leads to the existence of one regime or the other.

The study of the evolution of the capsule shape also showed that key information on the regime and relaxation dynamics could be obtained from the temporal evolution of the longitudinal half-length L_x of the capsule. We therefore proposed to model relaxation using a simple Kelvin–Voigt model assembled in series, with a point mass to account for inertial effects. The model predicts the evolution of L_x very effectively and enables the determination of the type of regime, the value of the Reynolds critical number and the time constants with very high accuracy.

Comparison with other experiments (Gires *et al.* 2016) demonstrated the existence of a bending stiffness and a membrane viscosity in the protein capsules considered in the study. It would therefore be interesting to incorporate these behaviors into the code. To implement bending stiffness, it will be possible to consider different approaches, such as those of Guckenberger *et al.* (2016) or Dupont (2014). Membrane viscosity could be implemented by using existing methods (Yazdani and Bagchi 2013). It would then be interesting to compare the results again with those of Gires *et al.* (2016) and modify the bending stiffness and membrane viscosity. This would offer us a more exhaustive understanding of the dynamics of the capsules under flow and enable us to identify the values of these constants, which are mechanical properties of the membrane.

8.5. Acknowledgements

This project received funding from Sorbonne University (Emergence project, which funded the PhD scholarship of B.S.) and from the European Research Council (ERC) under the European Union's Horizon 2020 research and innovation programme (Grant agreement No. ERC-2017-COG - MultiphysMicroCaps).

8.6. References

- Bando, K. and Yamaguchi, Y. (2017). Mechanical characterization of APA microcapsules by parallel-plate compression. *Journal of Membrane and Separation Technology*, 6, 40–47.
- Barthès-Biesel, D., Walter, J., Salsac, A.-V. (2010). Flow-induced deformation of artificial capsules. In *Computational Hydrodynamics of Capsules and Biological Cells*, Pozrikidis, C. (ed.) Taylor & Francis/CRC Press, London.
- Bell, J.B., Colella, P., Glaz, H.M. (1989). A second-order projection method for the incompressible Navier-Stokes equations. *Journal of Computational Physics*, 85(2), 257–283.
- Beyer, R.P. and Leveque, R.J. (1992). Analysis of a one-dimensional model for the immersed boundary method. *SIAM Journal on Numerical Analysis*, 29(2), 332–364.
- Carin, M., Barthès-Biesel, D., Edwards-Lévy, F., Postel, C., Andrei, D.C. (2003). Compression of biocompatible liquid-filled HSA-alginate capsules: Determination of the membrane mechanical properties. *Biotechnology and Bioengineering*, 82(2), 207–212.
- Chorin, A.J. (1969). On the convergence of discrete approximations to the Navier-Stokes equations. *Mathematics of Computation*, 23(106), 341–353.
- Desai, S., Perkins, J., Harrison, B.S., Sankar, J. (2010). Understanding release kinetics of biopolymer drug delivery microcapsules for biomedical applications. *Materials Science and Engineering: B*, 168(1–3), 127–131.
- Diaz, A., Barthès-Biesel, D., Pelekasis, N. (2001). Effect of membrane viscosity on the dynamic response of an axisymmetric capsule. *Phys. Fluids*, 13, 3835–3838.
- Dubreuil, F., Elsner, N., Fery, A. (2003). Elastic properties of polyelectrolyte capsules studied by atomic-force microscopy and RICM. *Eur. Phys. J. E*, 12, 215–221.
- Dupont, C. (2014). Biomécanique de capsules en écoulement. PhD Thesis, Université de Technologie de Compiègne.
- Fery, A. and Weinkamer, R. (2007). Mechanical properties of micro- and nanocapsules: Single-capsule measurements. *Polymer*, 48, 7221–7235.

- Gires, P.-Y., Barthès-Biesel, D., Leclerc, E., Salsac, A.-V. (2016). Transient behavior and relaxation of microcapsules with a cross-linked human serum albumin membrane. *Journal of the Mechanical Behavior of Biomedical Materials*, 58, 2–10.
- Guckenberger, A., Schraml, M.P., Chen, P.G., Leonetti, M., Gekle, S. (2016). On the bending algorithms for soft objects in flows. *Computer Physics Communications*, 207, 1–23.
- Helfer, E., Harlepp, S., Bourdieu, L., Robert, J., MacKintosh, F.C., Chatenay, D. (2000). Microrheology of biopolymer-membrane complexes. *Phys. Rev. Lett.*, 85, 457–460.
- Henning, S., Edelhoff, D., Ernst, B., Leick, S., Rehage, H., Suter, D. (2012). Characterizing permeability and stability of microcapsules for controlled drug delivery by dynamic NMR microscopy. *Journal of Magnetic Resonance*, 221, 11–18.
- Hu, X.-Q., Salsac, A.-V., Barthès-Biesel, D. (2012). Flow of a spherical capsule in a pore with circular or square cross-section. *Journal of Fluid Mechanics*, 705, 176–194.
- Hu, X.-Q., Sévénicié, B., Salsac, A.-V., Leclerc, E., Barthès-Biesel, D. (2013). Characterizing the membrane properties of capsules flowing in a square-section microfluidic channel: Effects of the membrane constitutive law. *Physical Review E*, 87(6), 063008.
- Ivanovska, I.L., Pablo, P. J.D., Ibarra, B., Sgalari, G., MacKintosh, F.C., Carrascosa, J.L., Schmidt, C.F., Wuite, G.J.L. (2004). Bacteriophage capsids: Tough nanoshells with complex elastic properties. *PNAS*, 101, 7600–7605.
- Krüger, T., Kaoui, B., Harting, J. (2014). Interplay of inertia and deformability on rheological properties of a suspension of capsules. *Journal of Fluid Mechanics*, 751, 725–745.
- Kusters, R., Van der Heijden, T., Kaoui, B., Harting, J., Storm, C. (2014). Forced transport of deformable containers through narrow constrictions. *Physical Review E*, 90(3), 033006.
- de Loubens, C., Deschamps, J., Georgelin, M., Charrier, A., Edwards-Lévy, F., Leonetti, M. (2014). Mechanical characterization of cross-linked serum albumin microcapsules. *Soft Matter*, 10, 4561–4568.
- de Loubens, C., Deschamps, J., Boedec, G., Leonetti, M. (2015). Stretching of capsules in an elongation flow, a route to constitutive law. *Journal of Fluid Mechanics*, 767, R3.
- Mendez, S., Gibaud, E., Nicoud, F. (2014). An unstructured solver for simulations of deformable particles in flows at arbitrary Reynolds numbers. *Journal of Computational Physics*, 256, 465–483.

- Mittal, R. and Iaccarino, G. (2005). Immersed boundary methods. *Annual Review of Fluid Mechanics*, 37, 239–261.
- Peskin, C.S. (1972). Flow patterns around heart valves: A numerical method. *Journal of Computational Physics*, 10(2), 252–271.
- Peskin, C.S. (2002). The immersed boundary method. *Acta Numerica*, 11, 479–517.
- Popinet, S. (2009). An accurate adaptive solver for surface-tension-driven interfacial flows. *Journal of Computational Physics*, 228, 5838–5866.
- Sarkis, B. (2018). Etude numérique de la relaxation de capsules confinées par couplage des méthodes Volumes Finis – Eléments Finis via la méthode des frontières immergées IBM : influence de l’inertie et du degré de confinement. PhD Thesis, Sorbonne University.
- Sato, K., Yoshida, K., Takahashi, S., Anzai, J.-I. (2011). pH- and sugar-sensitive layer-by-layer films and microcapsules for drug delivery. *Advanced Drug Delivery Reviews*, 63(9), 809–821.
- Singh, M., Hemant, K., Ram, M., Shivakumar, H. (2010). Microencapsulation: A promising technique for controlled drug delivery. *Research in Pharmaceutical Sciences*, 5(2), 65.
- Skalak, R., Tozeren, A., Zarda, R.P., Chien, S. (1973). Strain energy function of red blood cell membranes. *Biophysical Journal*, 13, 245–264.
- Walter, J. (2009). Couplage intégrales de frontières–éléments finis : application aux capsules sphériques et ellipsoïdales en écoulement. PhD Thesis, Université de Technologie de Compiègne.
- Walter, J., Salsac, A.-V., Barthès-Biesel, D., Le Tallec, P. (2010). Coupling of finite element and boundary integral methods for a capsule in a Stokes flow. *International Journal for Numerical Methods in Engineering*, 83, 829–850.
- Wang, Z., Sui, Y., Salsac, A.-V., Barthès-Biesel, D., Wang, W. (2016). Motion of a spherical capsule in branched tube flow with finite inertia. *Journal of Fluid Mechanics*, 806, 603–626.
- Yan, S., Min, L., Ding, X., Chen, F., He, X., Xu, C., Zhou, H., Wang, Q., Hao, L., Zou, J. (2016). Hematoporphyrin monomethyl ether polymer contrast agent for ultrasound/photoacoustic dual-modality imaging-guided synergistic high intensity focused ultrasound (HIFU) therapy. *Scientific Reports*, 6, 31833.
- Yazdani, A. and Bagchi, P. (2013). Influence of membrane viscosity on capsule dynamics in shear flow. *Journal of Fluid Mechanics*, 718, 569–595.
- Zhang, Y., Chan, H.F., Leong, K.W. (2013). Advanced materials and processing for drug delivery: The past and the future. *Advanced Drug Delivery Reviews*, 65(1), 104–120.

Conclusion

Words and Things

Valérie DEPLANO¹, José-Maria FULLANA² and Claude VERDIER³

¹*CNRS, IRPHE, Ecole Centrale Marseille,*

Aix-Marseille University, France

²*Institut Jean Le Rond d'Alembert, CNRS UMR 7190,*

Sorbonne University, Paris, France

³*Laboratoire Interdisciplinaire de Physique (LIPhy, UMR 5588),*

Grenoble Alpes University & CNRS, France

The light that this book sheds on biomechanical modeling applied to blood flow in large vessels provides elements for further reflection on numerical model applications in clinical research and experimental protocols.

One of the major benefits of modeling and numerical simulation applied to medicine is the decision support role it is set to play in the near future. Indeed, in the coming years, it is expected that the patient will be “digitized” before entering the operating room to enable the medical team to improve diagnosis and prepare an interventional procedure through a virtual operation.

Ongoing advances in medical imaging such as high-resolution ultrasound, MRI, high-frequency 3D elastography, confocal endomicroscopy, or optical coherence tomography will provide medical staff with a very precise image of the internal structure of the human body and, in particular, of the functions/relationships between tissues/organs/flows, all in real time.

The addition of patient-specific numerical simulations will provide comprehensive information concerning the biological system studied. Thus, one can readily imagine a three-dimensional reconstruction of the patient’s mechanical structures (tissues, organs, vessels and bone) based on medical

Biological Flow in Large Vessels,

coordinated by Valérie DEPLANO, José-Maria FULLANA, Claude VERDIER. © ISTE Ltd 2022.

Biological Flow in Large Vessels: Dialog Between Numerical Modeling and In Vitro/In Vivo Experiments,
First Edition. Valérie Deplano; José-Maria Fullana and Claude Verdier.

© ISTE Ltd 2022. Published by ISTE Ltd and John Wiley & Sons, Inc.

imaging, which will be introduced as input data for numerical calculation tools. The predictive results of these tools will then be added to clinical and biological analyses for more informed medical decision-making. The capabilities and advantages of the numerical tool are significant because, in addition to decision support, it will also be possible, for example, to simulate virtual interventions to inform the medical team of mechanical changes in terms of fluid flows or resulting solid displacements, or to take into account the mechanical impacts induced remotely from the field of intervention.

The numerical studies on aortic aneurysms or bifurcations as well as the application of complete fluid mechanics equations, proposed in the chapters written by the teams at St-Etienne, Marseille and Paris Saclay, illustrate this last point. In the case of aortic aneurysm, it is now known that open surgery induces a high rate of renal complications. Innovative, mini-invasive approaches such as fenestrated (fEVAR), chimney (chEVAR) and periscope (pEVAR) EVAR have thus been developed to treat complex aortic aneurysms and preserve target vessel perfusion. The advantages of these endovascular techniques over conventional open repair are a reduction in mortality and morbidity. In the chapter by the St-Etienne team, numerical studies, an element seen as complementary to endovascular techniques, assist in defining and improving specific, safer procedures and allow virtual testing of prototypes before they go into production. The chapter written by the Marseille team demonstrates that the description and analysis of flow behaviors in some geometric singularities of the cardiovascular system, native or pathological, can be correlated with the evolution dynamics of cardiovascular pathologies using existing associations between the spatiotemporal distributions of certain hemodynamic markers/indexes and in vivo observation of deleterious clinical events. The definition of hemodynamic markers derived from numerical simulations for very precise pathologies, supported by in vitro/in vivo tests, is one of the areas set to develop in the future in engineering–medicine interactions. Finally, the chapter by the Paris-Saclay team clearly shows that the role of hemodynamics in endothelium dysfunction can only be fully elucidated through interactions between mechanics and biology.

The implementation of real-time numerical simulations will also be one of the major challenges for dedicated medical applications in the next few years. It is clear that the intended use is comparable to that of today's ultrasound system, which has the ability to provide real-time and continuous information to the physician during their clinical analysis. Here, in particular, two main avenues are opening up: the first is to reflect in parallel

on the technological advances in applied and theoretical computing, and the second concerns the development of reduced models.

The possibilities offered by theoretical and applied computing in terms of computational speed through mass parallelization and high-performance computing (HPC), which are existing options for solving complex computational problems, combined with GPU programming and rapid storage capacity, mean that complete, real-time physiopathological flow computations will become reality tomorrow. The creation of large databases and their rapid and reliable processing by machine learning, or indeed deep learning with the advent of quantum computers, point to the multiple possibilities of implementing “complete” numerical models in creating tools to predict pathology evolution and other medical applications.

Nevertheless, real-time computation remains, for the moment, a dream, a complete simulation of fluid mechanics in a typical case like those presented in this book currently taking days of computation time. The second avenue is reduced models, which are faster and increasingly accurate. This more affordable alternative is now widely studied and applied in research laboratories, although it has not yet entered clinical routine on a massive scale. Reduced models are models that are derived from the complete equations of fluid and solid mechanics and, by reducing dimensions, they enable rapid numerical computations. An overview of these was given in two of the chapters. The first, proposed by the INRIA team, presents virtual liver surgery using reduced modeling. Liver lobes are notably represented by 0D models in order to simulate the ablation of one or more lobes during a hepatectomy. The numerical data thus obtained, placed in comparison with clinical experience, then provide elements of discussion to explain non-trivial phenomena of flow increase and decrease in the liver. The second chapter is presented by the Sorbonne University team with the study of a stenosis and the associated pressure drop. Regardless of the causes, vessel blockage affects hemodynamics, and rapid information on the entire blood network is necessary for rapid and early diagnosis. Reduced-order models (0D and 1D) are then developed to determine, in real time, the pressure drop associated with the passage of a flow through a stenosis and to thus propose a pathological marker for clinical use.

Another rather fascinating aspect of numerical simulations applied to blood flows concerns the study of the dynamics of flexible objects in a blood flow. These objects may be red blood cells, white blood cells or indeed capsules. Their mechanical behavior under flow is of major interest in

helping to understand their dynamics. The chapter by the Grenoble team shows that advances in understanding the dynamics of micro-circulation allow us to consider interactions at the interface between medicine, physics and mechanics, particularly in the context of erythrocyte pathologies, because of the increasingly predictive nature of the models. The chapter by the Montpellier team thus presents a tool designed to analyze the collective motions of these objects, paving the way for new theoretical developments in terms of the dynamics of blood cells and their interaction in flow.

From the point of view of modeling and implementation of coupled equations (solids and fluids), the theoretical and numerical approaches of fluid–structure interaction are quite recent compared to developments in fluid flow models or rigid solid mechanics. Theoretical and algorithmic efforts are yet to be produced. In the case of capsules, an overview of which is presented in the chapter written by the Compiègne team, relatively new numerical schemes are implemented. The role of numerical simulations here is to understand the dynamics of capsules in order to control their navigation in blood flow and their behavior in complex geometries, ultimately to modulate and control the distribution of an active principle to a specific target, with multiple applications.

In addition to taking into account fluid–structure couplings, whether complete or reduced, future models will need to be more evolved and integrate growth and remodeling processes, whether natural or caused by the evolution of the pathology or associated surgical or endovascular treatments.

The models of the future will need to describe the correlations between mechanisms taking place at different spatial scales, in order to link molecular, cellular and tissue aspects to those of the organ.

In the future, solutions will have to be found so that the complexity of such spatiotemporal models can be understood.

The dialog established between the medical field and research in mechanics for the living, numerical modeling and mathematics will have to be sustained, and interdisciplinarity extended to other scientific fields, such as biology and bioinformatics.

This book, we hope, forms part of that movement.

Marseille, Paris and Grenoble, March 2021

List of Authors

Jean-Noël ALBERTINI
Service de Chirurgie
Cardiovasculaire
CHU Saint-Etienne
France

Stéphane AVRIL
Mines Saint-Etienne
University of Lyon
Sainbiose INSERM U1059
Jean Monnet University
Centre CIS
Saint-Etienne
France

Abdul I. BARAKAT
Ecole Polytechnique
Palaiseau
France

Sabrina BEN-AHMED
Service de Chirurgie Vasculaire et
Médecine Vasculaire
CHU Limoges
France

Alain BÉROD
IMAG
CNRS
University of Montpellier
and
Sim&Cure
Montpellier
France

Nathalie BODDAERT
Hôpital Necker Enfants Malades
APHP
Centre M3C
Paris
France

Christophe CHNAFA
IMAG
CNRS
University of Montpellier
and
Sim&Cure
Montpellier
France

Francesca CONDEMI
Mines Saint-Etienne
University of Lyon
Sainbiose INSERM U1059
Jean Monnet University
Centre CIS
Saint-Etienne
France

Valérie DEPLANO
CNRS
IRPHE
Ecole Centrale Marseille
Aix-Marseille University
France

Jean-Pierre FAVRE
Service de Chirurgie
Cardiovasculaire
CHU Saint-Etienne
France

C. Alberto FIGUEROA
Department of Biomedical
Engineering
University of Michigan
Ann Arbor
USA

José-Maria FULLANA
Institut Jean Le Rond d'Alembert
CNRS UMR 7190
Sorbonne University
Paris
France

Morgane GARREAU
IMAG
CNRS
University of Montpellier
and
ALARA Expertise
Strasbourg
France

Etienne GIBAUD
IMAG
CNRS
University of Montpellier
France

Carine GUIVIER-CURIEN
CNRS
IRPHE
Ecole Centrale Marseille
Aix-Marseille University
France

Pierre-Yves LAGRÉE
Institut Jean Le Rond d'Alembert
CNRS UMR 7190
Sorbonne University
Paris
France

Anthony LARROQUE
IMAG
CNRS
University of Montpellier
France

Stephanie LINDSEY
IMAG
CNRS
University of Montpellier
France

Marco MARTINS AFONSO
IMAG
CNRS
University of Montpellier
France

Pascal MATTÉOLI
IMAG
CNRS
University of Montpellier
France

Simon MENDEZ
IMAG
CNRS
University of Montpellier
France

Rodrigo MENDEZ ROJANO
IMAG
CNRS
University of Montpellier
France

Dorian MIDOU
IMAG
CNRS
Univeristy of Montpellier
France

Franck NICLOUD
IMAG
CNRS
University of Montpellier
France

Sanjay PANT
Swansea University
Wales

Thomas PODGORSKI
CNRS
Université Grenoble Alpes
France

Thomas PUISEUX
IMAG
CNRS
University of Montpellier
and
ALARA Expertise
Strasbourg
France

Francesca RAIMONDI
Hôpital Necker Enfants Malades
APHP
Centre M3C
Paris
France

Eugenio ROSSET
Service de Chirurgie Vasculaire
CHU Clermont-Ferrand
INSERM
Université Clermont Auvergne
France

Anne-Virginie SALSAC
Université de Technologie
de Compiègne
France

Bruno SARKIS
Sorbonne University
Paris
and
Université de Technologie
de Compiègne
France

Julien SIGÜENZA
IMAG
CNRS
University of Montpellier
and
Sim&Cure
Montpellier
France

Pierre TARACONAT
IMAG
CNRS
University of Montpellier
and
Horiba Medical
Grabels
France

Jeanne VENTRE
Institut Jean Le Rond d'Alembert
CNRS UMR 7190
Sorbonne University
Paris
France

Claude VERDIER
Laboratoire Interdisciplinaire
de Physique (LIPhy, UMR 5588)
Grenoble Alpes University & CNRS
France

Irene E. VIGNON-CLEMENTEL
Inria Saclay Ile-de-France
Research Center
France

Guillermo VILAPLANA
Ecole Polytechnique
Palaiseau
France

Vladeta ZMIJANOVIC
IMAG
CNRS
Univeristy of Montpellier
France

Index

0D model, 164, 169
1D model, 164, 173, 175, 176, 178,
179
3D model, 153

A, B

aggregation, 6, 18, 19, 21–27, 31
aortic aneurysm, 44, 45, 59, 63, 97
arterial stenoses, 163, 164, 173, 179
biomechanical models, 70, 77, 85
blood, 44–46, 58, 59, 63
 flows, 70, 72, 73, 183, 184, 191
branches, 109, 110, 113–119, 123,
124, 126, 128, 130–134

C, D

clinical data, 139, 142, 144–146
computational fluid dynamics, 45, 63,
186

deformation, 209, 211, 213, 218, 220,
224

E, F

endothelium, 111–115, 134
endovascular aneurysm repair
(EVAR), 44
 chimney, 50
 fenestrated, 50
Fåhræus, 29
finite-element method (FEM), 215
finite-volume fluid solver, 209, 223
fluid-structure interactions, 209

H

hemodynamics
 markers, 95
 model, 142
hemoglobin, 7, 8, 11, 12, 15
hyperelastic, 209

I, L

immersed boundary method, 209
inflammation, 111–113, 136
large-eddy simulations, 185
looping flow, 121
lumped parameter model, 140, 141, 152

M

medical
 application, 163, 179
 devices, 196
 imaging, 183, 193
membrane, 5, 8–11, 13–16, 22–25
microcapsules, 208
microcirculation, 10–12, 26–31
model parameterization, 139, 157
multi-ring model, 164, 165, 167, 171, 172, 179
multiscale modeling, 143

N

Navier–Stokes equations, 164–166, 179
network, 2, 3, 6, 9, 10, 13, 18, 21, 22, 24–31
non-Newtonian, 6, 17, 18, 20
numerical simulations, 210, 218, 223

O, P

oscillatory shear index (OSI), 129, 130
parameter identification, 144, 145
pathologies, 7, 11, 13–15, 31
patient-specific, 139, 141–144
plaque rupture, 112, 113
platelet activation state, 47

pressure drop, 165, 169, 170, 175–179

R

red blood cells, 184, 187, 189, 190, 195
reduced model, 141, 144, 145, 148, 150
reduced order model, 163, 164, 177, 179
relaxation, 207, 209, 217, 220–224
renal artery, 44–46, 52, 55, 56, 58
Reynolds number, 116, 118, 119, 122–126, 128, 134

S

shear-thinning, 18, 20, 21
skewness, 126, 131–133, 135
stenosis, 44, 45, 50, 52, 53, 78–80, 84, 85, 95

T

thrombosis, 109, 112, 113, 196, 197
thrombus formation, 95–98
time-varying, 145, 149, 151, 152
turbulence, 185, 186, 193

V, W

validation, 184–189, 199
valve prostheses, 73
vortical structures, 72
wall shear stress, 44, 62, 85–88, 90–94, 114, 115, 117–130, 133–135, 164
Womersley solution, 165, 171